Investigation of Ceria-Based Redox Materials for Thermochemical Solar Fuel Production

Von der Fakultät für Maschinenwesen der Rheinisch-Westfälischen Technischen Hochschule Aachen zur Erlangung des akademischen Grades eines Doktors der Ingenieurwissenschaften genehmigte Dissertation

vorgelegt von

FRIEDEMANN CALL

Berichter: Univ.-Prof. Dr.-Ing. Robert Pitz-Paal
Apl. Prof. Dr. rer. nat. habil. Martin Schmücker

Tag der mündlichen Prüfung: 10.11.2014

Preface

This work was accomplished at the Institute of Solar Research at the German Aerospace Center (DLR) in the context of the Virtual Institute SolarSynGas, a project funded by the Initiative and Networking Fund of the Helmholtz Association of German Research Centers.

I am using this opportunity to express my gratitude to Univ.-Prof. Dr.-Ing. Robert Pitz-Paal, Co- director of the Institute of Solar Research, for supervising my work and for the fruitful dialogue, as well as Prof. Dr. rer. nat. habil. Martin Schmücker for acting as the second examiner and, even more important, for the countless constructive discussions regarding my results. I also want to thank Univ.-Prof. h. c. (RU) Dr.-Ing. Dipl.-Wirt.Ing. Thomas Gries for acting as the president of the examination board.

I gladly honor the support provided by Dr. Martin Roeb. He guided my research and always shared feedback that was more than helpful to accomplish this thesis. I express my warm thanks to Dr. Christian Sattler for his trust and confidence in me and his backing during the last years. I appreciate very much that Dr. Heike Simon, Nicole Knoblauch, and Lamark de Oliveira have assisted me with their comprehensive competence in laboratory and chemical issues. I also thank Tijana Paraknewitz for her synthesis and characterization work.

Many thanks go to all other PhD students and colleagues of my institute for providing such a welcoming and excellent work atmosphere. In particular, I would like to thank Dr. Matthias Lange, who fought the same thermochemical cycle and shared his findings as well his frustrations in an always inspiring way; Daniel Maldonado Quinto, who kept me motivated at all times; Jan Felinks and Dr. Martina Neises, for sharing my office for several years and keeping the working atmosphere more than decent; Dr. Nicolas Bayer-Botero, for his critical but fruitful comments, and Dr. Stefan Brendelberger for his constructive ideas and advice.

This thesis would not have been possible without the grand encouragement given by my family throughout all my life that I can always rely on. I want to thank my Mother, Simon and Christoph for their trust and never ending support.

for my father

Abstract

The overarching goal of this thesis is to pave the way towards the commercialization of solar-driven thermochemical cycles harnessing the redox reaction of ceria with water and CO_2 to produce solar fuels. Because preliminary process analysis identified the material properties as the major bottleneck, this thesis focused on the improvement and evaluation of ceria. Doping with zirconia and rare-earth metals served as the approach to improve its properties, while thermogravimetry analysis was used as the method to experimentally evaluate its performance.

Screening campaigns of various powder compositions identified the most promising doped compositions. The beneficial effect of doping was ascribed to modifications of the crystal structure that, in the case of zirconia, facilitate the reduction and, in the case of rare-earth metals, enhance the bulk diffusion. For following experimental campaigns, porous and dense pellets made of pure ceria and the most promising doped materials were manufactured. Investigations on the reaction kinetics of these pellets carried out in the thermobalance qualitatively assessed the impact of doping and microstructure. Since a quantitative interpretation of the experimental data seemed unreasonable, the determination of reliable reaction rates was left to subsequent research.

The reduction extent δ in equilibrium-state at varying conditions of the doped-material was studied in a second campaign using pellets. Within a physical reaction model, the dependency of δ on temperature and partial pressure of oxygen was described. Based on the derived relations, Ellingham diagrams were established that convey the reduction enthalpy and entropy as a function of δ. Employing both, the δ-relation and the function of the reduction enthalpy in a process model, which considers the major losses, estimated the maximum solar-to-fuel efficiencies of pure ceria as well as of the doped materials. A parametric study, including partial pressure of oxygen, temperature, heat recuperation and concentrating system, revealed solar-to-fuel efficiencies of the doped materials to be twice as high compared to pure ceria. Suitable doping improves the efficiency, in particular, at a temperature as low as 1200°C, which should facilitate the technical realization of the process considerably. However, because such low temperatures correspond to low specific yields, the mass flow of the material through the receiver drastically increases. The implications of high mass flows on the feasibility of the process are manifold and initiate various objectives to future research. Especially, investigating the correlation between reduction rate and heat incorporation/transfer is essential to further assess the potential of the process.

Zusammenfassung

Das Ziel der vorliegenden Arbeit ist die Weiterentwicklung von solarbetriebenen thermochemischen Kreisprozessen, die mithilfe der Redox Reaktion von Ceroxid Synthesegas produzieren. Da die vorläufige Prozessanalyse vor allem die Materialeigenschaften als entscheidend für die potentielle Effizienz identifiziert hat, beschäftigt sich diese Arbeit in erster Linie mit der Weiterentwicklung und Evaluierung des Materials Ceroxid. Das Dotieren mit Zirkonoxid und Metallen der Seltenen Erden diente dabei als Ansatz, die Eigenschaften zu verbessern sowie die thermogravimetrische Analyse als Methode zur experimentellen Evaluierung des Umsatzes.

In Screening Kampagnen mit verschiedenen Mischungsverhältnissen der Ausgangsstoffe wurden die aussichtsreichsten Dotierungen bestimmt. Dabei kann die positive Auswirkung des Dotierens der Modifikation der Kristallstruktur zugeschrieben werden, die bei der Dotierung mit Zirkon die Reduktion erleichtert und bei der Dotierung mit Selten Erden die Diffusion verbessert. In den darauf folgenden Studien wurden sowohl dichte als auch poröse Pellets aus den aussichtsreichsten Zusammensetzungen hergestellt. Erste Untersuchungen der Kinetik mithilfe einer Thermowaage zeigten den deutliche Einfluss der Dotierung und der Mikrostruktur. Da diese Daten eine quantifizierte Interpretation nicht erlaubten, wird die genaue Bestimmung der Kinetik zukünftigen Forschungsarbeiten überlassen.

Der Umfang der Reduktion δ der dotierten Materialen wurde in Gleichgewichtsversuchen unter variierenden Bedingungen untersucht und die dabei bestimmte Abhängigkeit von der Temperatur und des Sauerstoffpartialdrucks innerhalb eines physikalischen Reaktionsmodells beschrieben. Aufbauend darauf wurden Ellingham Diagramme der Redoxreaktionen erstellt, die in Abhängigkeit von δ Aufschluss über die Reaktionsenthalpie und –entropie geben. Durch die Kombination des Verhaltens von δ und der Reaktionsenthalpie wurde ein Prozessmodell erstellt, das unter Berücksichtigung der Hauptverluste die Effizienz der Umwandlung von solarer Energie in Brennstoff kalkuliert. Im Rahmen einer Parameterstudie, die den Einfluss des Sauerstoffpartialdrucks, der Temperatur, der Wärmerückgewinnung und des solarkonzentrierenden Systems vergleicht, wurde eine Verdopplung der Prozesseffizienz durch das Dotieren festgestellt. Besonders bei niedrigen Temperaturen von 1200°C sind die Verbesserungen signifikant. Diese niedrigen Temperaturen können einerseits die technische Realisierung des Prozesses entscheidend verbessern, anderseits führen sie zu relativ niedriger spezifischer Aktivität des Materials, was wiederum sehr hohe Massenströme des Materials im Receiver/Reaktor zur Konsequenz hat. Die Handhabung solcher hohen Massenströme wird dementsprechend eine Hauptaufgabe der zukünftigen Erforschung dieser Kreisprozesse sein. Dabei sollte besonders der Zusammenhang zwischen Wärmeeinkopplung und -transport und der Reaktionskinetik im Fokus der Untersuchungen stehen.

Contents

Nomenclature

Symbols

$a(\mathrm{M})$	activity of a solid reactant M	
a_H	fitting parameter reduction enthalpy change	$\mathrm{kJ} \cdot 0.5\ \mathrm{mol}_{\mathrm{O_2}}^{-1}$
A_H	fitting parameter reduction enthalpy change	$\mathrm{kJ} \cdot 0.5\ \mathrm{mol}_{\mathrm{O_2}}^{-1}$
A_{rec}	aperture of the receiver	m^2
$A_{\mathrm{red,\ ox}}$	prefeactor/frequency factor of reduction or oxidation	s^{-1}
a_S	fitting parameter reduction entropy change	$\mathrm{J} \cdot \mathrm{K}^{-1} \cdot 0.5\ \mathrm{mol}_{\mathrm{O_2}}^{-1}$
A_S	fitting parameter reduction entropy change	$\mathrm{J} \cdot \mathrm{K}^{-1} \cdot 0.5\ \mathrm{mol}_{\mathrm{O_2}}^{-1}$
β	temperature rate	$\mathrm{K{\cdot}min}^{-1}$
C	solar concentration ratio	
c_{M}	concentration of liquid solution of nitrates (M = Ce, Zr, Y, La, Sm, Gd)	$\mathrm{mol} \cdot \mathrm{l}^{-1}$
c_{mat}	molar heat capacity	$\mathrm{J} \cdot \mathrm{K}^{-1}$
$c(\mathrm{I})$	concentration of I ($\mathrm{I} = \mathrm{O_2}, \mathrm{V_{\ddot{O}}}, \mathrm{Ce}^{3+}, \mathrm{Ce}^{4+}$)	mol per unit
D_0	diffusion coefficient	m
δ	reduction extent of a metal oxide MO / amount of oxygen released during reduction ($\mathrm{M}_a\mathrm{O}_b \rightarrow \mathrm{M}_a\mathrm{O}_{b-\delta} + {}^{\delta}/_{2}\mathrm{O_2}$)	
$\Delta\delta_{\mathrm{d\text{-}d}}$	difference in reduction extent of two dense pellets	
$\Delta\delta_{\mathrm{p\text{-}d}}$	difference in reduction extent of one porous and one dense pellet	
$\delta(T, p(\mathrm{O_2}))$	delta dependence on temperature and partial pressure of oxygen (equilibrium calculations)	
δ_{max}	assumed max reduction extent for equilibrium calculations	
$\delta_{\mathrm{max,\ stoic}}$	maximium stoichiometrical reduction extent (for pure ceria $\delta = 0.5$)	
d	pellet diameter	mm
ϵ	emissivity	
E_{aux}	auxiliary energy of TCCs	J
E_{fuel}	energy stored in the produced fuel	J
$E_{\mathrm{H_2}}$	higher heating value of hydrogen	J
$\varepsilon_{\mathrm{hr}}$	heat recuperation effectiveness	
$E_{\mathrm{red,\ ox}}$	activation energy of reduction or oxidation	

ΔE	difference between activation energies of reduction and oxidation	
$\eta_{\text{elec to pump}}$	efficiency to convert electricity into pumping work	%
$\eta_{\text{heat to elec}}$	heat-to-electricity efficiency	%
η_{opt}	optical efficiency	%
$\eta_{\text{opt}}^{\text{dish}}$	assumed annual optical efficiency of a dish system	%
$\eta_{\text{opt}}^{\text{tower}}$	assumed annual optical efficiency of a tower system	%
$\eta_{\text{solar to fuel}}$	solar-to-fuel efficiency	%
$\eta_{\text{thermal to fuel}}$	thermal-fuel-efficiency	%
$f_{\eta}^{\varepsilon_{\text{hr}}}$	change in efficiency by increasing ε_{hr}	%
$f_{\eta}^{T_{\text{red}}}$	change in efficiency by increasing T_{red}	%
ΔG^0	change in standard Gibbs energy during a reaction	J
$\Delta G_{\text{red, } T_{\text{ox}}}$	change in Gibbs energy during oxidation at T_{ox}	J
$\Delta G_{\text{red, } T_{\text{red}}}$	change in Gibbs energy during reduction at T_{red}	J
h	pellet height	mm
ΔH_{red}	reduction enthalpy	J
ΔH^0	change in enthalpy during a reaction	J
$\Delta H_{f, T_{\text{ox}}}^{\text{H}_2\text{O, CO}_2}$	formation enthalpy of water or carbon dioxide at T_{ox}	J
ΔH_{mat}	enthalpy difference between reduced and oxidized metal oxide	J
$\Delta H_{\text{red, } T_{\text{ox}}}$	change in enthalpy during oxidation at T_{ox}	J
$\Delta H_{\text{red, } T_{\text{red}}}$	change in enthalpy during reduction at T_{red}	J
k	equilibrium rate constant	
$k_{\text{red, ox}}$	rate constants of reduction or oxidation	
k_s	surface reaction rate constant	
l_d	characteristic diffusion length scale	m
l_{index}	qualitative diffusion length of a pellet indicated by the index	s
Δm	relative mass change regarding the oxidized mass	%
$\Delta m'_{\text{ox}}$	relative mass change rate during oxidation in respect to the oxidized mass	$\%\cdot\text{min}^{-1}$
Δm_{max}	maximum relative mass change regarding the oxidized mass	%
$\Delta m_{\text{red, ox}}$	relative mass change during reduction or oxidation	%
m_{initial}	initial mass of a smple subjected to thermogravimetric analysis	mg
m_{pel}	pellet mass	mg
M_{ox}	molar weight of the oxidized material	$\text{mol}\cdot\text{gr}^{-1}$
M_{red}	molar weight of the reduced material	$\text{mol}\cdot\text{gr}^{-1}$
$\dot{m}_{\text{mat}}$	mass flow of the redox material in a reactor	$\text{kg}\cdot\text{s}^{-1}$
n	oxygen partial pressure dependence (equilibrium calculations)	

$n_m(CO)$	specific CO yield per gram oxidized material and cycle	$mmol_{CO} \cdot gr_{mat}^{-1}$
$n_m(O_2)$	specific O_2 yield per gram oxidized material and cycle	$mmol_{O_2} \cdot gr_{mat}^{-1}$
$n_n(CO)$	molar CO yield per mol oxidized material and cycle	$mmol_{CO} \cdot mol_{mat}^{-1}$
$n_n(O_2)$	molar O_2 yield per mol oxidized material and cycle	$mmol_{O_2} \cdot mol_{mat}^{-1}$
$\dot{n}$	reaction rate (explanation: $\dot{n}_{CZ,\,CZS}$ (cycle, regime))	$mmol_{O_2} \cdot gr_{mat}^{-1} \cdot min^{-1}$
$\dot{n}_{fuel}$	molar fuel production rate	$mol_{CO,\,H_2} \cdot min^{-1}$
P_{index}	qualitative porosity of a pellet indicated by the index	
P_{cond}	thermal conduction losses	W
P_{conv}	thermal convection losses	W
Φ	pellet porosity	%
$p(O_2)$	partial pressure of oxygen	Pa
P_{rera}	radiation losses	W
P_{sol}	incident solar power	W
P_{th}	heat flux usable for the reaction	W
Q	heat	J
$Q_{H_2O,\,CO_2}$	sensible heat of educt gases H_2O or CO_2	J
Q_{mat}	sensible heat of the oxidized metal oxide	J
Q_{mech}	heat equivalent for mechanical work to move the redox material	J
Q_{ox}	heat release during during oxidation	J
Q_{pump}	heat equivalent for pumping work	J
Q_{sweep}	sensible heat of the sweep gas	J
R	ideal gas constant	$J \cdot mol^{-1} \cdot K^{-1}$
$r_{M^{x+}}$	radius of a cation of the metal M with the valence x [Shan 76]	nm
σ	Stefan-Boltzmann constant	$W \cdot m^{-2} \cdot K^{-4}$
ΔS^0	change in standard entropy during a reaction	J
ΔS_{conf}	configuration entropy change during reduction	$J \cdot K^{-1}$
ΔS_{dev}	deviation between configuration entropy and solid-state entropy change	$J \cdot K^{-1}$
ΔS_{mat}	entropy difference between reduced and oxidized metal oxide	$J \cdot K^{-1}$
$\Delta S_{red,\,T_{ox}}$	change in entropy during oxidation at T_{ox}	$J \cdot K^{-1}$
$\Delta S_{red,\,T_{red}}$	change in entropy during reduction at T_{red}	$J \cdot K^{-1}$
s	starch content	wt. %
$S_{T_{ox}}^{H_2,\,CO}$	entropy of hydrogen or carbon monoxide at T_{ox}	J
$S_{T_{ox}}^{H_2O,\,CO_2}$	entropy of water or carbon dioxide at T_{ox}	J
$S_{T_{red}}^{O_2}$	entropy of oxygen at T_{red}	J
t	time	s

T_{ox}	oxidation temperature	°C or K
$\Delta T_{ox \rightarrow red}$	temperature difference between oxidation and reduction	°C or K
T_{red}	reduction temperature	°C or K
$u(v)$	standard uncertainty of the mean of the measurand v	
V_i	volumes of nitrate solutions ($i = x, y, z$)	ml
W_{pump}	pumping work	J
X_{ox}	relative oxidation extent with respect to all cerium atoms	at.% $Ce^{3+\rightarrow 4+}$
X_{red}	relative reduction extent with respect to all cerium atoms	at.% $Ce^{4+\rightarrow 3+}$
x	Zr content x of $Ce_{1-x}Zr_xO_2$	
y	trivalent content y of $Ce_{0.85-y}Zr_{0.15}RE_yO_{2-0.5y}$	
z	cerium content z with $z = 1 - x - y$	

Chemical Fomulars

Al_2O_3	aluminium(III) oxide, also known as alumina
Ar	argon
Ce'_{Ce}	reduced cerium lattice atom Ce^{3+} (Kröger-Vink notation)
Ce_{Ce}	oxidized cerium lattice atom Ce^{4+} (Kröger-Vink notation)
Ce_2O_3	cerium(III) oxide, also known as reduced ceria ($Ce_2O_3 = CeO_{1.5}$)
CeO_2	cerium(IV) oxide, also known as ceria, cerium oxide or cerium dioxide
$C_6H_8O_7$	citric acid monohydrate
CO_2	carbon dioxide
CO	carbon monoxide
Fe_3O_4	iron(II,III) oxide, also known as magnetite
FeO	iron(II) oxide, also known as wüstite
H_2	hydrogen
M_aO_b	metal oxide of the element M
MO_{ox}	oxidized metal oxide
MO_{red}	reduced metal oxide
$NiFe_2O_4$	nickel ferrite
NiO	nickel(II) oxide
O_2	oxygen
$RE(NO_3)_2$	rare-earth(III) nitrate hexahydrate (RE = Ce, Y, La, Sm or Gd)
RE_2O_3	rare-earth oxide (RE = Y, La, Sm or Gd)
RE	rare-earth elements (RE = Y, La, Sm or Gd)
$V_{\ddot{O}}$	oxygen vacancy (Kröger-Vink notation)
ZrO_2	zirconium(IV) oxide, also known as zirconia or zirconium dioxide

ZnO	zinc oxide
$ZrO(NO_3)_3$	zirconium(IV) oxynitrate hydrate

Abbrevation and Acronyms

C	short name of pure ceria pellets (CeO_2)
CZ	short name of ceria-zirconia pellets ($Ce_{0.85}Zr_{0.15}O_2$)
CZL	short name of lanthanum-doped ceria-zirconia pellets ($Ce_{0.82}Zr_{0.15}La_{0.03}O_{1.99}$)
CZS	short name of smarium-doped ceria-zirconia pellets ($Ce_{0.82}Zr_{0.15}Sm_{0.03}O_{1.99}$)
DLR	Deutsches Zentrum für Luft- und Raumfahrt e.V. (German Aerospace Center)
DNI	direct normal irradiance 1000 $W \cdot m^{-2}$
EDS	energy dispersive X-ray spectroscopy
GUM	guide to the expression of uncertainty in measurement
MFC	mass flow controller
MS	mass spectrometer
ox	oxidation of a material
red	reduction of a material
SEM	scanning electron microscopy
SOFC	solid oxide fuel cells
TCC	**t**hermo**c**hemical **c**ycles based on redox materials producing fuel solely from regenerative resources
TGA	thermogravimetric analysis
XRD	X-ray dffraction

1 Introduction

The Urgent Need

Being one of the last generations that is not directly effected by fossil fuel depletion, we are in charge of assuring a continuous and secure transition to a sustainable energy supply. It is in our times' responsibility to find solutions avoiding that following generations not only suffer from the depletion of fossil fuels, but also from a global shortage of energy supply. The consequences of this scenario for the social and political stability around the globe would be disastrous. Hence, along with the issue of global warming and its associated climate change, the future energy supply is undeniably the major challenge our generation is facing [Murr 12, Hook 13].

Taking into account the increasing global energy demand, various scenarios describe different paths to guide us through the transition towards an energy supply system in 2050 that mainly depends on carbon-neutral technologies [IEA 12]. In all of these scenarios, solar energy plays a major role, being the most abundant renewable energy source available on earth. However, due to its intermittent nature, the storage on a truly massive scale is pivotal to the extensive use of solar energy. In this regard, the storage in form of chemical bounds is very promising, since they feature energy contents of up to 100 times higher than the best batteries. The chemical storage of solar energy implies in particular the solar-driven production of hydrogen and carbon monoxide, thus, the production of solar fuels. The mixture of both gases is referred to as synthesis gas or syngas, which serves as a universal precursor for the synthesis of a very broad variety of chemical substances such as gaseous and liquid synthetic fuels, polymers, ammonia, fertilizers, methanol, etc. [Newm 12]. Hence, solar fuels not only store solar energy, but also act as a future energy carrier for the transport sector and the chemical industry.

Figure 1.1 presents the major routes to produce solar fuels [Gard 09]. The routes either employ the radiation of the sun in form of each photon (blue) or by concentrating the direct irradiance to obtain heat (red) [Trai 12]. Some routes imply direct conversion from solar energy into fuel, others produce electricity as energy carrier to drive an electrolysis (gray). The latter are a viable technology to produce fuel mainly in form of hydrogen; the former offer greater potential, since they avoid intermediate energy conversion. Among those direct routes, thermolysis and thermochemical cycles promise the highest thermo-

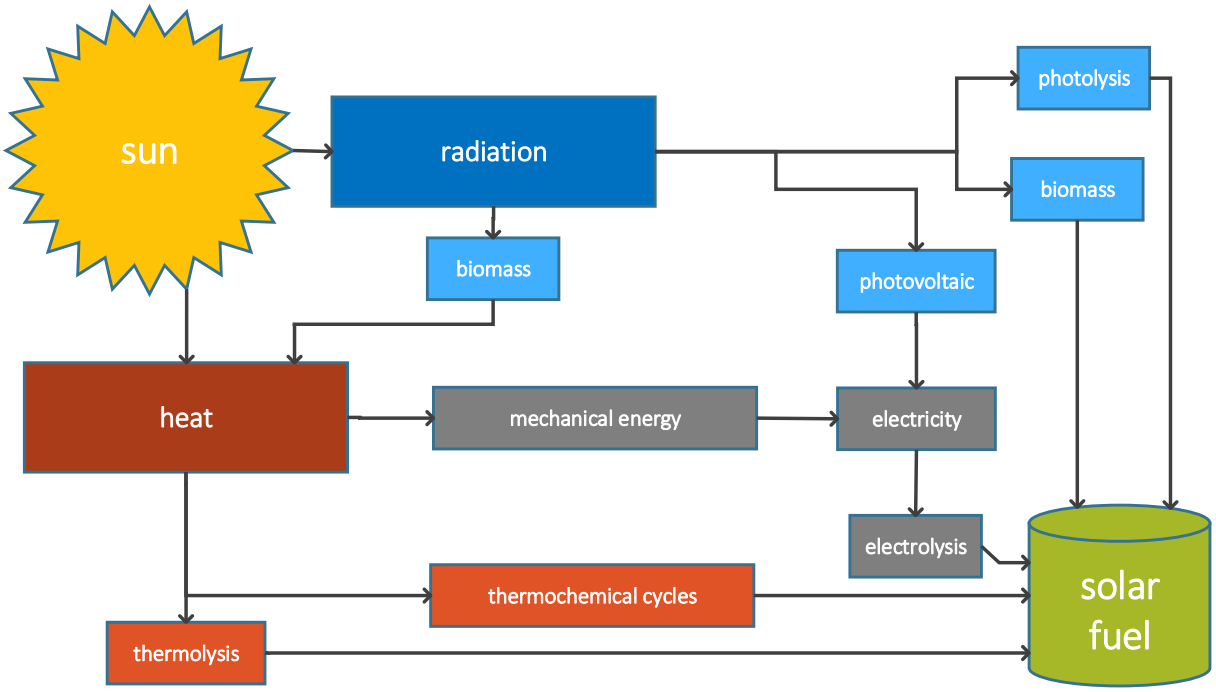

Figure 1.1: Routes for long-term storage of solar energy into solar fuels.

dynamical efficiencies [Sieg 13]. Both routes employ heat provided by concentrated solar power (CSP) to decompose water or carbon dioxide into hydrogen or carbon monoxide. However, reasonable fuel production yields via direct gas splitting of the thermolysis require at least temperatures of 2000°C, imposing extraordinary requirements on materials and reactor design [Pric 04]. To avoid these high temperatures, thermochemical cycles make use of redox reactions. Therewith, high efficiencies are enabled, while operating at feasible temperature levels. Nevertheless, thermochemical cycles are still in their research phase. This thesis aims to contribute to the fundamental understanding of these cycles to be able to improve them.

The Thermochemical Solution

In principle, processes that produce fuel based on redox materials have an arbitrary number of steps. With an increasing number of steps, on the one hand, a lower temperature is needed for each step, but on the other hand, this results in a decrease of the maximum thermodynamic efficiency of the cycle [Perk 04]. Two-step cycles represent the best combination of feasible reaction temperatures and thermodynamic efficiency and are therefore investigated within this thesis.

Figure 1.2 illustrates the fundamental principle of solar-driven thermochemical cycles that employ a two-step redox reaction to produce solar fuels solely from the regenerative resources water and carbon dioxide. In these cycles, the redox material commonly consists

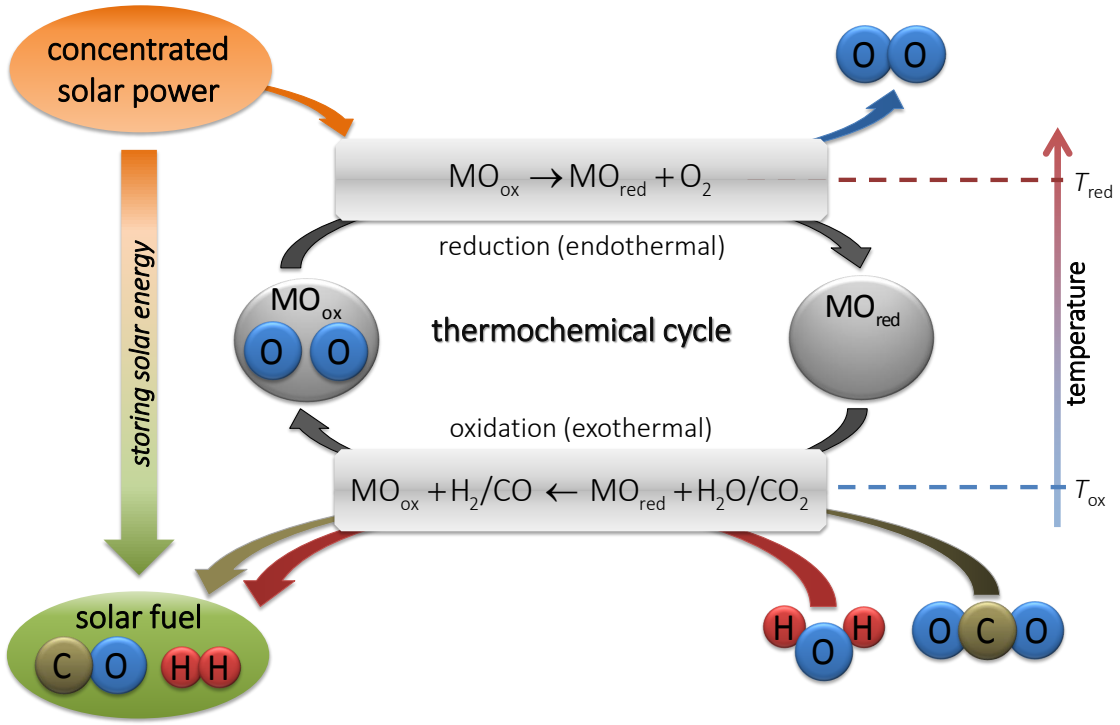

Figure 1.2: Schematic of a solar-driven thermochemical cycle employing a two-step redox reaction to produce solar fuels. MO_{ox} and MO_{red} denotes the oxidized and reduced metal oxide, respectively.

of a metal oxide MO that changes its valence. In other words, oxygen is incorporated into (oxidation) or released from (reduction) the crystal structure of the material [Roeb 12]. In the first step, the reduction, the metal oxide releases oxygen due to the solar-driven, endothermic dissociation of the metal oxide either to the elemental metal or the lower-valence metal oxide. In the following step, the reduced metal oxide produces fuel in form of carbon dioxide or hydrogen solely from the renewable resources water and carbon monoxide. This reaction, referred to as oxidation, implies the exothermic incorporation of oxygen into the metal oxide. In the subsequent reduction step, this incorporated oxygen is released, closing the cycle. Both, the reduction and the oxidation require certain temperature levels. Commonly, the former requires temperatures of more than 1200°C to become thermodynamically favorable, whereas the latter needs temperatures of more than 500°C to become kinetically feasible.

The Present Study

The overarching goal of this thesis is to pave the way towards the commercialization of such thermochemical two step cycles producing solar fuels. Motivated by a fundamental process analysis, which identified the redox material as the major bottleneck, thermodynamical calculations were carried out that determined ceria as the currently most

promising material to be employed in such cycles. According to literature, doping ceria is the most auspicious method to improve its properties in order to contribute to the set goal.

The present study focuses on experimental investigations of ceria within the framework of four consecutive objectives. After identifying the *optimal doping* of ceria to enhance its fuel productivity per cycle by means of thermogravimetric screening, the impact of doping and microstructure on the *reaction kinetics* is determined. In addition to that, the *equilibrium reducibilities* of the doped-material are evaluated with the aid of a methodology developed within this thesis, which derives the essential thermodynamical data of a redox material from thermogravimetric analyses. Based on this data, the *potential of the doped-material* for the application in solar fuel production cycles is assessed within a process model that energetically estimates the overall efficiency.

2 Motivation and Background

This chapter presents the motivation for this thesis and provides the theoretical background. In the first section, a brief process analysis identifies the main barrier to commercial success of storing solar energy via two-step **t**hermo**c**hemical **c**ycles (TCCs) based on redox materials to produce solar fuels. The analysis points out the necessity to improve the redox material, because it is identified as the major bottleneck. On the basis of fundamental thermodynamical considerations, ceria is selected to undergo further investigations. Background information on ceria that is found in the solid oxide fuel cell literature as well as recent publications in the solar fuel community reveal the most promising approach to improve the properties of ceria: Doping ceria with zirconia and rare-earth elements. A chronological literature review presents the state of the art of ceria applied in TCCs. The formulation of the problem that this thesis tackles and the presentation of the course of investigation completes this chapter.

Contents

2.1 From Sun to Fuel with Redox Materials

The following gives an insight into the fundamental energetic relations of two-step thermochemical cycles based on redox materials producing fuel solely from regenerative resources. Therewith, crucial system implications concerning the employed redox material are revealed.

Simplified, the process of storing solar energy into a fuel via a redox reaction is divided into three parts: A concentrating system, a reactor and an auxiliary unit. Each part involves mainly one of the three quantities, P_{sol}, Q and E_{aux} as illustrated in figure 2.1. Solar irradiation P_{sol} is collected and concentrated by an optical system (e.g. heliostats) and reflected onto a receiver that absorbs the irradiation and converts it into the heat Q. This heat Q drives the reduction reaction and heats up the reactants. Radiation losses P_{rera} also occur and a heat recuperation with an effectiveness ε_{hr} can be employed between the reduction and the oxidation to recuperate the sensible heat as well as the heat released during oxidation. The reduction of the metal oxide requires additional auxiliary energy E_{aux} to remove the released oxygen and to maintain a certain oxygen partial pressure $p(O_2)$.

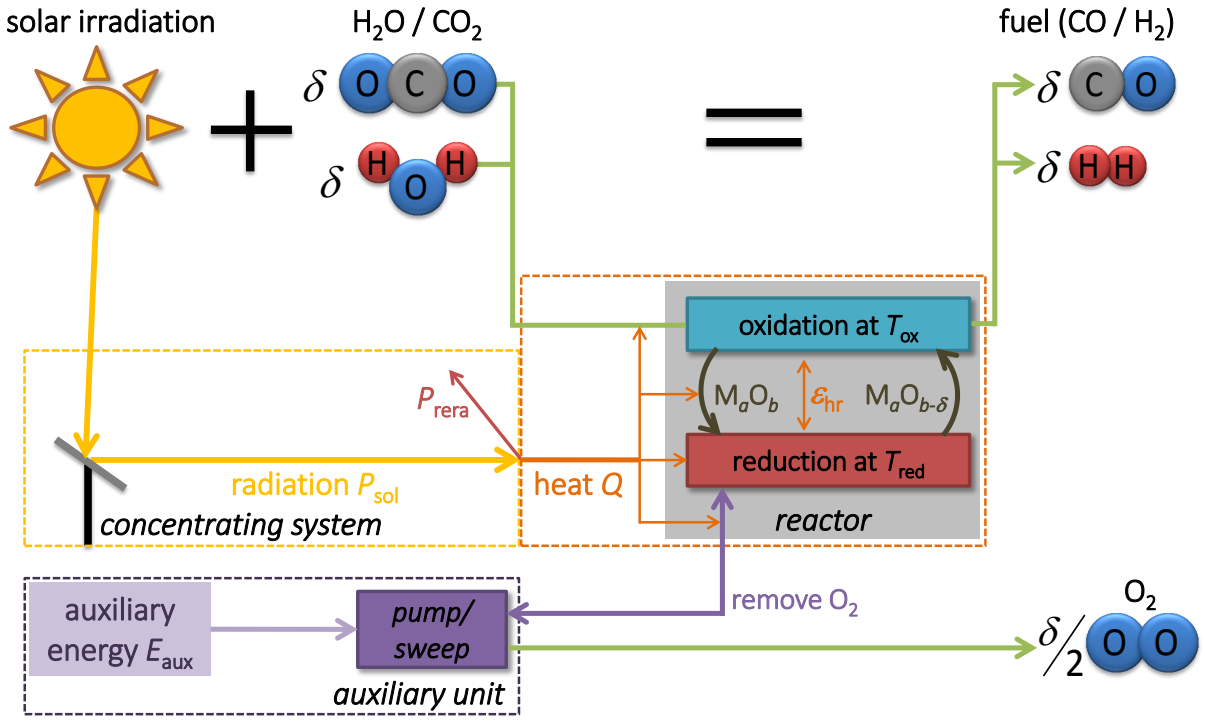

Figure 2.1: Simplified process schematic of the thermochemical solar fuel production.

The structural formula of the metal oxide in its oxidized state is given by M_aO_b. In order to quantify the amount of fuel produced per mol metal oxide M_aO_b, it is convenient to introduce the absolute reduction extent δ, yielding the following chemical formulas:

- Reduction (red):

$$M_aO_b \rightleftharpoons M_aO_{b-\delta} + {}^{\delta}/_{2}O_2 \tag{2.1}$$

  δ denotes the amount of oxygen that is released during reduction and quantifies the reduction extent of a redox material. It is a reasonable performance number to assess redox materials, because it is also the upper limit for the amount of produced fuel during the

- Oxidation (ox):

$$M_aO_{b-\delta} + \delta(CO_2/H_2O) \rightleftharpoons M_aO_b + \delta(CO/H_2) \tag{2.2}$$

- The net reaction is, in the case of water splitting, given by

$$\delta H_2O \quad \rightleftharpoons \quad \delta H_2 + {}^{\delta}/_{2}O_2 \tag{2.3}$$

  and in the case of carbon dioxide splitting by

$$\delta CO_2 \quad \rightleftharpoons \quad \delta CO + {}^{\delta}/_{2}O_2. \tag{2.4}$$

The reduction extent δ at certain process conditions (mainly, the reduction temperature T_{red} and the partial pressure of oxygen $p(O_2)$) is material specific and will be discussed in more detail in section 2.2. The three quantitiesP_{sol}, E_{aux} and Q are directly or indirectly linked to δ. In order to roughly estimate the system implications of solar fuel production with redox materials, it is convenient to exemplarily calculate several relations based on material properties that are reported in literature. Ceria serves as the material candidate that produces pure H_2 with an energy content of 286 kJ·mol^{-1} (higher heating value) [Panl 75, Erma 13]. Similar calculations were published by Felinks and Brendelberger [Bulf 15]. Keep in mind that the following analysis should only provide a basic idea of the fundamental energetics of TCCs and does not claim completeness. A thorough process analysis concerning the energetics involved is provided in chapter 7.

Concentrating System

The endothermic reduction of the metal oxide requires high temperatures which are provided through the concentration of direct solar irradiation with optical systems. Curved mirrors concentrate the irradiation onto a receiver with an efficiency η_{opt}. A detailed description of the losses caused by the concentrating system itself goes beyond the scope of this work and is found elsewhere [Rome 07]. The receiver absorbs the irradiation. With an optical efficiency η_{opt}, the usable heat Q is given by

$$Q = \eta_{opt} \cdot P_{sol} - P_{cond} - P_{rera} - P_{conv} \tag{2.5}$$

The thermal losses due to conduction P_{cond} and due to convection P_{conv} are neglected, since perfect insulation of the reactor is assumed and P_{conv} is only a minor contribution compared to the radiation losses P_{rera} in the case of TCCs [Lang 14]. According to the Stefan–Boltzmann law, the theoretical radiation losses of several concentration levels C versus the temperature are illustrated in figure 2.2.

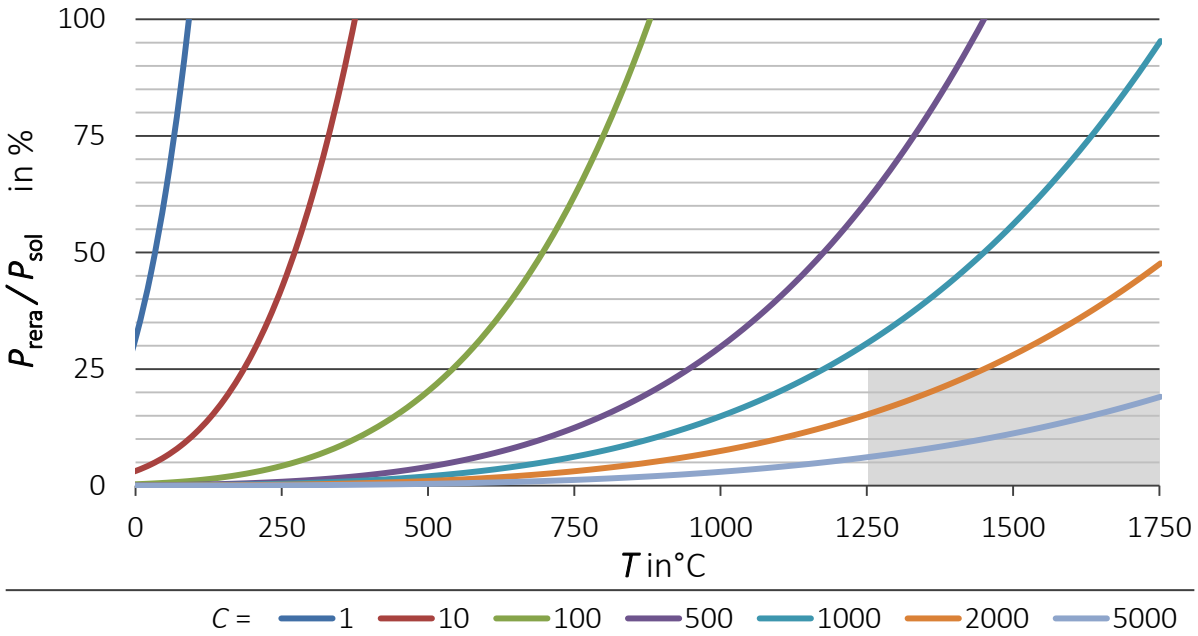

Figure 2.2: Theoretical radiation losses of the receiver vs. its T for different concentration ratios C. Assuming an ambient temperature of 20°C, a solar flux of 1000 W·m^{-2} and blackbody properties.

To keep the radiation losses at reasonable levels, concentration ratios of approximately $C = 5000$ are required when aiming at temperatures above 1300°C. Only point focusing systems can provide such high concentration ratios [Rome 07]. Because higher concentrations are linked to higher costs of the optical system, however, decreasing the reduction temperature T_{red} aids the technological realization of TCCs. Furthermore, lowerering T_{red} leads to significant lower radiation losses P_{rera}, since $P_{rera} \propto T_{red}^4$.

Reactor

In the following, an operation mode of the reactor is introduced that assumes mass transport of the material within the reactor (between oxidation and reduction chamber). However, there are other modes to operate the process [Mill 08, Lout 10, Chue 10a, Roeb 11, Sck 12]. The reactor comprises generally two reaction chambers as illustrated in figure 2.1. The reduction is carried out in the irradiated chamber at the high temperature ($T_{red} \gtrsim 1200$°C) and consumes heat (endothermic reaction). When the reduction process is completed, the material leaves the reduction chamber and enters the oxidation cham-

ber. Before the oxidation starts, the material needs to be cooled down to the oxidation temperature $T_{ox} \sim 800°C$. This waste heat might be recuperated as explained later. To oxidize the material, H_2O and/or CO_2 are introduced. The gases are split to produce fuel. No heat input is required during oxidation, since the reaction is exothermic. When the oxidation is completed, the material is transported back to the reduction chamber. There, the material is heated to the reduction temperature T_{red} and reduced again to close the cycle. Q is the heat that is usable for the entire process, assuming no other thermal losses than radiation. In the process, Q is consumed by

1. the reduction enthalpy ΔH_{red} of the metal oxide; this energy equals the solar energy chemically stored in the metal oxide
2. heating the redox material from T_{ox} to T_{red} (heat Q_{mat})
3. heating the reactants H_2O and CO_2 (heat $Q_{H_2O,\,CO_2}$)
4. heating the sweep gas if used during reduction (heat Q_{sweep})

This gives:

$$Q = \Delta H_{red} + Q_{mat} + Q_{H_2O;\,CO_2} + (Q_{sweep}) \tag{2.6}$$

Implementation of heat recuperator with an effectiveness ε_{hr} decreases the necessary sensible heats Q_{mat}, $Q_{H_2O;\,CO_2}$ and Q_{sweep}. Hence, more energy can be used to reduce the metal oxide. Since the reduction extent δ limits the overall cycle productivity, ideally, δ should equal the stoichiometric maximum (for ceria: $\delta_{max,\,stoic.} = 0.5$). However, there are technical reasons to not fully reduce the material, thus, to operate with non-stoichiometrically reduced material. Reasons are, for instance, time limitations of the reduction step or reduction conditions that are insufficient to fully reduce the material. Moreover, the full reduction usually results in a phase change of the material that implies structural problems such as volume changes leading to damages of the structured materials.

If only a fraction of the metal oxide is reduced, a certain mass of the material does not react actively. Depending on δ, the fraction of non-reacting material might be a significant amount of material that is solely heated up and cooled down. In the case of ceria, the ratio of active to passive material equals 2δ. Assuming a temperature difference between oxidation and reduction $\Delta T_{ox \rightarrow red}$ of a few hundred Kelvin and a δ of less than 5% of $\delta_{max,\,stoic}$, the ratio of sensible heat Q_{mat} and reduction enthalpy ΔH_{red} equals values that represent a significant penalty on the overall efficiency. In this regard, the incorporation of an efficient heat recuperation is highly beneficial [Erma 13]. Figure 2.3 illustrates the crucial impact of the temperature difference $\Delta T_{ox \rightarrow red}$ and the heat recuperation effectiveness ε_{hr} on the basis of ceria.

In general, high efficiencies require small Q_{mat}:ΔH_{red} ratios; the smaller the better. Hence, to achieve a reasonable overall efficiency, it is pivotal to either increase δ or to decrease $\Delta T_{ox \rightarrow red}$. Furthermore, the process requires an efficient heat recuperation, in particular

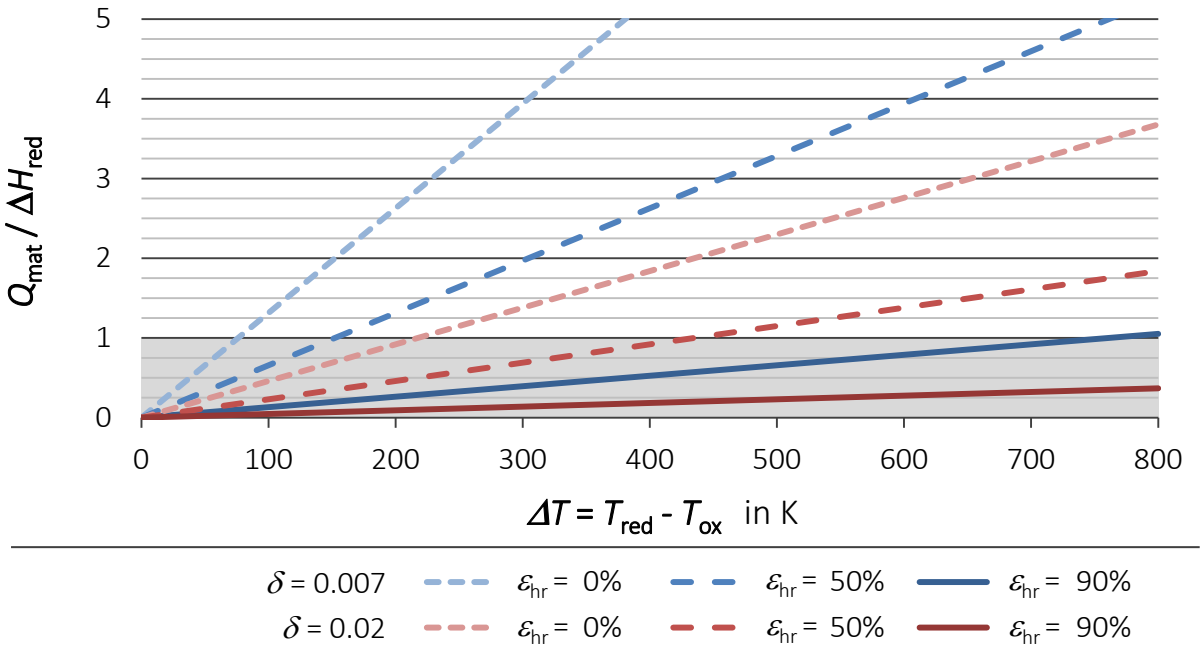

Figure 2.3: Ratio of sensible heat Q_{mat} to reduction enthalpy ΔH_{red} as a function of the temperature gap between oxidation and reduction temperatures (T_{ox} to T_{red}) of two δ assuming different heat recuperation effectiveness ε_{hr}. As the reference material, pure ceria was employed with heat capacities and reduction enthalpies derived from [Erma 13].

in the case of small δ.

Auxiliary Unit

Besides the temperature T_{red}, the reduction reaction depends on the partial pressure of oxygen $p(O_2)$. The thermodynamics of the redox reaction are further discussed in section 2.2. Generally, decreasing the partial pressure of oxygen $p(O_2)$ increases the amount of released oxygen and therewith the reduction extent δ. Either vacuum pumping or sweeping with an inert gas removes the released oxygen and provides the necessary low partial pressure of oxygen $p(O_2)$ within the reactor during reduction. Both ways are accompanied by the consumption of additional energy which is referred to as auxiliary energy E_{aux}. The vacuum pumping requires work in form of electricity or, in the case of steam ejectors, thermal energy. When sweep gas is employed, it has to be recycled to be purified from oxygen, which requires separation energy. Theoretically, a heat recuperation system may provide some of the auxiliary energy E_{aux}. However in this basic analysis, this possibility is not further investigated.

Figure 2.4 depicts the ratio of auxiliary energy E_{aux} to the energy stored in produced fuel E_{aux}:E_{fuel} in the case of ceria. For this calculation, H_2 serves as the fuel with an energy content of 286 kJ·mol^{-1} (higher heating value).

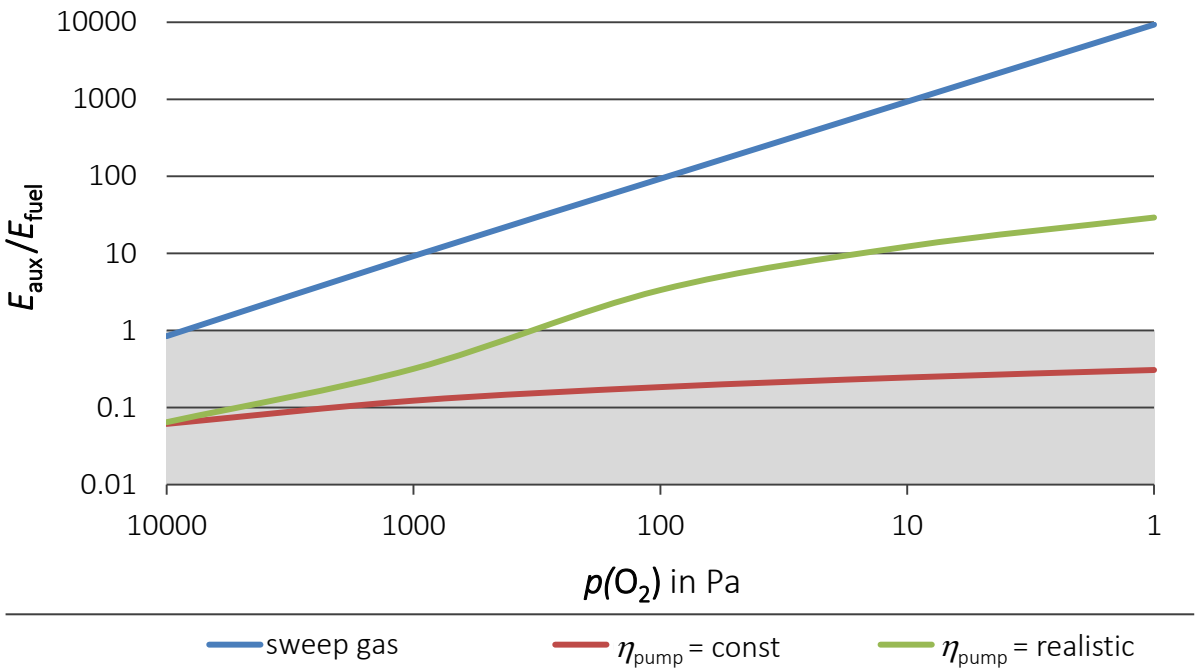

Figure 2.4: Ratio of auxiliary energy to the energy stored in produced fuel E_{aux}:E_{fuel} depending on the pressure of oxygen $p(O_2)$. E_{fuel} denotes the higher heating value of hydrogen. Calculation parameters are derived from [Erma 13] in the case of pure ceria.

In the case of sweep gas, the amount of energy necessary for purification is correlated to $p(O_2)$ drastically. Decreasing $p(O_2)$ by one order of magnitude yields an increase of the ratio E_{aux}:E_{fuel} by one order of magnitude. Using sweep gas with $p(O_2)$ of less than 0.001 bar, ratios $E_{aux} : E_{fuel} > 100$ are obtained that are likely to result in efficiencies impeding TCCs from commercialization. In the case of vacuum pumping, the situation is not as dramatic. Assuming realistic pump efficiencies, reasonably small $E_{aux} : E_{fuel}$ ratios are possible for partial pressures as small as 10^{-3} bar [Bren 14, Feli 14, Bulf 15]. Note that for other materials the absolute numbers differ, but the trend is similar.

Conclusions

Employing redox materials for solar-driven thermochemical fuel production leads to crucial system implications for the three quantities P_{sol}, E_{aux} and Q. To enhance the overall process efficiency the following fundamental relations have to be considered:

- A decrease of the reduction temperature T_{red} decreases radiation losses P_{rera} and therewith increases the solar energy that can be converted to heat Q usable for the process. From a technical point of view, decreasing T_{red} leads to required concentration ratios that are lower than 5,000, resulting in cost reduction as well as facilitation of the concentrating system.

- At constant reaction conditions, doubling the reduction extent δ approximately doubles the produced amount of fuel, which doubles the stored energy E_{fuel} and therewith, significantly enhances the overall process efficiency. Apart from that, increasing δ decreases the demand of sensible heat Q_{mat} of the redox material required during cycling per unit of fuel produced. Q_{mat} corresponds to the energy required for heating the redox material M_aO_b from the oxidation temperature T_{ox} to T_{red}. Therewith, the share of the heat Q that can actually be consumed by the reduction of the material increases. Besides, these basic calculations emphasize the importance of efficient heat recuperation, especially, when operating at small δ.
- Increasing the partial pressure of oxygen $p(O_2)$ allowed during reduction drastically decreases consumption of auxiliary energy E_{aux}, because the demand of either sweep gas or vacuum pumping decreases. Based on values reported for pure ceria available in literature, increasing $p(O_2)$ by one order of magnitude decreases E_{aux} by a factor of 5 to 10.

Considering these fundamental relations, the importance of the quantities δ, T_{red} and $p(O_2)$ becomes obvious. Since all three are in particular material specific, an efficient redox material is the key to feasible solar fuel production. The enhancement of the properties of the material is the most direct approach to augment the overall process efficiency. Hence, the material might be referred to as the bottleneck of this technology. The identification and the understanding of optimal materials is pivotal to the commercialization of TCCs.

Further requirements on the materials concern their stability as well as their costs. From a technical point of view, material properties such as heat conduction and emissivity are essential criteria to select a material to be applied in TCCs.

2.2 The Bottleneck: The Redox Material

In the previous section, the importance of the applied material was discovered and the crucial impact of the reaction conditions on the overall process efficiency discussed. In particular, an efficient reduction of the material is pivotal for high overall process efficiencies. The key parameters in this regard are the reduction extent δ, the reduction temperature T_{red} and the partial pressure of oxygen $p(O_2)$. The following section introduces the thermodynamical requirements for the material yielding Ellingham diagrams. Based on these diagrams, a material assessment is performed.

2.2.1 Thermodynamical Requirements

Inspired by the work of Meredig and Wolverton, a framework that thermodynamically evaluates the gas splitting reaction is introduced [Mere 09]. Concerning the reduction at

the temperature T_{red} (equation: 2.1) and the oxidation at the temperature T_{ox} (equation: 2.2), the following thermodynamical expressions

$$\Delta G_{\mathrm{red},T_{\mathrm{red}}} = \Delta H_{\mathrm{red},T_{\mathrm{red}}} - T_{\mathrm{red}}\Delta S_{\mathrm{red},T_{\mathrm{red}}} \leq 0 \tag{2.7}$$

$$\Delta G_{\mathrm{ox},T_{\mathrm{ox}}} = \Delta H_{\mathrm{ox},T_{\mathrm{ox}}} - T_{\mathrm{ox}}\Delta S_{\mathrm{ox},T_{\mathrm{ox}}} \leq 0 \tag{2.8}$$

must be satisfied. Here, ΔG refers to the change of Gibbs energy, ΔH to the enthalpy change and ΔS to the entropy change during reduction or oxidation at the temperatures T_{red} or T_{ox}. ΔH and ΔS consist of the enthalpy and entropy changes of every reactant. According to equations 2.1 and 2.2, those reactants are O_2, H_2O and H_2 or CO_2 and CO, and the reduced and oxidized metal oxide $M_aO_{b-\delta}$ and M_aO_b, respectively. ΔH is expressed either as the heats of formation ΔH_{f} or the enthalpies of the compound with respect to its composition. ΔS is expressed with the standard entropy. This gives

$$\Delta G_{\mathrm{red},T_{\mathrm{red}}} = \Delta H_{\mathrm{mat}} - T_{\mathrm{red}} \cdot \left(\Delta S_{\mathrm{mat}} + {}^1\!/_2 S^{\mathrm{O_2}}_{T_{\mathrm{red}}}\right) \tag{2.9}$$

$$\Delta G_{\mathrm{ox},T_{\mathrm{ox}}} = -\Delta H_{\mathrm{mat}} - \Delta H^{\mathrm{H_2O,\,CO_2}}_{\mathrm{f},T_{\mathrm{ox}}} - T_{\mathrm{ox}}\left(S^{\mathrm{H_2,\,CO}}_{T_{\mathrm{ox}}} - S^{\mathrm{H_2O,\,CO_2}}_{T_{\mathrm{ox}}} - \Delta S_{\mathrm{mat}}\right). \tag{2.10}$$

Here, $S^{\mathrm{O_2}}_{T_{\mathrm{red}}}$ denotes the entropy of O_2 at T_{red}. $S^{\mathrm{H_2,\,CO}}_{T_{\mathrm{ox}}}$ and $S^{\mathrm{H_2O,\,CO_2}}_{T_{\mathrm{ox}}}$ correspond to the entropies at T_{ox} of either H_2 and H_2O in the case of water splitting, or CO and CO_2 in the case of carbon dioxide splitting. $\Delta H^{\mathrm{H_2O,\,CO_2}}_{\mathrm{f},T_{\mathrm{ox}}}$ denotes the enthalpy accompanied with the formation of either CO_2 and H_2O at T_{ox}. The quantities that only depend on the redox material are:

- **Redox enthalpy change**
  The enthalpy difference between reduced and oxidized metal oxide $M_aO_{b-\delta}$ and M_aO_b, respectively, given by the difference between the formation enthalpies:

$$\Delta H_{\mathrm{mat}} \equiv \Delta H^{\mathrm{M_aO_{b-\delta}}}_{\mathrm{f}} - \Delta H^{\mathrm{M_aO_b}}_{\mathrm{f}} \tag{2.11}$$

- **Redox entropy change**
  The entropy difference between $M_aO_{b-\delta}$ and M_aO_b:

$$\Delta S_{\mathrm{mat}} \equiv S^{\mathrm{M_aO_{b-\delta}}} - S^{\mathrm{M_aO_b}} \tag{2.12}$$

  Since O_2 is released during the reduction of the metal oxide, a change in the degrees of freedom of the atoms within the crystal structure might occur. In most of the materials, a negative ΔS_{mat} is expected, since decreasing the number of atoms yield fewer vibrational degrees of freedom. However, there are some material systems that exhibit positive ΔS_{mat}, because of the creation of oxygen vacancies within their crystal structure during reduction.

The quantities ΔH_{mat} and ΔS_{mat} must be considered as the most important design variables of the redox system, since they state, whether the use of a material is thermodynamical favorable towards TCCs, as demonstrated in the following. In equilibrium $\Delta G = 0$, equations 2.9 and 2.10 are solved to evaluate the dependency of ΔH_{mat} on ΔS_{mat}:

$$\boldsymbol{\Delta H_{mat}} = {}^{1}\!/_{2}\, T_{red} S^{O_2}_{T_{red}} + T_{red} \cdot \boldsymbol{\Delta S_{mat}} \tag{2.13}$$

$$\boldsymbol{\Delta H_{mat}} = -\Delta H^{H_2O/CO_2}_{f,T_{ox}} - T_{ox}\left(S^{H_2/CO}_{T_{ox}} - S^{H_2O/CO_2}_{T_{ox}}\right) + T_{ox} \cdot \boldsymbol{\Delta S_{mat}} \tag{2.14}$$

The calculations are carried out with the aid of FactSage 6.1 and its databases, since FactSage contains the entropies and enthalpies of the gases [Bale 02, Bale 09]. Figure 2.5 (top) displays the thermodynamically favorable regions of the two equations, for the reduction at varying partial pressures of oxygen (beneath the solid lines) and oxidation with water (above the dashed lines) and carbon dioxide (above the dotted lines) at varying temperatures. The solid lines denote equation 2.13 at several partial pressures of oxygen and $T_{red} = 1500°C$. The dashed lines denote equation 2.14 at several oxidation temperatures T_{red} and gas pressures of $p(CO_2) = p(H_2O) = 1$ bar.

Materials featuring ΔH_{mat} and ΔS_{mat} values that correspond to points above a dashed line are able to split CO_2 and H_2O at the denoted temperature. For large negative ΔS_{mat}, the region favoring the splitting reaction decreases with decreasing the oxidation temperature T_{ox}. For $\Delta S_{mat} \gtrsim -45$ JK^{-1} per 0.5 mol O_2, decreasing T_{ox} enhances the splitting thermodynamics. Concerning the reduction at $T_{red} = 1500°C$, ΔH_{mat} and ΔS_{mat} values are necessary that are beneath a solid line presenting the allowed partial pressure of oxygen $p(O_2)$. Decreasing the partial pressure of oxygen $p(O_2)$, significantly increases the region of ΔH_{mat} and ΔS_{mat} values that favor the reduction.

Favorable thermodynamics for both, oxidation and reduction are achieved in the intersecting region of dashed and solid lines. As roughly calculated in section 2.1, only partial pressures of oxygen $p(O_2) \geq 10^{-3}$ bar presumably are feasible. The corresponding regions of ΔH_{mat} and ΔS_{mat} values is displayed with the gray areas in figure 2.5 that favor both reduction and oxidation with water (bright and dark gray area) and CO_2 (dark gray area) under feasible conditions. Generally speaking, for the investigated reduction temperatures both reactions become favorable, when

- the partial pressure of oxygen $p(O_2)$ during reduction is low enough,
- the oxidation temperature T_{ox} is low enough (respectively the temperature difference $\Delta T_{ox \rightarrow red}$ between T_{ox} and T_{red} large enough),
- or ΔS_{mat} is large positive.

Low $p(O_2)$ or low T_{ox} (large $\Delta T_{ox \rightarrow red}$) lead to less efficient processes, as discussed in the previous section. Therefore, it is reasonable to develop materials featuring large positive ΔS_{mat}, because these are in particular promising for the application in TCCs. Figure 2.5

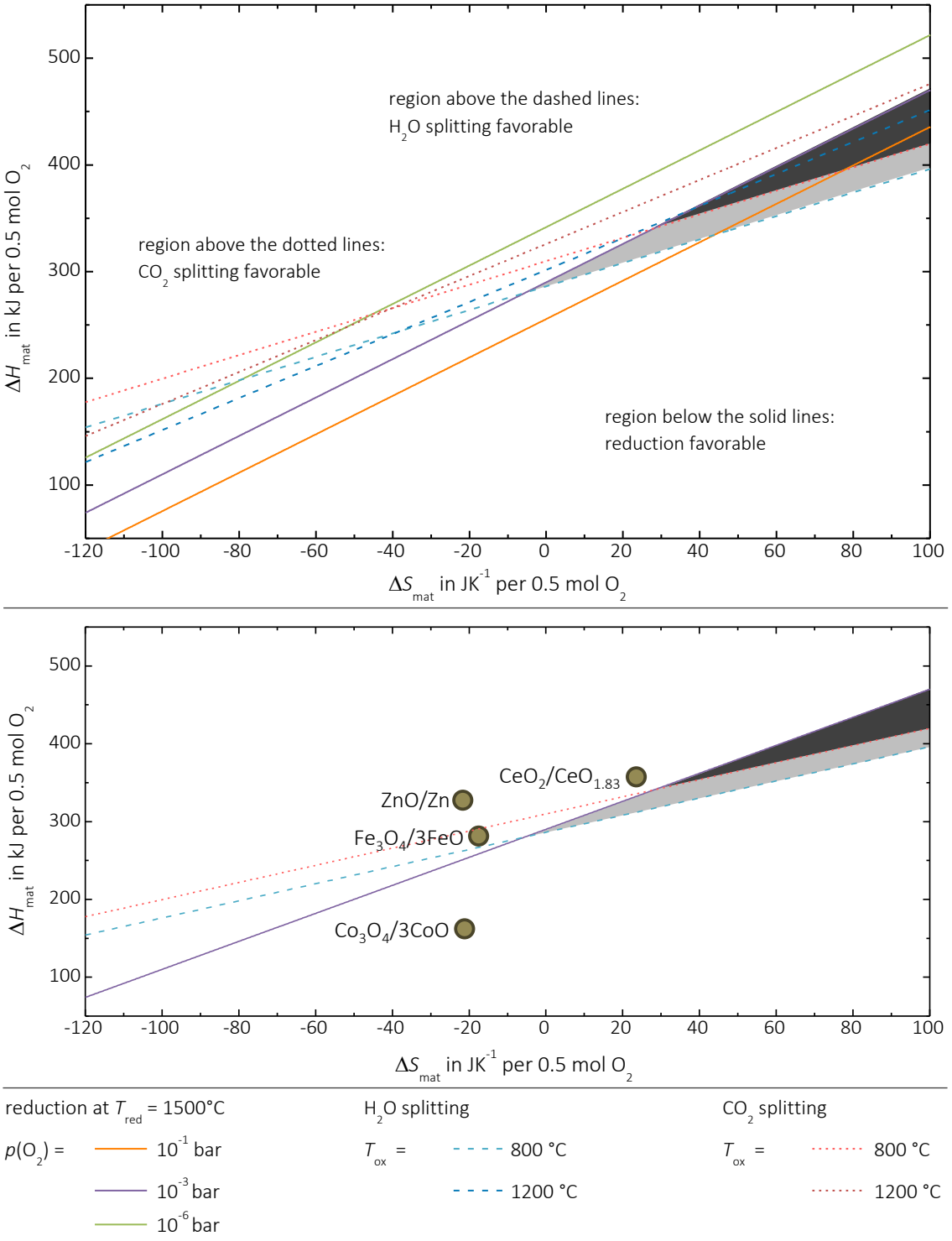

Figure 2.5: Top: Pairs of ΔH_{mat} and ΔS_{mat} that favor reduction (beneath solid lines) and gas-splitting (above dashed lines: water splitting; above dotted lines: CO_2 splitting) under varying reaction conditions. Bottom: Implementation of interesting materials into the thermodynamical framework. Thermodynamical data were derived from FactSage. Concerning feasible reaction conditions ($p(O_2) = 10^{-3}$ bar, $T_{red} = 1500°C$ and $T_{ox} = 800°C$), the bright gray area marks pairs of ΔH_{mat} and ΔS_{mat} that favor reduction and water splitting and the dark gray area, also CO_2 splitting is favored.

bottom shows the ΔH_{mat} and ΔS_{mat} values of interesting materials that could be derived from FactSage. None of the materials favor both reactions at ones at the conditions that were defined to be feasible. However, ceria is relatively close to the gray area.

2.2.2 Material Assessment: Ellingham Diagrams

Ellingham diagrams are plots of the change in the standard Gibbs energy ΔG^0 with respect to the temperature T for various reactions such, as the formation of oxides, sulfides etc. of various elements [Monk 44]. If the investigated reaction does not imply a change in heat capacity, for instance, due to a phase transition of a reactant, the diagram displays a straight line. In metallurgy, Ellingham diagrams are used to predict the equilibrium temperature T between a metal, its oxide and oxygen. Keep in mind that the term oxidation may not only imply the splitting reaction of water, but also the oxidation of the material with oxygen as it is the case in the following.

At a glance, such diagrams rank metal oxide systems concerning their CO_2- and H_2O-splitting abilities and state, whether they are thermally reducible. Beyond that, they provide the information which temperature and partial pressure of oxygen is required for the reduction. These characteristics make Ellingham diagrams an expressly material screening tool for TCCs.

Ellingham diagrams result from the second law of thermodynamics [Atki 06]:

$$\Delta G^0 = \Delta H^0 - T \cdot \Delta S^0 \tag{2.15}$$

ΔG^0 is the change in standard Gibbs energy during a reaction. Accordingly, ΔH^0 denotes the standard enthalpy change and ΔS^0 the standard entropy change. For an oxidation reaction

$$x\mathrm{M} + 0.5\mathrm{O_2} \rightleftharpoons \mathrm{M}_x\mathrm{O} \tag{2.16}$$

ΔG^0 is described with a relation of the temperature T and the equilibrium rate constant k as

$$\Delta G^0 = -RT \ln k = -RT \cdot \ln \frac{a(\mathrm{M}_x\mathrm{O})}{a^x(\mathrm{M}) \cdot p^{0.5}(\mathrm{O_2})} \tag{2.17}$$

Here, a denotes the activities of the solid reactants. The choice of the pure oxide and the pure metal in its standard states makes the activities of M and M_xO unity, which gives

$$\Delta G^0 = 0.5RT \cdot \ln p(\mathrm{O_2}) \tag{2.18}$$

Ellingham lines are constructed by plotting equation 2.15 for a specific redox reaction at standard conditions. As long as the line is below the x-axis ($\Delta G^0 = 0$ at $p(O_2) =$ 1 bar), the oxidation is favored; above the x-axis, the back reaction (reduction) is favored. An intersection of x-axis and reaction line identifies the equilibrium temperature. Every

point in an Ellingham diagram represents a combination of T and $RT \cdot \ln p(O_2)$, thus by substitution of T into $RT \cdot \ln p(O_2)$ the corresponding partial pressure of oxygen is obtained. Due to equation 2.18, oxygen isobars are straight lines with a slope of $R \cdot \ln p(O_2)$ radiating from the origin of the diagram ($T = 0$ K, $\Delta G^0 = 0$). Thereby, a nomographic scale for partial pressures of oxygen $p(O_2)$ may be placed along the right-hand edge of the diagram. Further explanations for constructing and reading Ellingham diagrams are found elsewhere [Gask 08, Jeff 08].

The Ellingham diagrams presented in this thesis exhibit thin gray lines corresponding to the isobars at oxygen partial pressures of $p(O_2) = 1$, 10^{-3} and 10^{-6} bar. The intersections of the dotted lines and the Ellingham lines of a reaction determine the equilibria temperatures at the different oxygen partial pressures $p(O_2)$. Note that these isobars are only of importance in the interpretation of the reduction step. Apart from that, Ellingham diagrams state, whether a material may split H_2O or CO_2 resulting in the production of syngas. This is because of the redox nature of both gas-splitting reactions:

$$\begin{aligned} CO + 0.5O_2 &\rightleftharpoons CO_2 \\ H_2 + 0.5O_2 &\rightleftharpoons H_2O \end{aligned}$$

The ΔG^0 of both reactions are plotted in the Ellingham diagrams presented in this thesis (H_2O and CO_2 equilibria line). In terms of the thermodynamics, oxidation reactions of metal/metal oxides that exhibit lower ΔG^0 values compared to the H_2O and CO_2 are able to decompose the gases. Visually, these reactions correspond to Ellingham lines that are beneath the CO_2/H_2O lines.

The ΔG^0 of 40 binary and ternary oxide reactions have been calculated with the aid of the software FactSage 6.1 and its databases Fact53 and SGPSBase. For the sake of convenience, only the Ellingham lines of the most promising redox systems, as discussed in literature are presented in the following [Aban 06a, Vish 11, Roeb 12]. Figure 2.6 displays the non-volatile redox systems of ferrites and ceria, and the volatile system of zinc oxide. The Ellingham diagrams of the other materials are found in the appendix in section A.1.

Ferrites contain Fe in the oxidation state Fe^{2+} and Fe^{3+}. The redox system of wüstite (FeO) or the mixture of NiO/FeO (and the spinel of iron oxide and iron mixed oxides) feature the splitting of water and carbon dioxide at temperatures around 700°C. The reduction is not thermodynamically favorable below the melting point of the monoxide as displayed with the end of the Ellingham line. However, the gap between the reaction lines and the $p(O_2) = 10^{-6}$ bar - isobar is relatively small. Being one of the first redox systems for TCCs, Nakamura et al. proposed the application of ferrites in the 70ties [Naka 77]. It is reported that the reducibility is improved by doping the spinel structure [Lore 08, Mill 08, Koda 09, Sche 10, Goko 11, Agra 12, Kane 12,

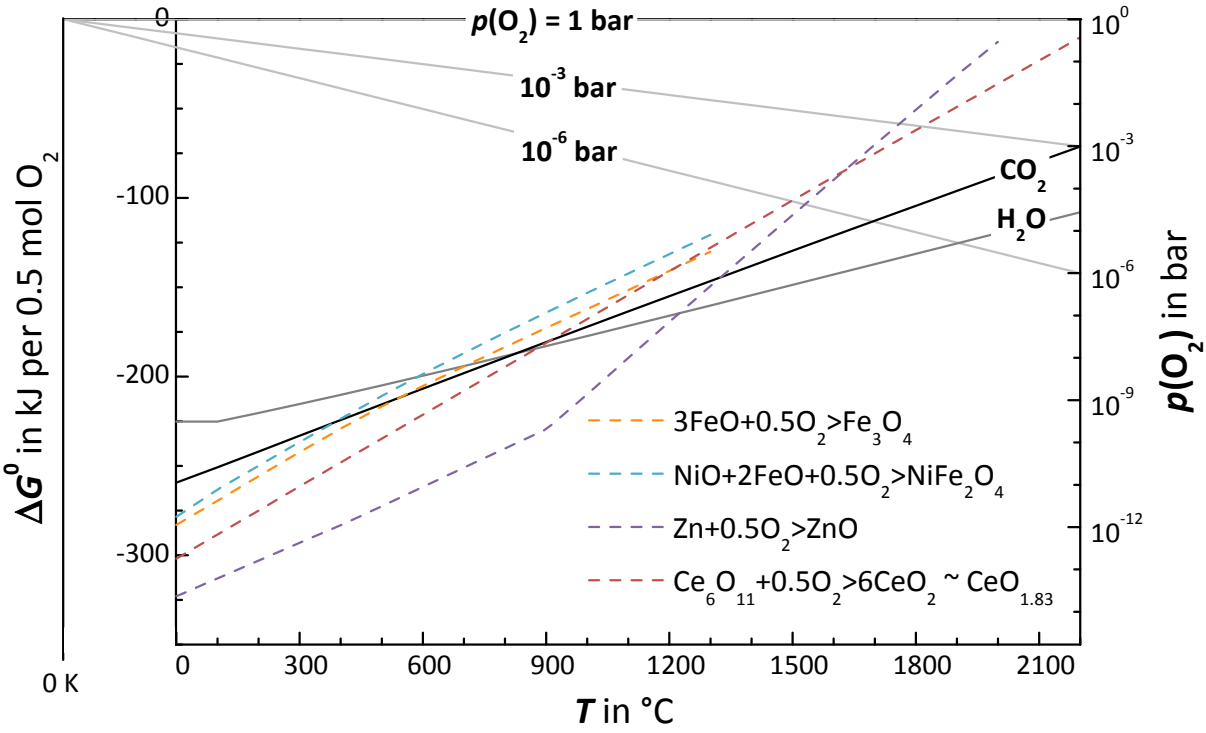

Figure 2.6: Ellingham diagrams of the most promising materials derived from FactSage calculations (databases Fact53 and SGPSBase).

Tama 12, Sche 13a]. In the Ellingham diagram, this trend is already visible for Ni-doping. The basic feasibility of doped ferrites were proven in the pilot plan of the European project HYDROSOL [Roeb 11, Sck 12]. Nevertheless, since the reduction temperature is still close to the melting point, ferrite-based materials are prone to sintering causing significant degradation.

Zinc oxide is applied in a redox system of the elemental Zn and Zn^{2+}. ZnO is reducible at 1500°C and $p(O_2) = 10^{-6}$ bar or even higher T/lower $p(O_2)$. The reduced form, elemental Zn, features the splitting in a wide temperature range up to 1200°C. However, Zn exhibits a melting point of 419°C and a boiling point of 907°C. Therefore, after reduction, the product gas stream (Zn + O_2 + carrier gas) has to be quenched in order to separate O_2 from Zn to obtain solid Zn. The quenching results in tremendous technical challenges especially for the reactor design and makes a continuous H_2 production almost impossible. Besides technical problems, the thermodynamics of this cycle are significantly downgraded by the quenching process. Due to the good reactivity of zinc towards H_2O and CO_2 splitting, however, the Zn/ZnO cycle is still one of the most promising approaches [Stei 02, Lout 10, Stam 12].

Ceria contains cerium in the oxidation state Ce^{3+} and Ce^{4+}. Besides the stoichiometric oxides, Cerium(IV)-oxide (CeO_2) and Cerium(III)-oxide (Ce_2O_3 = $CeO_{1.5}$), there are so-called non-stoichiometric compounds due to the generation of oxygen vacancies within the crystal structure. These compounds feature a positive entropy change

ΔS_{mat}. The database SGPSBase contains the information of two non-stoichiometric phases, Ce_6O_{11} (= $CeO_{1.833}$, β-phase) and Ce_7O_{12} (= $CeO_{1.714}$, $\delta\tau$-phase) [Trov 13]. Because the β-phase features the best properties concerning reducibility, only this Ellingham line was plotted in figure 2.6. Below 800°C, Ce_6O_{11} splits CO_2 and H_2O. In addition, the reduction of CeO_2 to Ce_6O_{11} is thermodynamically favorable below 1500°C at $p(O_2) = 10^{-6}$ bar. Ceria was first proposed as a water-splitting material by Otsuka et al. [Otsu 85]. Recent literature confirms its outstanding position as a promising material for the application in H_2O-splitting as well as CO_2-splitting processes [Chue 10a, Erma 13, Goko 13, Le G 13, Sche 13b].

From these three promising redox systems, ceria is selected to undergo further investigations, because of its promising thermodynamical features and its significant better stability. In addition, the non-stoichiometry of ceria that results in $\Delta S_{mat} > 0$ meeting the requirements of the thermodynamical framework introduced in section 2.2.1. Promising results were already published in the solar fuel community [Chue 10a, Call 13, Goko 13, Le G 13]. It is also worth noting that many dopants have not been evaluated yet in terms of improvements for the use of ceria in TCCs, leaving substantial room for optimization.

2.3 Ceria

Ceria is of central interest for this thesis, as explained previously. Therefore, introducing the main properties of this substance seems reasonable. In particular, of interest is the redox reaction of ceria and the possibility to enhance the reduction features by doping. A literature review regarding the application in TCCs provides an insight into the feasibility.

Ceria, also known as cerium(IV) oxide, is an oxide of the rare-earth metal cerium. Its chemical formula is CeO_2 and it appears as a pale yellow-white powder. As it is the case of most rare-earth compounds, ceria is basically of low toxicity. Ceria is prone to sintering at high temperatures. Major sources of ceria are found in igneous, sedimentary and metamorphic rocks. The principle cerium ores mined today are Bastnasite, Monazite and Loparite [Sche 02]. With 64 ppm, cerium is far more abundant in the upper earth's crust than any other rare-earth element. For comparison only, copper features 60 ppm and tin 2.3 ppm [Ahre 95].

Pure stoichiometric CeO_2 exhibits a calcium fluoride (fluorite) type structure (fcc) with space group Fm3m over the whole temperature range from room temperature to melting temperature. This structure consists of a cubic close packed array of cerium atoms and a cubic primitive arrangement of oxygen atoms. Each cerium cation is coordinated by eight equivalent nearest neighbor oxygen anions at the corner of a cube, each anion being tetrahedrally coordinated by four cations [Trov 02, Adac 04]. Figure 2.7 illustrates

the crystal structure of ceria.

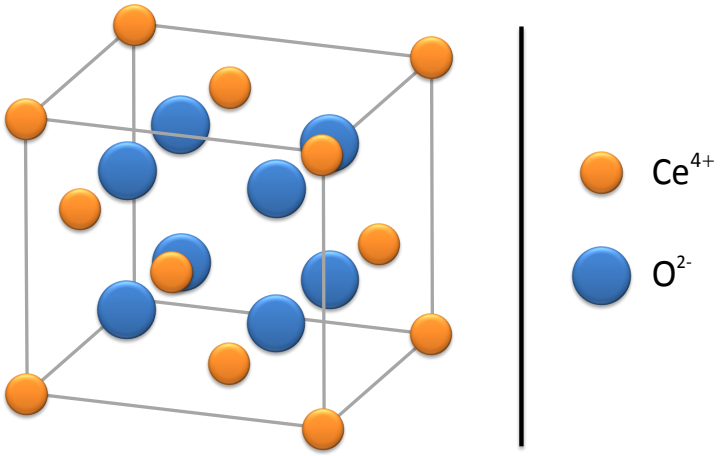

Figure 2.7: Scheme of the crystal structure of ceria.

Mainly, ceria is used in ceramics, as a catalyst or catalyst support, to sensitize photosensitive glass and to polish glass and stones [Sche 02]. The remarkable ability of ceria to display large oxygen non-stoichiometry without changing its crystal structure is essential to many applications in electrochemistry as well as in catalysis [Gopa 12]. Because of this property, ceria is referred to as an oxygen storage material. It is in particular employed as a catalytic converter in automotive applications as well as an electrolyte in solid oxide fuel cells. The non-stoichiometry is quantified with the reduction extent δ.

Ceria stores and releases oxygen, and forms surface and bulk vacancies. This process results in the change of the oxidation state of the cerium ions from Ce^{3+} to Ce^{4+} and vice versa. Using the Kröger-Vink notation [Kroe 56], this process is described as follows:

$$O_O + 2Ce_{Ce} \rightleftharpoons 0.5O_2(gas) + V_O^{\cdot\cdot} + 2Ce'_{Ce}$$

Here, Ce'_{Ce} denotes the reduced ceria atom Ce^{3+}. The negative charge compared to the normal lattice Ce^{4+} (Kröger-Vink notation: Ce_{Ce}) is balanced by oxygen vacancies $V_O^{\cdot\cdot}$. The oxygen in the crystal structure O_O is released in form of oxygen gas O_2.

Applying the property of non-stoichiometric oxygen storage in TCCs modifies the general process reactions (equations 2.1 and 2.2), as follows:

- Reduction (red)

$$CeO_2 \rightleftharpoons CeO_{2-\delta} + \delta/2 O_2 \tag{2.19}$$

  δ denotes the amount of oxygen that is released during reduction. Its stoichiometrical maximum value is $\delta_{max,\ stoic} = 0.5$ corresponding to the complete reduction, i.e. all cerium ions change their valence from +4 to +3.

- Oxidation (ox):

$$CeO_{2-\delta} + \delta(CO_2/H_2O) \rightleftharpoons CeO_2 + \delta(CO/H_2) \tag{2.20}$$

To improve the process and make it commercially feasible, in particular, the reduction conditions (reduction temperature T_{red} and partial pressure of oxygen $p(O_2)$) have to be improved. Due to the non-stoichiometry of the reduction of ceria, the enhancement of the reduction extent δ is also expedient. These necessities imply in the case of ceria-based materials the following:

- Improvement of bulk reduction, since it is known to be difficult. [Aneg 06].
- Prevention of sintering, because low surface areas may result in low reactivity [Mill 09].
- Enhancement of diffusivity of oxygen within the crystal structure, as it is beneficial for the reducibility [Aban 06b].

To modify ceria accordingly, the approach of doping ceria with various elements is very promising and introduced in the following.

2.3.1 Doping Ceria

The addition of a cationic element M^{y+} into the structure of ceria may influence the reducibility in various ways. For instance, doping with ions M^{y+} that display a lower valence than Ce^{4+} increases the density of oxygen vacancies and therewith the oxygen ion mobility. Doping with ions with the same valence but with a lower ionic radius than Ce^{4+} lead to modifications of the crystal structure that aid the reducibility [Aban 10]. Because thermodynamical data of the redox reaction of doped-ceria are unavailable, the identification of efficient dopants and material compositions featuring optimized redox properties requires an experimental study.

A pivotal criteria to select promising dopants to undergo the experimental stage is their solubility in ceria. This depends on the elastic energy W that is introduced in the lattice attributed to differences in ionic radii [Kim 89]. The larger the elastic energy W per substituted ion, the lower is the solubility. The Vegard's slope criteria fairly predicts the solubility limits [Vega 21, Naka 10]. On the one hand, as long as the dopant cation feature radii close to the radius $r_{Ce^{4+}}$ of Ce^{4+}, the fluorite structure is very tolerant to dissolution of up to 40% of foreign oxides. On the other hand, Vegard's law indicates that oxides with cations much smaller or bigger than Ce^{4+} the solubility is very limited. For instance in the case of Co^{2+} or Ni^{2+}, the solubility is less than 1 at.%. Nevertheless, the line of promising candidates is extensive. Isovalent dopants, such as Zr^{4+} feature excellent solubilities in ceria as well as it is reported for trivalent rare-earth dopants RE^{3+} [Moge 00]. This is because of the fact that rare-earth cations feature an ionic radius and an electronegativity

close to those of cerium [Hern 11].

Zirconia Doping

Zirconia is the most common oxide of zirconium (ZrO_2) and is used for a variety of applications as catalysts, electrolytes for solid-oxide fuel cells, and structural materials [Yash 13]. The principal economic source of zirconium is the zirconium silicate mineral, zircon ($ZrSiO_4$) with a yearly production of approximately one mega ton [Niel 10]. Zirconia features high thermal stability and a high melting point of 2715°C. At room temperature, it adopts a monoclinic crystal structure, equaling a distorted fluorite-type structure. In this structure, the coordination number of Zr^{4+} cations is seven, which is smaller than that of fluorite-type oxides [Yash 13].

As reported in many experimental studies within the catalysis community, doping CeO_2 with Zr^{4+} improves the resistance against sintering at high temperatures [Pijo 95, Vida 01, Di M 05b, Delg 13]. However, the intrinsic role of Zr^{4+} as a sintering inhibitor is yet not fully understood [Kasp 99, Yang 06]. Some authors theoretically explained this improved thermal stability with the formation of associated point defects between Zr^{4+} and Ce^{3+} [Janv 98]. The diffusivity of these defects limits the sintering rate. However, as generally observed for ceramic-type materials, the sintering behavior of ceria is strongly effected by the pore curvature and pore radius [Di M 05b]. Besides the increased thermal stability, many investigations evidenced an enhanced reducibility of ceria-zirconia solid solutions, although the substitution Ce^{4+} for Zr^{4+} does not necessitate the formation of charge compensation in form of vacancies [Di M 04, Chen 10, Boar 11]. The corresponding enhanced oxygen storage capacity made ceria-zirconia solid solution the state-of-the-art material of three way emission control catalysts [Aneg 13].

Introducing Zr^{4+} in the fluorite lattice of CeO_2 induces structural modifications attributed to the smaller dimension of Zr^{4+} ions compared to Ce^{4+} ([Shan 69]: 0.084 nm vs. 0.097 nm) [Kasp 00, Di M 04]. At room temperature, compositionally homogenous $Ce_{1-x}Zr_xO_2$ occurs in various phases with crystal structures depending on the Zr content x. For high Zr contents $x \gtrsim 0.9$ a monoclinic crystal structure is reported. For Zr contents lower than $x \approx 0.4$, $Ce_{1-x}Zr_xO_2$ adopts a cubic structure. At intermediate Zr contents, various tetragonal phases are observed [Trov 96, Yash 13].

Rare-Earth Metal Doping

Rare-earth (RE) elements are a set of the fifteen lanthanides plus scandium and yttrium. These non-toxic materials are natural resources with unique properties making them essential to emerging technologies [Adac 04]. Despite their name, RE elements are in fact not especially rare. Each element is more common in the earth's crust than silver

or gold, while yttrium, neodymium and cerium are more common than lead. The yearly world's production of RE materials is in the range of 100,000 tons and their scope of applications is manifold. Catalysis is one of the major application fields of RE elements, representing 20% of the total market worldwide [Maes 00]. The glass industry uses RE oxides for coloration of glass pieces. For instance, glass colored with neodymium shows pink and purple colors. RE phosphors are manufactured as luminescent materials in color televisions and lamps [Adac 04, chap. 9].

Rare-earth oxides are promising candidates as electrolytes or anode materials in solid oxide fuel cells (SOFC). For instance, trivalent-doped ceria materials are widely investigated as the electrolyte material for SOFC, due to showing all three main requirements for a SOFC electrolyte: oxygen diffusivities at temperatures in the range of 700°C to 900°C, chemical stability and sinterability [Zhu 03, Fu 10, Maha 11].

Besides zirconia doping, doping with rare-earth cations is a widely discussed approach to enhance the catalytic properties of ceria. Since ceria is part of the same subgroup, rare-earth elements feature similar chemical properties making rare-earth oxides RE_2O_3 one of the most suitable dopant materials. Due to the lower valence of the dopant RE^{3+} compared to the host Ce^{4+} ion, the introduction of trivalent cations in the fluorite structure of ceria requires charge compensation, creating oxygen vacancies. With the aid of the Kröger-Vink notation, this creation is described as follows [Chat 13]:

$$RE_2O_3 \xrightarrow{CeO_2} 2RE'_{Ce} + V_O^{\cdot\cdot} + 3O_O \tag{2.21}$$

Here, O_O and $V_O^{\cdot\cdot}$ denote oxygen ions on oxygen lattice sites and doubly charged oxygen vacancies, respectively [Kroe 56]. These vacancies enhance the oxygen conductivity significantly, which in turn, promotes the reduction kinetics. The scheme of the resulting defect structure is depicted in figure 2.8. One oxygen vacancy is created per two trivalent ions. Divalent-doping for instance (Ca^{2+}) induces even more oxygen vacancies - one vacancy per dopant ion. Due to the higher radius mismatch of divalent compared to trivalent dopants, however, trivalent dopants exhibit much higher solubility [Ni 08].

Concerning the application in thermochemical solar fuel processes, doping ceria solely with trivalent dopants is not promising. Trivalent-doping alone promotes the sintering of ceria, yielding relatively low specific surfaces [Maha 11]. This is due to the high amount of vacancies in the crystal structure, enhancing not only the transport of the anion oxygen, but also of the cations. Such high densities and low specific surfaces are beneficial for the application as an SOFC electrolyte, but not for the application in TCCs. Here, high specific surfaces to feature enhanced fuel production are presumably needed. Particularly, the oxidation benefits from high specific surfaces, because it is a solid-gas reaction. Taking into account the high temperatures of the reduction step T_{red}, the increased sinterability is more likely to be disadvantageous for the cyclability.

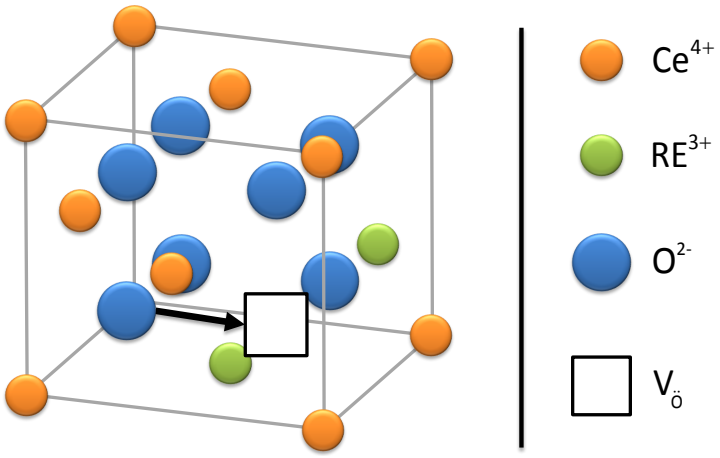

Figure 2.8: Scheme of the defect structure of trivalent doped ceria.

Pretests of solely trivalent-doped ceria evidenced increased sintering and no enhancement of the reduction performance was observed. Therefore, it is reasonable to employ ternary oxides based mainly on CeO_2-ZrO_2-RE_2O_3, instead of solely trivalent-doped ceria CeO_2-RE_2O_3. The ternary oxides combine higher thermal resistance due to the zirconia doping as well as increased oxygen diffusivity due to the trivalent doping. [Aneg 13]. Therewith, near-optimal reactivities for oxygen storage and release at high temperatures are expected.

The selection of the trivalent-dopants to undergo the experimental stage was guided by the SOFC community, which mainly discusses the dopants Y^{3+}, La^{3+} , $Sm^{3+}$and Gd^{3+} [Adac 04, chap. 9].

2.3.2 Chronology: Solar Fuels with Ceria

In the following time bar, the research progress of ceria as the redox material for TCCs is chronologically displayed. Thereby, the most important research groups are named and their major publications briefly described.

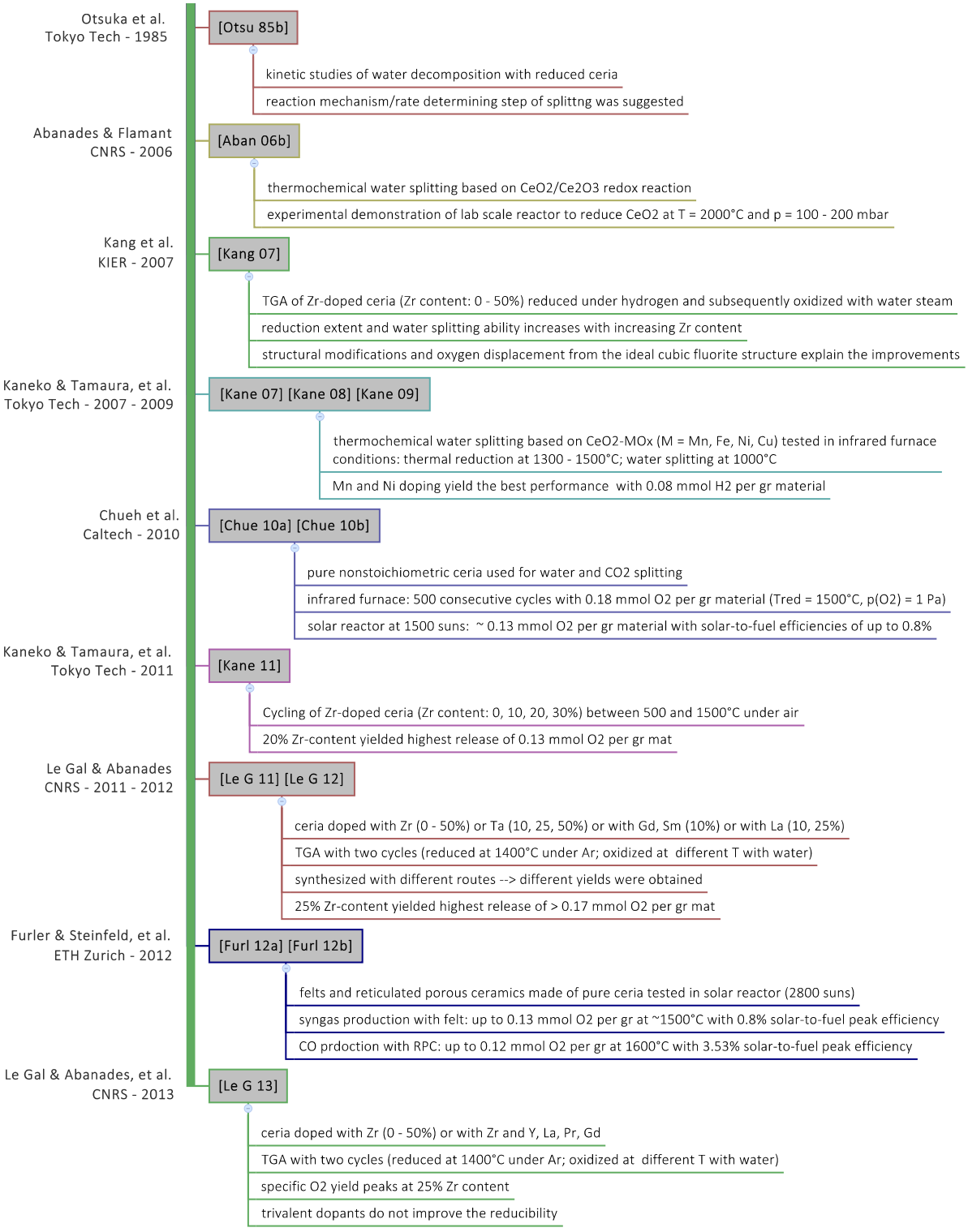
Otsuka et al.
Tokyo Tech - 1985
[Otsu 85b]
kinetic studies of water decomposition with reduced ceria
reaction mechanism/rate determining step of splittng was suggested
Abanades & Flamant
CNRS - 2006
[Aban 06b]
thermochemical water splitting based on CeO2/Ce2O3 redox reaction
experimental demonstration of lab scale reactor to reduce CeO2 at T = 2000°C and p = 100 - 200 mbar
Kang et al.
KIER - 2007
[Kang 07]
TGA of Zr-doped ceria (Zr content: 0 - 50%) reduced under hydrogen and subsequently oxidized with water steam
reduction extent and water splitting ability increases with increasing Zr content
structural modifications and oxygen displacement from the ideal cubic fluorite structure explain the improvements
Kaneko & Tamaura, et al.
Tokyo Tech - 2007 - 2009
[Kane 07] [Kane 08] [Kane 09]
thermochemical water splitting based on CeO2-MOx (M = Mn, Fe, Ni, Cu) tested in infrared furnace conditions: thermal reduction at 1300 - 1500°C; water splitting at 1000°C
Mn and Ni doping yield the best performance with 0.08 mmol H2 per gr material
Chueh et al.
Caltech - 2010
[Chue 10a] [Chue 10b]
pure nonstoichiometric ceria used for water and CO2 splitting
infrared furnace: 500 consecutive cycles with 0.18 mmol O2 per gr material (Tred = 1500°C, p(O2) = 1 Pa)
solar reactor at 1500 suns: ~ 0.13 mmol O2 per gr material with solar-to-fuel efficiencies of up to 0.8%
Kaneko & Tamaura, et al.
Tokyo Tech - 2011
[Kane 11]
Cycling of Zr-doped ceria (Zr content: 0, 10, 20, 30%) between 500 and 1500°C under air
20% Zr-content yielded highest release of 0.13 mmol O2 per gr mat
Le Gal & Abanades
CNRS - 2011 - 2012
[Le G 11] [Le G 12]
ceria doped with Zr (0 - 50%) or Ta (10, 25, 50%) or with Gd, Sm (10%) or with La (10, 25%)
TGA with two cycles (reduced at 1400°C under Ar; oxidized at different T with water)
synthesized with different routes --> different yields were obtained
25% Zr-content yielded highest release of > 0.17 mmol O2 per gr mat
Furler & Steinfeld, et al.
ETH Zurich - 2012
[Furl 12a] [Furl 12b]
felts and reticulated porous ceramics made of pure ceria tested in solar reactor (2800 suns)
syngas production with felt: up to 0.13 mmol O2 per gr at ~1500°C with 0.8% solar-to-fuel peak efficiency
CO prdoction with RPC: up to 0.12 mmol O2 per gr at 1600°C with 3.53% solar-to-fuel peak efficiency
Le Gal & Abanades, et al.
CNRS - 2013
[Le G 13]
ceria doped with Zr (0 - 50%) or with Zr and Y, La, Pr, Gd
TGA with two cycles (reduced at 1400°C under Ar; oxidized at different T with water)
specific O2 yield peaks at 25% Zr content
trivalent dopants do not improve the reducibility

2.4 Outlining the Research

Research Objective

Nowadays, so-called solar fuel processes that use concentrated solar power to thermochemically produce fuels via a two-step redox reaction are still in the research phase. The overarching goal of this thesis is to pave the way towards the commercialization of such processes. Basic process analysis identifies the redox material as the major bottleneck of process efficiency and points out the demand to improve the performance of the applied material. Particularly, improvements of the reduction step are pivotal, implying the enhancement of the reducibility of the material quantified in the absolute reduction extent and the facilitation in terms of the reduction conditions. Here, the reduction temperature and the allowed partial pressure of oxygen are of major interest.

A thermodynamical screening of more than 40 redox systems with the aid of Ellingham diagrams identified ceria as the most promising redox material available. Although pure ceria principally features the properties to be employed in TCCs, the technical realization of the process demands significant improvements of the reducibility of ceria. Doping ceria with various elements is the most obvious approach to provide such improvements. However, due to the lack of thermodynamical data as well as literature data to evaluate the potential of doped-ceria materials for the solar fuel production, an experimental approach is required. The main research objectives are:

Identification of the optimal dopants and dopant content in ceria regarding the fuel productivity quantified in specific yields and regarding the long-term stability.

Determination of the kinetics of the oxidation and reduction and the impact of doping as well as microstructure on the kinetics.

Evaluation of the dependence of the reduction extent on reduction conditions and, therewith, evaluation of the thermodynamics of the doped materials.

Assessment of the potential of the doped materials for the application in solar fuel processes in terms of efficiency.

Course of Investigation

After introducing the materials and methods employed in this thesis in chapter 3, four chapters pursue the main research objectives. Each chapter focuses on one research objective.

Chapter 4 encompasses the impact of zirconia and rare-earth doping on the redox per-

formance of ceria. Experimental campaigns of powder materials with the aid of thermogravimetry analysis were carried out to determine the specific yields of fuel production and oxygen release depending on the composition. Accordingly, the optimal compositions of doped-ceria materials were identified. To assess the impact of doping on the long-term stability, the most promising compositions identified were subjected to long-term experiments of up to 100 cycles. Microstructural characterization by means of XRD and SEM completes the experimental investigation.

Because the requirements on the kinetics are very high to assure efficient cyclic operation, to assess the process the determination of reliable reaction rates are ineluctable. However, since thermogravimetry exhibits methodical deficits to estimate such rates and no other, more suitable testing facility was available, the kinetical study presented in chapter 5 solely focuses on a qualitative analyzes of the impact of doping and microstructure on the kinetics. Accordingly, in combination with microstructural characterization, test series employing pellets were carried out in the thermobalance to study both, oxidation and reduction to gain fundamental insight into the kinetics as well as to create objectives for subsequent research.

In chapter 6, an experimental campaign with pellets is described that evaluates the reduction thermodynamics of pure ceria as well as the optimal doped compositions. With the aid of a thermobalance, the equilibrium reducibilities at varying reduction temperatures and several partial pressures of oxygen were determined. Therewith, the improvement of the reducibility caused by doping was quantified with respect to the reaction conditions. By applying a thermodynamical reaction model, the dependence of the reduction extent on both, temperature and partial pressure of oxygen was calculated, yielding functions to determine the reducibilities of the various compositions for arbitrary reaction conditions. These functions were applied to assess the Gibbs energy of the redox reaction and to construct Ellingham diagrams. Those diagrams serve as a tool to display the fundamental relations of the reaction conditions of the reduction as well as the ability of a material to split water and carbon dioxide. Furthermore, the diagrams convey the enthalpy and entropy changes due to the redox reaction.

The last experimental chapter, chapter 7 evaluates the potential of the doped materials to overcome the barriers for the technical realization. To gain a realistic idea of the potential of the doped-materials, an innovative reactor design, which was recently reported, was employed. A parametric study varying the temperature, partial pressure of oxygen and heat recuperation effectiveness in two concentrating concepts was performed. Therewith, the doped materials were ranked with respect to pure ceria as well as to the process conditions, yielding potential limitations of the feasibility of the process.

Chapter 8 concludes the most important findings of this thesis and displays the perspective for upcoming studies that aim to further understand and enhance ceria-based materials concerning their application in solar-fuel processes.

3 Materials and Methods

The following chapter introduces the materials and methods that are employed in this thesis. To evaluate measurement uncertainties, the guide to the expression of uncertainty in measurement (GUM) is applied. Doped-ceria powder materials were synthesized via an auto-combustion route. A fraction of the powder materials was further manufactured to dense as well as to porous pellets. Thermogravimetric analysis (TGA) assessed the performance of both, powder and pellet materials. X-ray diffraction (XRD) and scanning electron microscopy (SEM) characterized the microstructure of the materials.

Contents

3.1 Uncertainty in Measurement

The uncertainties of the experimental results in this work are expressed as the standard uncertainty according to the *guide to the expression of uncertainty in measurement* (GUM) [GUM]. The GUM classifies the evaluation of uncertainty in *type A* and *type B*. Mainly in this thesis, the standard uncertainty $u(v)$ of the mean of the measurand v was estimated based on statistical methods (GUM: *type A*). In some cases, $u(v)$ was estimated by applying the procedure of *type B*, based on error margins due to manufacturers data or own experience. The results are presented as $\langle v \rangle \pm u(v)$. The combined standard uncertainty $u(w)$ of a value w depending on various input quantities v_i with uncertainties $u(v_i)$ is given by:

$$u(w) = \sqrt{\sum \left(\frac{\partial f}{\partial v_i} \right)^2 \cdot u^2 (v_i)} \tag{3.1}$$

The estimation of the uncertainty of each experimental procedure/measurement will be discussed in its own section.

3.2 Synthesis

3.2.1 Powder Route

Various routes are able to synthesize ceria-based materials that exhibit homogenous distribution of the dopants within the crystal structure. One may distinguish between solid to solid synthesis and wet chemical synthesis. Solid to solid routes are the oldest and most-common routes to synthesize multi-component systems by direct reaction of solid compounds at high temperatures. These low-cost methods may produce solid materials on the industrial scale [Adac 02]. However, long sintering durations at high temperatures as well as the possibility of non-homogeneity make these routes inapt to provide the materials for this thesis. By contrast, wet chemical routes are more feasible because of their process conditions. Literature primarily discusses coprecipitation, sol-gel and combustion routes to synthesize ceria-based materials. In a coprecipitation synthesis, the oxide is precipitated from a liquid solution of dissolved salts, e.g. nitrates [Llus 10]. The main difficulty is the simultaneous precipitation of all components at once, which is crucial to obtain segregation-free target compositions. The sol-gel route involves chemical and physical processes associated with hydrolysis, polymerization, gelation, condensation, drying and densification [Henc 90]. Downsides of this route are the numerousness steps accounting for close monitoring of the process and the high costs of the raw material (in the case of metal alkoxides). Combustion processes feature a rapid thermal degradation of precursors with oxygen at relatively low temperatures producing homogenous powders in the nanometer scale [Hwan 06, Dega 09]. In particular, these routes are suitable to

synthesize non-crystalline single-phase multi-component oxides.

At this stage of the research of doped ceria for solar fuel processes, economical considerations concerning the synthesis play a minor role, because primarily material screening has to be done. It is solely crucial to synthesize single phase doped-ceria materials that exhibit excellent homogeneity via a synthesis route that is convenient in terms of complexity and duration. Auto-combustion routes perfectly meet these demands.

In literature, various types of combustion routes are reported [Liu 12]. They have in common a sequence of exothermic chemical reactions between an oxidant and a fuel, which produce heat or both heat and light in form of either flames or a glow. The investigated materials were synthesized via the citrate-nitrate auto-combustion route similar to ones reported elsewhere [Peng 02, Alif 03, Maha 05, Hoss 07]. This route makes use of an reduction-oxidation type exothermic reaction. As precursors, nitrates containing the desired metal cations are mixed with citric acid. The citric acid serves as a chelating agent for the metal ions as shown in figure 3.1. In addition, the citric acid provides the fuel for the

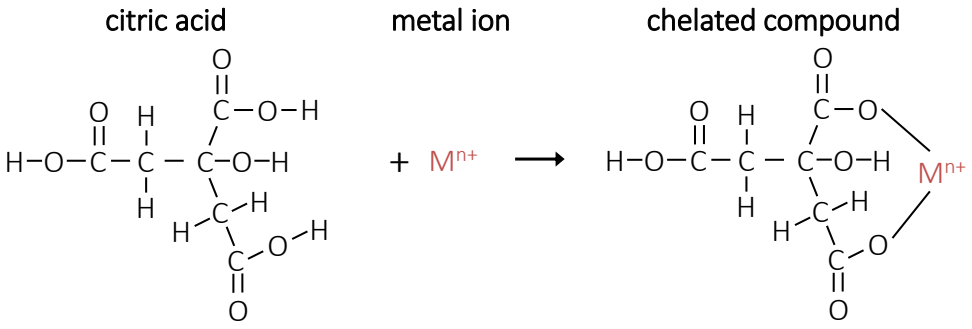

Figure 3.1: Chelation mechanism of citric acid with a metal ion.

auto-combustion process. Heating the mixture induces the nitrates to decompose. The released oxygen acts as an in-situ oxidizing agent causing the ignition of the carbon that is present in the citric acid. The exothermic burning of carbon causes the temperature to increase. Therefore, the completion of the reaction requires no further heating.

The synthesis route was practically conducted as presented in figure 3.2. The precursors of the redox powders are listed in table 3.1. For the sake of convenience, the solid nitrates containing the cation M were dissolved in deionized water to produce a liquid solution with a concentration c_M. Desired amounts of these liquid solutions were mixed in a reaction vessel made of quartz. Citric acid, also dissolved in deionized water, was added to the nitrates in a molar ratio of 1:2 (cations:citric acid). Water evaporation at 95°C on a heating plate under continuous stirring yielded a yellow-colored gel. Heating this gel to 200°C for 20 minutes resulted in a swollen foam exhibiting a very low density. During slow heating to 500°C, the auto combustion occurred leaving a fine oxide powder in the reaction vessel. Subsequent calcination in the reaction vessel in a muffle furnace at 800°C for 1h under air ensured the removal of remaining carbonaceous species. For

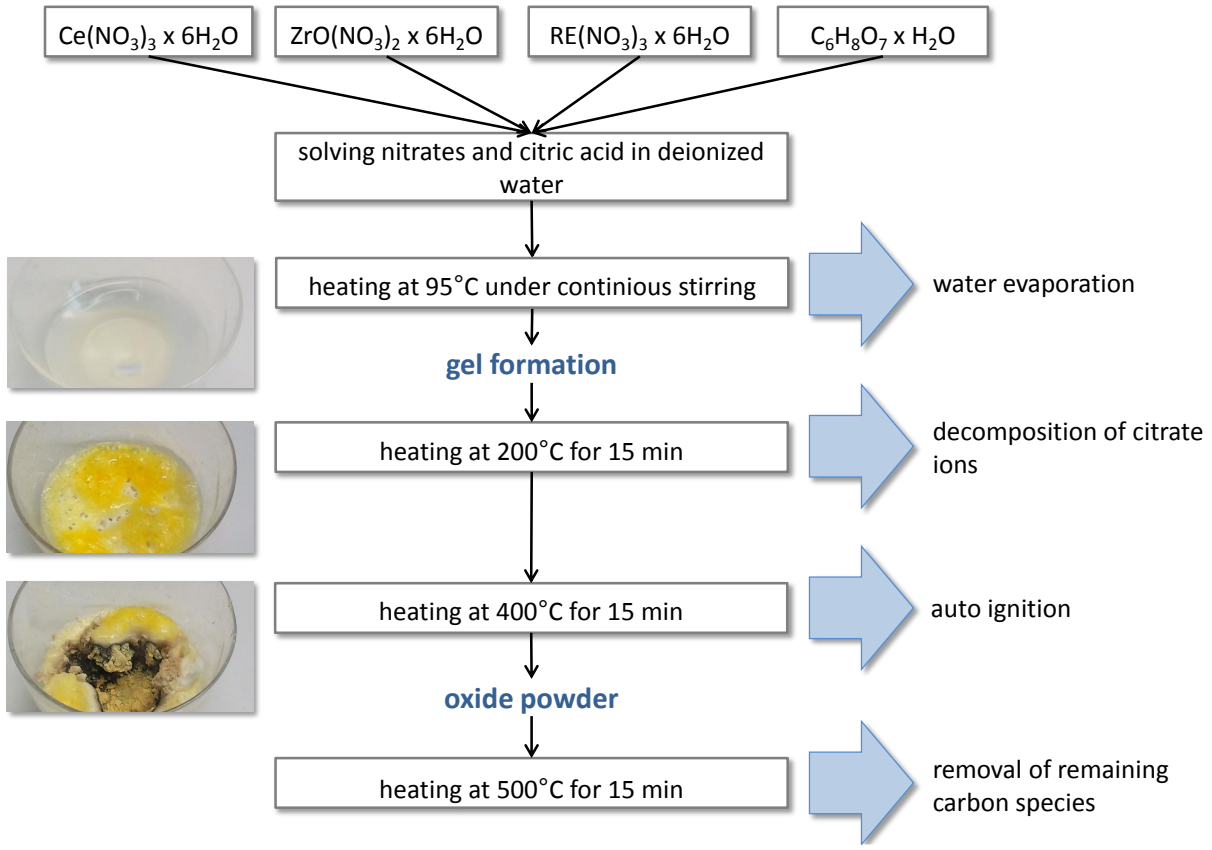

Figure 3.2: Citric auto combustion route employed for powder synthesis. RE denotes rare-earth elements (RE = Y, La, Sm and Gd).

Table 3.1: Chemical precursors dissolved in deionized water. The resulting solutions have the concentration c_M (M = Ce, Zr, Gd, Sm, La and Y).

substances	formula	purity	distributor	c_M in mol·l^{-1}
citric acid monohydrate	$C_6H_8O_7$	> 99%	Merck	2
cerium(III) nitrate hexahydrate	$Ce(NO_3)_3$	>99.9%	Merck	0.2
zirconium(IV) oxynitrate hydrate	$ZrO(NO_3)_2$	>99.9%	Sigma Aldrich	0.2
yttrium(III) nitrate hexahydrate	$Y(NO_3)_3$	>99%	Merck	0.1
lanthan(III) nitrate hexahydrate	$La(NO_3)_3$	>99.9%	Alfa Aesar	0.1
samarium(III) nitrate hexahydrate	$Sm(NO_3)_3$	>99.9%	Alfa Aesar	0.1
gadolinium(III) nitrate hexahydrate	$Gd(NO_3)_3$	>99.9%	Alfa Aesar	0.1

each composition, at least two batches were synthesized to guarantee reproducibility.

For the powder test campaign presented in chapter 4, volumes of approximately 40 ml were mixed to obtain powder masses of approximately 0.5 g. Powders that were further processed to pellets were synthesized in batches of more than 5 g. Pellets investigations are described in chapter 5 and 6.

3.2.2 Quantification of the Synthesis

In this work, solid solutions of either ceria and zirconia or solid solutions of ceria, zirconia and one trivalent rare-earth oxide are investigated, that are described with the following formula:

$$Ce_zZr_xRE_yO_{2-y/2} \tag{3.2}$$

The three quantities x, y and z quantify the content of each cation: The zirconium content x, the rare-earth content y (RE = Y, La, Sm, Gd) and the resulting cerium content z with $z = 1 - x - y$. The oxygen fraction is reduced due to the trivalence of the rare-earth elements. Note that for $y = 0$ only ceria-zirconia solid solutions are described. The contents of the various elements, i.e. the composition of the material, determine intensive properties of the material such as the molar weight of the oxidized material M_{ox}:

$$M_{ox} = zM_{Ce} + xM_{Zr} + yM_{RE} + (2 - 0.5y)M_O, \tag{3.3}$$

where M_{Ce} denotes the molar weight of cerium, M_{Zr} of zirconium, M_{RE} of the employed rare-earth element and M_O of oxygen. Since solely cerium changes its valance from IV to III, the maximum oxygen release during reduction is correlated to the cerium content z. Hence, the molar weight of the fully reduced material is given by:

$$M_{red} = zM_{Ce} + xM_{Zr} + yM_{RE} + (2 - y/2)M_O - z/2M_O = M_{ox} - z/2M_O \tag{3.4}$$

For the maximum mass loss Δm_{max} assuming complete reduction of the material, equation 3.3 and 3.4 lead to:

$$\Delta m_{max} = 1 - \frac{M_{ox}}{M_{red}} = 0.5z \cdot \frac{M_O}{M_{ox}} \tag{3.5}$$

Since the intensive properties Δm_{max} and M_{ox} are applied to calculate performance quantities (see section 3.3), uncertainties of x, y and z will directly influence the performance values derived from experimental campaigns. The contents x, y and z correspond to the volumes V_x, V_y and V_z of the nitrate solutions with their concentrations c_M mixed together in the first step of the synthesis. A content i of a cation M is given by:

$$i = \frac{V_i \cdot c_M}{V_x \cdot c_{Zr} + V_y \cdot c_{RE} + V_z \cdot c_{Ce}} \tag{3.6}$$

with $i = x, y, z$ and M = Ce, Zr, Y, La, Sm and Gd. The volumes V_x, V_y and V_z were adjusted with the aid of various volumetric pipettes (class AS) with volumes 0.5 ml $\leq V_{pipette} \leq$ 50 ml. A statistical analysis of ten independent observations estimated the mean volumes of the pipettes with their standard deviation of less than $\pm$0.03 ml. For each observation, the pipettes were filled completely with deionized and the drained water was weighed with an analytical balance (precision of $\pm$0.1 mg). The concentration c_M of the liquid solutions

is given by:

$$c_M = \frac{m_M}{V_{flask}} \tag{3.7}$$

where m_M denotes the mass of the solid nitrate and V_{flask} the volume of the employed reaction vessel. The balance features a precision of ±0.1 mg leading to relative uncertainties of less than 0.01% for masses m_M of more than 5 g that were the minimum amounts to produce the solutions. The nitrates were funneled into volumetric flasks with volumes 100 ml $\leq V_{flask} \leq$ 1000 ml that were subsequently filled with deionized water. The flask volumes exhibit relative error limits of less than 0.1%.

The relative standard uncertainties $u_r(\Delta m_{max})$ and $u_r(M_{ox})$ estimated by combining the standard uncertainties of x, y and z are less than 0.2%. Compared to the relative standard uncertainties of the measurands obtained in thermobalance runs of approximately 5%, these small uncertainties are negligible and are not considered in further analysis. Table 3.2 presents the powder materials synthesized and investigated in this thesis.

Table 3.2: Synthesized powder materials.

material	x	y
CeO_2	-	-
$Ce_{1-x}Zr_xO_2$	0.026, 0.051, 0.076, 0.126, 0.151 0.177, 0.200, 0.225, 0.252, 0.376	-
$Ce_{0.85-y}Zr_{0.15}Y_yO_{2-0.5y}$	0.15	0.013, 0.025, 0.076, 0.2
$Ce_{0.85-y}Zr_{0.15}La_yO_{2-0.5y}$	0.15	0.025, 0.05, 0.075, 0.1 0.125, 0.15, 0.2
$Ce_{0.85-y}Zr_{0.15}Sm_yO_{2-0.5y}$	0.15	0.013, 0.025, 0.076, 0.2
$Ce_{0.85-y}Zr_{0.15}Gd_yO_{2-0.5y}$	0.15	0.013, 0.025, 0.076, 0.2

3.2.3 Pellet Manufacturing

The pellets were manufactured within the scope of the master thesis of Tijana Paraknewitz [Para 13]. Powders were slightly mixed with polyethylene glycol dissolved in ethanol using a pestle. Amounts of 600 to 1200 mg of the dried mixtures were uniaxially pressed with 110 MPa into a pellet using a cylindrical extrusion die and sintered at 1650°C for 2 h. Two types of pellets were manufactured: Dense and porous.

- Before pressing dense pellets, the powders were ball-milled in a planetary micro mill pulversiette7 (Fritzsch, Germany) using grinding balls made of ZrO_2 with diameters of 1.5 mm in a grinding balls to powder weight ratio of 60:1. Isopropanol (Sigma-Aldrich, purity >98%) was used as the dispersing agent in a powder to isopropanol weight ratio of 10:1. The milling was performed for ten minutes at a

velocity of 500 rpm and repeated three times.

- To obtain porous structures, rice starch (Sigma-Aldrich) was added to the powder in a ratio of 10 to 30 wt.%. The starch featured particle size of 1 to 8 µm. During the firing process, the powder burns out and leaves pores. Digital image analyzes estimate porosities of approximately 60 to 70% [Para 13].

Table 3.3 summarizes the pellets manufactured and investigated in this thesis. Pellet examples are shown in figure 3.3.

Table 3.3: Manufactured and investigated pellet materials.

short name **d** ≡ dense **p** ≡ porous	**mass** m_{pel} in mg ±0.01 mg	**height** h in mm ±0.1 mm	**diameter** d in mm ±0.1 mm	**starch content** s in wt.% ±1 wt.%	**porosity** Φ in % ±5 %
			C≡ CeO_2		
C:d**600**	589.75	0.8	12.4	-	6
C:d1200	1180.03	1.7	12.4	-	7
C:p**10**	562.34	1.5	12.1	**10**	50
C:p20	587.76	2.1	12.4	20	64
C:p30	582.90	2.4	12.0	30	67
			CZ≡ $Ce_{0.85}Zr_{0.15}O_2$		
CZ:d600	592.54	1.0	11.6	-	8
CZ:d1200	1182.36	2.0	11.6	-	8
CZ:p10	588.72	1.7	12.3	10	55
CZ:p20	590.70	2.2	12.3	20	65
CZ:p30	590.73	3.1	12.3	30	75
			CZL≡ $Ce_{0.825}Zr_{0.15}La_{0.025}O_{1.99}$		
CZL:d600	591.69	1.1	11.2	-	8
			CZS≡ $Ce_{0.825}Zr_{0.15}Sm_{0.025}O_{1.99}$		
CZS:d600	591.10	1.1	11.3	-	8
CZS:d1200	1177.49	2.0	11.3	-	9
CZS:p10	586.42	1.7	11.8	10	52
CZS:p20	548.02	1.9	11.7	20	60
CZS:p30	583.07	3.3	11.6	30	74

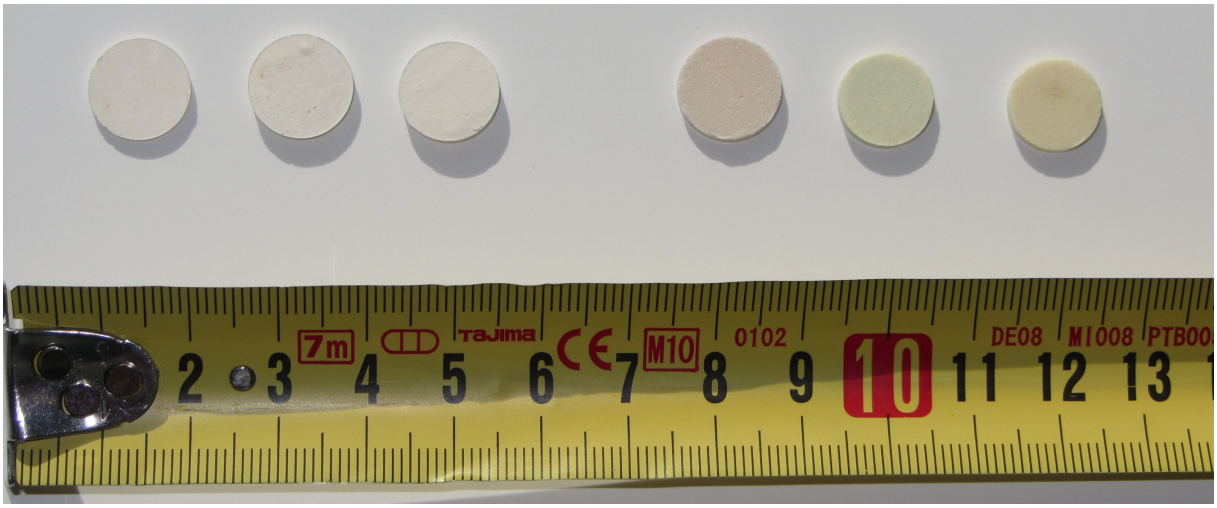

Figure 3.3: Different types of pellets investigated in this thesis. From left to right: C:p10, C:p20, C:p30, C:d1200, CZ:d1200, CZS:d1200. The short names are explained in table 3.3.

3.3 Performance Testing via Thermogravimetric Analysis

Thermogravimetric analysis (TGA) is a method that measures the mass change of a sample while it is subjected to a specified temperature program consisting of heating, cooling and isothermal steps. The basic instrumental requirements are a precision balance and a furnace that can be linearly programmed [Coat 63]. A device fulfilling these requirements is referred to as a thermobalance. Commonly, a thermobalance is swept with a gas flow during the experiment to obtain a certain atmosphere or to sweep gaseous species released from the sample. Since reducing or oxidizing atmospheres are permitted, a thermobalance is able to simulate thermochemical gas splitting cycles. Connected to a mass spectrometer that monitors the gas outlet of the furnace, it is a powerful tool to assess the performance of redox materials towards thermochemical fuel production. The results from a thermogravimetric run are presented by mass change Δm versus time t (or temperature T) graphs.

3.3.1 Experimental Proceeding

The TGA facility employed in this thesis consists of a thermobalance STA 449 F3 Jupiter (Netzsch, Germany) and a mass spectrometer GSD-301-C2 (Pfeiffer Vacuum, Germany) and is part of the thermo-analytical laboratory of CeraStorE®. Figure 3.4 shows the test facility. The thermobalance is monitored with the Software Netzsch Messung 5.2 and the mass spectrometer with Pfeiffer Quadstar 32-bit 7.0.

The interior of the device is shown in figures 3.5. The balance system is located in the

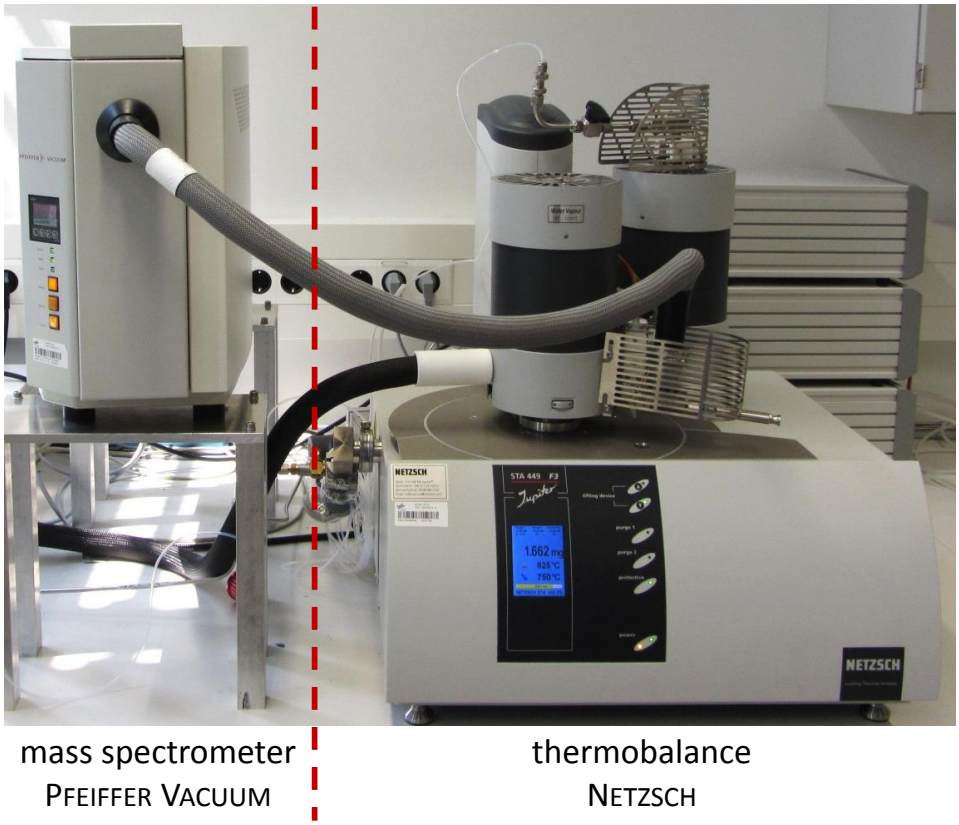

Figure 3.4: TGA test facility located in the CeraStorE® consisting of a thermobalance Netzsch STA 443 Jupiter F3 and a mass spectrometer Pfeiffer GSD-301-C2, which is connected to the gas exhaust.

lower part of the device. The precision of the balance is ±1 µg. A sample carrier is connected to the balance system, entering the protective tube, which is shielded with a radiation shield in order to reduce thermal losses of the upper part (furnace). The balance system and the furnace are swept with the *protective* gas; two other gases, $purge_{red}$ and $purge_{ox}$, only sweep the furnace of the STA. Three mass flow controllers (MFC) adjust the gas composition and gas flow. The direction of the gas flow is denoted by the arrows and the gas is released at the gas outlet, which is connected to the mass spectrometer. Additionally, during the pellet test campaigns, an oxygen sensor (λ-sensor) measures the partial pressure of oxygen $p(O_2)$ of the gas outlet. The chamber is linked to an evacuating system in order to assure an inert atmosphere at the beginning of each experiment. Table 3.4 provides an overview of the gases applied in this thesis.

The $purge_{red}$ and $purge_{ox}$ gases sweep the sample during reduction and oxidation, respectively. The *protective* gas sweeps the entire device starting at the balance system with 20 $ml \cdot min^{-1}$ incessantly to impede humidity from entering the balance system, guaranteeing a steady weighing signal. To assure consistent gas atmosphere in particular during reduction, the same inert gas is connected to the *protective* as well as to the $purge_{red}$ ports. For this purpose, argon-based gases were selected with different oxygen concentrations;

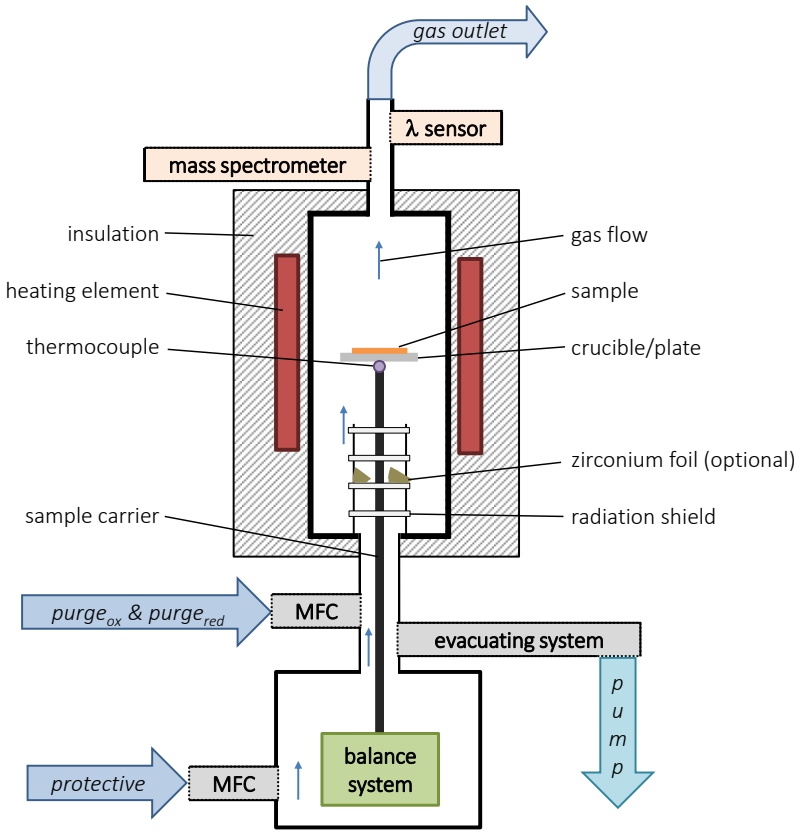

Figure 3.5: Schematic of the thermobalance interior.

Argon gas with a standard purity of 5.0 is employed as well as test gases purchased from Praxair (Germany), which are predefined mixtures of 5.7 Ar with 5.0 O_2.

In order to oxidize the material, two gases are available to be used as *purge*$_{ox}$: CO_2 and synthetic air. A second furnace allows the use of water steam but is limited to temperatures of 1250°C during reduction. Since the investigated materials require higher reduction temperatures and during experiment the furnaces cannot be changed, the water steam furnace is not applicable. Hence, no water splitting cycles – i.e. no H_2 production cycles – were carried out in this work. In the following, differences in the experimental procedure of powder testing and pellet testing are described.

Powder Test Campaigns

In the test campaign presented in chapter 4, powder materials with varying compositions are investigated. Before TGA experiments, those materials were calcined at 1400°C for 1h in a Pt crucible. Samples with masses $m_{\text{initial}} = 25\,\text{mg}$ were placed on an Al_2O_3 plate (13 mm in diameter) that was covered with a Pt-foil. During the experiment, Ar 5.0 swept the thermobalance. The gas had a nominal oxygen concentration $c(O_2) \leq 10$ ppm. Approximately one gram zirconium foil that was placed in the furnace acted as an oxygen

Table 3.4: Gases employed in the experimental campaigns.

used as	**gas**	**flow rates** in ml·min^{-1}	nominal[a] **$c(O_2)$ & $c(CO_2)$** in vol.%	resulting[b] **$p(O_2)$, $c(CO_2)$ & $c(O_2)$** in Pa or vol.%	**chapter**
protective and purge$_{red}$	Ar 5.0	85	$c(O_2) \leq 0.001$	$p(O_2) \approx 0.5$[c]	4
	test gas 1	85	$c(O_2) = 0.0099$	$p(O_2) \approx 27$ - 49[d]	5 / 6
	test gas 2	85	$c(O_2) = 0.0978$	$p(O_2) \approx 125$[d]	6
	test gas 3	85	$c(O_2) = 0.988$	$p(O_2) \approx 1270$[d]	6
purge$_{ox}$	CO_2 4.8	5	$c(CO_2) \geq 99.998$	$c(CO_2) \approx 6$[e]	4
		50		$c(CO_2) \approx 60$[e]	6
	synthetic air	30	$c(O_2) = 20$	$c(O_2) \approx 8$[e]	5 / 6

[a] Nominal oxygen and CO_2 concentrations $c(O_2)$ & $c(CO_2)$ of the raw gas according to manufacturer's data.
[b] Estimated partial pressures and concentrations at the sample. According to pretests, varying room pressures and λ-sensor calibrations, a relative uncertainty of 10% is assumed.
[c] Derived from comparing maximum reducibilities obtained in calibration runs of pure ceria with literature values [Panl 75]. The calibration runs comprised long reduction steps of more than 4 h at different temperatures providing equilibrium conditions.
[d] Derived from oxygen concentrations measured with the oxygen sensor that was connected to the gas outlet.
[e] During oxidation, *purge*$_{ox}$ is introduced with a certain flow rate and *purge*$_{red}$ is reduced by this rate to keep the total flow rate constant. The denoted concentrations correspond to the volumetric fraction of CO_2 and O_2, respectively.

getter and absorbed oxygen entering the measuring cell due to random leakage. Thereby, low oxygen partial pressure of oxygen of approximately $p(O_2) \approx 0.5$ Pa were obtained. Such low $p(O_2)$ were necessary to assure mass changes during cycling that are large enough to be reasonably analyzed, especially, since the powder campaign was supposed to screen materials exhibiting only slight compositions variations. The value of 0.5 Pa was estimated as explained in footnote[c] of table 3.4. Zirconium only reacts sufficiently with O_2, when it is heated to temperatures >300°C [Zeli 66]. Placing the foil on the forth level of the heating shield (see figure 3.5) assures that the temperature of the foil is sufficiently high to absorb oxygen when the sample is heated to temperatures close to the reduction temperature T_{red}. When the oxidation temperature of 900°C is applied, the temperature at the Zr-foil is as low that no oxidation occurs. This was evidenced by isothermal tests at 900°C, which resulted in no changes of the mass of the Zirconium foil. Hence, the zirconium foil solely absorbs oxygen during reduction and not during oxidation when lower temperatures are applied to the sample. The powder materials were oxidized with CO_2 in a mixture of 6 vol.% CO_2 (4.8) in Ar (5.0). The flow rate was set to 85 ml · min^{-1} for all powder experiments.

Pellet Test Campaigns

Chapters 5 and 6 present the results of the pellet experiments. The pellets were placed on an Al_2O_3 plate (13 mm in diameter covered with a Pt-foil). During reduction, the measuring cell was swept at several flow rates with one of the test gases (see table 3.4). During the experiments, various reduction temperatures T_{red} were applied making the use of the oxygen getter (Zr-foil) unreasonable. The Zr-foil would lead to varying partial pressures of oxygen due to its temperature dependence. Therefore, an oxygen sensor was installed measuring the partial pressure of oxygen $p(O_2)$ of the exhaust gases. The oxidation was performed under a mixture of synthetic air and Ar, resulting in an oxygen concentration $c(O_2) = 8\%$.

3.3.2 Analyzing the Results

As mentioned above, the thermobalance can simulate thermochemical gas splitting cycles in order to evaluate the performance of a material towards solar fuel production. A cycle consists of

1. the reduction: A heating step to a reduction temperature T_{red} followed by an isothermal step. Both steps were performed under an inert Ar atmosphere.
2. the oxidation: A cooling step to a oxidation temperature T_{ox} followed by an isothermal step. At the beginning of the isothermal step, the atmosphere were changed to an oxidizing atmosphere for a certain amount of time.

The cycles were repeated as often as required. The signal Δm is corrected by means of reference experiments with an empty sample holder in order to filter all systematic effects that occur due to buoyancy (because of temperature changes) or changing the gas atmosphere. These experiments are referred to as blank runs. If not stated differently, all presented TGA data are already corrected.

The mass loss Δm_{red} during thermal reduction corresponds to the oxygen release; the mass gain Δm_{ox} during the oxidation to the oxygen uptake of the material. Figure 3.6 illustrates the estimation of mass losses Δm_{red} and Δm_{ox} according to the regulation EN ISO 11358. The mass spectrometer confirms the redox reaction, detecting O_2 during reduction. Note that oxidation might already occur during cooling and without introducing $purge_{ox}$, due to the oxygen contained in the applied gases *protective* and $purge_{red}$. For instance, the oxygen concentration of test gas 3 is $c(O_2) \approx 1\%$, which is sufficient to reoxidize the sample during cooling.

In the case of experiments performed with powder materials (chapter 4), the uncertainty of Δm_{red} and Δm_{ox} are obtained according to *type A* (GUM). Three to five samples per composition were subjected to cycling runs, which were individually corrected with five independent blank runs that were conducted periodically during the test campaign.

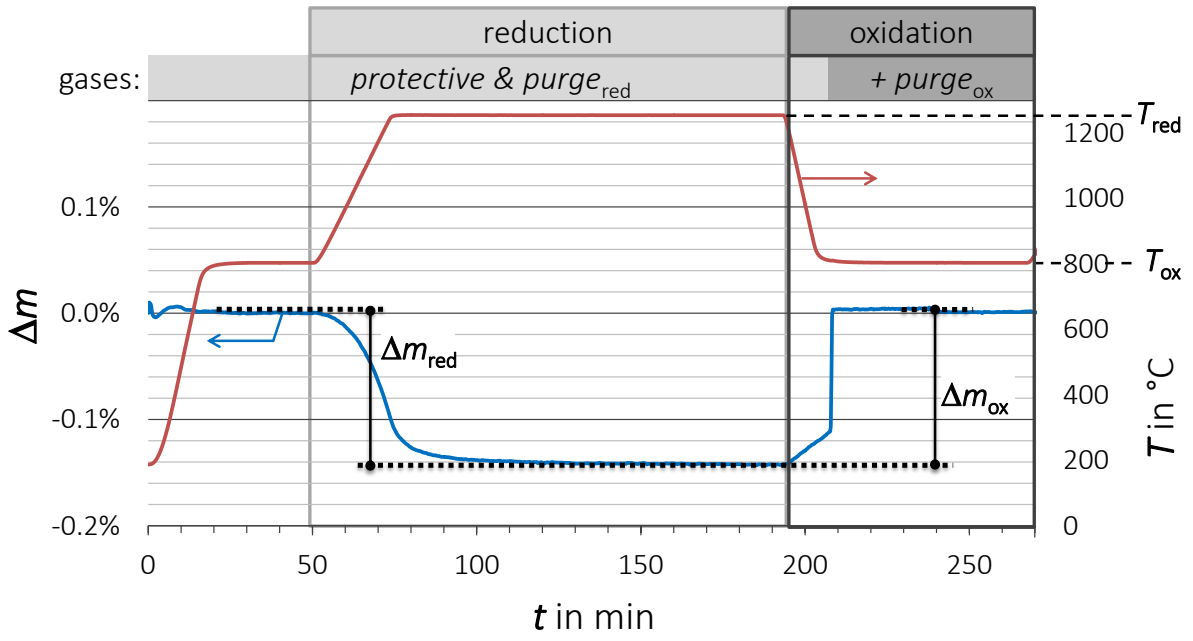

Figure 3.6: Example cycle of a TG experiment. Determination of Δm_{red} and Δm_{ox} according to the regulation EN ISO 11358.

Chapter 5 and 6 show the investigations of pellet materials. Since repetition of each experiment could not be performed, the uncertainty of the reduction mass loss $u^{pel}(\Delta m_{red})$ was evaluated according to *type B* (GUM). Based on an exemplary repetition of the experiment of one pellet (see appendix figure A.10), the standard deviation of the mean $\langle \Delta m_{red} \rangle$ of the three runs was estimated. This standard deviation serves as the upper and lower error limit a for the other pellet experiments. Assuming a triangular probability distribution, the *type B* standard uncertainty $u^{pel}(\Delta m_{red})$ of pellet experiments is given by

$$u^{pel}(\Delta m_{red}) = \frac{a}{\sqrt{6}} \tag{3.8}$$

Derived Quantities

Δm_{red} and Δm_{ox} allow the calculation of following quantities, which estimate the redox performance of the material:

- The **relative redox extents** X_{red} and X_{ox}, i. e. the mol ratio of reduced/oxidized cerium atoms to the total amount of cerium atoms (in at.% $Ce^{4+\rightarrow 3+}$ and at.% $Ce^{3+\rightarrow 4+}$, respectively).

$$X_{red,\,ox} = \frac{\Delta m_{red,\,ox}}{\Delta m_{max}} \tag{3.9}$$

Δm_{max} denotes the maximum mass change obtained when all cerium atoms change their valence. (see equation 3.5). The redox extent convey the information about the theoretical room for improvement in terms of the redox reaction. When, for instance,

$X_{red} = 100\%$, the material operates as good as stoichiometry allows. Starting from a completely oxidized ceria, X_{red} is linked to the absolute reduction extent δ as follows: $X_{red} = 2 \cdot \delta$.
The redox extent does not contain information concerning the mass that has to be heated every cycle to produce a certain amount of fuel.

- In order to assess the performance of the material towards a technical realization, **specific yields** are introduced: the specific O_2 yield $n_m(O_2)$ during reduction and CO yield $n_m(CO)$ during oxidation in the case of oxidation with CO_2 (in $mmol_{O_2}$ and $mmol_{CO}$ per gram oxidized material, respectively):

$$n_m(O_2) = 0.5\frac{\Delta m_{red}}{M_O} \tag{3.10}$$

$$n_m(CO) = 0.25\frac{\Delta m_{ox}}{M_O} \tag{3.11}$$

M_O denotes the molar weight of one oxygen atom (15.9994 $g \cdot mol^{-1}$). Note that the specific yields are not influenced by intensive material quantities derived in section 3.2.2, but only depend on the mass changes Δm_{red} and Δm_{ox}. The specific yields allow the estimation of the mass flows of the redox material necessary to produce a certain amount of fuel. This information is one of the key parameters to develop a reactor concept in terms of dimensions.
Doping ceria will inherently influence the specific yields. On the one hand, the molar weight changes. For instance, with increasing Zr-content the molar weight decreases, due to the lower molar weight of zirconium compared to cerium. On the other hand, the load of active sites (cerium) and therewith the actual activity of the material decreases.

- Changes of the molar weight due to doping do not inherently influence the **molar yields** O_2 and CO: $n_n(O_2)$ and $n_n(CO)$ (in $mmol_{O_2}$ and $mmol_{CO}$ per mmol oxidized material, respectively):

$$n_n(O_2) = n_m(O_2) \cdot M_{ox} \tag{3.12}$$

Molar yields are particularly interesting for comparing the effect of various dopants incorporated in the same amount.

Due to stoichiometrics of the cycle reactions, the reduction performance limits the fuel productivity. Provided that full reoxidation is achieved, the maximum amount of produced fuel corresponds to the amount of oxygen released in the precedent reduction. Any increases in oxygen yields are beneficial for the overall process efficiency $\eta_{solar\ to\ fuel}$. To compare diverse materials, a performance enhancement is defined as an increase in the molar or specific O_2 yields $n_n(O_2)$ or $n_m(O_2)$ at the same reduction conditions. This enhancement corresponds to an improved fuel production.

3.3.3 Methodical Improvements

Pretests discovered methodical problems concerning the investigation of redox reaction by means of thermogravimetric analysis. Figure 3.7 illustrates one of the first experiments performed with ceria-based materials in the employed thermobalance.

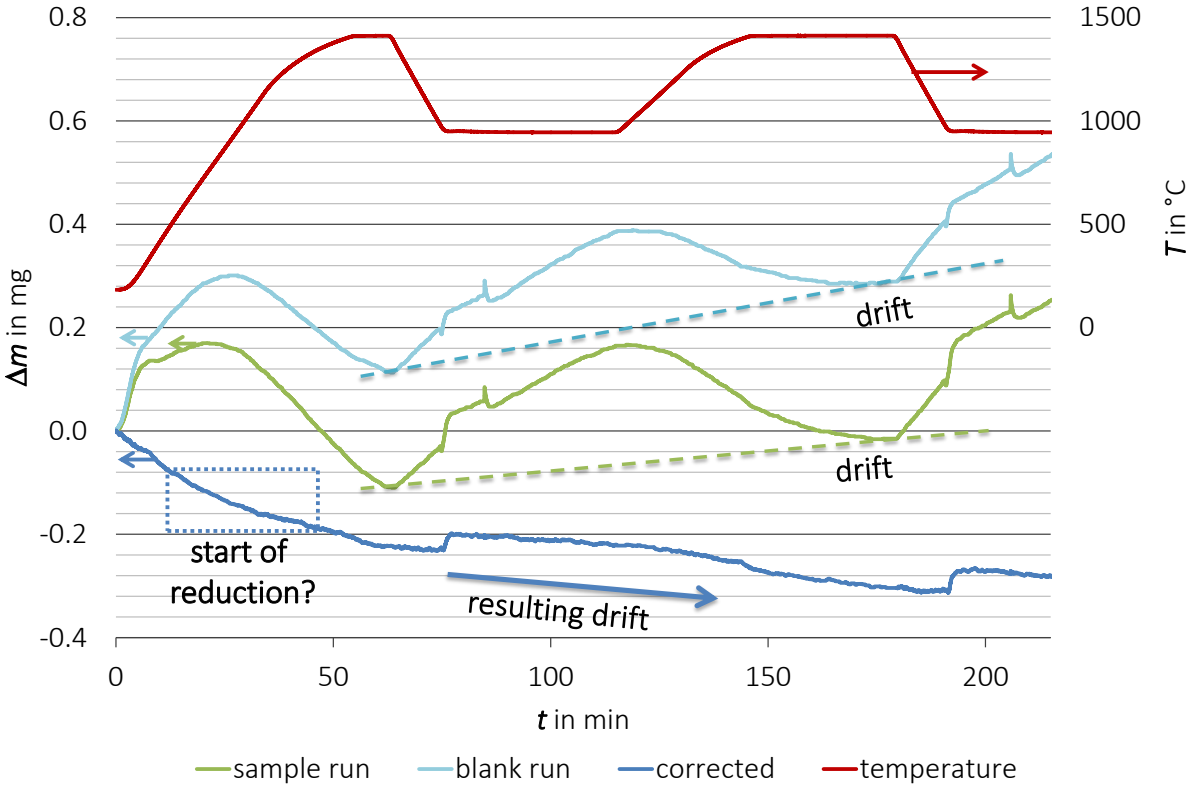

Figure 3.7: Pretest performed in the beginning of this thesis. Corrected correspond to the sample run subtracted by the blank run. Sample: Powder material of CeO_2 with a mass of 10 mg.

The following issues impede a reasonable analysis of the data:

1. The identification of the actual reduction start is indistinct making the estimation of Δm_{red} of the first reduction impossible. In addition, during the first heating of experiments carried out in the thermobalance, the mass signal exhibits measurement artifacts.

2. Due to its volume, the crucible employed in the pretests limits the sample masses to approximately 5 mg. Under the investigated process conditions (T and $p(O_2)$), reducing ceria leads to relative mass changes of less than 0.5%. Accordingly, the absolute mass loss at the end of a reduction is approximately 25 µg, which is close to the error limit of the thermobalance of 1 µg.

3. The mass signal of the employed thermobalance exhibits a drift differing in shape from one experiment to another. This drift effects sample as well as correction runs.

Therefore, correction runs may not filter this artifact accurately.

According to this, following modifications of the experimental procedure and improvements of the analysis were conducted to solve the methodical problems:

1. A preheating step to 1300°C with subsequent cooling to the oxidation temperature T_{ox} was performed. Thereby, the following reduction does not suffer from random effects influencing the mass signal. At T_{ox}, CO_2 was introduced to reoxidize the material that might be reduced during preheating. Hence, a complete reoxidized material is subjected to the first reduction and a distinct start of the reduction is assured.
2. A minimum sample mass of 25 mg was subjected to TGA experiment in order to obtain significant mass changes during the redox reaction.
3. The mass-signal drifts of sample as well as correction runs are individually calculated with the aid of an excel tool (Microsoft) that was developed in the scope of the thesis. In most of the cases, a polynomial regression could describe the drift accurately. Subtraction yields the undrifted data as shown exemplarily in the case of a blank run in figure 3.8.

3.4 Characterization Methods

X-ray Diffraction

X-ray diffraction (XRD) analyzes the crystallographic structure of the materials. XRD was performed with CuK_α radiation with the aid of a computer-controlled diffractometer D-5000 (Siemens, Germany). The material was placed on a sample holder with 2 cm in diameter that consists of monocrystalline silicon.

Scanning Electron Microscopy

Scanning electron microscopy (SEM) characterizes the microstructure of the powder as well as of the pellet samples. The characterization was carried out with a Ultra55 (Zeiss, Germany). Maximum magnifications of 900,000x are feasible with this equipment. Besides imaging of the microstructure, the elemental composition is quantitatively estimated using energy dispersive X-ray spectroscopy (EDS) unit (Oxford). Small amounts of a few µg of the powder materials were placed on sample holders made from aluminum. To investigate pellets, polished cross-sections of pellets were embedded in epoxy resin. The samples were coated with platinum by vapor phase deposition to assure their conductivity.

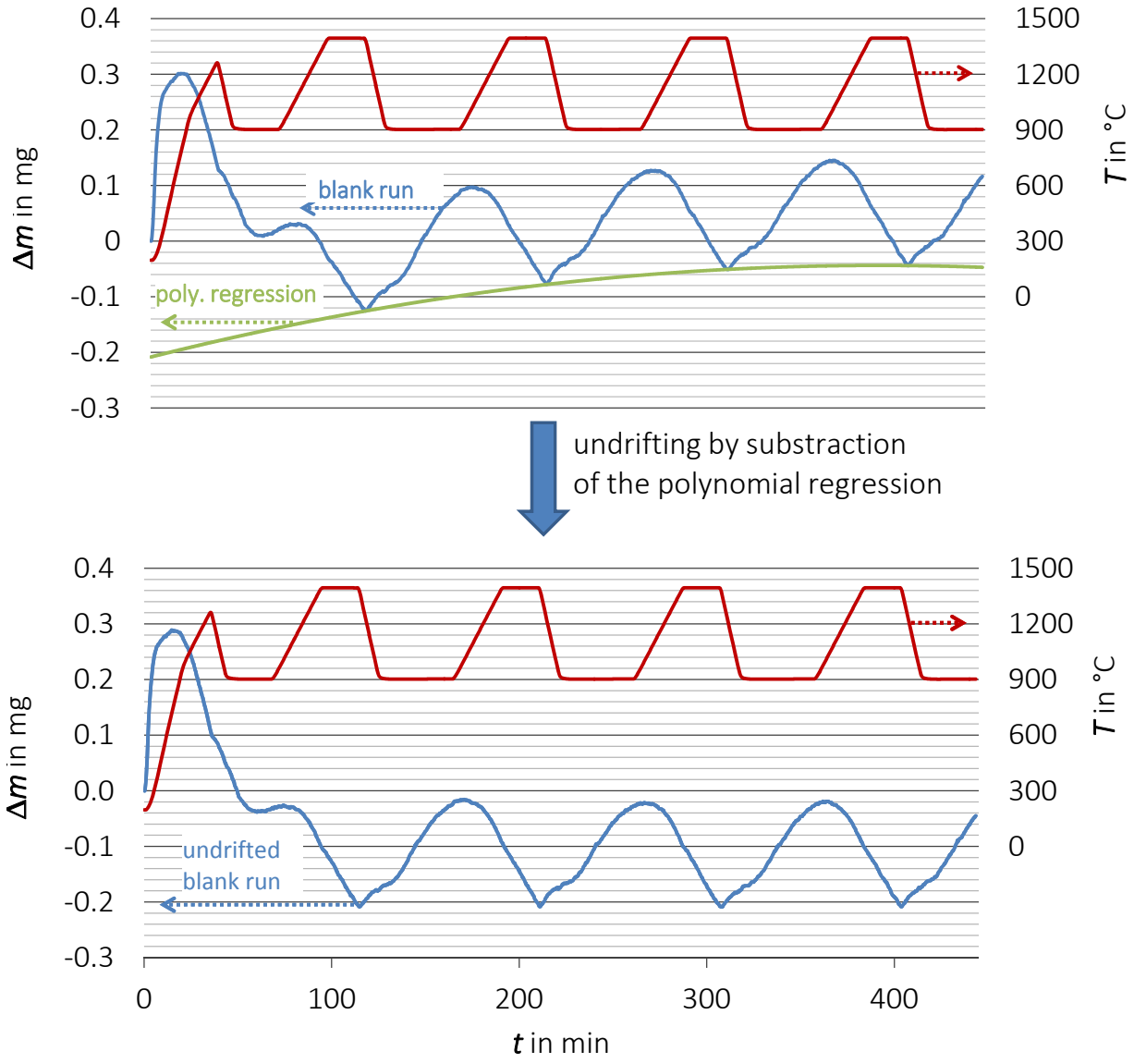

Figure 3.8: Example of "undrifting" data (blank run).

4 Optimizing the Doping of Ceria

One of the major barriers to technical success of thermochemical solar fuel production concerns the properties of the redox material. Improvements regarding the performance of the material as well as its long-term stability are necessary to make thermochemical solar fuel production competitive. In the case of ceria, doping is a promising approach to enhance its redox properties. This implies the substitution of cerium for foreign ions.

This chapter encompasses the evaluation of promising dopants such as zirconium and rare-earth ions to estimate their optimal content in ceria. Literature ascribes zirconia doping not only the ability to stabilize the microstructure of ceria, but also the facilitation of the reducibility. Lower-valent dopants are well-known in the solid oxide fuel cell community to improve the oxygen diffusivity within ceria, due to the creation of oxygen vacancies. In particular, rare-earth oxides are promising, because they feature chemical properties similar to ceria. Some of the results were already published in [Call 13]. The first section of this chapter focuses on improving the fuel productivity. Because of the absence of theoretical data, optimization of the composition requires an experimental approach that screens the powder materials in short-term experiments. The best compositions identified are subjected to long-term experiments in the second section. Therewith, the impact of doping on the cycle stability is investigated. The chapter concludes with the identification of compositions that are selected to be processed to pellets.

Contents

4.1 Fuel productivity

The term "fuel productivity" primarily implies the fuel (CO and/or H_2) yield per amount redox material (per g, mol or l) per cycle. According to the relation between produced fuel and released oxygen (equations 2.3 and 2.4), the specific/molar oxygen yield per cycle also serves as a performance number. However, comparison of the fuel productivity of various materials is complicated, because of accomplishing the cycling under different reaction conditions and testing devices. For instance, the reduction of zinc is carried out at much higher temperatures and requires a complicated processing due to phase changes. The oxygen yield per cycle of zinc might equal the one of ceria, but the quantification "per cycle" implies significant differences. Hence, the estimated fuel productivity solely bears the comparison within the same class of material that is investigated under the same reaction conditions.

The fuel productivity is evaluated with the aid of a thermobalance that performed four successive cycles. The data of a typical TGA run is shown in figure 4.1. After a pre-heating step to 1300°C with subsequent cooling to 900°C (not shown here), four similar cycles were performed consisting of a reduction step (heating to 1400°C with 20 K·min^{-1}; isothermal step for 20 minutes under Ar 5.0 corresponding to $p(O_2) = 5 \times 10^{-6}$ bar as

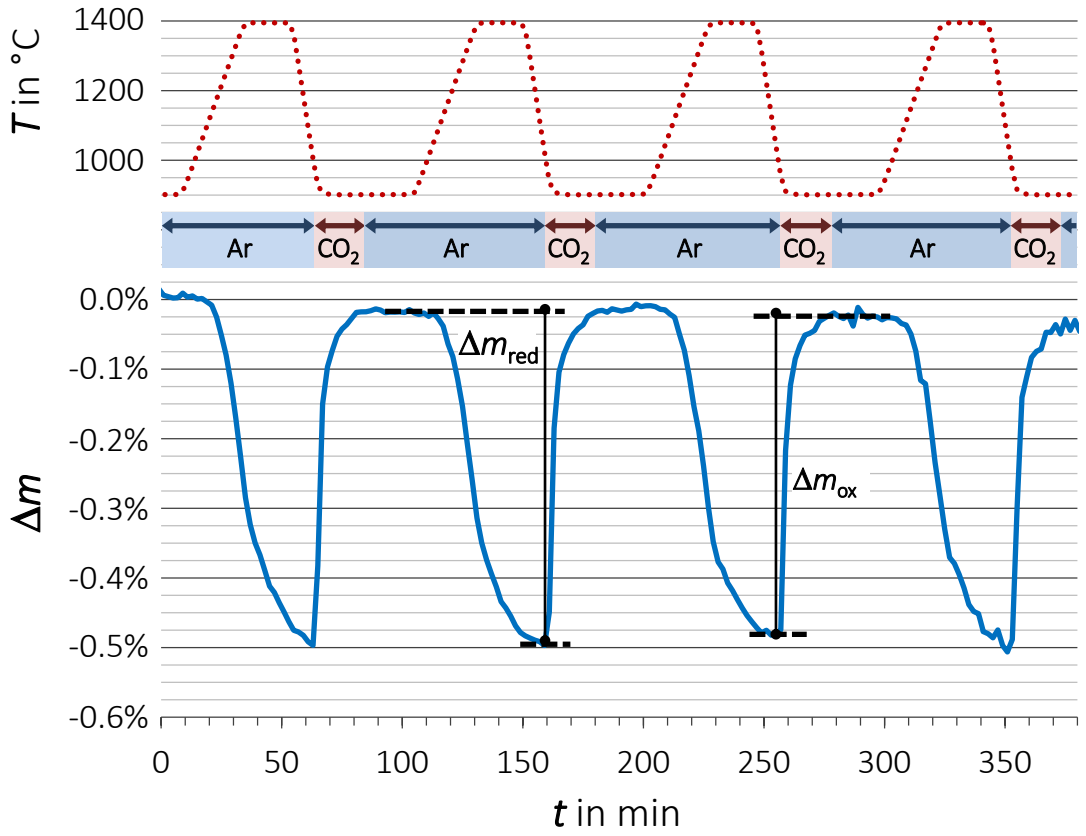

Figure 4.1: TGA program (temperature and atmosphere) applied in powder experiments and corresponding mass change versus time. Composition: $Ce_{0.85}Zr_{0.15}O_2$.

discussed in table 3.4) and a splitting step (cooling to 900°C with 50 K·min^{-1}; isothermal step for 20 minutes under 6 vol.% CO_2 4.8 in Ar 5.0 and 20 minutes under Ar 5.0). The mass gain and loss alternately occur in the cyclic reaction along with the temperature variation. During the heating process from 900°C to 1400°C, the reduction starts at about 1200°C corresponding to a sharp mass loss. The reaction rate markedly increases with temperature. As the temperature plateau begins, the Δm curve exhibits an inflection point representing a gradual reaction deceleration. This behavior was also observed from other groups and attributed to the rate-limiting transition between the surface reaction and the bulk reaction [Le G 11a]. At the end of the isothermal step, the reduction is close to completion. Upon cooling to 900°C, CO_2 is injected into the measuring cell causing a sharp mass increase. The oxidation reaction is significantly faster than the reduction and does not slow down before $\Delta m \approx -0.1\%$ is reached. After 20 minutes injecting CO_2, the sample mass approximates its initial value equaling full reoxidation.

4.1.1 Zirconia Doping

4.1.1.1 Results

The reducibility and CO_2-splitting ability of $Ce_{1-x}Zr_xO_2$ compositions with varying x is assessed via successive cycling in the thermobalance. x ranges from 0 to 0.375. Characterization of the samples is performed with the aid of XRD and SEM.

Performance

Figure 4.2 summarizes the calculated relative redox extents X_{red} and X_{ox} depending on the zirconia content x, based on the obtained Δm_{red} and Δm_{ox}. For each cycle, the reduction extent approximates its following oxidation extent. Only the first oxidation seems incomplete. This might be due to difficulties to determine the actual starting point of the reduction, resulting in values of X_{red} of the first reduction that are slightly too high. The redox extents marginally decrease in the first two cycles until they stabilize in the last two cycles. For further discussion only the third and fourth cycle is taken into account, because of the high uncertainties of the first two cycles. The redox extent augments with increasing Zr content from $X_{red/ox} \approx 7\%$ observed for pure ceria to $X_{red/ox} \approx 12\%$ for compositions in the range of 15% to 22.5% Zr content.

Specific yields are necessary to assess the performance of the material towards a technical realization of the process. They convey information essential for the reactor design, estimating the mass required to obtain a certain amount of fuel. The specific yields of O_2 and CO averaged over the third and fourth cycle is depicted in Figure 4.3. The ranking based on the specific yield determines the optimal Zr-content to be 15%. $Ce_{0.85}Zr_{0.15}O_2$ re-

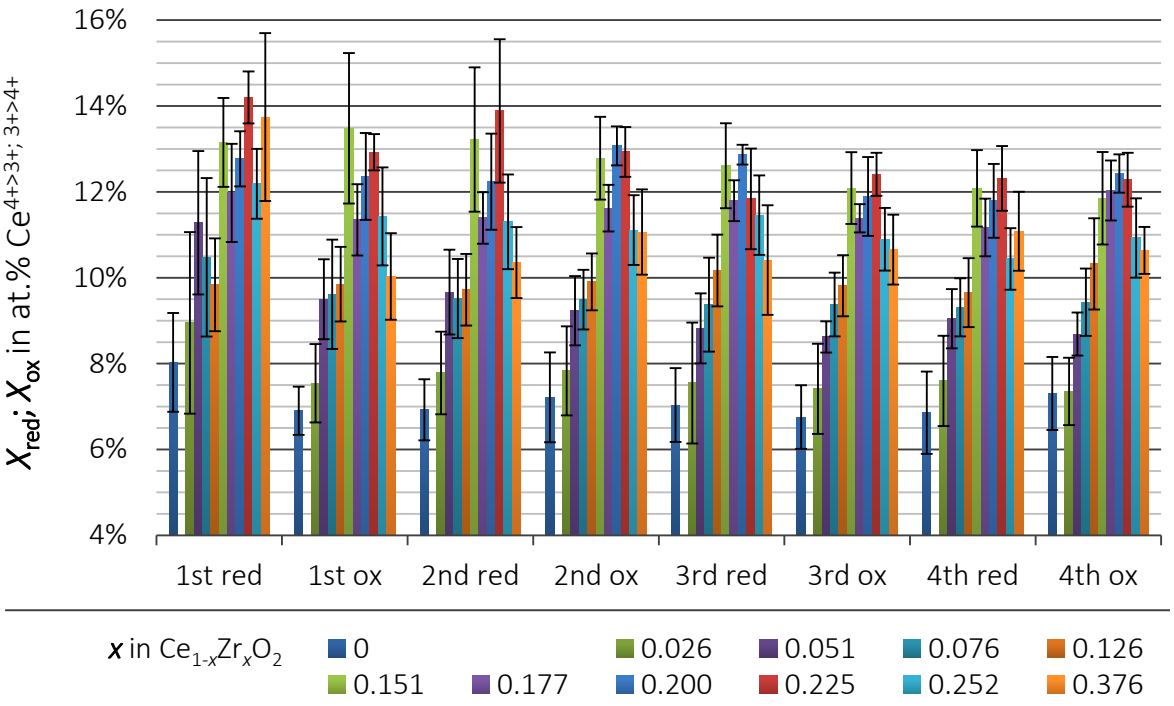

Figure 4.2: Relative redox extents X_{red} and X_{ox} of $Ce_{1-x}Zr_xO_2$ compositions plotted versus each step (reduction conditions: 20 min at 1400°C, 5.0 Ar; oxidation conditions: 20 min at 900°C, 6 vol.% CO_2).

leases 0.155±0.016 $mmol_{O_2} \cdot g_{mat}^{-1}$ during reduction and produces 0.305±0.026 $mmol_{CO} \cdot g_{mat}^{-1}$ during oxidation, respectively. This represents an increase of approximately 50% with respect to pure ceria.

Characterization

The SEM imaging discovers no significant changes in the particle structure of the material caused by zirconia doping. The phase analysis carried out with XRD of all materials showed a cubic fluorite structure as observed for pure ceria with a peak shift to high 2θ angle with increasing Zr content (see appendix figure A.5). The obtained patterns agree with literature data [Alif 03].

4.1.1.2 Discussion

The results indicate that the substitution of Ce^{4+} for isovalent Zr^{4+} enhances the reducibility, which is in concert with earlier studies [Trov 97, Lema 01, Di M 05a, Zhou 07, Aban 10, Kane 11, Le G 11b, Le G 12, Le G 13]. For some authors, the enhancement is attributed to modifications in the crystal structure, which are confirmed by XRD. During reduction from Ce^{4+} to Ce^{3+}, the lattice expand, because of the bigger dimensions of Ce^{3+}. This transition results in a stress that suppresses further reduction. The introduction of

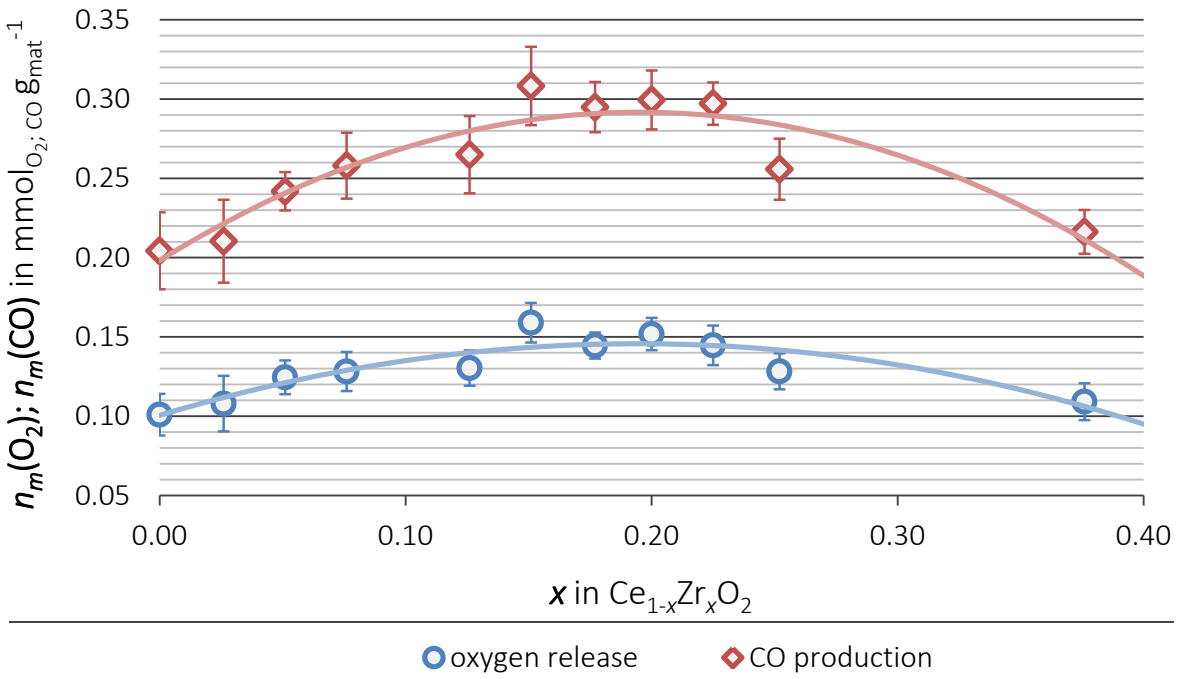

Figure 4.3: Specific yields $n_m(O_2)$ and $n_m(CO)$ calculated from TGA runs of $Ce_{1-x}Zr_xO_2$ versus the Zr content x (average yields over cycle three and four).

the smaller Zr^{4+} compensates for the expansion of the crystal lattice [Kane 11, Le G 13]. Theoretical calculations of CeO_2–ZrO_2 solid solutions showed that the introduction of 10 at.% Zr^{4+} substantially lowered the reduction energy of Ce^{4+} [Bald 97]. However, for higher Zr contents the reduction energy remained approximately constant.

Recently, Kuhn et al. fitted a point defect model to TGA data indicating a decline in the reduction enthalpy with increasing Zr-content up to 20%, consistent with the findings in the present study [Kuhn 13]. Kuhn et al. also suggested that the smaller Zr^{4+} drives the formation of oxygen vacancies caused by the reduction of Ce^{4+} to Ce^{3+}. This is due to the fact that Zr^{4+} prefers a lower coordination with oxygen (e.g. $Zr^{[7]}$ in monoclinic ZrO_2) in contrast to $Ce^{[8]}$. Further explanation is given by Vanpouke et al. [Vanp 14]. They studied ceria doped with group IV elements within a DFT framework. For varying Zr-content in ceria, they estimated the defect formation energies to be more than one order of magnitude lower compared to pure ceria. They also found IVb elements (Ti, Zr, Hf) more likely to be dispersed in the bulk of ceria grains than segregated to the surface regions of ceria.

The reaction conditions required to reduce ceria-based materials are one of the major barriers to technical success of the process. Particularly, the high temperature T and/or the low partial pressure of oxygen $p(O_2)$ cause a significant decrease on the process efficiency as discussed in section 2.1. Recently, Ermanoski et al. exemplarily estimated the process efficiency depending on the amount of released oxygen δ (see equation 2.19 on page 20) [Erma 13]. Thereby, Ermanoski et al. introduced a routine that fit thermogravimetric data of pure ceria for a wide range of temperatures and oxygen partial pressures

$p(O_2)$ published by Panlener et al. [Panl 75]. Based on this routine, the specific yields $n_m(O_2)$ depending on T and $p(O_2)$ of pure ceria are assessable and depicted in Figure 4.4. At a reduction temperature of $T_{red} = 1400°C$ and an oxygen partial pressure of $p(O_2) = 5 \times 10^{-6}$ bar (vertical solid line), pure ceria releases approximately 0.1 $mmol_{O_2} \cdot g_{mat}^{-1}$ (blue circle). In our experiments, ceria liberates 0.101 ± 0.016 $mmol_{O_2} \cdot g_{mat}^{-1}$, demonstrating agreement with the literature data. The most efficient composition $Ce_{0.85}Zr_{0.15}O_2$, releases 0.155 ± 0.016 $mmol_{O_2} \cdot g_{mat}^{-1}$ (red square). Pure ceria does not release this amount until a temperature of 1460°C is reached or $p(O_2)$ is further decreased by one order of magnitude. In other words, Zr-doping saves 60 K or one order of magnitude of $p(O_2)$. Hence, Zr-doping significantly enhances the process efficiency.

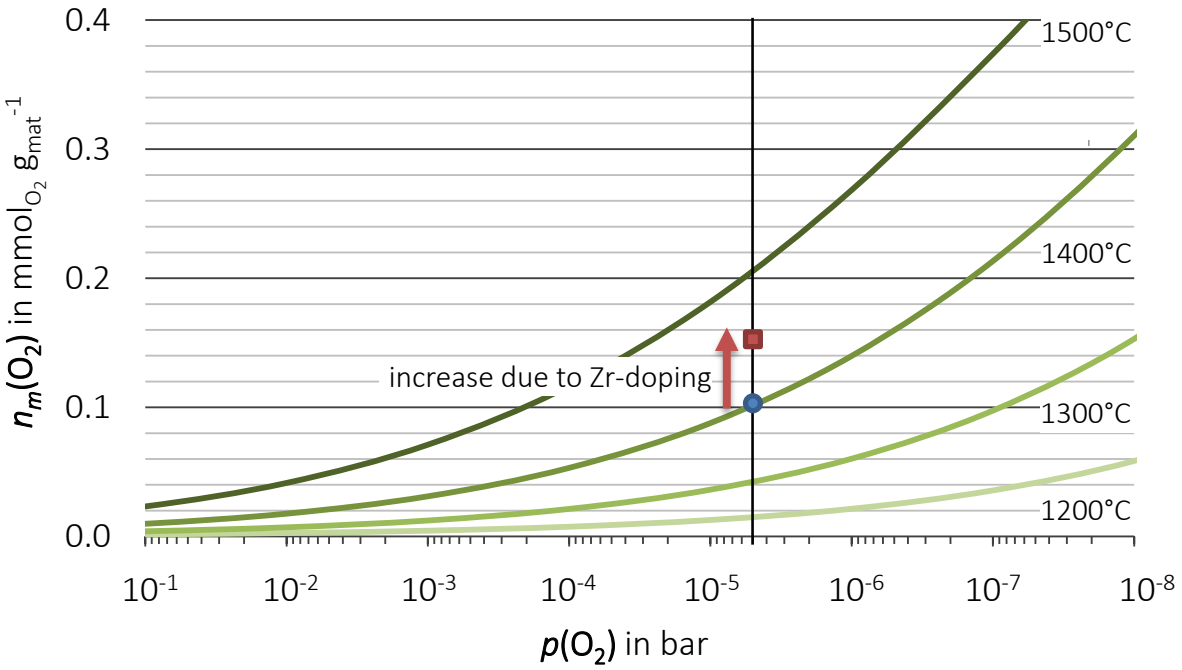

Figure 4.4: Enhancement of the reduction conditions caused by zirconia doping compared to pure ceria. The dashed lines were calculated based on a fitting routine published by Ermanoski et al. [Erma 13] who fitted data of Panlener et al. [Panl 75]. The vertical solid line marks $p(O_2) = 5 \times 10^{-6}$ bar, which was achieved in the thermobalance. The blue circle represents the result obtained at 1400°C for pure ceria; the red square for $Ce_{0.85}Zr_{0.15}O_2$.

4.1.2 Rare-Earth Doping

Due to the results from the Zr-doping experimental campaign, the Zr content x was fixed to 15% for the rare-earth doped compositions $Ce_{0.85-y}Zr_{0.15}RE_yO_{2-0.5y}$. The content y of the dopants RE = Y^{3+}, La^{3+}, $Sm^{3+}$and Gd^{3+} was altered from 0 to 20%. Accordingly, the Ce content $z = 0.85 - y$ decreases. As mentioned above, trivalent-doping induces

oxygen vacancies. One vacancy is induced per two trivalent ions, explaining the oxygen stoichiometry of $2 - 0.5y$.

4.1.2.1 Results

Successive cycling with the aid of the thermobalance estimated the performance of trivalent-doped CeO_2-ZrO_2 solid solutions. The as-prepared and cycled samples were characterized with the aid of XRD and SEM. The solely Zr-doped material, $Ce_{0.85}Zr_{0.15}O_2$, serves as the reference material.

Performance

Exemplarily for the other trivalent dopants, the results of the lanthanum-doped ceria-zirconia ($Ce_{0.85-y}Zr_{0.15}La_yO_{2-0.5y}$) is discussed in more detail. Figure 4.5 summarizes the calculated relative redox extents X_{red} and X_{ox} depending on the lanthanum content y.

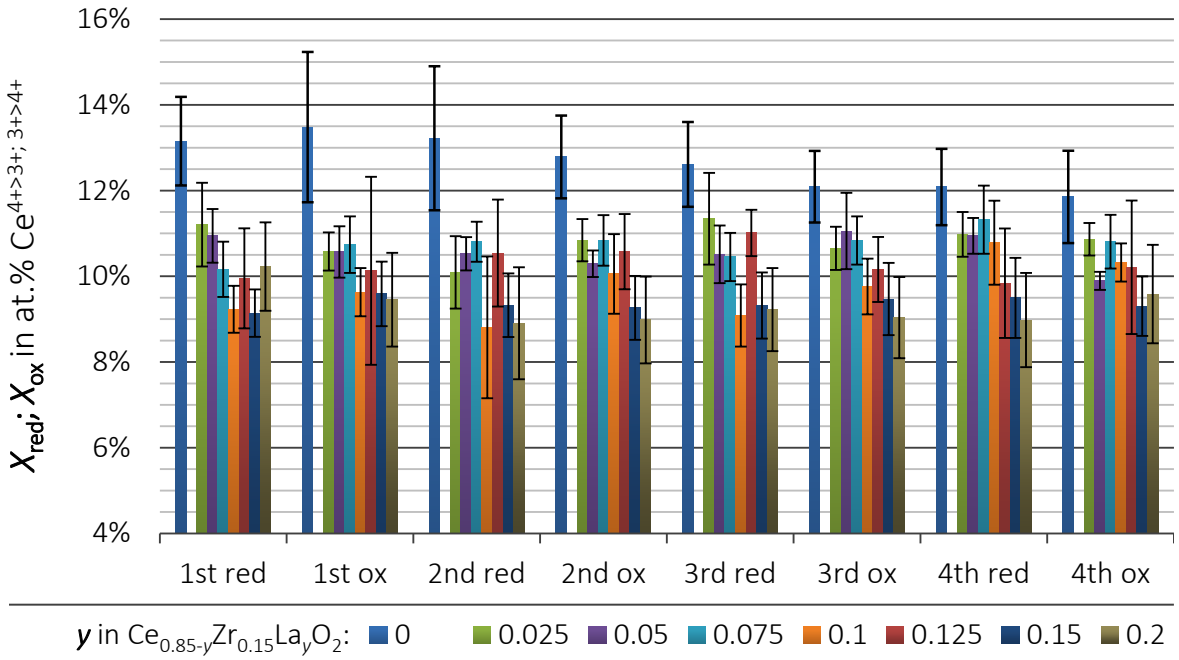

Figure 4.5: Relative redox extents X_{red} and X_{ox} of $Ce_{0.85-y}Zr_{0.15}La_yO_{2-0.5y}$ compositions plotted versus each step (reduction conditions: 20 min at 1400°C, 5.0 Ar; oxidation conditions: 20 min at 900°C, 6 vol.% CO_2).

As it was found for the Zr doping test series (see chapter: 4.1.1), the reduction extent approximates its following oxidation extent. Thus, complete reoxidation is achieved. The redox extents of the reference composition marginally decrease in the first two cycles until they stabilize in the last two cycles. The $Ce_{0.85-y}Zr_{0.15}La_yO_{2-0.5y}$ compositions, however, exhibit no performance decrease with increasing cycle number. Regarding these four

cycles, La doping slightly enhances the stability of the fuel productivity. This relation is further investigated in long-term cycling experiments. In terms of redox performance, La doping does neither improve X_{red} nor X_{ox}. The fraction of ceria atoms that change their valance with respect to the overall amount of ceria atoms decreases with increasing La content y.

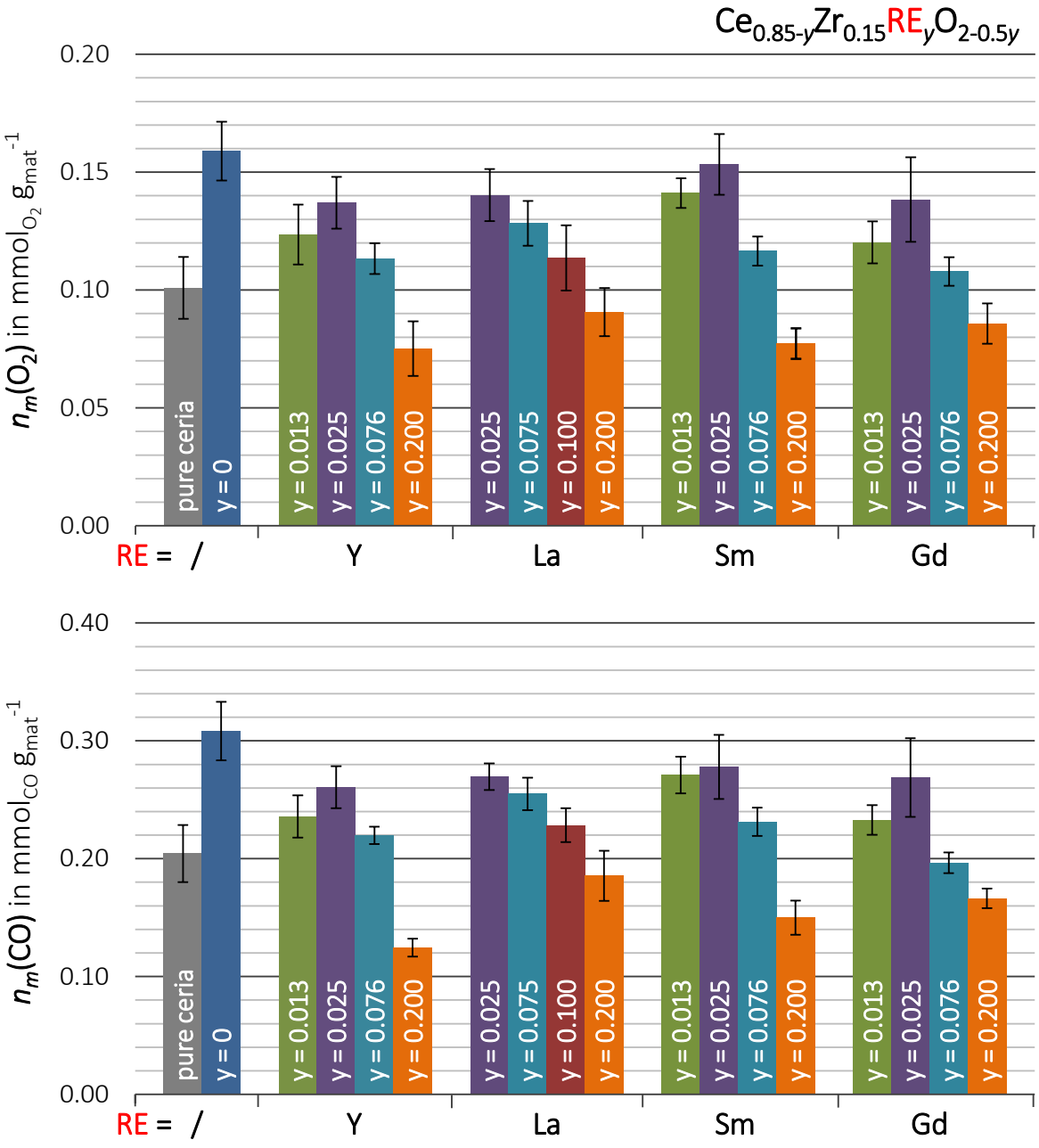

Figure 4.6: Specific yields $n_m(O_2)$ (top) and $n_m(CO)$ (bottom) derived from TGA cycling of the rare-earth doped materials $Ce_{0.85-y}Zr_{0.15}La_yO_{2-0.5y}$ (RE = Y, La, Sm, Gd) with $0 \leq y \leq 0.2$ compared to pure ceria (gray) and $Ce_{0.85}Zr_{0.15}O_2$ (dark blue) (averaged over cycle three and four). Note that the content y in the case of Lanthanum (La) differs from the other contents.

The specific yields $n_m(O_2)$ and $n_m(CO)$ of the ternary materials are shown in figure 4.6. The values were calculated from three independent experiments based on averages of the third and fourth cycle, due to high uncertainties of the first two cycles. The reference material $Ce_{0.85}Zr_{0.15}O_2$ releases 0.159 ± 0.012 $mmol_{O_2} \cdot g_{mat}^{-1}$ during reduction and produces 0.308 ± 0.025 $mmol_{CO} \cdot g_{mat}^{-1}$ during oxidation, respectively. This represents an increase of approximately 50 % with respect to pure ceria. The 1-2% trivalent doped materials produce approximately 15% less CO per cycle ($0.26 - 0.27$ $mmol_{CO} \cdot g_{mat}^{-1}$). Only, the Sm-doped materials feature performances of 0.295 ± 0.101 $mmol_{CO} \cdot g_{mat}^{-1}$, which equals the yields of the reference material $Ce_{0.85}Zr_{0.15}O_2$ within the error limits. For higher trivalent contents of $y = 0.75; 0.1; 0.2$, the performance decreases; for some compositions, the yields decrease to values smaller than those of pure ceria.

As it is the case for Zr-doping, introducing a foreign dopant into ceria influences the molar weights and therewith inherently the specific yields. For instance, a yttrium content of $y = 0.2$ in the reference ceria-zirconia solid solution leads to a molar weight of the oxidized material of $M_{Ce_{0.65}Zr_{0.15}Y_{0.2}O_{1.9}} = 152.9$ $g \cdot mol^{-1}$, whereas a gadolinium content of $y = 0.2$ exhibits a molar weight of $M_{Ce_{0.65}Zr_{0.15}Gd_{0.2}O_{1.9}} = 166.5$ $g \cdot mol^{-1}$. In order to filter this effect on the specific yields, it is reasonable to study the molar yields $n_n(O_2)$ and $n_n(CO)$ in $mmol_{O_2;\, CO_2} \cdot mmol$. Figure 4.7 shows the molar yields depending on the cerium content z, which is decreasing with increasing trivalent content y ($z = 0.85 - y$).

Generally, the yields $n_n(O_2)$ and $n_n(CO)$ decrease with decreasing cerium content z. The trivalent-doped materials with $y = 0.2$ perform only half as good, compared to the reference material, $Ce_{0.85}Zr_{0.15}O_2$, which releases 26.2 ± 2.1 $mmol_{O_2} \cdot mmol_{mat}^{-1}$ and produces 50.8 ± 4.1 $mmol_{CO} \cdot mmol_{mat}^{-1}$, For small trivalent contents $y \leq 0.025$, the performance reaches values similar to the reference material. In particular, the Sm-doped material exhibit the same yields. In between, for $0.025 < y < 0.2$, the yields decrease with increasing z in a similar way as observed for the solely Zr-doped materials.

Characterization

As it was found for Zr-doped ceria, SEM imaging discover no significant changes in the particle structure of the material caused by rare-earth doping. In the appendix, all XRD patterns are presented (Y-doping: A.6, La-doping: A.7, Sm-doping: A.8, and Gd-doping: A.9). Exemplarily, figure 4.8 displays the patterns of the materials with the highest rare-earth dopant load.

All materials feature a cubic fluorite structure as observed for pure ceria. Compared to the reference material, $Ce_{0.85}Zr_{0.15}O_2$, the peaks are more or less shifted to low 2θ angle depending on the dopant. The smallest dopant, Y^{3+} with $r_{Y^{3+}} = 0.102$ nm, lead to almost no shifting. The largest dopant, La^{3+} with $r_{La^{3+}} = 0.116$ nm results in the most significant shifting. In between, Gd^{3+} and Sm^{3+} doping with $r_{Gd^{3+}} = 0.105$ nm and

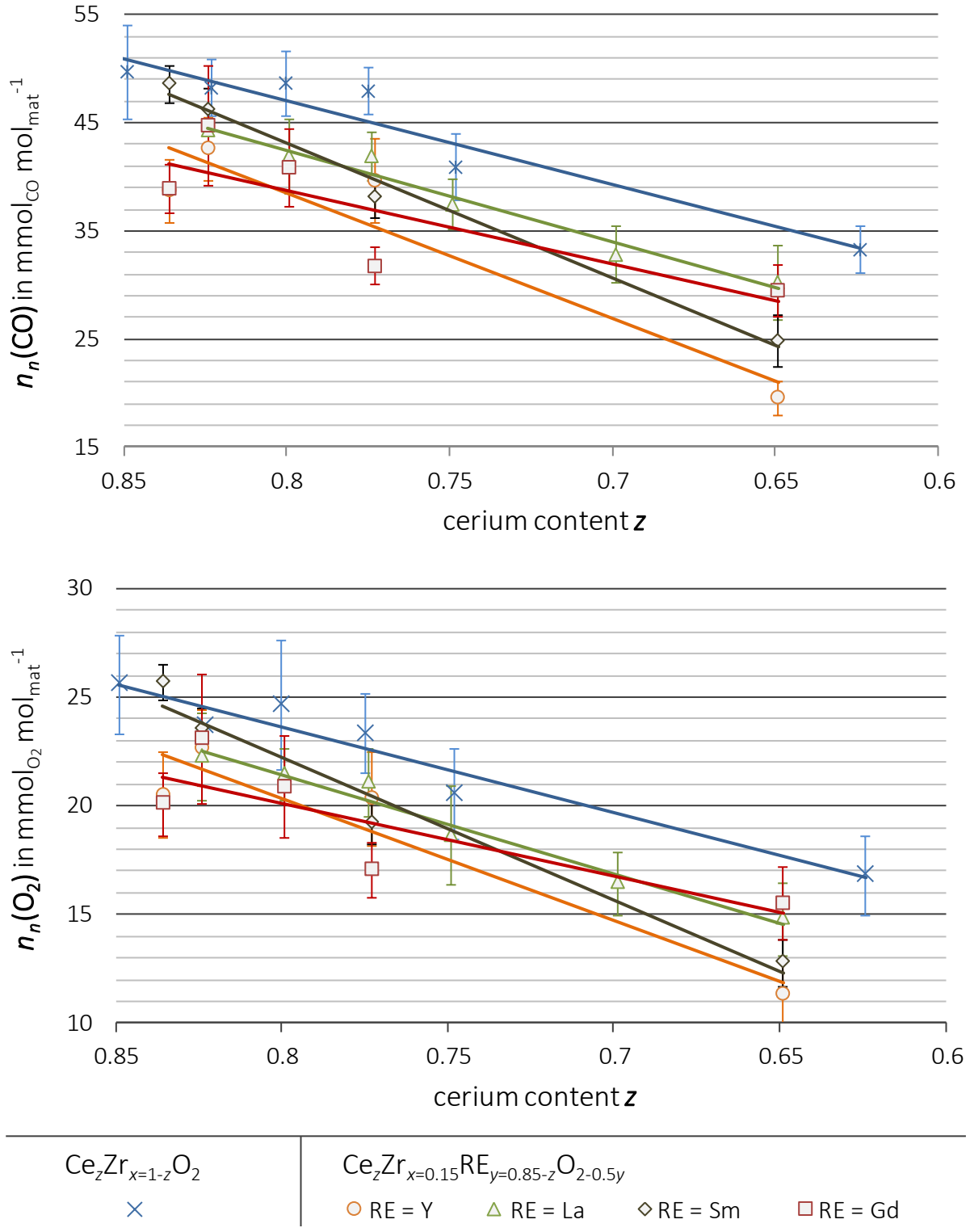

Figure 4.7: Molar yields $n_n(O_2)$ (top) and $n_n(CO)$ (bottom) versus the cerium content $z = 1 - x - y$ calculated from TGA runs of $Ce_{0.85}Zr_{0.15}O_2$ (blue) with $0 \leq x < 0.4$ compared to the rare-earth doped materials $Ce_{0.85-y}Zr_{0.15}RE_yO_{2-0.5y}$ (RE = Y, La, Sm, Gd) with $0 \leq y \leq 0.2$ (average over cycle three and four). The solid lines, representing linear fits of the data of each dopant, shall simplify the visualization of the various trends.

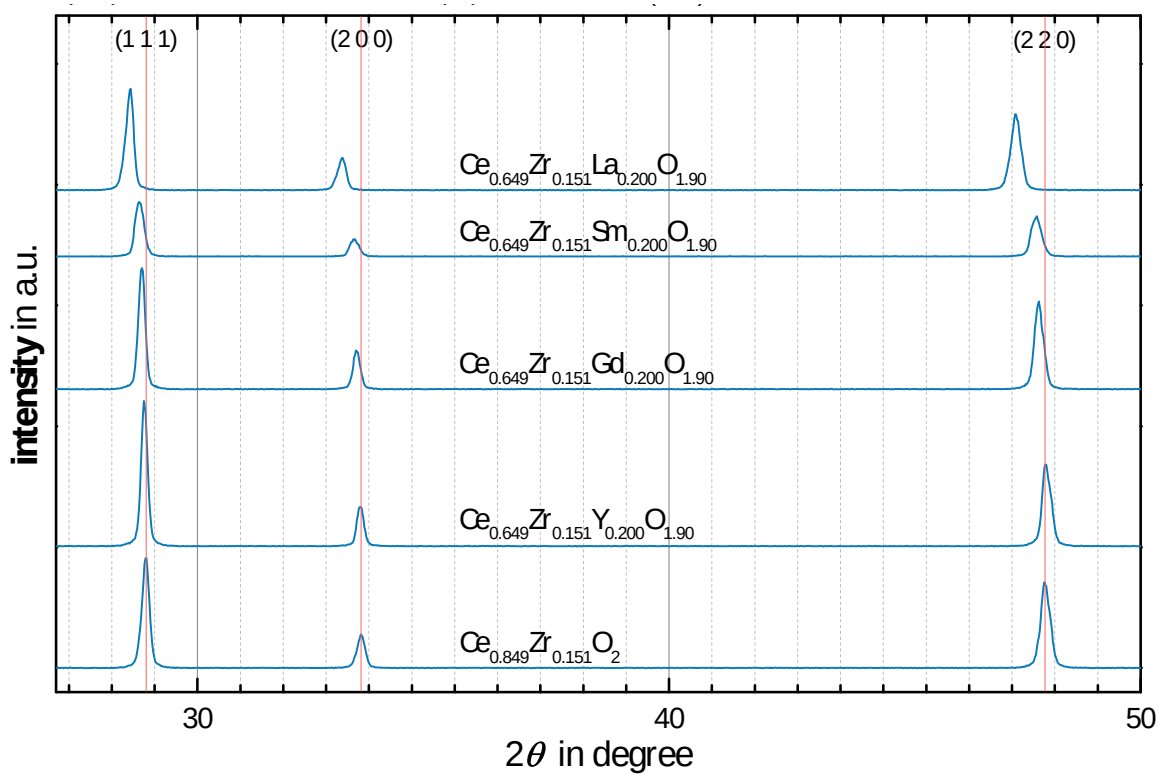

Figure 4.8: XRD patterns of rare-earth doped compositions with 20% content.

$r_{Sm^{3+}} = 0.108$ nm, respectively, result in moderate shifting. In comparison, the effective ionic radii of cerium are $r_{Ce^{3+}} = 0.114$ nm and $r_{Ce^{4+}} = 0.097$ nm. All radii were found in [Shan 76] for eight coordinated cations. The shifting towards low 2θ corresponds to higher unit cell parameters, caused by the doping with larger ions compared to the tetravalent cerium. The larger the ion, the larger the shifting. This agrees to expectations due to Vegard's law and to results reported in the literature of rare-earth doped ceria [Xin 10].

4.1.2.2 Discussion

Rare-earth doping of the reference CeO_2-ZrO_2 composition, $Ce_{0.85}Zr_{0.15}O_2$, does not enhance the reduction and oxidation yields. None of the employed dopants RE = Y^{3+}, La^{3+}, $Sm^{3+}$and Gd^{3+} in $Ce_{0.85-y}Zr_{0.15}RE_yO_{2-0.5y}$ lead to an improved fuel productivity compared to $Ce_{0.85}Zr_{0.15}O_2$. This contradicts to the expectation that the higher oxygen vacancy concentration is beneficial for the reducibility. With increasing RE content y, the ceria content z decreases and therewith, the amount of active species, explaining the decreasing yields. For increasing x in $Ce_{1-x}Zr_xO_2$, this trend is similar but not as pronounced. The best composition found in this test campaign is the slightly Sm-doped $Ce_{0.825}Zr_{0.15}Sm_{0.025}O_{1.99}$.

The oxygen yields obtained with small RE contents $y < 0.03$ agree to results recently obtained by Le Gal et al. [Le G 13]. The authors investigated similar compositions and also observed no improved reducibility. With $Ce_{0.82}Zr_{0.14}RE_{0.04}O_{1.98}$ (RE = Y, La, and Pr or

a combination of those), they obtained 0.138 $mmol_{O_2} \cdot g_{mat}^{-1}$ for the second cycle. However, the lack of error margins and no further cycles make it difficult to assess the validity of the values. Reviewing the literature, the rationale behind the ineffectiveness of rare-earth doping remains unknown. My suggestion to explain the results is given in the following. As discussed for the CeO_2-ZrO_2 compositions, zirconia compensates for the expansion of the crystal lattice, when cerium changes its valence from 4+ to 3+. Rare-earth doping causes an additional strain in the crystal structure due to the bigger ionic radii compared to Ce^{4+}. Hence, some of the beneficial effect of the zirconia is already consumed and, compared to the $Ce_{1-x}Zr_xO_2$ compositions, less oxygen is released.

Plotting the oxygen release of the various compositions versus the ionic radii as presented in figure 4.9, reveals a trend. With increasing ionic radii the decrease in the yields is slightly reduced. This effect is increasing with increasing dopant content. Some authors modeled the effect of dopant ionic radius on the dopant-vacancy interaction [Butl 83, Catl 83]. They found the ionic conductivity to increase with increasing radii and ascribe their results to the relaxation of the dopant towards the oxygen vacancy. Small dopant ions increase the stability of the crystal structure, while for larger dopant ions, there is an energy associated with reducing the strain in the crystal structure, when an oxygen vacancy is introduced into a neighboring site. Other authors modeled the behavior of ceria using statistical thermodynamics or Monte Carlo simulation and percolation theory [Adle 93, Stap 99]. They found similar relations. However, these models may not exactly rationalize the observed trend, since the denoted publications only studied rare-earth doped CeO_2 and not rare-earth doped CeO_2-ZrO_2 solutions.

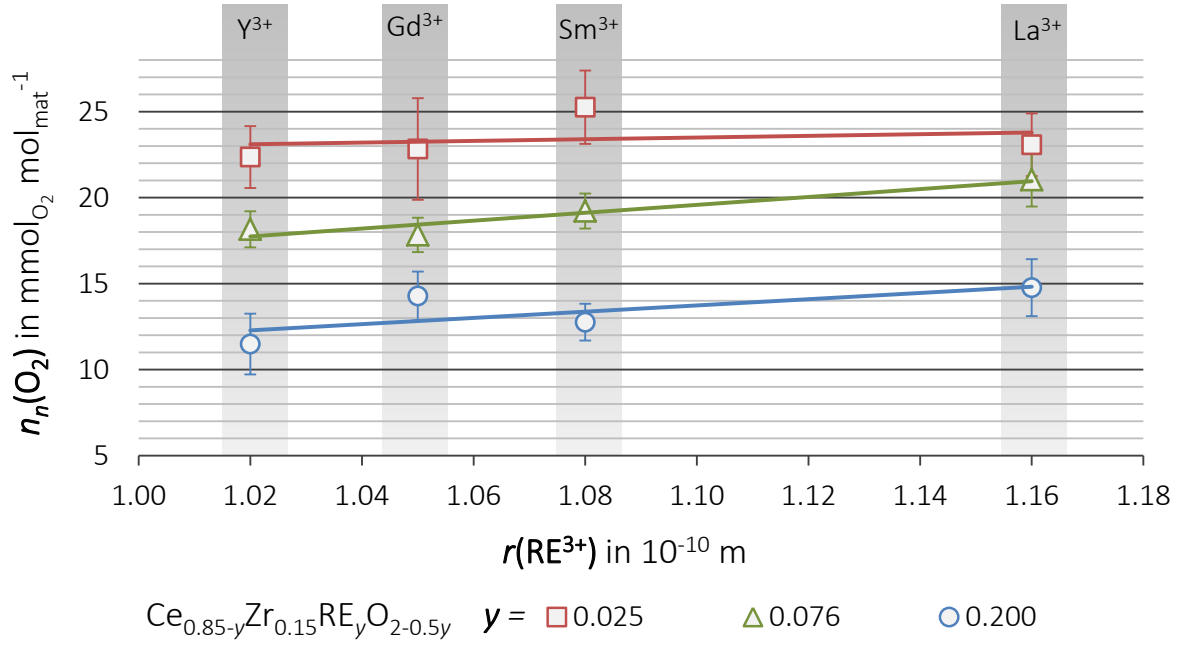

Figure 4.9: Molar yields $n_n(O_2)$ calculated from TGA runs of $Ce_{0.85-y}Zr_{0.15}RE_yO_{2-0.5y}$ (RE = Y, La, Sm, Gd) with $y = 0.025; 0.076; 0.2$ plotted versus the ionic radii (average yields over cycle 3-4). Effective ionic radii are given from [Shan 76] for eight coordinated cations.

4.2 Long-term Stability

The long-term stability of the redox material effects the economic feasibility and is one of the major barriers to technical success of thermochemical cycles producing solar fuel. The life period of the material directly influences the investments. Moreover, continuous degradation of the performance of the material causes lower fuel productivity that results in decreasing process efficiencies. In the past, especially ferrite-based materials suffered from long-term cycling at temperatures close to the melting point. Presumably, ceria-based materials may exhibit an improved long-term behavior, because they feature much higher melting points of > 2000°C.

To evaluate the long-term stability, several 16-cycle experiments were consecutively performed with the same powder sample. The two most efficient compositions $Ce_{0.85}Zr_{0.15}O_2$ and $Ce_{0.825}Zr_{0.15}Sm_{0.025}O_2$ were subjected to this long-term cycling. The same temperature program was employed for all cycles similar to the one used in the last section: a reduction step (heating to 1400°C with 20 K·min^{-1}; isothermal step for 20 minutes under Ar 5.0, corresponding to $p(O_2) = 5 \times 10^{-6}$ bar as discussed in table 3.4) and a splitting step (cooling to 900°C with 50 K·min^{-1}; isothermal step for 20 minutes under 6 vol.% CO_2 4.8 in Ar 5.0 and 20 minutes under Ar 5.0).

4.2.1 Results

Performance

The specific yields $n_m(O_2)$ and $n_m(CO)$ versus the cycle number are depicted in Figure 4.10 as well as the corresponding CO:O_2 ratio r (reduction with its following oxidation). Provided that the oxidation is complete, $r = 2$ (see equation 2.4 on page 7). The yields of the $Ce_{0.85}Zr_{0.15}O_2$ sample decrease slightly but continuously with increasing cycle number. After 100 cycles, the material only releases 0.100 ± 0.014 mmol O_2 and produces 0.195 ± 0.016 mmol CO per gram and cycle, respectively. These quantities correspond to a decrease of more than 30% of the initial value (first cycle). The ratio r equals two only for the first cycles. With increasing cycle number, r continuously declines to ratios of $r \approx 1.8$. Since r is defined as the ratio of the CO yield to the O_2 yield of the previous reduction, ratios $r < 2$ indicate incomplete reoxidation of the material. Hence, with increasing cycle number, the twenty minutes under CO_2 are not sufficient to ensure complete reoxidation. In turn, only a smaller amount of cerium atoms are reduced in the following cycle.

The yields of the $Ce_{0.825}Zr_{0.15}Sm_{0.025}O_2$ sample are significantly more stable compared to the $Ce_{0.85}Zr_{0.15}O_2$ results. With increasing cycle number, the oxygen yield $n_m(O_2)$ and the CO yield $n_m(CO)$ exhibit a negligible decrease. The ratio r slightly decreases but keeps values over 1.9 for the entire campaign.

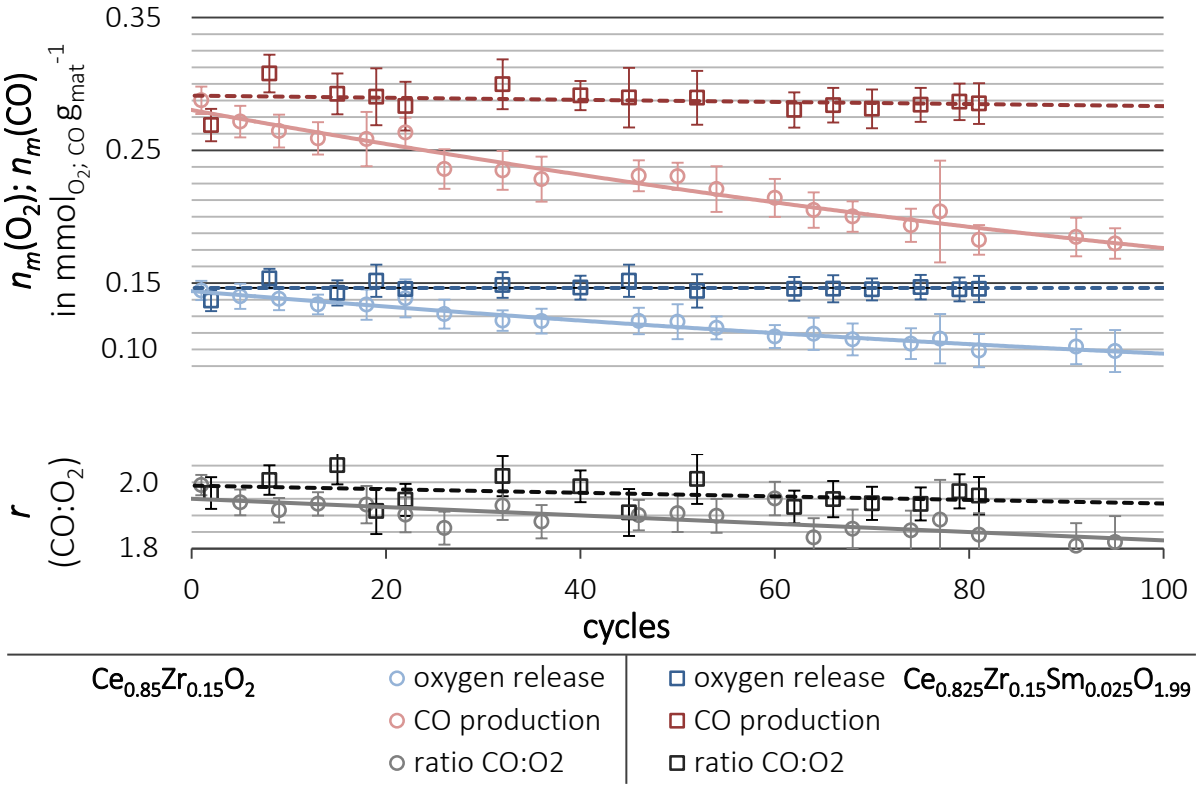

Figure 4.10: Specific yields $n_m(O_2)$ and $n_m(CO)$ calculated from long-term TGA runs of $Ce_{0.85}Zr_{0.15}O_2$ and $Ce_{0.825}Zr_{0.15}Sm_{0.025}O_{1.99}$ (data averaged over 4 cycles). Ratio r of CO:O_2 release (stoichiometrical: $r = 2$).

Characterization

XRD of the samples before and after the cycling show no significant differences. Both materials maintain their crystal structures confirming phase stability. SEM imaging of the materials before and after long-term cycling is presented in figure 4.11. The imaging reveals that particle and grain sizes of the material significantly increase while cycling. The grains of $Ce_{0.85}Zr_{0.15}O_2$ grow from sizes less than 1 µm after four cycles to sizes of 1 - 3 µm after 100 cycles and agglomerate to particles of more than 40 µm. In the case of the $Ce_{0.825}Zr_{0.15}Sm_{0.025}O_2$ sample, the grain growth is not as pronounced compared to $Ce_{0.85}Zr_{0.15}O_2$. After 80 cycles, grain sizes of 0.5 to 1.5 µm are observed. The particles, however, also agglomerate to sizes of more than 40 µm. Accordingly, both powder samples suffer from sintering during long-term cycling, which results in a significant decrease in the specific surface.

4.2.2 Discussion

The oxygen release is limited to the oxidation of the precedent cycle. When the material is not fully reoxidized, the oxygen release decreases, which is displayed by a decreasing

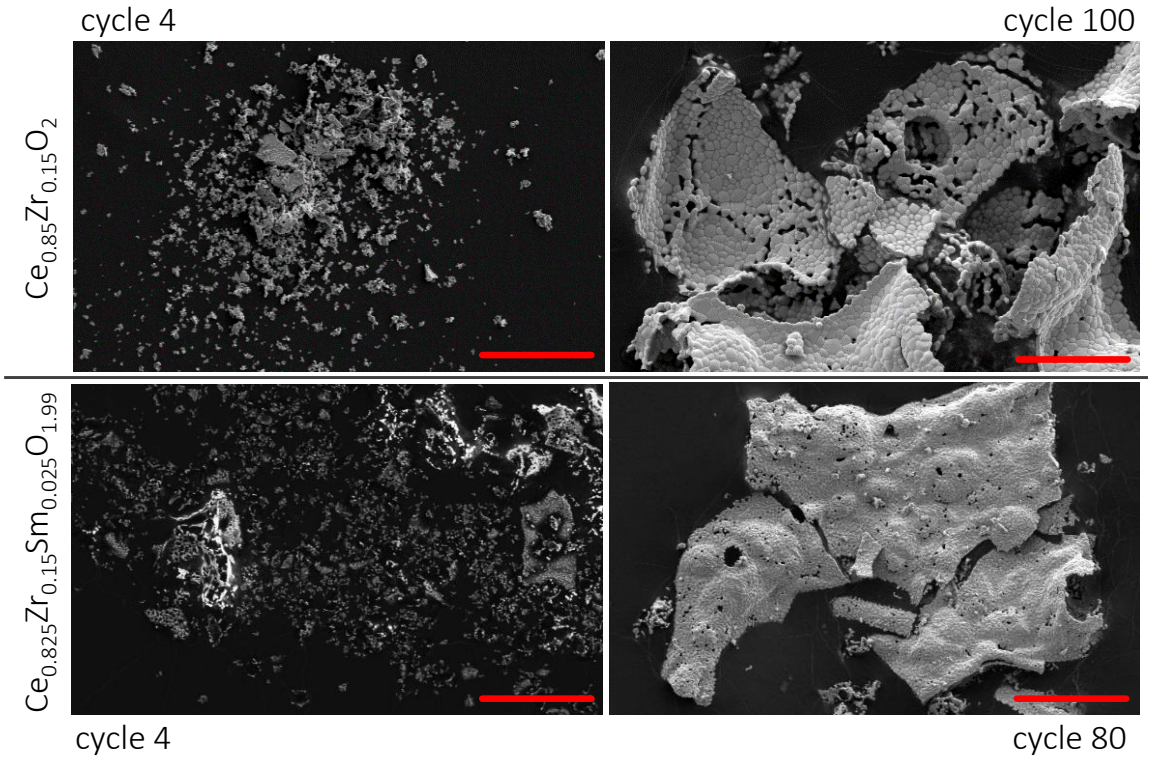

Figure 4.11: SEM images before and after long-term cycling of $Ce_{0.85}Zr_{0.15}O_2$ and $Ce_{0.825}Zr_{0.15}Sm_{0.025}O_{1.99}$. The red bar corresponds to 20 µm.

$CO:O_2$ ratio r. That is the case for the $Ce_{0.85}Zr_{0.15}O_2$ sample. The decrease in the overall performance may result from declining oxidation kinetics. For the following discussion, keep in mind that the slope of Δm_{ox} corresponds to the oxidation rate as well as to the specific amount of produced CO per minute. Introducing the specific CO production rates $\dot{n}_{CZ}$(cycle, regime) for $Ce_{0.85}Zr_{0.15}O_2$ and $\dot{n}_{CZS}$(cycle, regime) for $Ce_{0.825}Zr_{0.15}Sm_{0.025}O_2$ shall simplify the discussion.

Figure 4.12 shows the data of the mass change during oxidation Δm_{ox} of three representative oxidation steps of the $Ce_{0.85}Zr_{0.15}O_2$ sample. As CO_2 is injected (minute 0), the oxidation immediately starts corresponding to a mass gain. In the beginning of all three oxidation steps, the mass change exhibits a sharp increase (regime I) that smoothly segues into a second regime (regime II) with a significantly lower slope. The lower the cycle number, the longer and steeper is regime I. Linear fitting calculates slopes of regime I, yielding CO production rates of $\dot{n}_{CZ}$(cycle 5, regime I) = 105 $\mu mol_{CO} \cdot g_{mat}^{-1} \cdot min^{-1}$, $\dot{n}_{CZ}$(55, I) = 73 $\mu mol_{CO} \cdot g_{mat}^{-1} \cdot min^{-1}$ and $\dot{n}_{CZ}$(95, I) = 37 $\mu mol_{CO} \cdot g_{mat}^{-1} \cdot min^{-1}$, respectively. The slope of regime II, however, is independent of the cycle number and is approximately constant featuring rates of $\dot{n}_{CZ}$(cycles 5; 55; 95 , regime II) $\approx$ 3.7 $\mu mol_{CO} \cdot g_{mat}^{-1} \cdot min^{-1}$. Eventually, this causes the decreasing oxidation extents with increasing cycle number, because the time CO_2 is introduced is fixed to 20 minutes for all experiments. Hence, the duration is not sufficient to completely reoxidize the material. In future experimental campaigns,

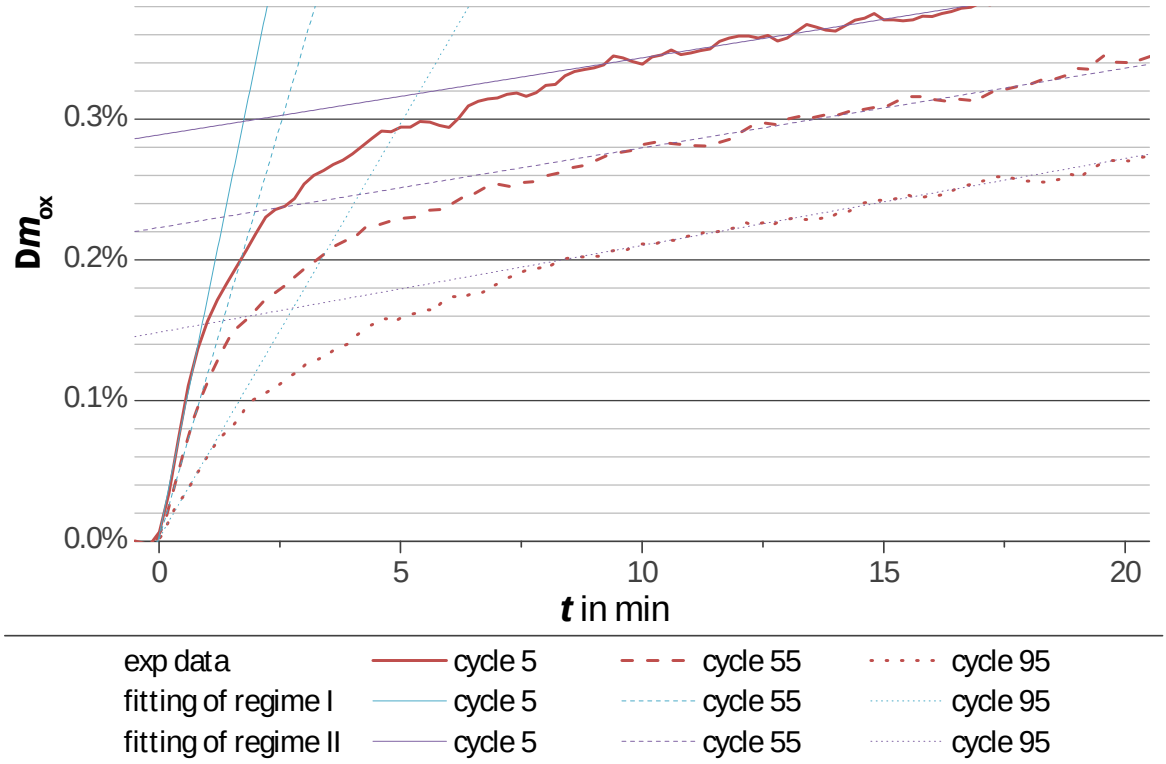

Figure 4.12: Course of Δm_{ox} of representative oxidation steps of $Ce_{0.85}Zr_{0.15}O_2$.

the duration of the oxidation step needs to be adjusted to obtain complete reoxidation.

In the case of the $Ce_{0.825}Zr_{0.15}Sm_{0.025}O_2$ sample, the yields are significantly more stable throughout the entire long-term cycling. Figure 4.13 compares the beginning of the oxidation of both samples, $Ce_{0.85}Zr_{0.15}O_2$ and $Ce_{0.825}Zr_{0.15}Sm_{0.025}O_2$. $\dot{n}_{CZS}$(I) is independent of the cycle number and equals to the rate of $Ce_{0.85}Zr_{0.15}O_2$ in cycle 5 $\dot{n}_{CZ}$(5,I). Cycle 80 shows the highest mass gain after the first two minutes, which is surprising at first sight. In the end of the oxidation step, however, the mass gains of the Sm-doped sample of all cycles and the one of cycle 5 of the $Ce_{0.85}Zr_{0.15}O_2$ sample feature similar values. Therefore, the unexpected higher mass gain of cycle 80 in the beginning of the oxidation might be rather attributed to experimental uncertainties. Summing up, the following relations for the reaction rates of $\dot{n}$(cycle number, regime) are obtained for regime I

$$\dot{n}_{CZ}(5,I) \approx \dot{n}_{CZS}(5,\ I) \approx \dot{n}_{CZS}(40,\ I) \approx \dot{n}_{CZS}(80,\ I) > \dot{n}_{CZ}(55,\ I) > \dot{n}_{CZ}(95,\ I)$$

and for regime II

$$\dot{n}_{max}(II) \approx \dot{n}_{CZ}(5;\ 55;\ 95,\ II) \approx \dot{n}_{CZS}(5;\ 40;\ 80,\ II)$$

where the index$_{CZ}$ denotes $Ce_{0.85}Zr_{0.15}O_2$ and the index$_{CZS}$ $Ce_{0.825}Zr_{0.15}Sm_{0.025}O_2$, and $\dot{n}_{max}$(II) denotes the maximum reaction rates of regime II, respectively.

At this point, it is reasonable to have a closer look on potential reaction rate limitations.

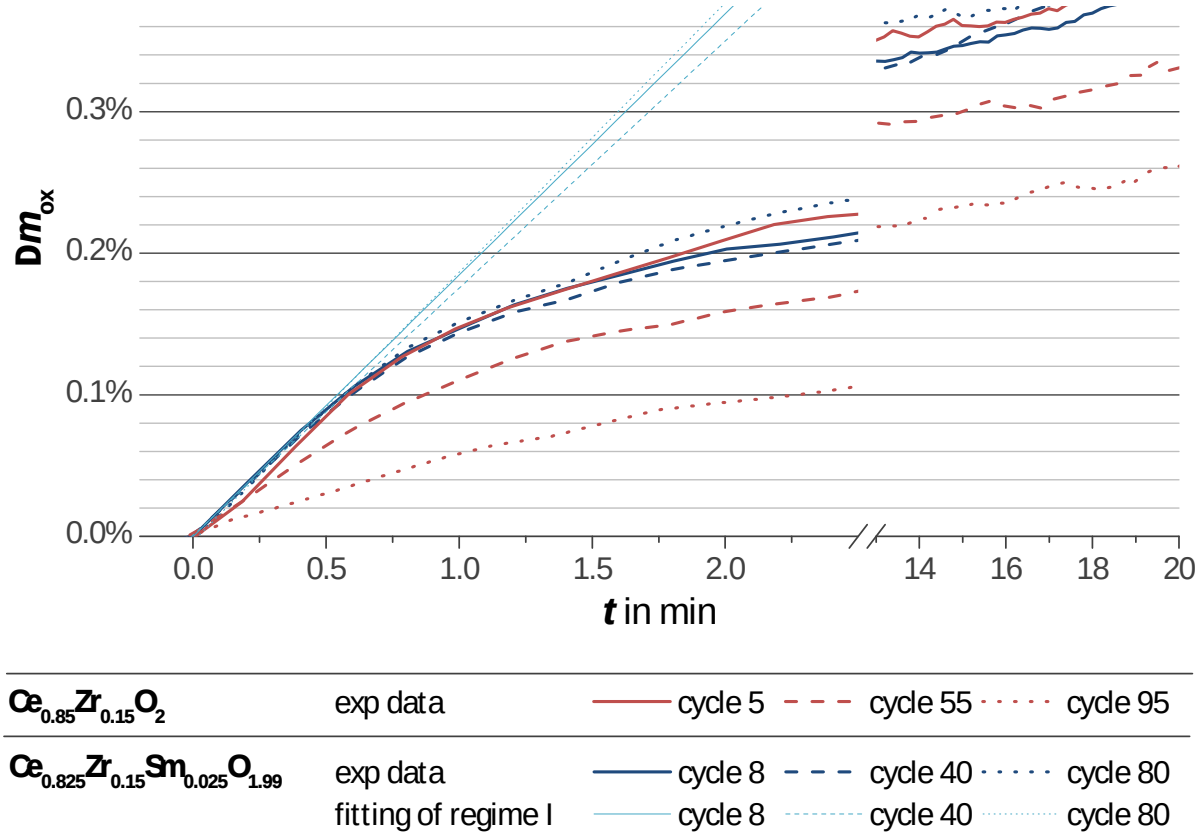

Figure 4.13: Course of Δm_{ox} of representative oxidation steps of $Ce_{0.85}Zr_{0.15}O_2$ and $Ce_{0.825}Zr_{0.15}Sm_{0.025}O_{1.99}$ and fits of regime I of the Sm-doped material.

Mainly, the heterogeneous oxidation reaction of the material with CO_2 consists of three serial steps [Gopa 14]:

- Mass transport of the reacting gases
- Reaction at the surface of the material
- Diffusion of the neutral oxygen species through the bulk of the material

The mass transport depends on the gas flow rate f, which is the same for the entire cycle in all experiments. Keep in mind that during oxidation, not only CO_2 has to be transported to the reaction sites but also CO needs to be transported away from the reaction sites. From a kinetical point of view, this is a major difference compared to the oxidation with O_2. The oxygen diffusion is quantified with the chemical diffusion coefficient D_O and the surface reaction with the surface reaction rate constant k_S.

Basic calculations might determine, whether the diffusion is likely to be rate limiting. Oxygen diffusivities D_0 of pure and Zr-doped ceria can be derived from literature [Chio 96, Gior 01]. At a temperature of 900°C, which was adjusted during oxidation, D_0 of at least $2 \times 10^{-9}\,m^2s^{-1}$ are reported. According to Einstein's relation, the characteristic diffusion

length scale l_d is as follows:

$$l_d = \sqrt{2D_0 t} \tag{4.1}$$

t denotes the time for the investigated reaction step. Looking at regime I, which lasts for approximately 30 seconds, the diffusion length scale l_d is about 75 µm, which is close to particle sizes displayed in figure 4.11 of 10 µm to 50 µm. Therefore, the diffusion cannot be precluded to be rate-limiting for regime I. Assuming $t = 600\,\mathrm{s}$, which is half of the time of the oxidation step, the diffusion length scale l_d is more than 1.5 mm. Hence, the oxygen diffusion is unlikely to be rate-limiting for regime II, which is observed for the last 18 minutes of the oxidation step.

To comprehensively discuss the results of both compositions, a short summary of the results seems convenient. For $Ce_{0.85}Zr_{0.15}O_2$, declining reaction rates of regime I were observed with decreasing specific surfaces. Therefore, regime I might correspond to the surface reaction as it was also suggested from other authors [Le G 11a]. However, for $Ce_{0.825}Zr_{0.15}Sm_{0.025}O_2$, no declining kinetics of the surface reaction were observed, although the material shows similar agglomeration. Regime II is independent of the decreasing surface and exhibits approximately constant reaction rates for all cycles and both compositions displayed by the maximum reaction rate $\dot{n}_{\mathrm{max}}$(II). Assuming regime II not to be controlled by diffusion as calculated above, it might be mass-transport limited. This is in particular likely to be the case considering the maximum $\dot{n}_{\mathrm{max}}$(II) rate observed in all cycles for both materials.

Among other terms, experiments that evaluate the exact kinetics must employ well-defined sample geometries and well-controlled gas flow dynamics [Gopa 14]. These requirements are by far not met by the presented long-term experiments of powder materials in a thermobalance, impeding a meaningful quantification especially of the surface reaction. Therefore, in the following, the findings are combined to derive my suggested reaction path that describes the oxidation reaction only in a qualitative manner.

Figure 4.14 presents the reaction path schematically. The upper section represents the reaction of cycle 5, the lower section the reaction of cycle 80. In both sections, the gas flow is directed upwards as denoted by the arrows. The shapes with bold gray frames represent the grains, the black dots the CO_2 molecules, and the red dots the CO molecules. The first column displays the exact beginning of the oxidation, at which the introduced CO_2 did not react yet, but only surrounds the grains. The second column denotes the state of the reaction of both, $Ce_{0.85}Zr_{0.15}O_2$ (green frame) and $Ce_{0.825}Zr_{0.15}Sm_{0.025}O_2$ (purple frame) after the first 0.5 minute, when regime I terminates.

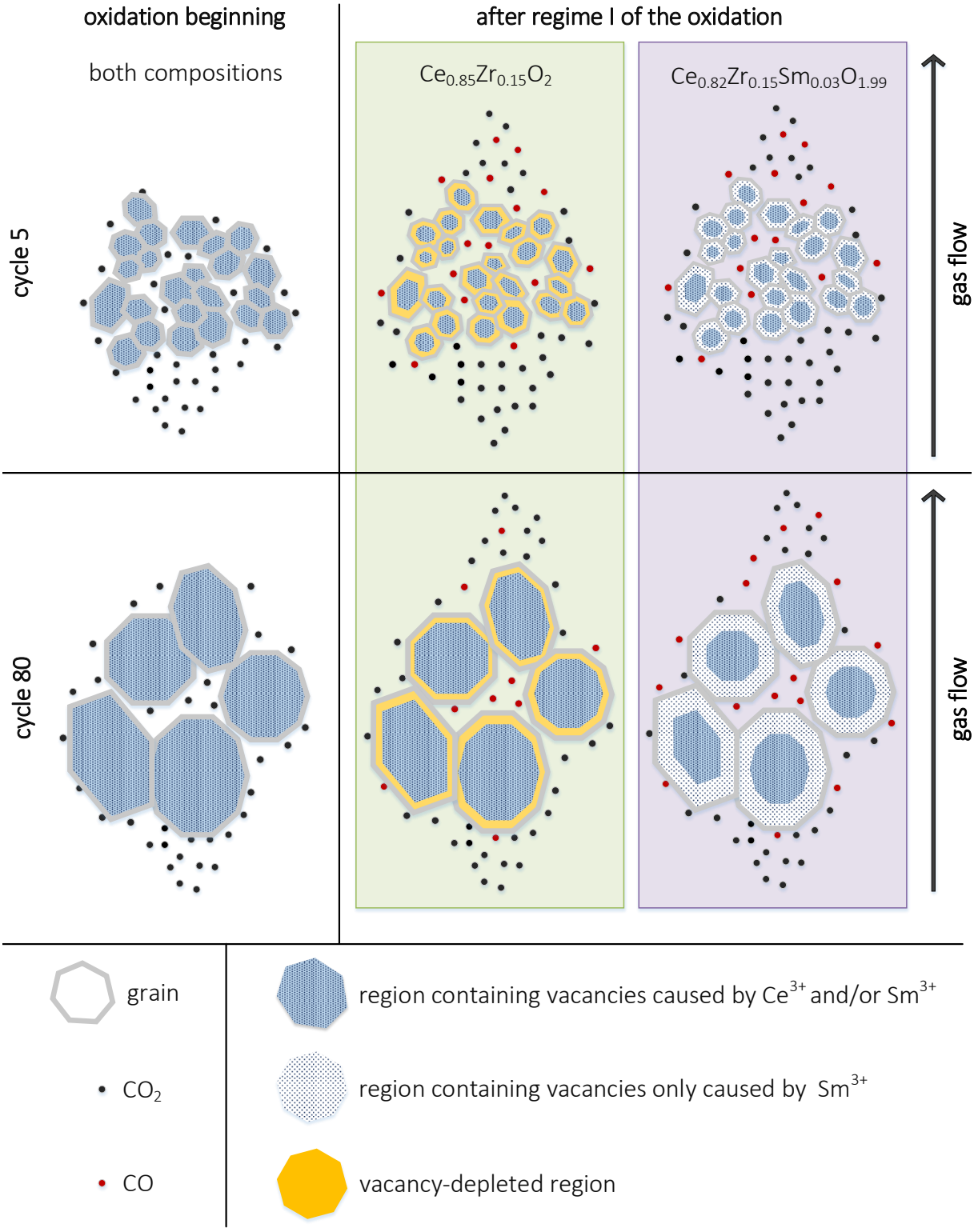

Figure 4.14: Schematic of the reaction path introduced to explain the findings of the long-term cycling. Detailed description is found in the text.

At the beginning of the reaction, the grains exhibit homogeneously distributed vacancies denoted by the dark blue points within the grains. With proceeding reaction, the surfaces of both compositions oxidize and the vacancies are filled. In the $Ce_{0.85}Zr_{0.15}O_2$ sample, vacancy-depleted regions are generated as denoted by the yellow area. However, since the Sm-doped sample exhibits vacancies due to the trivalent Sm^{3+}, the region near the surface still contains vacancies that aid the reaction rate. When the grains and particles are small enough, such regions might not effect the reaction rate agreeing to the experimental results. However, when the grain and particle sizes increase, the oxidation rate of the $Ce_{0.85}Zr_{0.15}O_2$ sample declines compared to the $Ce_{0.825}Zr_{0.15}Sm_{0.025}O_2$ sample, because the vacancy-depleted regions effect the reaction path more significantly.

Recent findings in the literature agree to this approach to explain the beneficial effect of Sm-doping for the oxidation kinetics. In ceria and its derivatives, oxygen vacancies play an important role in the surface reaction kinetics [Yoko 04]. Hernandez et al. reported that the presence of oxygen vacancies correlates with an increase in the catalytic performances [Hern 10]. The surface reaction kinetics are proportional to the ionic conductivity that, in turn, is linked to the amount of oxygen vacancies. One rationale behind this is the direct interaction of the surface defects with the reactive gas phase [Hern 11]. The defect vacancies at the surface directly enhance the surface reaction. Investigations of trivalent-doped ceria ($Ce_{0.8}Gd_{0.2}O_{1.9}$) confirm a significantly enhanced surface oxygen exchange compared to pure ceria [Anan 12]. Apart from that, the creation of oxygen vacancies within the bulk material is beneficial for the oxidation kinetics, due to the enhanced oxygen diffusivity [Maha 11, Chat 13, Delg 13].

The reaction path displayed in figure 4.14 explains the stabilizing effect on the kinetics of Sm-doping. When the Sm-doping enhances the surface reaction as well as surface-near bulk reaction, the doping should also lead to higher reaction rates of low cycle numbers. In other words, it is still not clear as to why regime II displays a maximum rate independent of the composition and the cycle number ($\dot{n}_{max}$(II)). A possible explanation, which is also included in figure 4.14, is to attribute these findings to a mass transport of the reacting gases that is insufficient. During regime I, there is primarily the CO_2 transport to the reaction sites. At the beginning of regime II, however, another rate limiting factor appears. Not only CO_2 has to be transported to the reaction sites, but also CO away from the reaction sites. This might hamper the reaction, in particular, in regions where the exchange is difficult, such as in the interspaces of particles that are not directly in contact with the gas stream, as depicted in figure 4.14. This explanation is in line with results of the pellet campaign described in section chapter 5.1.

4.3 Conclusions

In this chapter, the effects of varying Zr content in CeO_2 and varying rare-earth content in $Ce_{0.85}Zr_{0.15}O_2$ on the fuel productivity were investigated. Therewith, optimal dopant contents concerning the highest CO production yields were identified. Long-term cycling of these optimal compositions assessed their cycling stability.

The results of the $Ce_{1-x}Zr_xO_2$ compositions indicate that a certain Zr content ($0.15 \leq x \leq 0.225$) enhances the reducibility and therefore the fuel productivity. Increasing the Zr-content to $x = 0.15$ improved the specific CO yields by 50% compared to pure ceria. Further increasing of the Zr-content to $x = 0.38$ diminished the specific yields to values of pure ceria. This finding agrees with theoretical studies attributing the improvements to lattice modification due to the incorporation of Zr^{4+}, which features smaller dimensions than Ce^{4+}. Zr^{4+} ions compensate for the expansion introduced by the transition from Ce^{4+} to Ce^{3+} that would suppress further reduction. Compared to pure ceria, the most efficient composition $Ce_{0.85}Zr_{0.15}O_2$ enhances the required reaction conditions by a temperature of 60 K or one order of magnitude of the partial pressure of oxygen $p(O_2)$.

Doping the optimized ceria (15 at.% Zr) with rare-earth ions leads to compositions of $Ce_{0.85-y}Zr_{0.15}RE_yO_{2-0.5y}$ with RE = Y^{3+}, La^{3+}, $Sm^{3+}$and Gd^{3+} and $0 < y \leq 0.2$. None of the compositions exhibits higher performances compared to the reference material, $Ce_{0.85}Zr_{0.15}O_2$. With increasing RE content y, the ceria content z decreases and therewith the amount of active species, explaining the decreasing yields. For increasing x in $Ce_{1-x}Zr_xO_2$, this trend is similar, but not as pronounced. The ineffectiveness of rare-earth doping agrees to recent publications. However, the rationale behind is not found in literature. A possible explanation due to crystallographic consideration is that the bigger trivalent ions compared to the tetravalent Ce^{4+} cause additional strain within the crystal structure. This strain adds to the strain introduced by oxygen vacancies created during reduction. The Zr^{4+} cannot compensate for this cumulative strain. Hence, compared to $Ce_{1-x}Zr_xO_2$, less oxygen is released. The best performing rare-earth doped material identified is the slightly Sm-doped $Ce_{0.825}Zr_{0.15}Sm_{0.025}O_{1.99}$, which approximates the performance of $Ce_{0.85}Zr_{0.15}O_2$.

Long-term cycling reveals differences in the degradation behaviors of $Ce_{0.85}Zr_{0.15}O_2$ and $Ce_{0.825}Zr_{0.15}Sm_{0.025}O_2$. The former suffers from linear degradation of the yields and of the CO:O_2 ratio r, which is attributed to declining oxidation kinetics, whereas the latter features stable yields and kinetics. Both powder samples exhibit significant sintering. The oxidation reaction exhibits two linear regimes. Regime I is steeper and might be ascribed to the surface reaction, since it is only observed for the first 30 seconds of the oxidation. For the $Ce_{0.85}Zr_{0.15}O_2$ sample, the slope of regime I declines with increasing cycle number. The rationale behind is found in a vacancy-depleted region that occurs in the grains. While cycling, the specific surface decreases and the impact of these regions

on the reaction rate increases, which leads to declining oxidation kinetics. In spite of that, $Ce_{0.825}Zr_{0.15}Sm_{0.025}O_2$ displays structural vacancies due to the Sm^{3+}, which remain during oxidation. These structural vacancies might enhance the oxygen bulk transport, resulting in a constant reaction rate of regime I independent of the specific surface. The second linear regime begins approximately one minute after regime I and remains until the end of the oxidation step. Here, the mass transport limits the rate, since (1), the same rate is observed for both compositions, independent of the decreasing specific surface and (2). the diffusion is unlikely to be rate limiting due to basic calculations. Since the geometry of the thermobalance limits the reaction impeding an analysis of material-specific rate limits, other techniques have to be employed such as secondary ion mass spectrometry and electrochemical impedance spectroscopy. They meet the requirements to reveal the material-specific properties of the reaction kinetics. Nevertheless, the results gained in long-term cycling allow the conclusion that rare-earth doping is in particular beneficial for the oxidation kinetics and hence, important for the technical realization of the process.

In short, the quintessence of this chapter is as follows:

Concerning the Zr content, $Ce_{0.85}Zr_{0.15}O_2$ is the composition with the highest fuel productivity. An increase of up to 50% is found compared to pure ceria.

Rare-earth doping in CeO_2-ZrO_2 solid solutions provides no improvements in terms of a higher fuel productivity. $Ce_{0.825}Zr_{0.15}Sm_{0.025}O_{1.99}$ is identified to exhibit at least similar yields as observed for $Ce_{0.85}Zr_{0.15}O_2$.

Concerning long-term cycling, rare-earth doping improves the oxidation kinetics and leads to constant fuel production for at least 80 cycles under the applied process conditions.

The enhanced kinetics of the rare-earth doped material is attributed to structural vacancies caused by the trivalent ion.

5 Reaction Kinetics

The previous chapter identified optimal doping compositions that were selected to undergo further investigations. Doping enhances the reducibility regarding both, the reaction conditions as well as the oxygen yield. The effect of doping ceria, especially with Zr and a trivalent cation, on the kinetics needs to be evaluated.

To improve the signal-to-noise ratio of experiments carried out in the thermobalance as well as to maintain a certain microstructure, from now on, pellets are employed for the experimental studies. Two types of microstructures were manufactured: Dense and porous pellets. Further details on the pellet manufacture is provided in section 3.2.3.

This chapter evaluates the kinetics of pellets made of ceria and doped-ceria qualitatively. After describing the reasons to preclude an in-depth kinetical analysis of thermogravimetric data, the first section focuses on the CO_2 oxidation. Therewith, the impact of doping and the microstructure on the CO_2-splitting ability is assessed at various oxidation temperatures. The reduction kinetics are investigated within the second section. Again, the impact of doping and the microstructure is investigated. The conclusion summarizes the results and recommends experimental methods to determine the reaction kinetics quantitatively.

Contents

Kinetics in the Thermobalance

Knowledge of the reaction kinetics is pivotal to assess the feasibility of the material to be employed in a solar reactor; the longer each of the reaction steps, the more solar irradiation is wasted. Hence, the kinetics directly influence the overall process efficiency $\eta_{\text{solar to fuel}}$. In particular, the kinetics of the reduction step effect $\eta_{\text{solar to fuel}}$, because the reduction is the predominant on-sun step of the process. Innovative reactor designs separate the reduction from the oxidation to optimize the reduction step independently [Erma 13]. Generally, the reaction kinetics involve two material-specific steps: the oxygen diffusion within the bulk of the material, correlated with the diffusion coefficient D_0, and the reaction at the surface, quantified with the surface reaction rate constant k_S [Gopa 14]. The kinetics of these steps serve as the maximum reaction rate achievable. The quantities D_0 and k_S are principally embodied in the rates of oxygen released or fuel produced, which are obtained in a thermobalance experiment.

Experiments carried out in a thermobalance exhibit gas flow dynamics that are poorly controlled as seen in figure 3.5 on page 38. The geometry of the thermobalance prevents the gas stream to flow through the sample, yielding only small fractions of reacting gas that directly interacts with the material. In this regard, employing randomly microstructured samples leads to additional uncertainties. Furthermore, large driving forces are required to reasonably analyze weight changes in a quantitative way. This particularly includes large changes in temperature or partial pressure of oxygen or the reacting gases H_2O or CO_2, resulting in non-linear effects. Overlapping of various reaction steps on the material side as well as on the processing side may occur: Surface reaction and oxygen diffusion versus mass transport and temperature gradients within the sample. Experiments aiming to directly reveal D_0 and k_S must use small perturbations from equilibrium and well-defined sample geometries as well as exhibit well-controlled gas flow dynamics [Gopa 14]. Secondary ion mass spectrometry and electrochemical impedance spectroscopy are especially promising to gain suitable experimental data.

From a technical point of view, the kinetics quantified in the thermobalance are very unlikely to correctly describe the kinetics of real applications in a (solar)-reactor. Inter alia, the heat introduction and temperature gradients significantly differ. A real reactor has to operate at high heating rates to be efficient – the thermobalance is limited to 50 $K \cdot min^{1}$ – and the sample in the thermobalance is heated with an electrical furnace instead of irradiation. This is especially crucial, since the heat incorporation into the bulk material is likely to be a limiting factor of the reduction rate in a solar reactor, which is further discussed in section 8.2. Additionally, in a real reactor, direct gas-solid contact, i.e. a gas flow through the material, is essential during oxidation, which can not be simulated in the thermobalance. Concerning the gas atmosphere during reduction, the introduction of a vacuum is a promising alternative to the use of sweep gas, as discussed in section 2.1 and recently reported in literature [Erma 13]. However, since the thermobalance is not

able to operate under vacuum, this approach cannot be evaluated.

Because of the described reasons, a thorough quantitative analysis of the reaction kinetics obtained in thermogravimetric experiments seems unreasonable. That is why the following two sections solely focus on a qualitative analysis of the impact of reaction temperature, employed microstructure and doping on the reaction kinetics. Therewith, fundamental directions in terms of material design shall be identified and ideas for future investigations created.

5.1 Oxidation

The long-term cycling presented in section 4.2 of powder samples of the compositions $Ce_{0.85}Zr_{0.15}O_2$ and $Ce_{0.825}Zr_{0.15}Sm_{0.025}O_{1.99}$ revealed the importance of fast oxidation kinetics to assure complete reoxidation. The cycling in the thermobalance lead to significant grain growth and agglomeration. In the following investigations, sintering during operation can be neglected, since the employed pellets were sintered at 1650°C during their manufacture.

5.1.1 Results

Figure 5.1 presents the temperature program applied to evaluate the oxidation kinetics at varying oxidation temperatures T_{ox}. Four consecutive cycles were performed consisting of a reduction step (heating to 1400°C with 20 K·min^{-1}; isothermal step for 60 minutes under a predefined mixture of Ar and O_2 corresponding to $p(O_2) = 5 \times 10^{-3}$ bar as discussed in table 3.4 on page 39) and a splitting step (cooling to 700, 800, 900 or 1000°C with 50 K·min^{-1}; isothermal step for 220 minutes under 60 vol.% CO_2 4.8 in Ar 5.0). Already during cooling to the oxidation temperature, reoxidation occurs due to the rather high partial pressure of oxygen $p(O_2)$. When CO_2 is injected, a sharp mass gain is observed (regime I) that smoothly segues in a slower reaction regime (regime II).

Four different pellets were subjected to this temperature program: Three dense pellets C:d1200 (CeO_2), CZ:d1200 ($Ce_{0.85}Zr_{0.15}O_2$) and CZS:1200d ($Ce_{0.825}Zr_{0.15}Sm_{0.025}O_{1.99}$), and one porous pellet CZ:p20 ($Ce_{0.85}Zr_{0.15}O_2$), which was fired with 20 wt.% rice starch. More information on the pellets is displayed in table 3.3. The microstructure of the pellets was investigated with the aid of SEM. Since the dense pellets exhibit similar microstructures, in figure 5.2 one image is exemplarily depicted for both types of microstructures: dense and porous. The porous pellet exhibit pore channels that are beneficial for the gas exchange during oxidation, whereas the dense pellets presumably feature no pore channels, but more or less single, closed pores with sizes of 1 to 4 µm. The grain sizes of the porous pellets range from 1 to 5 µm, which is in the range of the powder samples after long-term

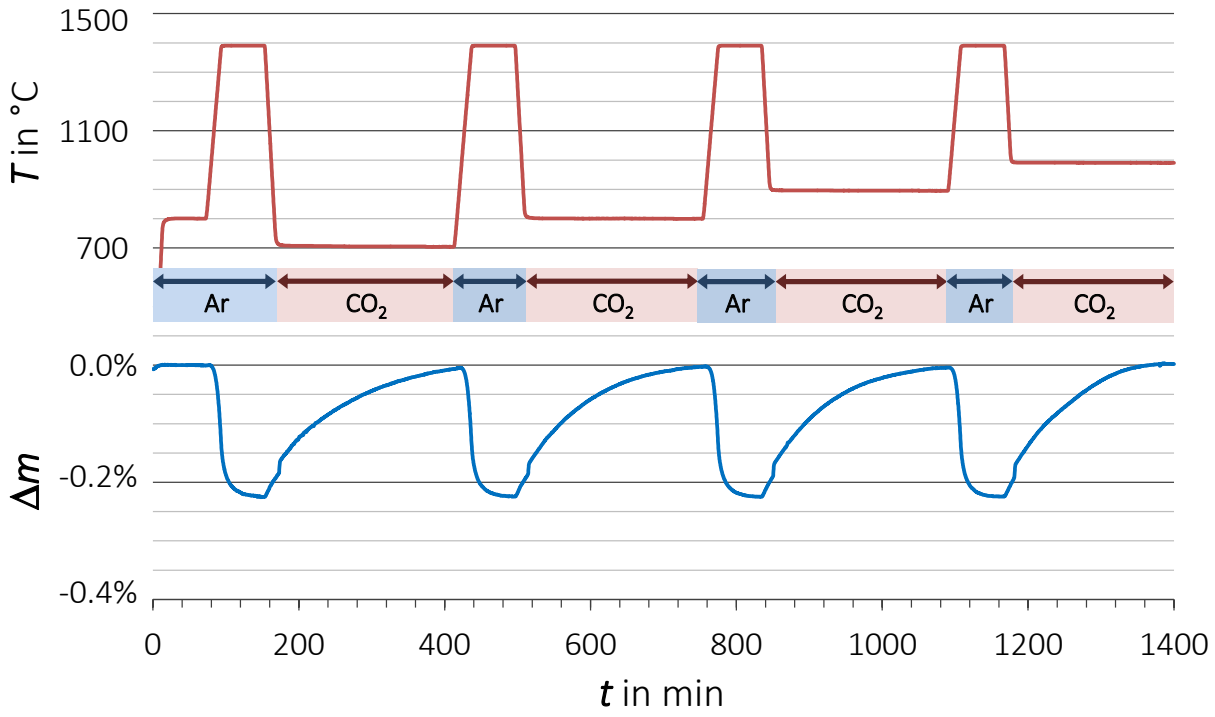

Figure 5.1: TGA program (temperature T and atmosphere) and corresponding mass change Δm versus time t to investigate the oxidation kinetics. Exemplary data of the $Ce_{0.825}Zr_{0.15}Sm_{0.025}O_{1.99}$ pellet CZS:d1200.

cycling. For the dense pellets, grain sizes from 5 to 20 µm are observed. Porosities of approximately 70% are estimated for the porous and 5% to 10% for the dense pellets. Such values were determined within a master thesis of Tijana Paraknewitz applying imaging analysis to SEM images of pellets [Para 13]. Furthermore, calculations basing on the dimension of the pellets and the theoretical density of pure CeO_2, $\rho = 7.2$ g·cm^{-3} [IFA 14], estimate similar values.

The results of the cycling are displayed in figure 5.3. The dense CeO_2 pellet C:d1200 exhibits the smallest reduction extent of $\delta \approx 0.11$, which corresponds to the equilibrium value of CeO_2 as obtained chapter 6. The oxidation is completed quickly, compared to the other dense pellets. Of the doped compositions, only the porous $Ce_{0.85}Zr_{0.15}O_2$ pellet CZ:p20 reaches the equilibrium state of $\delta \approx 0.34$. This pellet also features high oxidation rates. The two dense pellets, CZ:d1200 and CZS:d1200 displaying the compositions $Ce_{0.85}Zr_{0.15}O_2$ and $Ce_{0.825}Zr_{0.15}Sm_{0.025}O_{1.99}$, respectively, feature incomplete reduction with respect to the equilibrium state and, at low temperatures, incomplete oxidation. At 700°C and 800°C, the Sm-doped pellet exhibits an enhanced oxidation rate compared to the $Ce_{0.85}Zr_{0.15}O_2$ pellet.

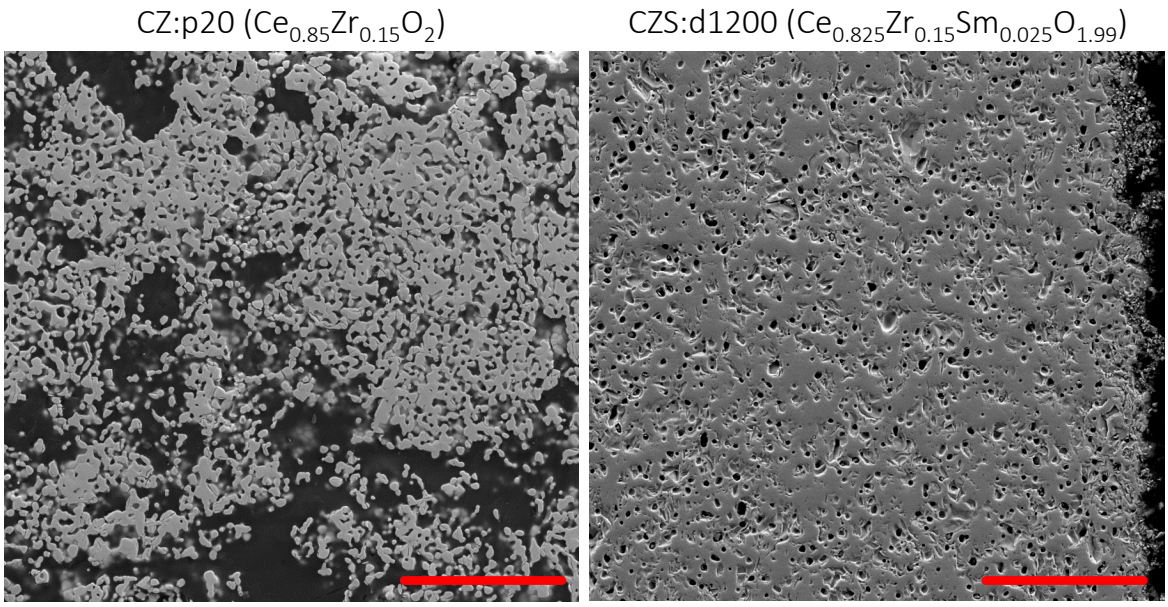

Figure 5.2: SEM images of polished cross-sections of the investigated pellets. Left: porous pellet CZ:p20 of $Ce_{0.85}Zr_{0.15}O_2$; right: dense pellet CZS:d1200 of $Ce_{0.825}Zr_{0.15}Sm_{0.025}O_{1.99}$. The red bar corresponds to 50 µm.

5.1.2 Discussion

Figure 5.4 compares the course of oxidation depending on the oxidation temperature T_{ox}. The gray area ranges from $t = 0$ to $t = 25$ min and encompasses the end of the previous reduction step and the cooling step to the oxidation temperatures T_{ox} under an Ar-O_2 mixture with a partial pressure of oxygen of $p(O_2) \approx 50$ Pa. The observed change in redox extent δ in this area denotes an reoxidation caused by the oxygen that is contained in the sweep gas. At the end of the gray area, at $t = 25$ min, the gas mixture is changed to a CO_2-Ar mixture with 60 vol.% CO_2. The various graphs are shifted in time (x-axis), so that the CO_2 introduction begins at $t = 25$ min for all of them. The oxidation features two regimes. For the following discussion, please keep in mind that the time dependency of the change in δ corresponds to the oxidation rate.

Regime I exhibits a relatively high oxidation rate, but only persists for less than 3 minutes. The share of regime I in the entire oxidation reaction shall be $X_{ox}^{\text{regime I}}$. For the dense pellets in general, $X_{ox}^{\text{regime I}}$ slightly increases with increasing temperature ranging from changes in δ of 0.001 to 0.004. For the porous pellet, the temperature dependency is completely different. At an oxidation temperature $T_{ox} = 700$°C, the reoxidation is already completed within regime I. At higher temperatures, $X_{ox}^{\text{regime I}}$ corresponds to changes in δ of approximately 0.01, which are significantly higher compared to the dense pellets. The increase of $X_{ox}^{\text{regime I}}$ is attributed to the significant higher specific surfaces and, in particular, to the open porosity. However, the rationale behind the significantly enhanced $X_{ox}^{\text{regime I}}$ at $T_{ox} = 700$°C remains unclear. Basically, decreasing the temperature should

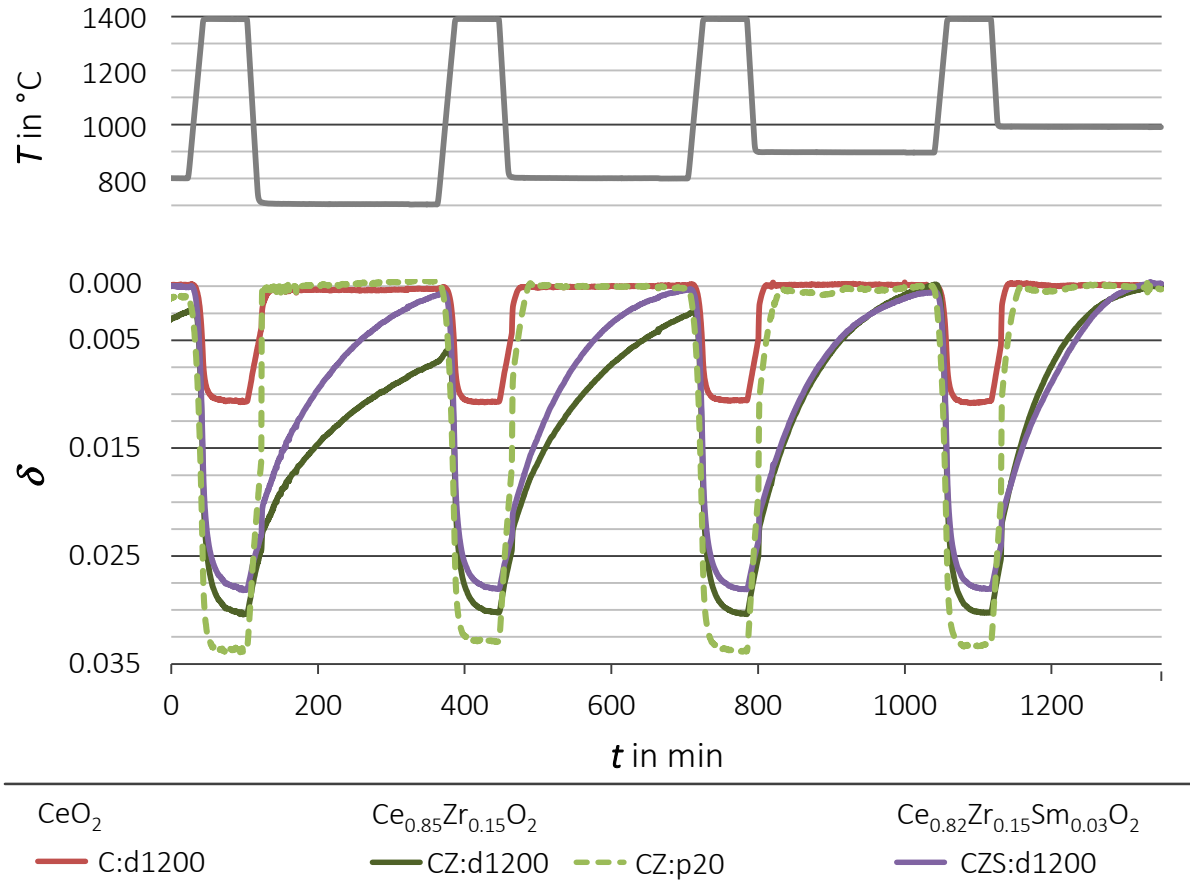

Figure 5.3: Reduction extent δ versus time t of TGA experiments employing several dense pellets C:d1200, CZ:d1200 and CZS:d1200 and one porous pellet CZ:p20 to study the oxidation at temperatures T_{ox} ranging from 700 to 1000°C. Table 3.3 on page 35 provides more details about the pellets.

slow down the kinetics. One possible explanation might be that air contaminated the CO_2 pipe of the thermobalance before experiment. This may also explain, why only the first oxidation displays such a deviation.

The second regime, regime II, lasts until either complete reoxidation is achieved ($\delta = 0$) or until the end of the oxidation step at $t = 250$ min. Regime II features a logarithmical shape. Generally, increasing T_{ox} increases the slope and hence, the reaction rate of regime II. This temperature dependence is in particular pronounced for the dense $Ce_{0.85}Zr_{0.15}O_2$ pellet CZ:d1200. Comparing the CZ:d1200 with the Sm-doped CZS:d1200, the improving effect of trivalent doping is distinct, as already observed in figure 5.3. This finding is in concert with the reaction path described in section 4.2, which ascribes the beneficial effect of trivalent doping to the enhanced oxygen diffusivities caused by the structural vacancies that are introduced due to the trivalence of Sm^{3+}. The distinctness of this diffusion enhancement shall increase with decreasing reaction temperature, which agrees to the experimental results. Having the diffusion enhancement in mind, a further conclusion can be drawn. Since the change in δ of the oxidation of CZ:d1200 and CZS:d1200 are

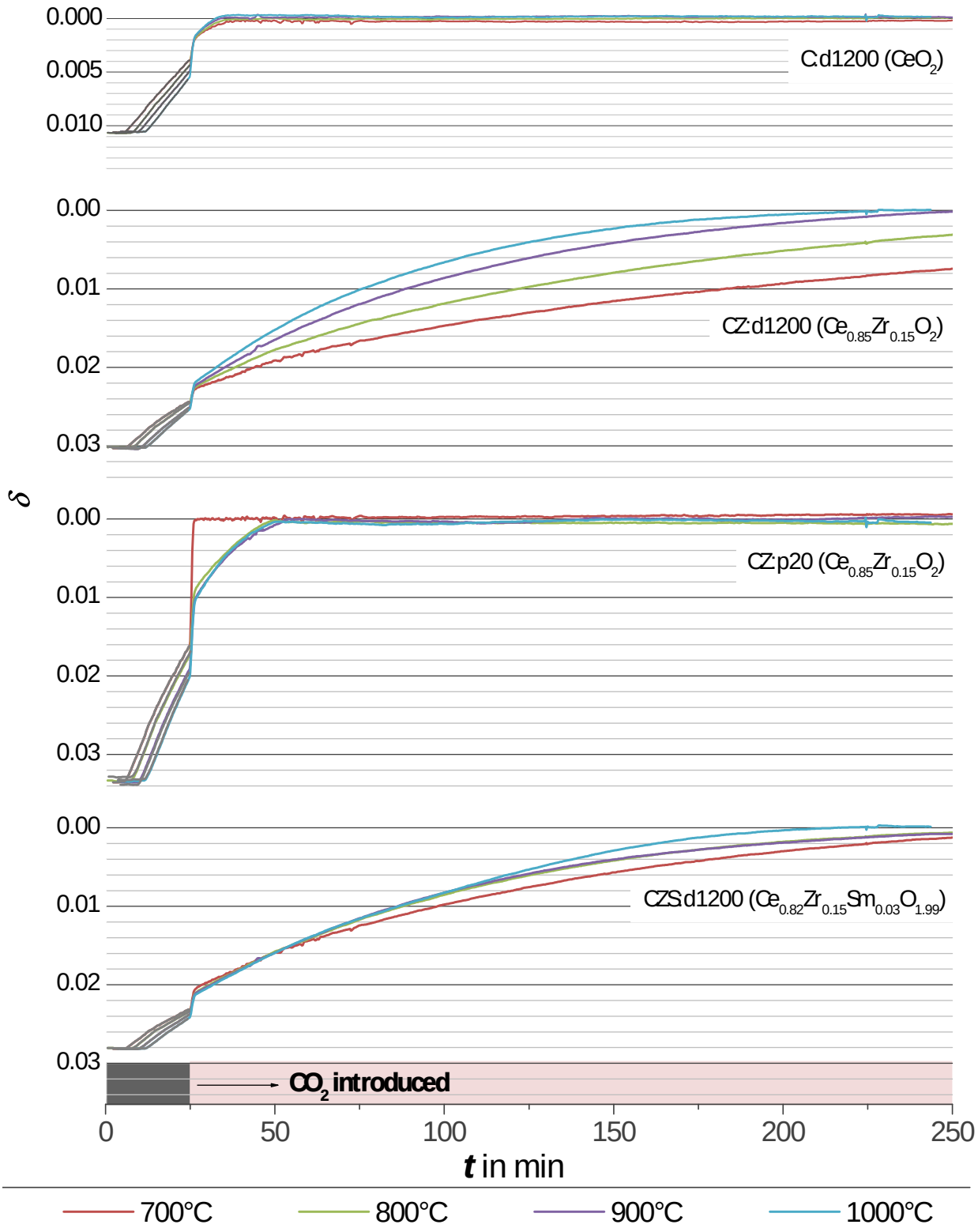

Figure 5.4: Course of the oxidation steps at varying oxidation temperatures T_{ox} of 700°C to 1000°C of each pellet derived from figure 5.3.

similar for temperatures $T_{ox} \geq 900$°C, the rate limitation might shift from diffusion controlled to either surface or mass-transport controlled. For the porous pellet, regime II is

significantly steeper. Considering the reaction path of section 4.2, the higher reaction rate of the porous material is attributed to better CO transport away from the reaction sites. This is reasonable due to the open porosity that shall provide enhanced gas exchange.

5.2 Reduction

The following conditions for the investigation of the reduction kinetics during heating have to be considered. While reducing, the material releases oxygen that needs to be transported away from the sample instantaneously. Otherwise, the partial pressure of oxygen $p(O_2)$ in the space around the sample increases drastically preventing an ongoing reaction. Optimally, the mass transport of oxygen is fast enough that no increase in $p(O_2)$ around the sample is detectable. Because of this requirement, the mass transport of oxygen is presumably one of the major challenges for the design of an efficient solar reactor. This assumption is especially true in the light of recently reported reduction durations. Bulfin et al. achieved equilibrium state of a porous ceria pellet (4.5 mm in diameter and 1 mm in height) in less than twelve seconds, while heating the sample by irradiation from room temperature to more than 1500°C under vacuum [Bulf 13].

To roughly evaluate the impact of the mass transport on the reduction rate in the thermobalance, pretests at varying sweep gas flows in the range of 20 to 200 ml·min^{-1} were performed. The results could hardly be discussed in a reasonable way because of the impact of the flow rate on the partial pressure of oxygen $p(O_2)$. Adjusting the gas flow changes the ratio of the sweep gas to the amount of gas (air) that enters the thermobalance due to random leakage. Therewith, the partial pressure of oxygen $p(O_2)$ changes, yielding different thermodynamical conditions, which overlapped the influence of the varied mass flows. Without exact knowledge of the gas flow dynamics, the potential mass transport limitations of the thermobalance remain hardly predictable. Therefore, the following experimental campaign solely attempts to qualitatively discuss the impact of microstructure and doping on the reduction rate and does not account for the change in $p(O_2)$ during reaction.

5.2.1 Results

Two dense pellets and two porous pellets of the compositions CeO_2 (C), $Ce_{0.85}Zr_{0.15}O_2$ (CZ), and $Ce_{0.825}Zr_{0.15}Sm_{0.025}O_{1.99}$ (CZS) were subjected to cycling experiments in the thermobalance. Four consecutive cycles were performed consisting of a reduction step (heating to 1400°C with 20 K·min^{-1}; isothermal step for 60 minutes under a predefined mixture of Ar and O_2 corresponding to $p(O_2) = 1 \times 10^{-3}$ bar as discussed in table 3.4 on page 39) and a splitting step (cooling to 800 with 50 K·min^{-1}; isothermal step for 30 minutes under a

synthetic air:Ar mixture with $p(O_2) = 0.08\,\text{bar}$).

Concerning the microstructure, the following shall provide the essential information of the four types of pellets employed: Two dense pellets with masses of almost 600 mg (d600) and 1200 mg (d1200), and two porous pellets fired with 10 wt.% (p10) and 30 wt.% (p30) rice starch with masses of almost 600 mg. A detailed characterization of the microstructure is found elsewhere [Para 13]. Table 3.3 on page 35 provides information regarding the dimensions of the pellets. The microstructural characterization of similar pellets with the aid of SEM is found in the previous section in figure 5.2. The dense pellets studied here feature similar microstructures. Only, the d600 pellets are approximately half as thick as the d1200. Compared to the porous pellets used in the last section, which were fired with 20 wt.% starch, the porous pellets studied here feature similar overall porosities within the error margins (table 3.3 on page 35), but differ in the type of porosity. The p10 pellets exhibit significantly less pore channels, whereas the p30 pellets display more and wider pore channels. To simplify the following discussion, a porosity property P is introduced that shall describe both, the pore channel density and the specific surface, yielding a relation for the four types of pellets: $P_{\text{p30}} \gg P_{\text{p10}} \gg P_{\text{d600}} \approx P_{\text{d1200}}$. The differences in P between porous and dense pellets and also between the two types of porous pellets should result in significantly different surface-reaction and mass-transport properties during reduction. Concerning the diffusion properties, a relevant parameter is the characteristic diffusion length l_d, which assesses the distance of an oxygen ion to diffuse from the bulk to the surface (see equation 4.1 on page 64). Due to the lack of porosity of the dense pellets, l_d is on the scale of mm due to the macroscopic thickness of approximately 0.5 mm of the d600 and 1 mm of the d1200 pellets. For the two porous pellets, l_d is maximum in the range of a few grains. The two porous pellets, p10 and p30, feature similar grain sizes of 1 to 5 µm sizes, being slightly bigger for p30 than for the p10. Therefore, for the four types of pellets, one may assume $l_{\text{p30}} \approx l_{\text{p10}} \ll l_{\text{d600}} < l_{\text{d1200}}$.

To preserve clarity, only one reduction step of the performed cycling is depicted in figure 5.5. In particular, the heating from 800°C to 1400°C ($0 < t < 30$ min) and the beginning of the isothermal step is presented. For all compositions, the porous pellets reduce faster compared to the dense pellets. The enhancement in reduction rate is very pronounced in the case of $Ce_{0.85}Zr_{0.15}O_2$. CZ:30p begins to reduce at temperatures as low as 900°C, whereas the Sm-doped porous pellets feature no significant reduction extent ($\delta > 0.001$) before reaching 1000°C. For the dense pellets, the thinner one, d600, reduces faster for all compositions. The dense pellets of the doped compositions start to reduce at temperatures higher than 1000°C. The δ of $Ce_{0.85}Zr_{0.15}O_2$ raises faster than observed for the Sm-doped pellets comparing the two d600 pellets as well as the d1200 pellets. Pure ceria exhibits reduction extents of $\delta > 0.001$ only when exceeding 1200°C. The ranking in the reduction rate between the 4 types of pellets is C:p30 > C:p10 > C:d600 > C:d1200. For all compositions and all types of microstructures, the curves flatten when reaching the isothermal temperature.

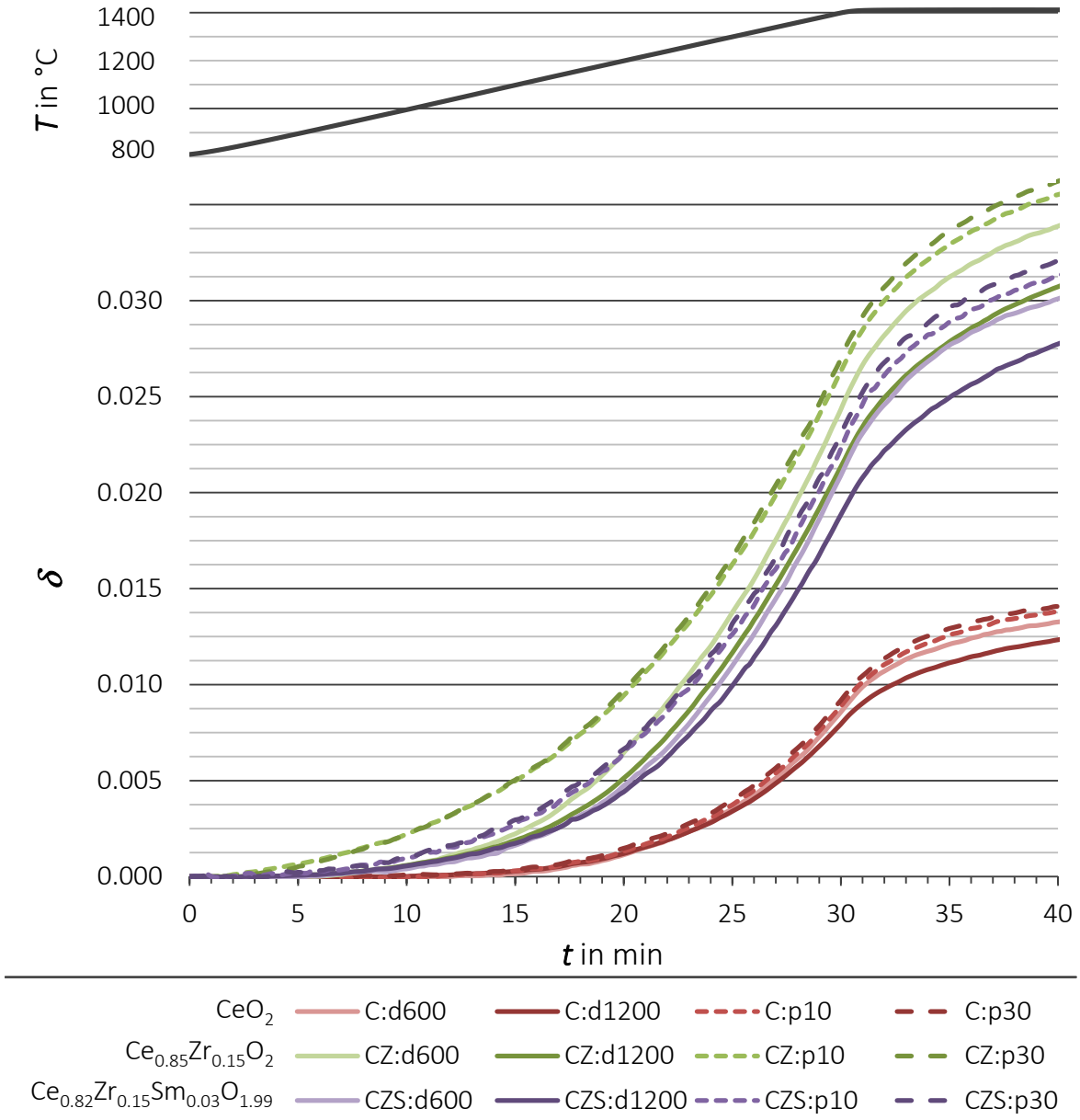

Figure 5.5: Reduction extent δ versus the time t of the reduction of various pellets (t = 0 to 30 min: heating step, t = 30 to 40 min: beginning of the isothermal step). Table 3.3 on page 35 provides more details about the pellets.

5.2.2 Discussion

Figure 5.6 visualizes the improvement in the redox extent δ due to open porosity with the aid of the difference $\Delta\delta_{p\text{-}d}$ between the redox extent of one of the two porous pellets $\delta^{p30;\,p10}$ and the dense pellet δ^{d600} of the same composition: $\Delta\delta_{p\text{-}d} = \delta^{p30;\,p10} - \delta^{d600}$. To assure compatibility, only the dense pellet d600 is applied for this relation, because it exhibits similar weights as the porous pellets. The highest improvement due to porosity is observed for $Ce_{0.85}Zr_{0.15}O_2$. Both porous CZ pellets feature similar $\Delta\delta_{p\text{-}d}$ in the first 15 minutes. At a temperature T of approximately 1100°C, $\Delta\delta_{p\text{-}d}$ begins to differ. My suggestion for the

rationale behind this behavior is as follows. The characteristic diffusion lengths of the three pellets are ranked as $l_{p30} \approx l_{p10} \ll l_{d600}$. However, since the porosity properties are $P_{p30} \gg P_{p10}$, the specific surface and the mass transport within the pellet may significantly differ. Because both pellets show very similar differences $\Delta\delta_{p\text{-}d}$ with respect to the dense pellet below $T = 1100°C$, the different porosities have no impact on the kinetics. Hence, at the beginning of the heating step, the reduction might only be diffusion-limited. For $T > 1100°C$, not only the reduction extent differs between dense and porous, but also between both porous pellets. Hence, the rate limit changes from only diffusion-controlled to also surface-reaction or mass-transport controlled at a temperature of $T_{shift} \approx 1100°C$.

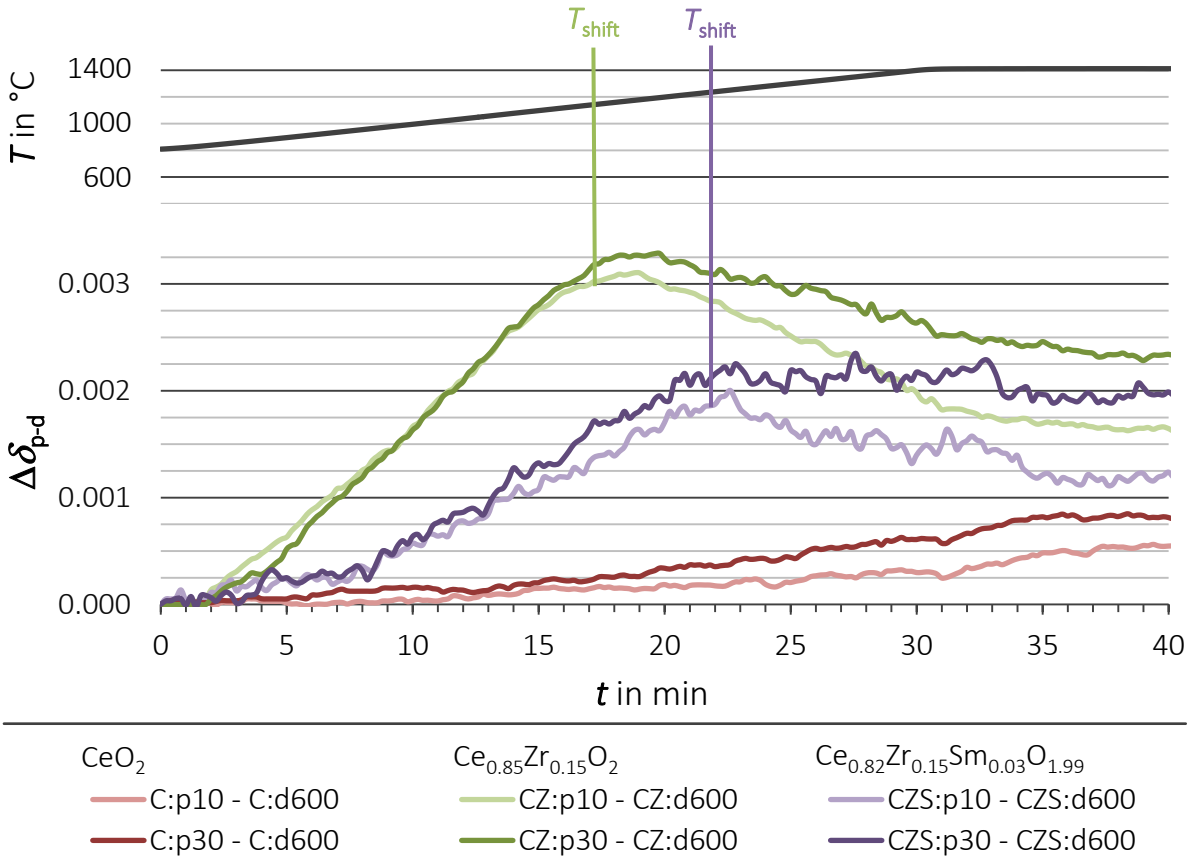

Figure 5.6: Difference in reduction extents $\Delta\delta_{p-d}$ between two porous pellets and the dense pellet d600.

The Sm-doped pellets show a similar behavior. The shift is observed at approximately $t \approx 22$ min corresponding to a temperature of $T_{shift} \approx 1250°C$. For CeO_2, different characteristics are observed. Both $\Delta\delta_{p\text{-}d}$ of the two porous pellets slightly but continuously differ. The more porous pellet, C:p30, features higher $\Delta\delta_{p\text{-}d}$ during the entire time, leading to the conclusion that the diffusion might not be the limiting factor in the beginning of the CeO_2 reduction under the employed conditions. Furthermore, the $\Delta\delta_{p\text{-}d}$ graph displays no maximum, hence, no shift temperature T_{shift} is identified.

Figure 5.7 illustrates the difference in the redox extent $\Delta\delta_{d\text{-}d}$ between the redox extents δ of the two dense pellets d600 and d1200: $\Delta\delta_{d\text{-}d} = \delta^{d600} - \delta^{d1200}$. Primarily, $\Delta\delta_{d\text{-}d}$ plotted versus t describes the time difference that is required to reach equilibrium state by the thicker d1200 pellet compared to d600. Since the main differences between the two dense pellets involves the characteristic diffusion length, the idea of this illustration is to determine the impact of the doping on the diffusivity. $\Delta\delta_{d\text{-}d}$ displays a peak slightly after the isothermal step begins. After the peak, $\Delta\delta_{d\text{-}d}$ of CeO_2 and $Ce_{0.85}Zr_{0.15}O_2$ exhibit a rather logarithmical slope, whereas $Ce_{0.825}Zr_{0.15}Sm_{0.025}O_{1.99}$ features a linear slope. The CZS:1200d achieves the equilibrium state much faster than the two other compositions, whereas the CZ pellet exhibits rather slow kinetics. Hence, Sm-doping considerably improves the diffusivity during reduction.

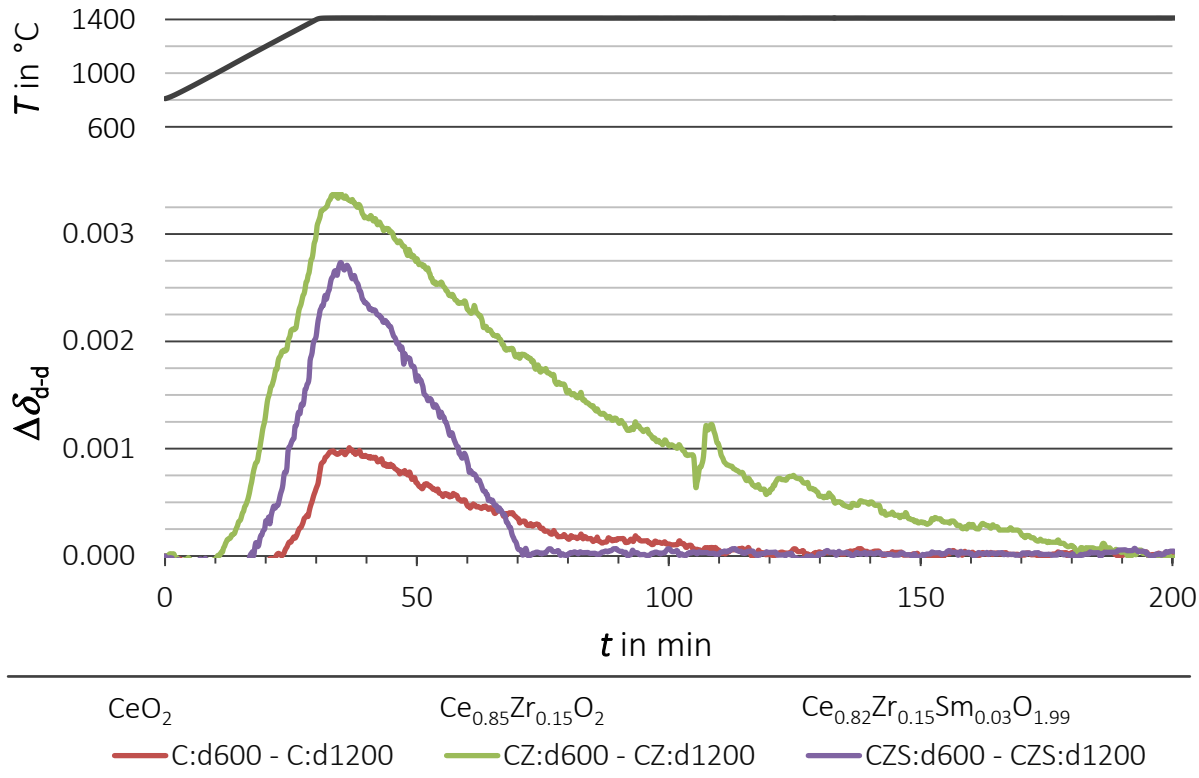

Figure 5.7: Difference in reduction extents $\Delta\delta_{d-d}$ between the two dense pellets.

5.3 Conclusions

Thermobalance experiments suffer from experimental deficits that impede a reliable analysis of the reaction rates in a quantitative manner. Primarily, these deficits comprise insufficient gas flow dynamics and the requirement of large driving forces implying large temperature changes or partial pressures of the reacting gases. Therefore, the investigations performed in the thermobalance presented in this chapter solely focused on assessing the fundamental impact of doping and microstructure on the reaction kinetics of ceria-based materials. In particular, the CO_2 splitting at oxidation temperatures ranging from $T_{ox} = 700°C$ to 1000°C and the reduction during heating were investigated. Pellets of the compositions CeO_2, $Ce_{0.85}Zr_{0.15}O_2$ and $Ce_{0.82}Zr_{0.15}Sm_{0.03}O_{1.99}$, exhibiting either dense or porous microstructures, were employed.

The dense $Ce_{0.82}Zr_{0.15}Sm_{0.03}O_{1.99}$ material exhibited enhanced oxidation kinetics compared to dense $Ce_{0.85}Zr_{0.15}O_2$ for temperatures $T_{ox} < 900°C$. This enhancement was attributed to the beneficial effect of Sm-doping on the oxygen diffusion, agreeing to results of the long-term cycling presented in section 4.2. For porous structures, the oxidation rate drastically increased due to higher gas exchange rates provided by open porosity. Therefore, the porous materials are the first choice in real application to assure sufficient kinetics. For the reduction, the doped materials showed improved reduction kinetics compared to pure ceria. In particular, the $Ce_{0.85}Zr_{0.15}O_2$ pellets featured higher reduction extents at much lower temperatures. Concerning the microstructure, porous materials reduced much faster at even lower temperatures, which was ascribed to faster diffusivity due to smaller characteristic diffusion lengths as in dense materials.

Doping significantly enhanced the reduction kinetics concerning both, the begin of the reduction as well as the rate. For the dense pellets, detectable reduction began at temperatures of 1000°C; for porous pellets in case of $Ce_{0.85}Zr_{0.15}O_2$, the reduction began already at temperatures as small as 900°C. Pure ceria started to reduce only above 1200°C. A shift from a solely diffusion-controlled regime to an either surface-reaction or mass-transport controlled regime was identified at a temperature of 1100°C for $Ce_{0.85}Zr_{0.15}O_2$ and 1250°C for $Ce_{0.82}Zr_{0.15}Sm_{0.03}O_{1.99}$. Ceria seemed not to be diffusion controlled under the employed conditions. Apart from that, the Sm-doping enhanced the oxygen diffusion within the bulk material. Doping with 2.5% Sm was found to be essential for a faster diffusion.

To further evaluate the kinetic relations obtained, a parametric study needs to be carried out that varies the process conditions of the oxidation (T_{ox} and CO_2 concentration) and reduction ($p(O_2)$ and heating rate) as well as considers other microstructures. To overcome the deficits of the thermobalance concerning the operation under vacuum and the relatively low heating rates, a device involving a vacuum chamber heated by an infrared furnace should be considered for this parametric study. In combination to this, experimental techniques should be employed that directly measure the material-specific

limitations of the kinetics, such as oxygen diffusivity and surface reaction. Among others, these techniques include secondary ion mass spectrometry [Lane 00] and electrochemical impedance spectroscopy [Lai 05]. Therewith, the determination of maximum reaction kinetics is enabled.

In short, the quintessence of this chapter is as follows:

Concerning oxidation and reduction, trivalent doping enhances the reaction kinetics in particular, for low temperatures, due to enhancing the oxygen diffusivity. Trivalent doping is in particular suggested to enhance the bulk diffusion.

To assure sufficiently high oxidation kinetics, the introduction of open porosity is essential. This is attributed to the improved gas-exchange.

6 Equilibrium-Reduction of Ceria-based Materials

To develop enhanced redox materials, the improvement of the reduction step is pivotal, as this step consumes most of the energy. This energy consumption is, inter alia, due to significant heat losses and relative high input of auxiliary energy. Improvements concerning the enhancement of the absolute reduction extent as well as the facilitation of the reaction in terms of its conditions are highly demanded. The facilitation particularly indicates a decrease of the necessary reduction temperature and/or an increase of the allowed partial pressure of oxygen. Assessing the relation between the reduction extent and the reaction conditions is crucial for the fundamental efficiency analysis of a material.

This chapter evaluates the reduction thermodynamics of pure ceria as well as the optimal doped compositions identified in the previous chapters. The first section presents experiments employing dense pellets to determine the equilibrium reducibility at varying reduction temperatures and partial pressures of oxygen. By applying a thermodynamical reaction model, the dependence of the reduction extent on both, temperature and partial pressure of oxygen is calculated, yielding a function to determine the reducibility for arbitrary reaction conditions. In the second section, the experimentally obtained functions are applied to assess the Gibbs energy and to construct Ellingham diagrams. These diagrams serve as a tool to display the fundamental relations of the reaction conditions of the reduction as well as the ability of a material to split water and carbon dioxide. Furthermore, the diagrams convey the enthalpy and entropy changes of the reduction. Concluding remarks complete this chapter.

Contents

6.1 δ as a function of T_{red} and $p(O_2)$

As aforementioned, the reduction extent δ is the most important performance number of a material employed in TCCs. It quantifies the amount of released oxygen during reduction and therewith, the amount of produced fuel during oxidation, provided that the material reoxidizes completely (see equations 2.3 and 2.4 on page 7). As recently reported, the efficiency of innovative reactor concepts that employ ceria-based materials are analyzed on the basis of a function $\delta(T_{red}, p(O_2))$ calculating the equilibrium δ depending on the reduction temperature T_{red} and the partial pressure of oxygen $p(O_2)$ [Erma 13]. Similar relations for the most-promising doped compositions identified in the previous chapter are required to evaluate the theoretical potential of these materials.

Experiments with the aid of a thermobalance were performed comprising long isothermal steps at various T_{red} and $p(O_2)$. T_{red} ranged between 1107°C and 1457°C in steps of approximately 50°C and four different $p(O_2)$ were applied ranging from 27 to 1270 Pa. Pellet materials were investigated that are calcined at a temperature of 1650°C, which is much higher than the highest investigated $T_{red} = 1457$°C. Therewith, no further sintering occurred during TGA experiments, as it was observed in the long-term cycling of the powder materials (section 4.2). Compared to the powder experiments, the reproducibility is significantly enhanced and the uncertainties of the results are reduced, because of sample masses twentyfold higher. The oxidation of pellets with CO_2 leads to impractically long durations of the oxidation step as seen in section 5.1. Therefore and since this chapter focuses on the reducibility and not on the CO_2 splitting ability, oxygen in form of synthetic air was employed to reoxidize the pellets.

6.1.1 Results

Due to practical reasons, the experiments were carried out in two individual programs, a low temperature program (1000 °C to 1250°C) and a high temperature program (1250 °C to 1450°C). Exemplary, the data of both runs is depicted in figure 6.1. Overall, eleven cycles with varying reduction T_{red} temperature were performed consisting of

- a heating step with 20 K·min^{-1} to T_{red}.
- an isothermal step long enough to obtain equilibrium state of the reduction reaction, confirmed by a stable mass signal exhibiting no further mass loss. Due to pretest, the durations of the isothermal steps varied from 60 minutes to 210 minutes.
- a cooling step to 800°C with 50 K·min^{-1}.
- an isothermal step of 60 minutes. In the first 30 minutes, synthetic air was introduced yielding a gas atmosphere with 8.3 vol.% O_2. Complete reoxidation was achieved in this step, confirmed by relative mass changes of 0% with respect to the initial mass.

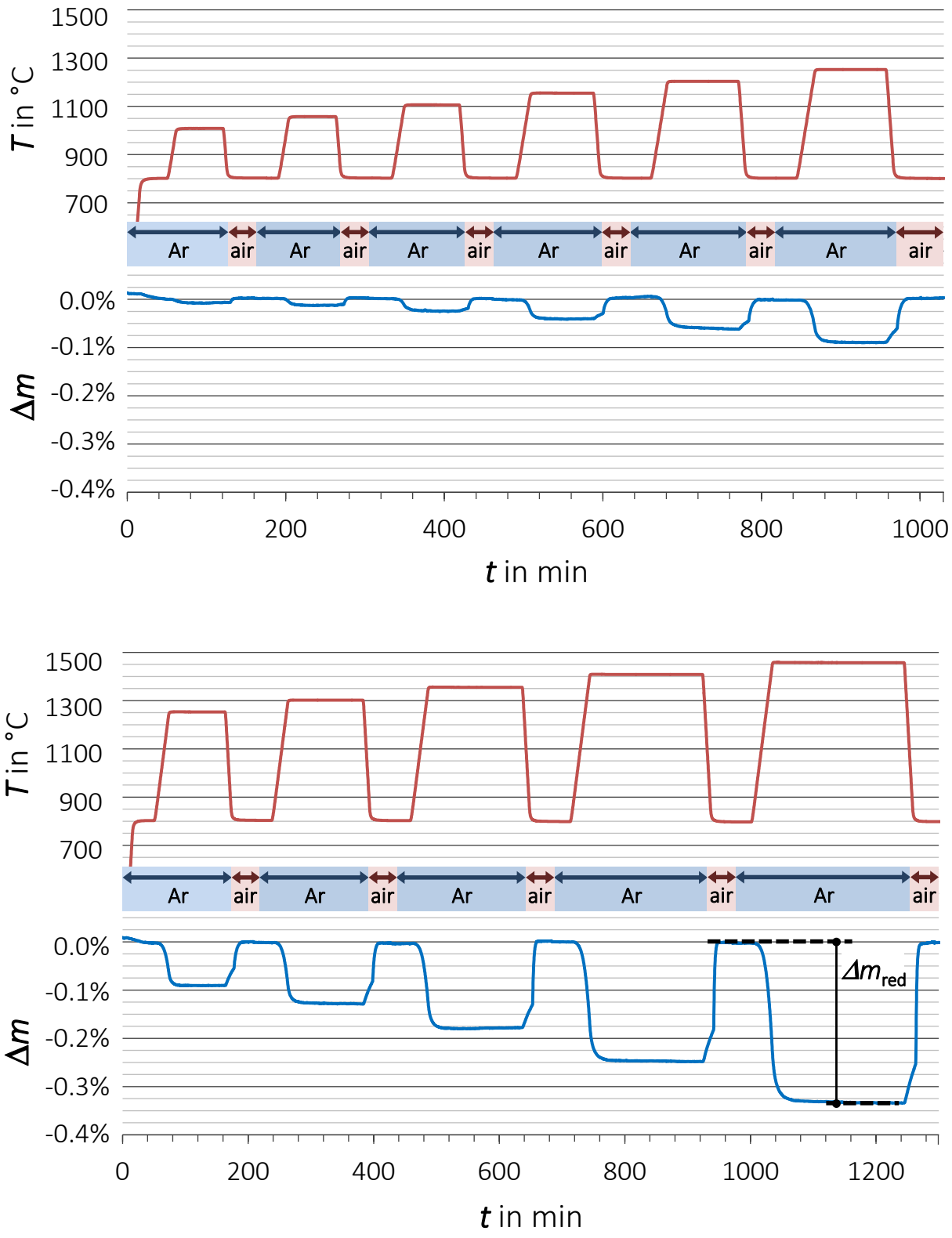

Figure 6.1: TGA program (temperature and atmosphere) and corresponding mass change vs. time of low (top) and high (bottom) temperature program applied in pellet experiments to evaluate the equilibrium state of the reduction. Exemplary data of $Ce_{0.82}Zr_{0.15}La_{0.03}O_{1.99}$.

Except the first 30 minutes of the isothermal step at 800°C, the thermobalance was swept with 85 ml·min^{-1} of a predefined mixture of Ar and O_2. An oxygen sensor measured the partial pressure of oxygen. For the high temperature program, four different partial pressures were achieved $p(O_2)$ = 27, 49, 125, 1270 Pa, respectively, with a relative uncertainty of $u(p(O_2))$ = 10%. Further details are displayed in table 3.4. Due to calibrations and statements of the manufacturer of the thermobalance, uncertainties of $u(T_{red})$ = 3°C were assumed for the reduction temperature T_{red}. Four dense pellets with similar weights of almost 600 mg were subjected to TGA cycling with the compositions:

CeO_2 $Ce_{0.85}Zr_{0.15}O_2$ $Ce_{0.82}Zr_{0.15}Sm_{0.03}O_2$ $Ce_{0.82}Zr_{0.15}La_{0.03}O_2$

Note that the denoted colors are used in the entire chapter to identify the four different materials. For detailed information of the pellets see table 3.3 in section 3.2.3.

To analyze the reducibility, the mass loss during reduction Δm_{red} is calculated as depicted in figure 6.1. The first two reductions of both, low and high temperature programs are not considered in the following, because of difficulties to identify their exact begin. Also, the second reduction of the low temperature program is not considered, due to calculated Δm_{red} that are too small regarding the error margins. Figure 6.2 shows the specific yield $n_m(O_2)$ of the high temperature step. The yields increase with increasing reduction temperature T_{red} and decreasing partial pressure of oxygen $p(O_2)$. Doping significantly enhances the specific yields. The $Ce_{0.85}Zr_{0.15}O_2$ pellet releases the most oxygen with up

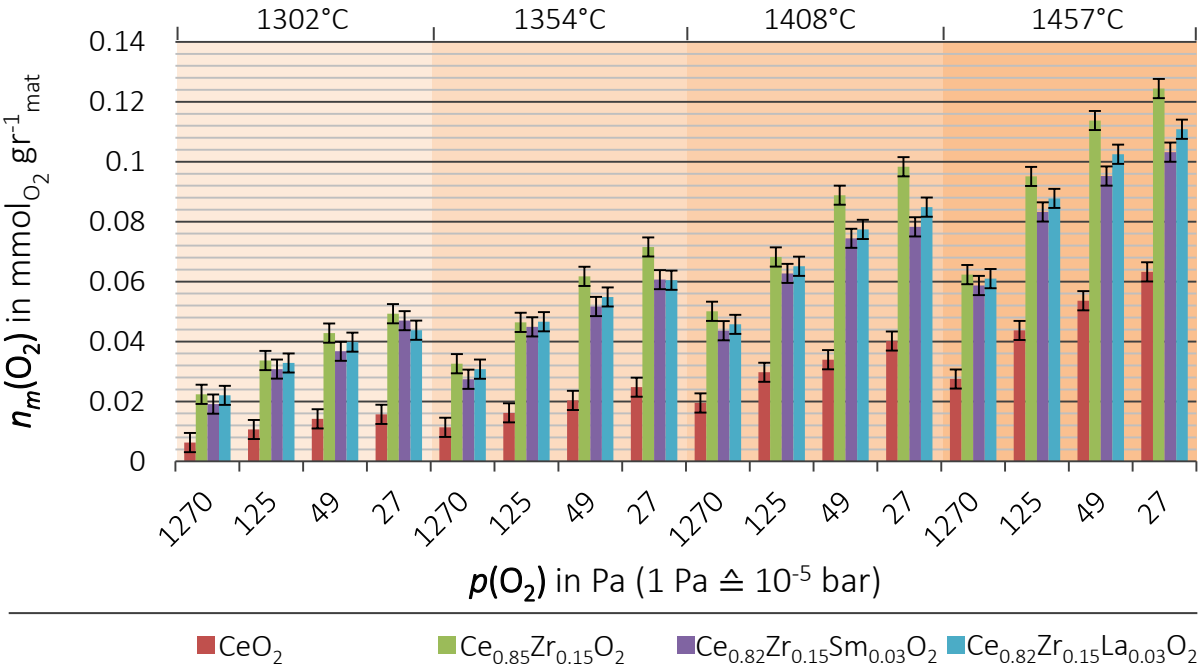

Figure 6.2: Specific yield $n_m(O_2)$ calculated from TGA experiments (high temperature program) of pellet materials at several reduction temperatures T_{red} and several oxygen partial pressures $p(O_2)$.

to $n_m(O_2) = 0.124 \pm 0.02$ $mmol_{O_2} \cdot g_{mat}^{-1}$. As observed for powder materials, trivalent doping leads to slightly lower yields. At almost all reduction conditions, the La-doped material performs slightly better compared to the Sm-doped material. Compared to ceria, which releases $n_m(O_2) = 0.063 \pm 0.02$ $mmol_{O_2} \cdot g_{mat}^{-1}$, all doped compositions show significant higher yields. Figure 6.3 illustrates of changing of either the reduction temperatures T_{red} or the oxygen partial pressures $p(O_2)$.

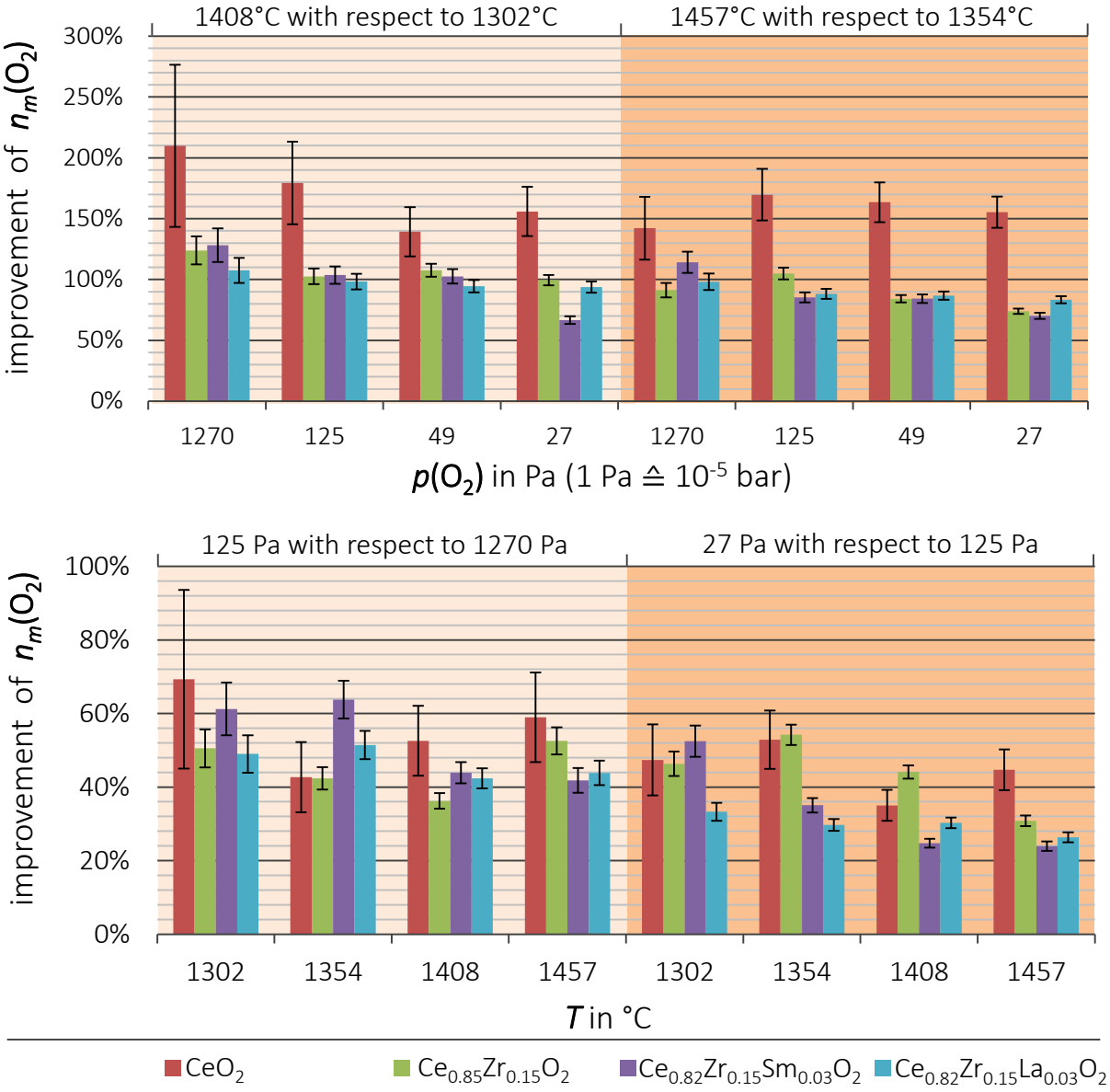

Figure 6.3: Impacts of higher reduction temperatures T_{red} or lower oxygen partial pressures $p(O_2)$ on the specific yields $n_m(O_2)$. Top: Relative improvements of $n_m(O_2)$ by means of an increase T_{red} by approximately 100 K versus $p(O_2)$ (left: relative improvements at 1408°C with respect to 1302°C / right: at 1457°C with respect to 1354°C). Bottom: Relative improvements of the $n_m(O_2)$ due to decreasing $p(O_2)$ by 0.5 - 1 order of magnitude versus T_{red} (Left: relative improvements at 125 Pa with respect to 1270 Pa / right: at 27 Pa with respect to 125 Pa). An improvement of 0% denotes no change of the yield $n_m(O_2)$.

The relative improvements by means of increasing the reduction temperatures T_{red} by approximately 100 K are presented in figure 6.3 (top). The improvements of pure CeO_2 is significantly more pronounced. At temperatures between 1300°C and 1500°C, increasing T_{red} by approximately 100 K leads to 140 - 200% more released oxygen per gram CeO_2. The doped materials display smaller relative improvements compared to pure ceria ranging from 120% at the lower temperature step and the highest $p(O_2)$ to 70% at the higher temperature step and the lowest $p(O_2)$, respectively. For almost all materials, the relative improvement slightly decreases with decreasing $p(O_2)$ for both denoted temperature steps. Only for pure ceria, a different behavior is observed for the higher temperature step.

Figure 6.3 (bottom) shows the impact of reducing the partial pressure of oxygen $p(O_2)$ on the specific oxygen yield $n_m(O_2)$. In contrast to the temperature impact on the oxygen yield improvement observed between pure ceria and doped-ceria, there are not such significant differences notable while reducing the partial pressure. Reducing the partial pressure by approximately one order of magnitude from 1270 Pa to 125 Pa improves the yields by 40 to 65%. Further reducing $p(O_2)$ by a factor of five leads to slightly smaller improvements of all materials except $Ce_{0.85}Zr_{0.15}O_2$. The relative improvements of the specific oxygen yield $n_m(O_2)$ trend to decrease with increasing T_{red} as exposed by the dashed lines.

Figure 6.4 compares the relative improvements of the specific oxygen yield $n_m(O_2)$ of the three doped compositions with respect to pure ceria. With increasing T_{red} and decreasing $p(O_2)$, the relative improvement decreases from values of approximately 200% to values of 70% to 100%. At low temperatures, the differences between the various dopings are not explicit, whereas for high T_{red} and low $p(O_2)$, $Ce_{0.85}Zr_{0.15}O_2$ exhibits higher relative improvements. Compared to the powder material test campaigns presented in chapter 4, the relative improvements caused by doping found here are significantly higher. This is explained by the lower partial pressure of oxygen of $p(O_2) = 0.5$ Pa applied in the powder experiments. For instance, at such low $p(O_2)$, $Ce_{0.85}Zr_{0.15}O_2$ showed only an improvement of 50% compared to pure ceria. This finding in consistent with the overall trend in figure 6.4. Hence, under worse conditions (lower T_{red} and higher $p(O_2)$), the enhancement due to doping is even more pronounced.

The results of the low temperature program is depicted in figure 6.5. Since pure CeO_2 features reducibilities in the low temperature program that are too low to be reasonably analyzed, the CeO_2 pellet was not subjected to this program. As observed in the high temperature campaign, the yields increase with increasing temperature T_{red} and decreasing partial pressure of oxygen $p(O_2)$. $Ce_{0.85}Zr_{0.15}O_2$ shows slightly higher yields followed by $Ce_{0.825}Zr_{0.15}La_{0.025}O_{1.99}$. However, these findings are not as significant, because the variations in the absolute numbers are within the error margins.

The observations gained within this experimental campaign concerning the dependencies of the reduction extents on changing the temperature T_{red} or the partial pressure of oxygen $p(O_2)$, are picked up again during the process analysis presented in chapter 7.

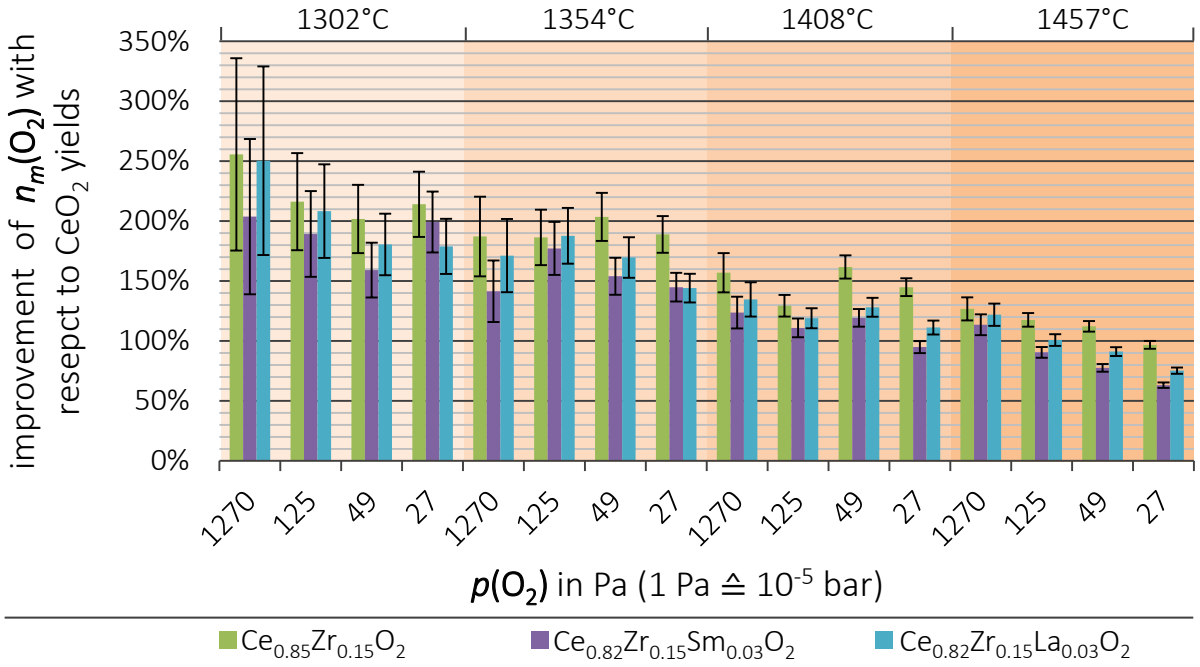

Figure 6.4: Relative improvement of the specific oxygen yields $n_m(O_2)$ with respect to pure ceria versus the reduction temperature T_{red} (four columns) and the oxygen partial pressures $p(O_2)$ (four bundles in each column). An improvement of 0% denotes no change of the yield.

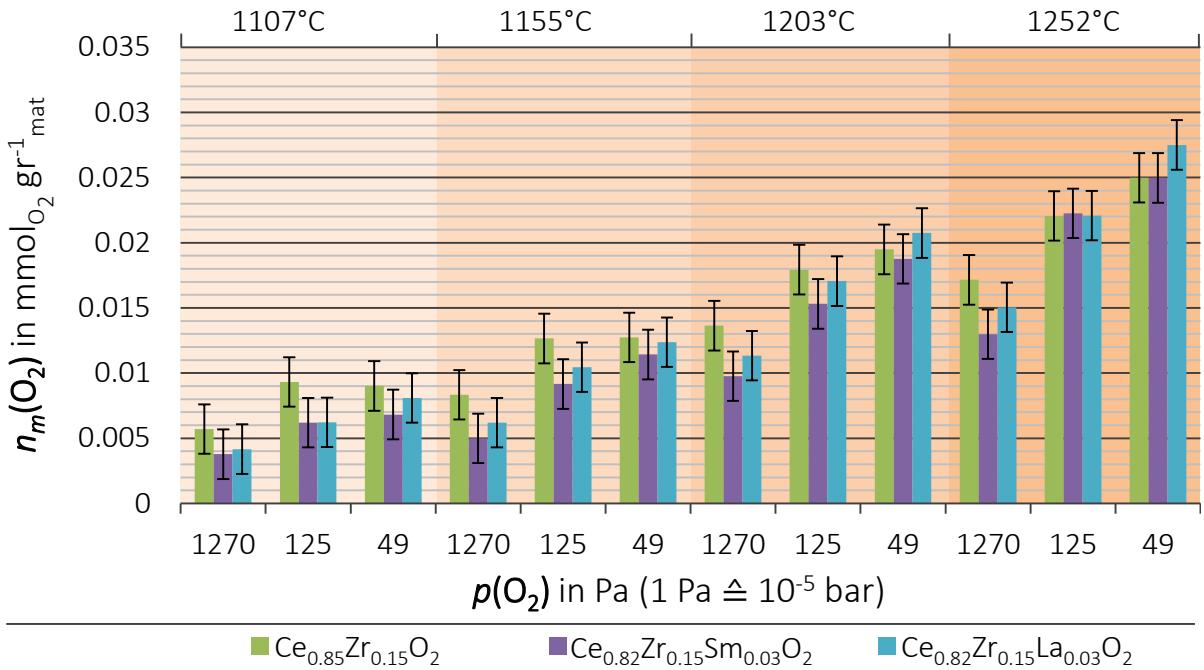

Figure 6.5: Specific yield $n_m(O_2)$ calculated from TGA experiments (low temperature program) of pellet materials at several reduction temperatures T_{red} and several oxygen partial pressures $p(O_2)$.

6.1.2 Discussion

In the following, an Arrhenius-based model is introduced similar to the one recently published by Bulfin et al. that describes the redox reaction [Bulf 13]. Figure 6.6 schematically depicts the model approach. Since equilibrium is achieved in the experiments, kinetical

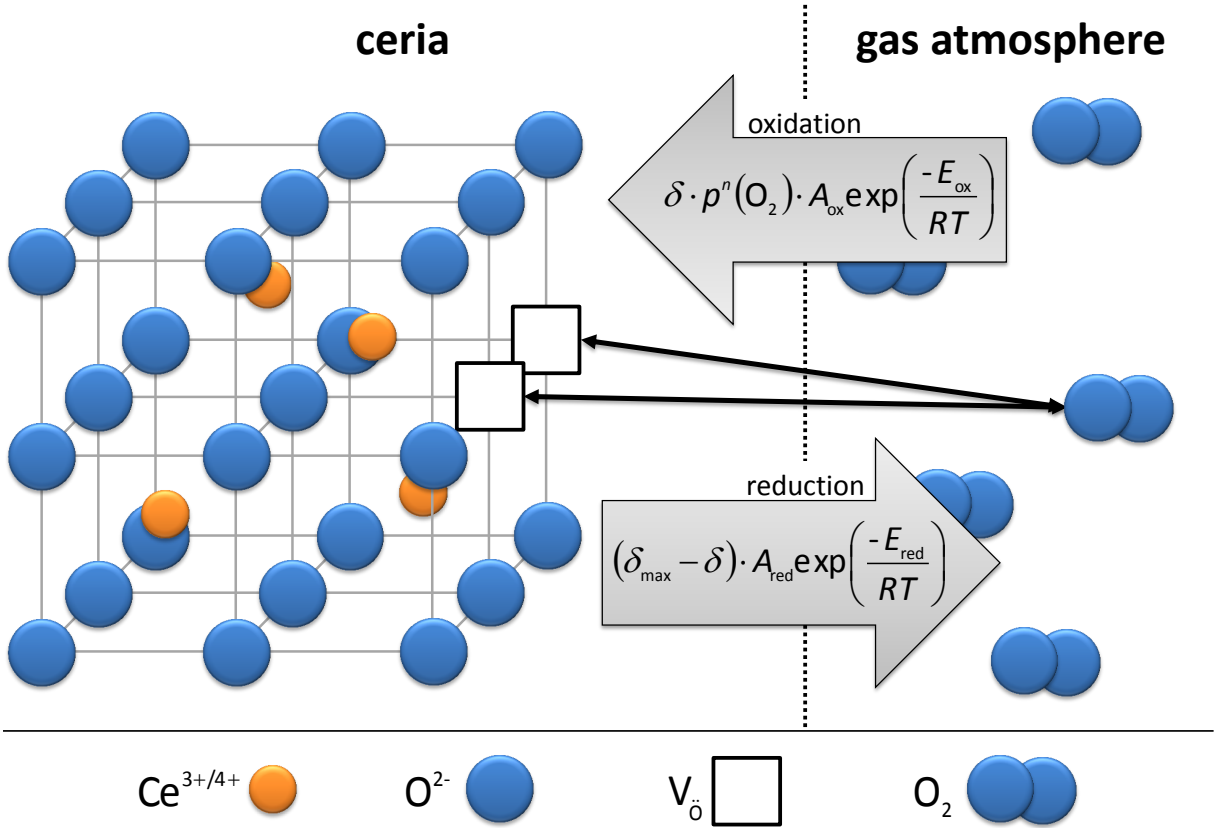

Figure 6.6: Schematic of the reduction and oxidation reactions of pure ceria in a gas atmosphere containing oxygen.

limitations such as oxygen diffusion or surface exchange are not considered in this model. The fundamental reaction is given by:

$$^1/_\delta CeO_2 \rightleftharpoons {}^1/_\delta CeO_{2-\delta} + {}^1/_2 O_2 \tag{6.1}$$

As aforementioned, the absolute redox extent δ is limited by $\delta_{\text{max stoic}} = 0.5$, representing the full reduction of all cerium ions from Ce^{4+} to Ce^{3+}, which corresponds to a phase change from CeO_2 to Ce_2O_3. This transition modifies the fundamental properties of the material. A model describing the redox reaction of CeO_2 may not be valid for the redox reaction of Ce_2O_3. Therefore, it is reasonable to limit the reduction reaction to a certain maximum value of δ, say δ_{max}. The reduction depends on the concentration of reducible cerium $c\left(Ce^{4+}\right)$. The oxidation depends on the oxygen concentration in the gas atmosphere $c\left(O_2\right)$ and the concentration of the oxygen vacancies $c\left(V_{\ddot{O}}\right)$ within the crystal structure. The rate of the change in the concentration of oxygen vacancies $\frac{d}{dt} c\left(V_{\ddot{O}}\right)$ is the

difference of the rate of oxygen that is released (reduction) and the rate of oxygen that is incorporated in the structure (oxidation):

$$\frac{d}{dt}c\left(V_{\ddot{O}}\right) = c\left(Ce^{4+}\right)k_{red} - c\left(V_{\ddot{O}}\right)c^{n}\left(O_2\right)k_{ox} \tag{6.2}$$

k_{red} and k_{ox} are the rate constants of reduction and oxidation, respectively, and n the oxygen partial pressure dependence. Dividing equation 6.2 by the concentration of cerium $c\,(\mathrm{Ce})$, which is constant during the experiment, makes the concentration terms of equation 6.2 unitless.

$$\frac{1}{c\,(\mathrm{Ce})}\cdot\frac{d}{dt}c\left(V_{\ddot{O}}\right) = \frac{c\left(Ce^{4+}\right)}{c\,(\mathrm{Ce})}k_{red} - \frac{c\left(V_{\ddot{O}}\right)}{c\,(\mathrm{Ce})}c^{n}\left(O_2\right)k_{ox} \tag{6.3}$$

With the parameters δ and δ_{max}, the concentration terms can be defined as $\frac{c\left(Ce^{4+}\right)}{c(Ce)} = \delta_{max} - \delta$ and $\frac{c\left(V_{\ddot{O}}\right)}{c(Ce)} = \delta$. The oxygen concentration in the gas atmosphere $c\,(O_2)$ is directly proportional to the partial pressure of oxygen $p(O_2)$. Applying these substitution in equilibrium, where reaction rate equals zero, an equilibrium condition is given by:

$$(\delta_{max} - \delta)\,k_{red} = \delta p^{-n}(O_2)k_{ox} \tag{6.4}$$

The rate constants of reduction and oxidation k_{red} and k_{ox} take the Arrhenius form:

$$k_{red;\,ox} = A_{red;\,ox}\exp\left(-\frac{E_{red;\,ox}}{RT}\right) \tag{6.5}$$

where $A_{red;\,ox}$ is the prefactor or frequency factor and $E_{red;\,ox}$ the activation energy of the reduction or oxidation, respectively. R denotes the universal gas constant.

This model approach leads to an equation that calculates the absolute redox extent δ depending on the temperature T and partial pressure of oxygen $p(O_2)$:

$$\delta\,(T,\,p(O_2)) = \frac{\delta_{max}\cdot\frac{A_{red}}{A_{ox}}\cdot p^{-n}(O_2)\cdot\exp\left(-\frac{\Delta E}{RT}\right)}{1+\frac{A_{red}}{A_{ox}}\cdot p^{-n}(O_2)\cdot\exp\left(-\frac{\Delta E}{RT}\right)} \tag{6.6}$$

with $\Delta E = E_{red} - E_{ox}$. In literature no reliable values for δ_{max} can be found that exactly mark the phase change of ceria. This is in particular true for the doped materials. Therefore, the maximum values according to stoichiometrics of material are assumed for δ_{max}. Those are for pure ceria $\delta_{max\,stoic} = 0.5$, for the Zr-doped material $\delta_{max\,stoic} = 0.425$ and for the rare-earth doped material $\delta_{max\,stoic} = 0.4125$.

Figure 6.7 compares the fitting results with the experimental data as well as with corresponding fits calculated with parameters reported by Bulfin et al., who fitted the data of Panlener et al. [Panl 75, Bulf 13]. The fittings based on the experimental data of this thesis match the data quite well. In contrast, the graphs based on the parameters reported in the literature describe the experimental data sufficiently only between 1400°C and 1500°C.

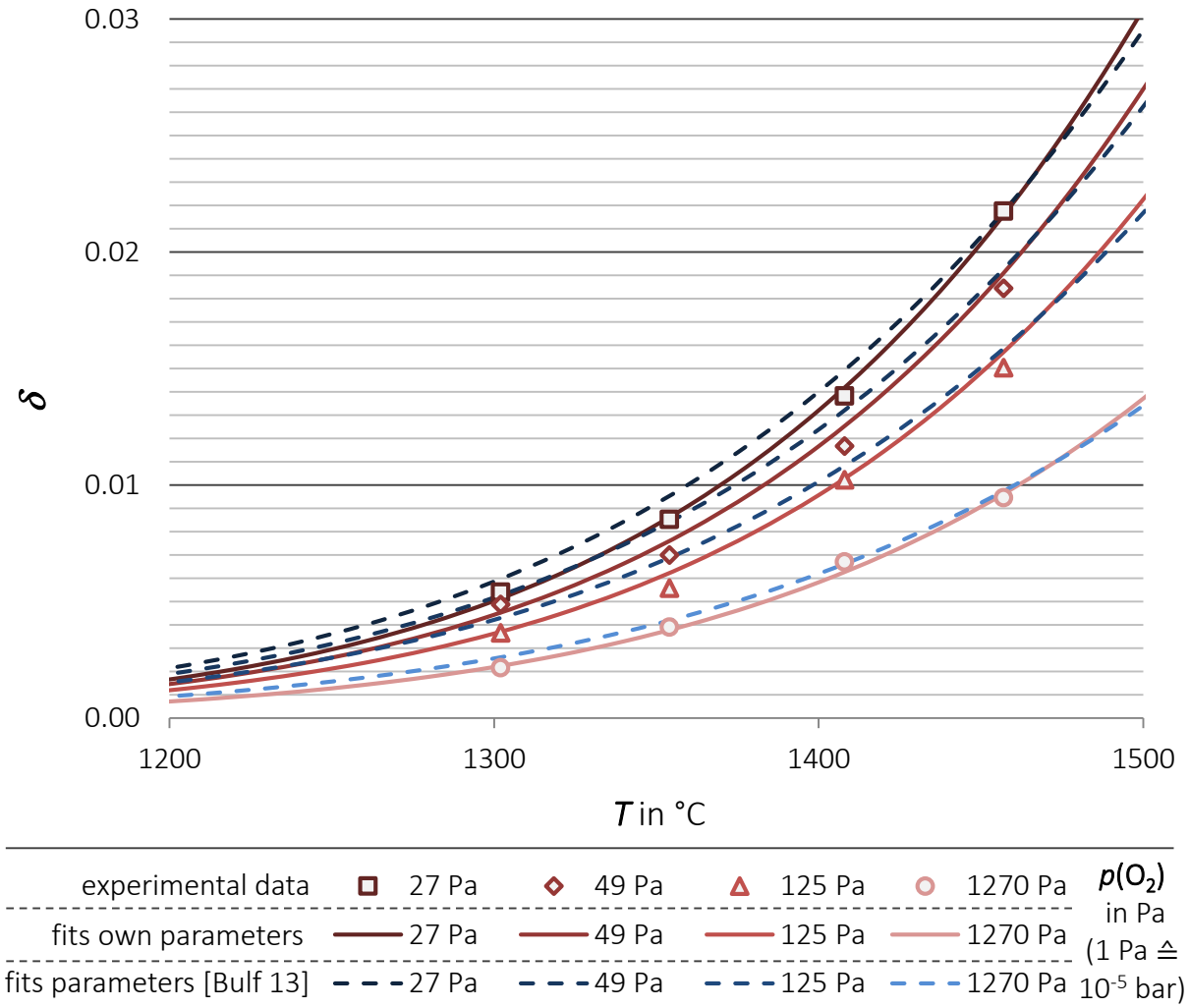

Figure 6.7: Absolute redox extents δ versus the reduction temperatures T_{red} at several partial pressures of oxygen $p(O_2)$. Data points represent the experimental results; their sizes correspond to the uncertainties of T_{red} and δ. Red lines correspond to least square fittings of the obtained experimental data with equation 6.6. Blue lines were calculated for the denoted $p(O_2)$ according to [Bulf 13].

At lower temperatures, the graphs predict a higher reducibility. The rationale behind this deviation is the different data employed to calculate the parameters. At $\delta > 0.05$, there is a drastic change in shape of $\delta\,(T,\ p(O_2))$ as reported from [Panl 75]. By the calculations of Bulfin et al., this change in shape is considered. In contrast, in this thesis only $\delta < 0.05$ were obtained. Hence, the fitting presented here does not consider the change in shape of $\delta\,(T,\ p(O_2))$ at $\delta = 0.05$.

With ceria, sixteen data points were obtained. In particular, the limited T_{red} range of 150 K and a $p(O_2)$ range of approximately two orders of magnitudes is problematic for an extensive application of the calculated $\delta\,(T,\ p(O_2))$ function. It remains unclear to which extent the calculated function can describe the shape of $\delta\,(T,\ p(O_2))$ for temperatures $T_{red} \geq 1500°C$ and/or $p(O_2) \leq 10\,Pa \mathrel{\widehat{=}} 10^{-4}\,bar$. From a technical point of view, however,

such conditions are not of major interest. They may result in penalties on the overall process efficiency $\eta_{\text{solar to fuel}}$ that may impede the commercialization of the process, as discussed in section 2.1. The investigated conditions supposedly correspond to the optimal match between fuel productivity of ceria and technical feasibility.

The fittings of the doped materials are presented in figure 6.8. For the doped materials, 28 data points are available covering a much bigger temperature range. For the highest partial pressure of oxygen $p(O_2)$, the doping enhances the performance by at least 100% as already discussed in figure 6.4 The best results were obtained for $Ce_{0.85}Zr_{0.15}O_2$. The rare-earth doped materials show a similar performance. However, the La-doped material exhibits slightly higher reducibility for the entire experimental campaign, which is in concert with findings presented in the previous chapter (section 4.1.2).

The obtained fitting parameters are presented in table 6.1. The parameters of ceria exhibit relatively high uncertainties due to the smaller number of data points. Especially, the ratio of the frequency factors A_{red}/A_{ox} suffer from a high relative uncertainty of approximately 40%. Here, Bulfin et al. reported a significant lower value of $A_{red}/A_{ox}{}^{\text{Bulfin}} = 8700 \pm 800$ bar^n. Also for the activation energy difference of reduction and oxidation ΔE, Bulfin et al. reports a lower value of $\Delta E^{\text{Bulfin}} = 195.6 \pm 1.2$ kJ·mol^{-1}, whereas the calculated pressure dependence n agrees within the error margins with $n^{\text{Bulfin}} = 0.218 \pm 0.0013$. In other publications, also values of $n = 1/5$ were reported [Panl 75, Dawi 86].

Table 6.1: Fitting parameters of $\delta\,(T_{red},\ p(O_2))$. Parameter δ_{max} is defined prior fitting as explained in the text. Parameters A_{red}/A_{ox}, n and ΔE of equation 6.6 calculated by least squares fitting of the experimental data presented in figures 6.2 and 6.5. The uncertainties denote the standard deviation and R^2 the coefficient of determination. The parameters were derived using the units K for T_{red} and bar for $p(O_2)$.

	δ_{max}	A_{red}/A_{ox} in bar^n	n -	ΔE in kJ·mol^{-1}	R^2
CeO_2	0.5	22700 ± 8900	0.2162 ± 0.0091	214.7 ± 5.4	0.9955
$Ce_{0.85}Zr_{0.15}O_2$	0.425	766 ± 178	0.1988 ± 0.0077	150.9 ± 3.1	0.9956
$Ce_{0.825}Zr_{0.15}Sm_{0.025}O_{1.99}$	0.4125	525 ± 116	0.1740 ± 0.0069	145.7 ± 2.8	0.9962
$Ce_{0.825}Zr_{0.15}La_{0.025}O_{1.99}$	0.4125	690 ± 60	0.1727 ± 0.0028	147.9 ± 1.2	0.9993

The results for the doped materials are more definite. The fittings of the data of $Ce_{0.85}Zr_{0.15}O_2$ and $Ce_{0.825}Zr_{0.15}Sm_{0.025}O_{1.99}$ exhibit a similar coefficient of determination R^2 as found for pure ceria, but the standard deviations of the parameters are considerably lower, especially for A_{red}/A_{ox}. By far, the best fitting parameters were obtained for the La-doped material with $R^2 = 0.9993$. Compared to pure ceria, values for A_{red}/A_{ox} were calculated that are smaller by a factor of 30 to 40. The obtained differences in the activation energies

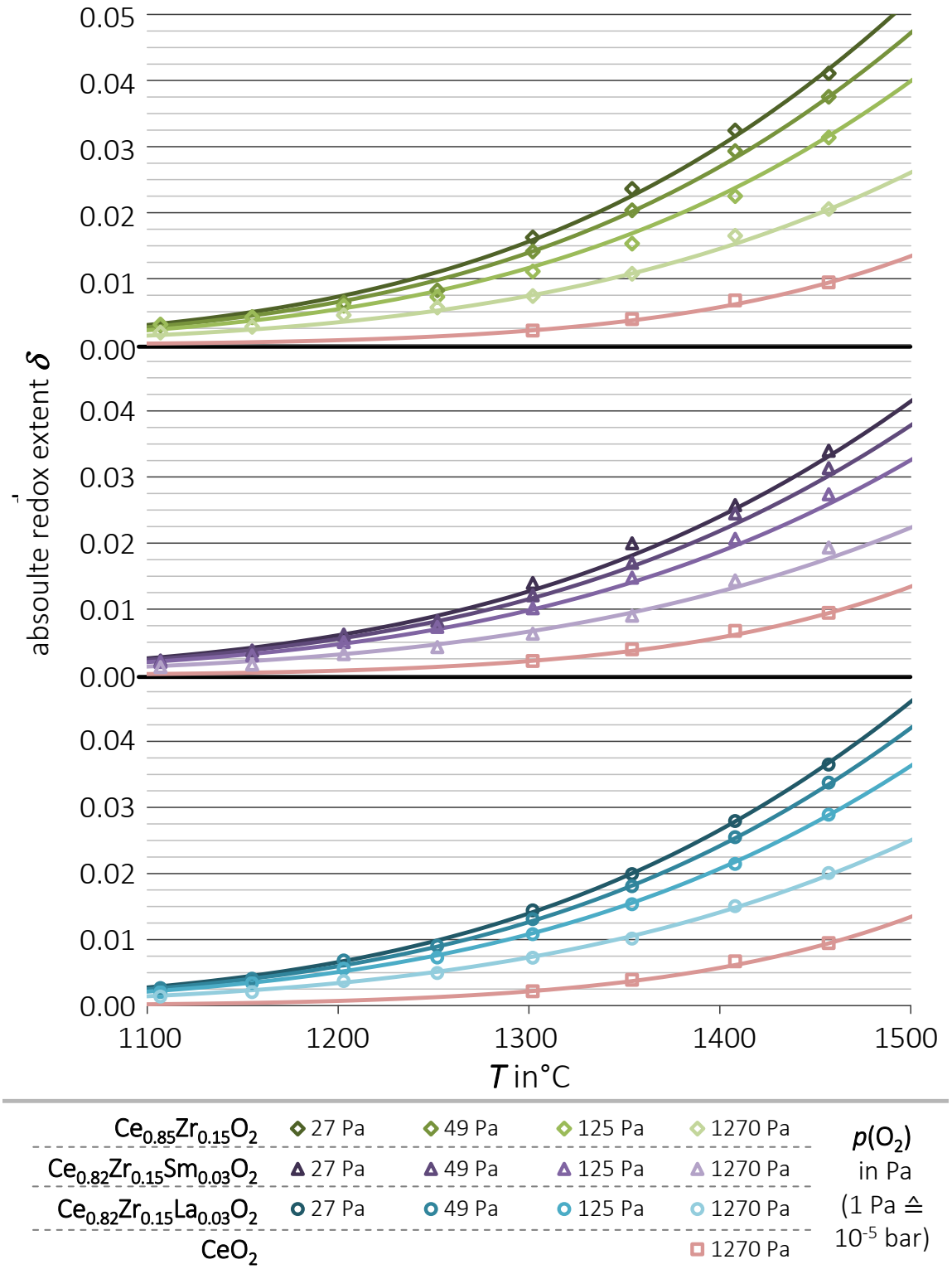

Figure 6.8: Absolute redox extents δ versus the reduction temperatures T_{red} at several partial pressures of oxygen $p(O_2)$. Data points represent the experimental results; their sizes correspond to the uncertainties of T_{red} and δ. Lines correspond to least square fittings of the data with equation 6.6 at the corresponding $p(O_2)$. Plotting the results of CeO_2 at $p(O_2)$ = 1270 Pa shall illustrate the impact of doping.

ΔE are smaller by 65 to 70 kJ·mol^{-1}. Since each of both values contain two further parameters, one for describing the reduction and one the oxidation reaction, it is impossible to quantitatively state the consequences for the two reactions.

The pressure dependence n describes the impact of oxygen around the material on δ with $\delta \propto p(O_2)^{-n}$. Hence, δ increases with decreasing $p(O_2)$ and increasing n. Doping, however reduces the impact of $p(O_2)$. Compared to CeO_2, $Ce_{0.85}Zr_{0.15}O_2$ features a value for n that is smaller by approximately 0.02. The rare-earth doped material exhibit even smaller n with a difference of approximately 0.04. The origin of the varying n calculated for the materials is not yet completely understood. As mentioned, n is supposed to describe the dependency of the δ on $p(O_2)$. However, as observed in the experimental campaign, the materials display relative changes in δ that are similar, when varying the partial pressure of oxygen, as presented in figure 6.3.

6.2 Gibbs Energy of the Redox Reaction

6.2.1 Ellingham Diagrams

Ellingham diagrams describe the change in the standard Gibbs energy ΔG of a certain reaction with respect to the temperature [Monk 44]. The following gives a short introduction of the most important fundamentals to Ellingham diagrams. For more details, please see section 2.2.2. In the case of ceria-based materials, they predict the couples of reduction temperature T_{red} and partial pressure of oxygen $p(O_2)$ at which the redox reaction of a certain δ is in its equilibrium or, in other words, is thermodynamically favorable. Note that one Ellingham line corresponds to exactly one δ. Plotting the equilibria lines of the water and CO_2 redox reaction in such diagrams determines, whether the oxidation of a certain δ via the splitting reaction is thermodynamically favorable.

The idea of the following section is to derive Ellingham diagrams for the investigated materials by employing the $\delta(T, p(O_2))$ equation 6.6. The parameters of which were calculated in the previous section as presented in table 6.1. In the first step, $p(O_2)$ were determined with the Software Engineering Equation Solver EES (F-Chart Software) by solving $\delta(T, p(O_2))$ for a fixed δ and varying T_{red}. Via the relation

$$\Delta G = -1/2 RT \cdot \ln p(O_2) \tag{6.7}$$

the values of ΔG were determined. The factor $1/2$ is due to the mass action law of the basic redox reaction of metal: $M + 1/2 O_2 \rightleftharpoons MO$. Plotting ΔG versus the temperature give a Ellingham diagram. Generally, the change in the standard Gibbs energy ΔG during reduction corresponds to the changes of the enthalpy ΔH_{red} and the entropy ΔS_{red} at T_{red}

[Atki 06]:

$$\Delta G = \Delta H_{\text{red}} - T \cdot \Delta S_{\text{red}} \tag{6.8}$$

Accordingly, the slope of the Ellingham diagrams correlates to ΔS_{red} and the intercept to ΔH_{red}, respectively. Keep in mind that Ellingham illustrate the oxidation reaction (oxidation with O_2). Hence, this enthalpy is negative. According to amount, this oxidation enthalpy equals the reduction enthalpy. To preserve clarity and not to introduce quantities that are only valid in this section, there will be no distinction between the two enthalpies.

Figure 6.9 presents the Ellingham diagram of pure ceria derived from several approaches:

- Equation 6.6 with parameters determined in this thesis
- Equation 6.6 with parameters reported by Bulfin et al. who fitted data of Panlener et al. [Panl 75, Bulf 13]
- FactSage calculations using the databases Fact53 and SGPSBase [Bale 02, Bale 09]

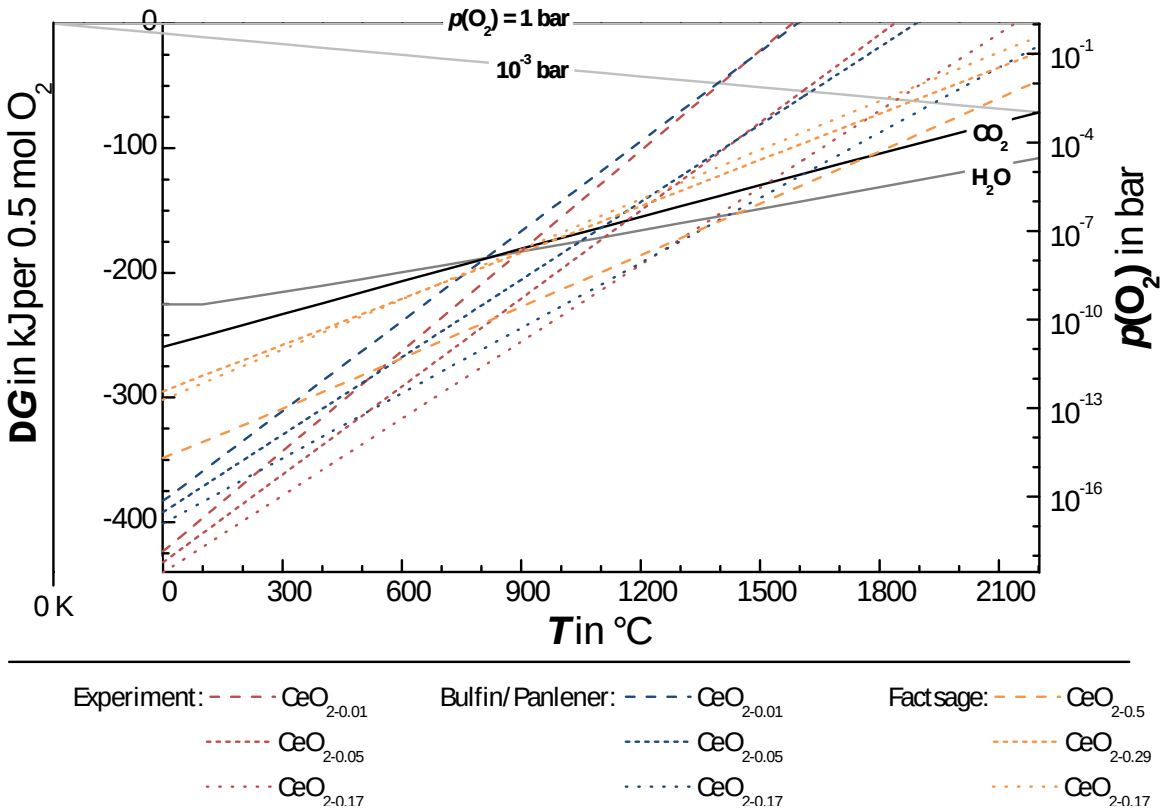

Figure 6.9: Ellingham diagram of pure ceria calculated with FactSage, derived from Bulfin and Panlener [Panl 75, Bulf 13] and from experiments performed in this thesis. Note that in FactSage only the ΔG of $\delta = 0.5; 0.29; 0.17$ are available, which differ from compositions of evaluated based on the experiments as well as based on Bulfin/Panlener. For instance, the $CeO_{2-0.17}$ line corresponds to the ΔG of the reaction $CeO_2 \rightleftharpoons CeO_{2-0.17} + {}^{0.17}/_{2}O_2$.

The red lines based on the experimental results of this thesis and the blue lines that based on the parameters of Bulfin et al. exhibit differences especially for low temperatures. This behavior corresponds to the fitting results plotted in figure 6.7. On the one hand, the red lines feature a higher slope and on the other hand a reduction enthalpy ΔH_{red}, which is larger. For conditions supposed to be feasible ($T_{red} \leq 1600°C$ and $p(O_2) \geq 10^{-5}$ bar), however, the deviation of the two approaches are sufficiently small. In contrast, the FactSage calculations deviates more significantly. The compositions available describe the thermodynamics of so-called long-range-order crystal structures such as Ce_6O_{11} and Ce_7O_{12}. These phases are referred to as β and $\delta\tau$, respectively [Trov 13]. The calculated ΔG solely base on theoretical considerations. Therefore, the involved data sets may not account for the non-stoichiometry of the crystal structure. This leads to slopes calculated by FactSage that are lower compared to the lines derived from the model approach. Nevertheless, for the reaction corresponding to an reduction extent of $\delta = 0.17$, the FactSage calculates similar ΔG for high partial pressures of oxygen $p(O_2) \geq 10^{-3}$ bar and/or high temperatures of $T_{red} \geq 1800°C$.

Figure 6.10 shows the Ellingham diagrams obtained for the investigated materials applying equation 6.6 with the parameters depicted in table 6.1.

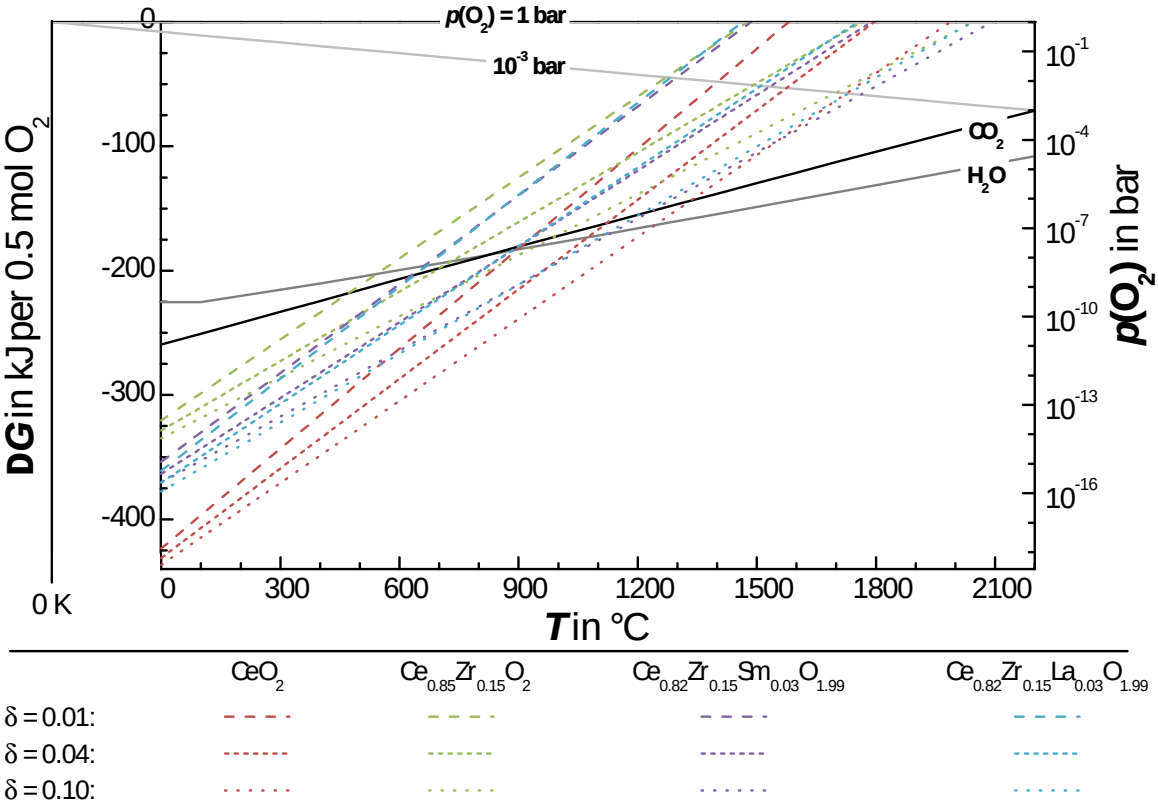

Figure 6.10: Ellingham diagram of pure ceria and doped ceria for several absolute reduction extents δ based on the experimental data of this thesis.

Two trends are observed:

- The intercept – ΔH_{red} – rather depends on the doping. Three different ranges of ΔH_{red} are identified: (1) CeO_2, (2) $Ce_{0.85}Zr_{0.15}O_2$ and (3) $Ce_{0.82}Zr_{0.15}RE_{0.03}O_{1.99}$. (RE = Sm, La)
- The slope – ΔS_{red} – rather depends on the reduction extent; the higher δ, the smaller the slope. As expected from figure 6.3, pure ceria features the highest increase with increasing temperature compared to the doped-materials.

For simplicity, in figure 6.11 only the ΔG lines of $\delta = 0.04$ are depicted. The reaction conditions necessary to obtain this reduction extent δ are still feasible. For instance, at a reasonable partial pressure of oxygen $p(O_2) = 10^{-3}$ bar, the reduction temperatures range between 1490°C and 1580°C. Such high temperatures are employed in recently published reactor concepts [Erma 13]. The major benefit from Ellingham diagrams is, on the one hand, to amplify the scope of the analysis concerning the impact of the doping on the reaction conditions T_{red} and $p(O_2)$ to obtain the same reduction extent. Through doping with 15% Zr, almost 100 K are so-called saved at $p(O_2) = 10^{-3}$ bar – at lower $p(O_2)$ even more. On the other hand, Ellingham diagrams may state, whether a material is able to split CO_2 or H_2O and the temperatures necessary, although the Ellingham diagrams

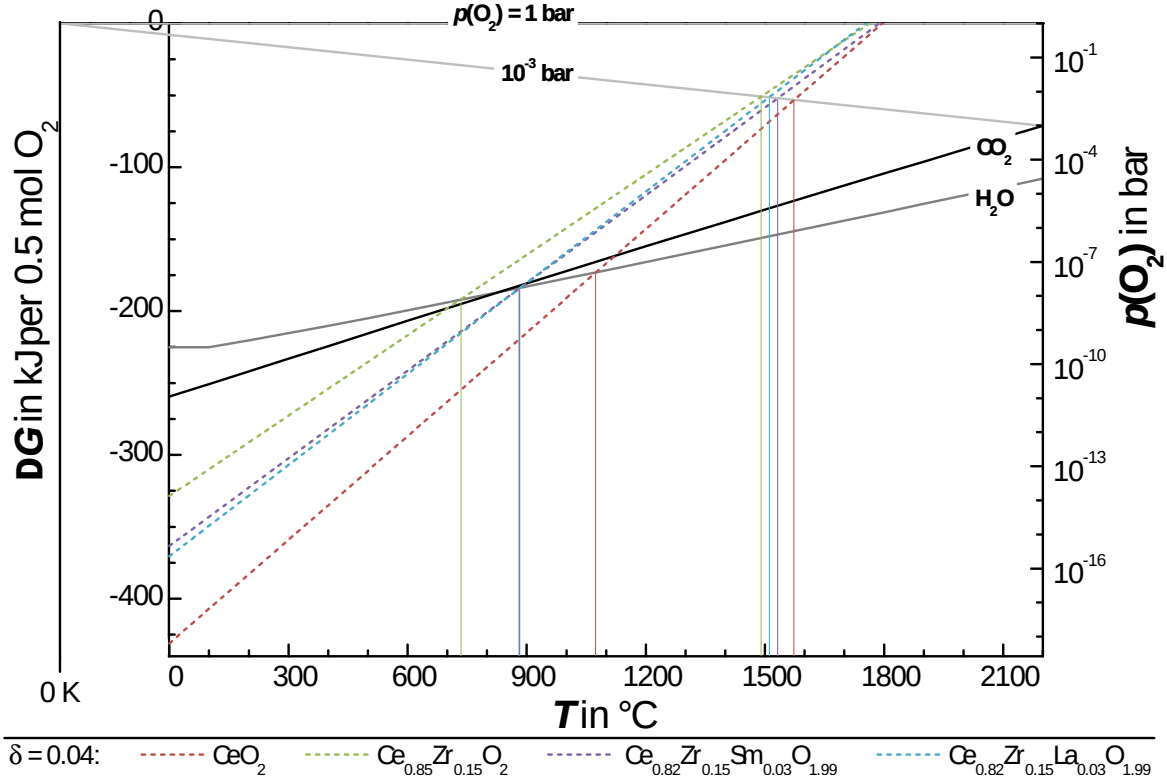

Figure 6.11: Ellingham diagram of pure ceria and doped ceria with a $\delta = 0.04$ based on experimental results of this thesis. The vertical lines shall exemplarily show how Ellingham diagrams are read.

solely base on experimental data of the reduction. This in particular is interesting in the case of water splitting, since its experimental realization is challenging. For instance, the employed thermobalance is not able to conduct both, reduction at these temperatures and subsequent water splitting. Keep in mind that the splitting reaction is by far more limited by kinetics, so that Ellingham diagrams may only provide an informative basis and should not be analyzed quantitatively regarding the splitting reactions. For instance, at a temperature of 300°C, $CeO_{2-0.04}$ is not capable to split water, although the line is below the H_2O-equilibria lines. Nevertheless, the Ellingham diagram show the qualitative impact of doping on the splitting reaction. The impact of doping on the splitting was already discussed in section 5.1.

6.2.2 Enthalpy and Entropy

According to equation 6.8, linear extrapolations of the Ellingham lines result in an intercept and a slope corresponding to the reduction enthalpy and entropy changes ΔH_{red} and ΔS_{red}, respectively. As recently discussed in literature, the dependence of reduction enthalpy ΔH_{red} on the reduction extent δ is crucial for the design of a reactor [Erma 13]. In figure 6.12, the ΔH_{red} for various δ in the range of $0.00002 \leq \delta \leq 0.2$ are depicted. The ΔH_{red} equals the ΔH_{mat} introduced in section 2.2.1, since the reduction involves no other enthalpy change than the one of the material.

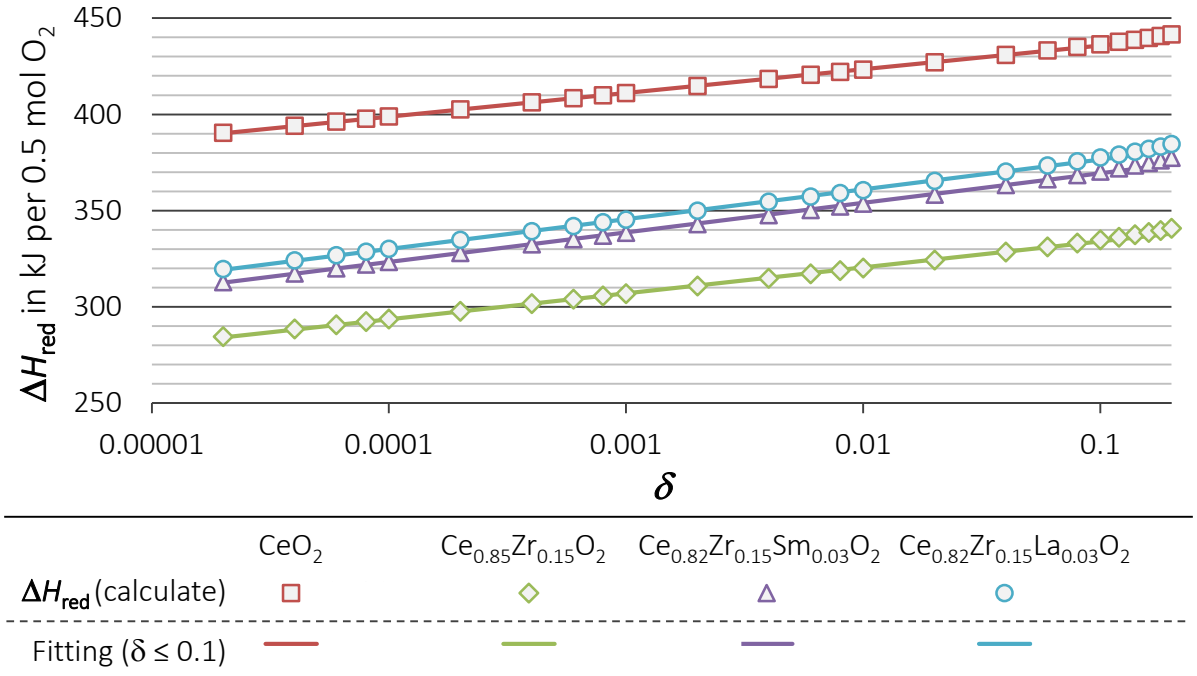

Figure 6.12: Comparison of the enthalpy change during reduction ΔH_{red} derived from Ellingham diagrams (intercept) versus the absolute redox extent δ. Dashed lines correspond to fittings of equation 6.9 for $\delta \leq 0.1$.

Generally, ΔH_{red} decreases with increasing δ. The constant slope in the logarithmical scale slightly changes for $\delta \geq 0.08$. Nevertheless, a simple two-parameter logarithmical approach to fit ΔH_{red} is reasonable:

$$\Delta H_{red} = a_H \ln \delta + A_H \tag{6.9}$$

The fitting parameters a_H and A_H calculated for $\delta \leq 0.1$ are presented in table 6.2.

Table 6.2: Parameters a_H and A_H of equation 6.6 calculated by least squares fitting of the ΔH_{red} data for $\delta \leq 0.1$ as presented in figures 6.12. The uncertainties denote the standard deviation and R^2 the coefficient of determination.

	a_H in kJ per 0.5 mol O_2	A_H in kJ per 0.5 mol O_2	R^2
CeO_2	5.359 ± 0.020	448.2 ± 0.1	0.9997
$Ce_{0.85}Zr_{0.15}O_2$	5.847 ± 0.026	347.3 ± 0.2	0.9996
$Ce_{0.825}Zr_{0.15}Sm_{0.025}O_{1.99}$	6.687 ± 0.031	384.8 ± 0.2	0.9996
$Ce_{0.825}Zr_{0.15}La_{0.025}O_{1.99}$	6.734 ± 0.031	392.1 ± 0.2	0.9996

Both, the slope a_H as well as intercept A_H significantly differ for all compositions. The fitting results will especially be beneficial for the first evaluation of the enhanced materials presented in section 7.1.

As mentioned in section 2.2.1, the thermochemical framework introduced by Meredig and Wolverton divide the entropy changes during reduction ΔS_{red} generally into two terms [Mere 09]:

$$\Delta S_{red} = \Delta S_{mat} + 0.5 S^{O_2}_{T_{red}} \tag{6.10}$$

here, ΔS_{mat} denotes the solid-state entropy difference between reduced and oxidized form of the material and $S^{O_2}_{T_{red}}$ the entropy of oxygen at the reduction temperature T_{red}. Due to the scale used in the Ellingham diagrams (kJ per 0.5 mol O_2), solely 0.5 of $S^{O_2}_{T_{red}}$ adds to ΔS_{red}.

In the following, ΔS_{mat} is assumed to be temperature independent, which is a reasonable assumption for ceria-based materials [Panl 75, Moge 00]. By contrast, for $S^{O_2}_{T_{red}}$, the temperature dependence must be considered due to its large influence. The molar entropy of 0.5 mol of O_2 ranges approximately from 110 to 130 JK^{-1} for temperatures between 900 to 1700°C. For a certain δ, $S^{O_2}_{T_{red}}$ is calculated at the temperature at which ΔG corresponding to this δ equals zero. The solid-state entropy difference ΔS_{mat} is now assessable. In figure 6.13, ΔS_{mat} versus the redox extent δ of the investigated materials is depicted.

Similar to the finding for the enthalpy change ΔH_{red}, the shape of ΔS_{mat} changes at

$\delta \approx 0.08$ and a simple two-parameter logarithmical approach was applied :

$$\Delta S_{mat} = a_S \ln(\delta) + A_S \tag{6.11}$$

The fitting parameters a_S, and A_S are presented in table 6.3. Due to limitations of the experimental data that are employed to derive the Ellingham diagrams and therewith ΔS_{mat}, the fitting is only performed for $\delta \leq 0.1$. Therewith, sufficiently high coefficients of determination R^2 were obtained. The solid lines in figure 6.13 illustrate the fittings.

Table 6.3: Parameters a_S and A_S of equation 6.11 calculated by least squares fitting of the difference in entropy ΔS_{mat} for $\delta \leq 0.1$ as presented in figures 6.13. The uncertainties denote the standard deviation and R^2 the coefficient of determination.

	a_S in JK^{-1} per 0.5 mol O_2	A_S in JK^{-1} per 0.5 mol O_2	R^2
CeO_2	-21.38 ± 0.19	37.1 ± 1.1	0.9993
$Ce_{0.85}Zr_{0.15}O_2$	-23.75 ± 0.28	-23.9 ± 1.6	0.9987
$Ce_{0.825}Zr_{0.15}Sm_{0.025}O_{1.99}$	-26.94 ± 0.32	-17.7 ± 1.8	0.9987
$Ce_{0.825}Zr_{0.15}La_{0.025}O_{1.99}$	-27.07 ± 0.32	-9.7 ± 1.8	0.9987

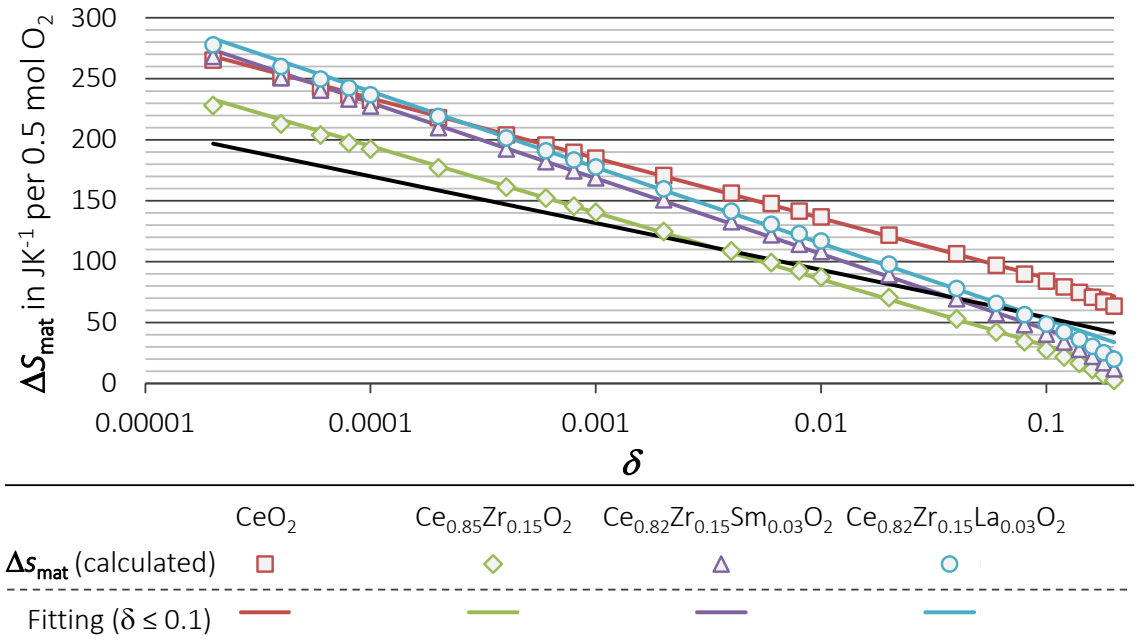

Figure 6.13: Solid-state entropy difference between reduced and oxidized form of the material ΔS_{mat} versus the absolute redox extent δ. Colored lines correspond to fittings of equation 6.11 for $\delta \leq 0.1$. The black line denotes the configuration entropy that is introduced in the following (equation 6.12).

For all materials, ΔS_{mat} decreases with increasing δ from values in the range of 225 - 280 JK^{-1} per 0.5 mol O_2 for $\delta = 0.00002$ to values close to 0 for $\delta = 0.2$. Pure ceria features the highest ΔS_{mat} for $\delta \geq 0.0001$ and the smallest decrease with increasing δ. Zirconia doping results in significant lower ΔS_{mat} of approximately $50 - 60$ JK^{-1} per 0.5 mol O_2. In between, trivalent-doped materials exhibit values of ΔS_{mat} similar to pure ceria for low δ and values similar to $Ce_{0.85}Zr_{0.15}O_2$ for large δ. Hence, the ΔS_{mat} decrease with increasing δ is more pronounced for trivalent-doped materials.

A reasonable explanation for the significant dependence of ΔS_{mat} on δ is found in the change of configuration entropy ΔS_{conf} during reduction due to the creation of vacancies. The molar configuration entropy is approximated by:

$$\Delta S_{conf} = n \cdot R \cdot (\delta \ln \delta + (1 - \delta) \ln (1 - \delta)) \tag{6.12}$$

R denotes the universal gas constant, n the number of possible arrangements in mol equaling the mewls of oxygen in the crystal structure (e.g. 2 for CeO_2) and δ the number of vacancies in mol, which is equal to the absolute reduction extent. A detailed derivation can be found elsewhere [Gott 98]. To compare the configuration entropy ΔS_{conf} with the ΔS_{mat} that is denoted for 0.5 mol of released O_2, ΔS_{conf} has to be scaled. A scaling factor of $1/\delta$ can be derived from equation 6.1. The configuration entropy ΔS_{conf} is illustrated in figure 6.13 (black line).

The amount of configuration entropy $1/\delta \cdot \Delta S_{conf}$ that comes along with the release of 0.5 mol O_2 differs from the entire solid-state entropy change ΔS_{mat}. This deviation is given by

$$\Delta S_{dev} = \Delta S_{mat} - 1/\delta \cdot \Delta S_{conf}. \tag{6.13}$$

and depicted versus δ in figure 6.14.

The deviation ΔS_{dev} is positive for small δ and decreases with increasing δ. It varies in number and shape for the materials. For almost all δ and compositions, pure ceria features the highest positive deviation. Positive ΔS_{dev} values imply that the configuration entropy ΔS_{conf} is not able to describe the entire entropy gain within the crystal structure during reduction. Vice versa, negative ΔS_{dev} values show an overestimation of the ΔS_{conf}. The origin of the deviation may lie in the uncertainties of the employed numbers ΔS_{mat} and ΔS_{conf}. The uncertainty of ΔS_{mat} strictly depends on the validity of the Ellingham diagrams, which is discussed in the appendix A.4. Accordingly, a relative uncertainty of 5% is assumed for the slope ΔS_{mat}. Hence, it is definitely too small to explain the significant differences between the four materials. Since the calculation of ΔS_{conf} bases on an ideal model approach and a mathematical approximation, the uncertainty cannot be quantitatively defined. However, it should be rather a systematical uncertainty that equally applies to all compositions and cannot explain the varying deviations of the materials.

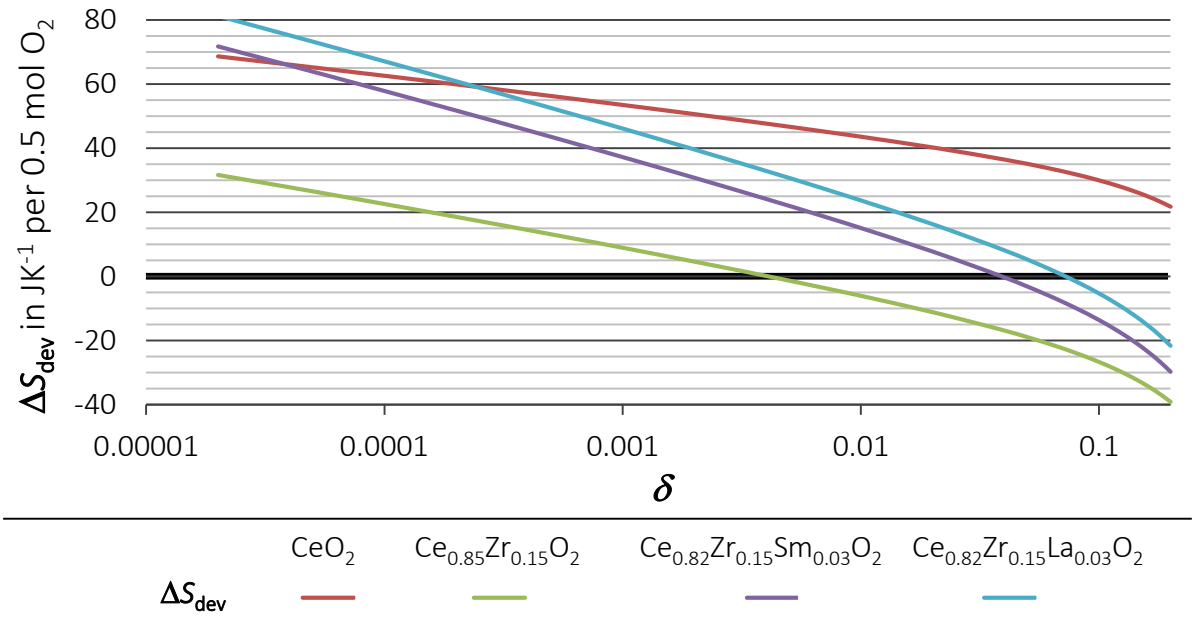

Figure 6.14: Difference in entropy ΔS_{dev} derived from equation 6.13 versus the absolute redox extent δ.

Assumed that the ΔS_{dev} of CeO_2 presents a systematical deviation, it could be applied as a correction of ΔS_{dev} of the other compositions. Simple subtraction yields ΔS_{dev} for the doped materials that are negative for almost all δ. Thus, the configuration entropy ΔS_{conf} is too large to correctly describe ΔS_{mat} (equation 6.12). This could be explained with the theory of solute vacancy pairs. In literature, some authors discuss a different distribution of vacancies in doped materials [Nowi 12]. Descriptively spoken, vacancy pairs or even clusters are created due to influences of the dopant on the crystal structure or even smaller scale relations. Thereby, the configuration entropy ΔS_{conf} may decrease due to the smaller number of possible arrangements n. In theory, this explains the smaller values of ΔS_{mat} for the doped compositions compared to pure ceria.

6.3 Conclusions

This chapter investigated the reduction extent δ in equilibrium depending on the temperatures T_{red} and partial pressures of oxygen $p(O_2)$. Four dense pellets with the compositions CeO_2, $Ce_{0.85}Zr_{0.15}O_2$, $Ce_{0.825}Zr_{0.15}Sm_{0.025}O_{1.99}$ and $Ce_{0.825}Zr_{0.15}La_{0.025}O_{1.99}$ were subjected to TGA experiments. The employed reduction temperatures T_{red} ranged from 1300°C to 1450°C in the case of CeO_2 and 1100°C to 1450°C in the case of the other materials; the partial pressures of oxygen $p(O_2)$ ranged from 27 Pa to 1270 Pa.

As expected, the equilibrium reducibility increased with increasing reduction temperature T_{red} and decreasing partial pressure of oxygen $p(O_2)$. At the best reduction conditions, $Ce_{0.85}Zr_{0.15}O_2$ released $0.124 \pm 0.003\,mmol_{O_2} \cdot g_{mat}^{-1}$, closely followed by the rare-earth doped materials. At the same conditions, CeO_2 featured yields of $0.063 \pm 0.003\,mmol_{O_2} \cdot g_{mat}^{-1}$. Comparing the specific oxygen yields $n_m(O_2)$ for two temperatures that are different by approximately 100 K, pure ceria featured relative improvements of up to 200%, whereas the doped materials released 70 to 120% more oxygen per gram. Decreasing the partial pressures of oxygen $p(O_2)$ from 1270 to 125 Pa led to relative improvements of $n_m(O_2)$ of 40 to 60%, trending to decrease with increasing temperature. Comparing the result $p(O_2)$=27 Pa and $p(O_2)$=125 Pa, improvements of 20% to 50% were observed exhibiting the same temperature dependence. The enhancement of the specific yield due to doping significantly increased with decreasing T_{red} and increasing $p(O_2)$ ranging from 60 to 250%. Taking into account this trend, these improvements are in concert with the improvements of 30 to 50% observed in powder experiments at a lower $p(O_2)$.

To evaluate a function $\delta(T, p(O_2))$ that describes the reducibility depending on the reaction conditions, an Arrhenius-type model was applied similar to one recently published [Bulf 13]. Besides prefactor A, activation energy E, and temperature T, the reduction depends on the amount of reducible cerium $(\delta - \delta_{max})$; the oxidation on the partial pressure of oxygen $p(O_2)$ and the reduction extent δ. In the equilibrium, in which the reduction equals the oxidation reaction, this approach yielded a function $\delta(T, p(O_2))$. Least square fitting resulted in parameters matching the data sufficiently. The equilibrium data solely allowed the calculation of the difference in the activation energy $\Delta E = E_{red} - E_{ox}$ and the relation of frequency factors $\frac{A_{red}}{A_{ox}}$ of the reduction and oxidation reaction. Hence, the fitting did not provide absolute changes in the activation energy of reduction or oxidation as a result of the doping. Nevertheless, the function $\delta(T, p(O_2))$ is crucial for the first evaluation of the incorporation of the new material in a reactor design.

With the aid of the function $\delta(T, p(O_2))$, the Gibbs energy ΔG was assessable. Therewith, Ellingham diagrams were constructed, which comprehensively illustrate the relation of reduction temperature T_{red} and partial pressure of oxygen $p(O_2)$. Moreover, Ellingham diagrams state, whether a material is able to split water and/or CO_2 and provide basic information concerning the splitting conditions. Due to thermodynamical relations, Elling-

ham diagrams also provide the enthalpy and entropy changes ΔH_{red} and ΔS_{red} during reduction. Fitting functions were established that describe the dependence of ΔH_{red} and ΔS_{red} on the reduction extent δ. The reduction enthalpy ΔH_{red} is of major interest for the design of reactors. The dependence of the reduction entropy ΔS_{red} on δ could be explained with the configuration entropy ΔS_{conf} generated due to the creation of vacancies. The deviation of ΔS_{conf} and ΔS_{red} depends on the doping, which can be attributed to solute vacancy pairs that reduce the share of ΔS_{conf}.

In short, the quintessence of this chapter is as follows:

Under worse reaction conditions (lower T_{red} and higher $p(O_2)$), the enhancement due to doping is more pronounced. The specific oxygen yields featured improvements of up to 200% compared to pure ceria.

A reaction model was employed that sufficiently fits the experimental data. The obtained function is able to describe the dependence of the reducibility on the reduction conditions.

Ellingham diagrams of the investigated materials were constructed illustrating fundamental relations of the reducibility and splitting ability of the materials.

Enthalpy and entropy of the reduction that are crucial to further evaluate the material were determined and fitted with respect to the reduction extent.

Starting from experiments in the thermobalance under varying reduction conditions, the fundamental thermodynamics of the materials were obtained. This "tool" developed in this chapter is of major interest for the evaluation of redox materials for the thermochemical fuel production.

7 Potential of Ceria-based Materials for Solar Fuel Production

The previous chapters revealed the applicability of ceria-based materials in thermochemical cycles producing solar fuels. Doping enhances the reducibility regarding both, the reaction conditions as well as the oxygen yields. Nevertheless, it remains unclear to which extent the doping of ceria may effect the overall efficiency of the process.

This chapter evaluates the potential of the doped materials to overcome the barriers to commercial success of TCCs. In the first section, a recently published reactor model is adapted to determine the solar-to-fuel efficiencies. As material-specific input data, the relations of the redox extent and the reduction enthalpy derived in the previous chapter are employed. As an expansion to the model, realistic efficiencies of the auxiliary unit are implemented and the application on a solar tower considered. In the second section, a parametric study is carried out that varies the partial pressure of oxygen, the reduction temperature and the heat recuperator effectiveness. Therewith, the doped materials are ranked with regard to pure ceria as well as to the process conditions. Within the discussion, potential process limitations are discovered. This chapter concludes with summarizing the main findings as well as discussing the discovered process limitations in the light of their technical implications.

Contents

7.1 The solar-to-fuel Efficiency

To reasonably assess the potential of the materials investigated in this thesis, model calculations that encompass the energetics of the entire process are ineluctable. Therewith, material-specific properties such as reaction temperatures and partial pressures of oxygen are analyzed regarding their effect on the overall process efficiency. A first idea of the process and its main components is given in section 2.1. Every model contains boundary conditions that depend on the employed concentrating system, reactor design and auxiliary unit, resulting in manifold ways to estimate the solar-to-fuel efficiency $\eta_{\text{solar to fuel}}$ [Mill 07, Furl 12b, Bade 13, Lapp 13]. Also, the depth of the analysis varies in a wide range from basic thermodynamical calculations to complex, dynamic simulations that consider real solar data to obtain realistic efficiencies on an annual basis [Lang 14].

Since it is beyond the means of this thesis to tackle the numerous options involved in the design of a process model and/or reactor design, a model is adapted that was recently published by Ermanoski et al. [Erma 13]. This model evaluates energetically the annual efficiency of a solar reactor operated in a dish concept with a secondary mirror. It employs only thermodynamical data and neglects kinetic limitations. This model is selected due to the following reasons. (1) The model applies ceria as the redox material. The published results base on functions to calculate the reduction extent $\delta\,(T_{\text{red}},\ p(O_2))$ and the reduction enthalpy $\Delta H_{\text{red}}(\delta)$, enabling the straightforward implementation of the functions obtained in chapter 6. (2) The design bases on continuously moving particles; a technology that recently drew great attention in the field of high-temperature reactors for concentrated solar power [Tesc 13, Wu 13]. (3) As mentioned in section 2.1, fundamental analysis emphasized the significance to include an efficient heat recuperation. In this regard, the use of a heat exchanger based on particles, which was recently published, represents a promising approach to instantiate efficient heat recuperation [Bren 14, Feli 14]. (4) The process applies vacuum pumping during reduction instead of gas sweeping, which may lead to significantly higher efficiencies [Erma 13].

The fundamental relations of this model are applicable to evaluate other continuously operating process designs featuring separate chambers for reduction and oxidation with a heat recuperation in between and vacuum pumping during reduction. Subsequent to the evaluation of the results for pure ceria obtained in chapter 6, the model is expanded with an approach to consider the pump efficiency more realistically. Besides the boundary conditions of the dish concept, which was suggested by Ermanoski et al., the boundary conditions of the solar-tower concept are also included. Basing on this expanded model, a parametric study employing $\delta\,(T_{\text{red}},\ p(O_2))$ and $\Delta H_{\text{red}}(\delta)$ relations obtained for CeO_2 and the doped materials is carried out to determine the solar-to-fuel efficiencies $\eta_{\text{solar to fuel}}$ at varying partial pressure of $p(O_2)$, reduction temperatures T_{red} and heat recuperation effectiveness ϵ_{HR}. Therewith, the enhancement of the efficiency of the materials with re-

spect to ceria, as well as the efficiencies concerning the two concepts, dish and tower, are discussed.

7.1.1 Model Description

In the following, the essential equations are introduced to assess the solar-to-fuel efficiency adapted from the model of Ermanoski et al. [Erma 13]. The term "fuel" refers to either pure hydrogen featuring the energy content of its higher heating value E_{H_2} or carbon monoxide with an energy content of its higher heating value E_{CO}. The oxidation is carried out at the temperature T_{ox} and is assumed to be complete. Hence, per 0.5 mol of O_2 released, exactly one mol of fuel is produced, neglecting incomplete reoxidation due to poor kinetics of the oxidation. Problems resulting from this assumption might be technically solved, because the reactions are realized in two chambers. The reduction is carried out at the temperature T_{red} and the partial pressure of oxygen $p(O_2)$. The parameters used for the calculations that are subjected to the parametric study are referred to as input parameters. The other, so-called fixed parameters are summarized in table 7.1. They are derived from [Erma 13]. The calculations were carried out using the software Engineering Equation Solver EES (F-Chart Software).

Table 7.1: Fixed parameters used for the calculations described in the following.

fixed parameter	label	value
direct normal irradiance	DNI	1 kW·m^{-2}
annual optical efficiency dish	η_{opt}^{dish}	83.75%
annual optical efficiency tower	η_{opt}^{tower}	60%
concentration ratio dish	C^{dish}	5000
concentration ratio tower	C^{tower}	2000
heat-to-electricity efficiency	$\eta_{heat\ to\ elec}$	40%
higher heating value hydrogen	E_{H_2}	286 kJ·mol^{-1}
oxidation temperature	T_{ox}	1100°C

Essential Equations

The solar-to-fuel efficiency to produce fuel with the solar power P_{sol} is given by

$$\eta_{solar\ to\ fuel} = \dot{n}_{fuel} \frac{E_{fuel}}{P_{sol}} \tag{7.1}$$

with $\dot{n}_{fuel}$ as the molar fuel production rate of the process. $\dot{n}_{fuel}$ is related to the oxygen release rate during reduction by $\dot{n}_{fuel} = 0.5\dot{n}_{O_2}$. P_{sol} is the solar direct normal irradiance DNI times the area A_{sol} of the concentrating system times the concentration ratio C:

$P_{sol} = DNI \cdot A_{sol} \cdot C$. Due to the selection of the dish concept, ratios as high as $C^{dish} = 5000$ are assumed. With an optical efficiency η_{opt}, the thermal power P_{th}, which accounts for heat flux usable for the reaction, is given by

$$P_{th} = \eta_{opt} \cdot P_{sol} - P_{cond} - P_{rera} - P_{conv} \tag{7.2}$$

The optical efficiency η_{opt} combines on an annual basis all important factors involved along the way from solar irradiation to the power that enters the reactor, such as mirror reflectivity, window transmission and solar intercept. Ermanoski supposed an optical efficiency for the dish-concept of $\eta_{opt}^{dish} = 83.75\%$. P_{cond} denotes the thermal losses due to conduction, which are neglected, since perfect insulation of the reactor is assumed. P_{rera} quantifies the power that is lost due to radiation losses and is calculated according to the Stefan-Boltzmann law

$$P_{rera} = \varepsilon \sigma A_{rec} T^4 \tag{7.3}$$

where ε denotes the emissivity of the cavity, σ denotes the Stefan–Boltzmann constant, A_{rec} the aperture of the receiver and T the temperature of the reactor. T equals the reduction temperature T_{red}. P_{conv} denotes the thermal losses due to convection, implying mainly the loss through the window of the reactor. However, compared to the radiation losses this is a minor contribution and can be neglected [Lang 14].

The molar fuel production rate is

$$\dot{n}_{fuel} = \frac{P_{th}}{Q} \tag{7.4}$$

here, Q accounts for the heat required for the production of one mol of fuel. According to this relation, the reactor efficiency is given by $\eta_{\text{thermal to fuel}} = \dot{n}_{fuel} \frac{E_{fuel}}{P_{th}}$. The heat Q is given by

$$Q = \Delta H_{red} + Q_{mat} + E_{aux} \tag{7.5}$$

where ΔH_{red} denotes the reduction enthalpy, Q_{mat} the sensible heat required for heating the redox material from T_{ox} to T_{red}, and E_{aux} the energy required for all other reactor needs. ΔH_{red} is calculated depending on δ with the relation established in chapter 6:

$$\Delta H_{red}(\delta) = a_H \ln \delta + A_H \tag{7.6}$$

The fitting parameters a_H and A_H for each of the four investigated materials are provided in table 6.2 on page 100. Assuming heat recuperation with an effectiveness ε_{HR}, Q_{mat} is calculated with

$$Q_{mat} = \frac{c_{mat}}{\delta}(T_{red} - T_{ox}) \cdot (1 - \varepsilon_{hr}) \tag{7.7}$$

where c_{mat} denotes the molar heat capacity of the redox material, which is assumed on the basis of values for pure ceria. The same c_{mat} is assumed for pure ceria as well as for the doped materials independent of the temperature. The auxiliary energy E_{aux} is given

by

$$E_{\text{aux}} = Q_{\text{H}_2\text{O},\,\text{CO}_2} + Q_{\text{pump}} + Q_{\text{mech}} - Q_{\text{O}_2} - Q_{\text{mat}} - Q_{\text{ox}}. \tag{7.8}$$

It encompasses, on the one hand, $Q_{\text{H}_2\text{O};\,\text{CO}_2}$ corresponding to the needs for heating the reactants CO_2 or H_2O, the heat equivalent for pumping the products from both chambers Q_{pump} and the heat equivalent for the mechanical work to move the redox material Q_{mech}. On the other hand, the negative terms of E_{aux} include the heat of the oxygen output stream Q_{O_2}, the sensible heat of the material Q_{mat} that has to be removed before oxidation and the heat released in the exothermic oxidation $Q_{\text{ox}} = \Delta H_{\text{red}} - E_{\text{fuel}}$. Note that negative results of E_{aux}, corresponding to unneeded waste heat, are excluded from calculations. Q_{mat} and Q_{ox} are available from the product gas stream leaving the oxidation chamber (either mixes of H_2O-H_2 or CO_2-CO). Considering a gas-gas heat recovery effectiveness of 95%, the heat $Q_{\text{H}_2\text{O},\,\text{CO}_2}$ required for heating the reactants is negligible small. Q_{mech} and Q_{O_2} are minor contributions compared to the other quantities and are neglected. The fraction of Q_{pump} consumed to pump the reacting gases through the oxidation chamber can also be neglected, when operated at pressures slightly higher than 1 bar. The major fraction of Q_{pump} is ascribed to the isothermal pumping work $W_{\text{pump}}^{\text{O}_2}$ for the oxygen stream, that is

$$W_{\text{pump}} = n_{\text{O}_2} R T_{\text{pump}} \cdot \ln \frac{p_0}{p\,(\text{O}_2)} \tag{7.9}$$

where $n_{\text{O}_2} = 0.5 n_{\text{fuel}} = 0.5$ mol, R denotes the universal gas constant, T_{pump} the pumping temperature, which is assumed to be $T_0 = 25°\text{C}$, and p_0 the standard atmospheric pressure of $p_0 = 101325$ Pa. The heat equivalent Q_{pump} of the pumping work W_{pump} is given by

$$Q_{\text{pump}} = \frac{W_{\text{pump}}}{\eta_{\text{heat to elec}} \cdot \eta_{\text{elec to pump}}} \tag{7.10}$$

where $\eta_{\text{heat to elec}}$ denotes the efficiency to convert heat into electricity and $\eta_{\text{elec to pump}}$ the efficiency to convert electricity into pumping work. Ermanoski et al. assumed the pumping efficiency constant with $\eta_{\text{elec to pump}}^{\text{Ermanoski}} = 40\%$ and hence, to be independent of the obtained pressure. In other words, the pumping efficiency to pull a vacuum up to 0.1 bar equals the efficiency to pull a vacuum to, for instance, up to 10^{-6} bar. This assumption is more than doubtful, as discussed in the following subsection.

The last equation needed for this model is the reduction extent δ with respect to the reduction temperature T_{red} and the partial pressure of oxygen $p(\text{O}_2)$ derived in chapter 6:

$$\delta\,(T_{\text{red}},\, p(\text{O}_2)) = \frac{\delta_{\max} \cdot \frac{A_{red}}{A_{ox}} \cdot p^{-n}(\text{O}_2) \cdot \exp\left(-\frac{\Delta E}{RT}\right)}{1 + \frac{A_{red}}{A_{ox}} \cdot p^{-n}(\text{O}_2) \cdot \exp\left(-\frac{\Delta E}{RT}\right)}. \tag{7.11}$$

The fitting parameters $\frac{A_{red}}{A_{ox}}$, ΔE, and n obtained for the investigated materials are provided in table 6.1 on page 93.

Results

In a first attempt, the model employs the same input parameters as it was published by Ermanoski et al.. Hence, a concentration ratio of $C^{\text{dish}} = 5000$, an annual optical efficiency of $\eta_{\text{opt}}^{\text{dish}} = 83.75\%$, and a reduction temperature of $T_{\text{red}} = 1500°\text{C}$ are assumed for the production of hydrogen with $E_{\text{fuel}} = E_{\text{H}_2}$. Figure 7.1 displays the results for heat recuperation effectiveness ε_{HR} of 50 and 75% of pure ceria with regard to the relations for δ and ΔH_{red} obtained in this thesis with the ones published by Ermanoski et al. The results based on the relations of this thesis yield slightly higher solar-to-fuel efficiencies $\eta_{\text{solar to fuel}}$ for higher $p(\text{O}_2)$, whereas for low $p(\text{O}_2)$, Ermanoski et al. determines slightly higher $\eta_{\text{solar to fuel}}$. The deviations in $\eta_{\text{solar to fuel}}$ correlate with deviations in the redox extent δ. The rationale behind is found in the different experimental data that Ermanoski employed to derive the relations for δ. Apart from that, the results show sufficient agreement.

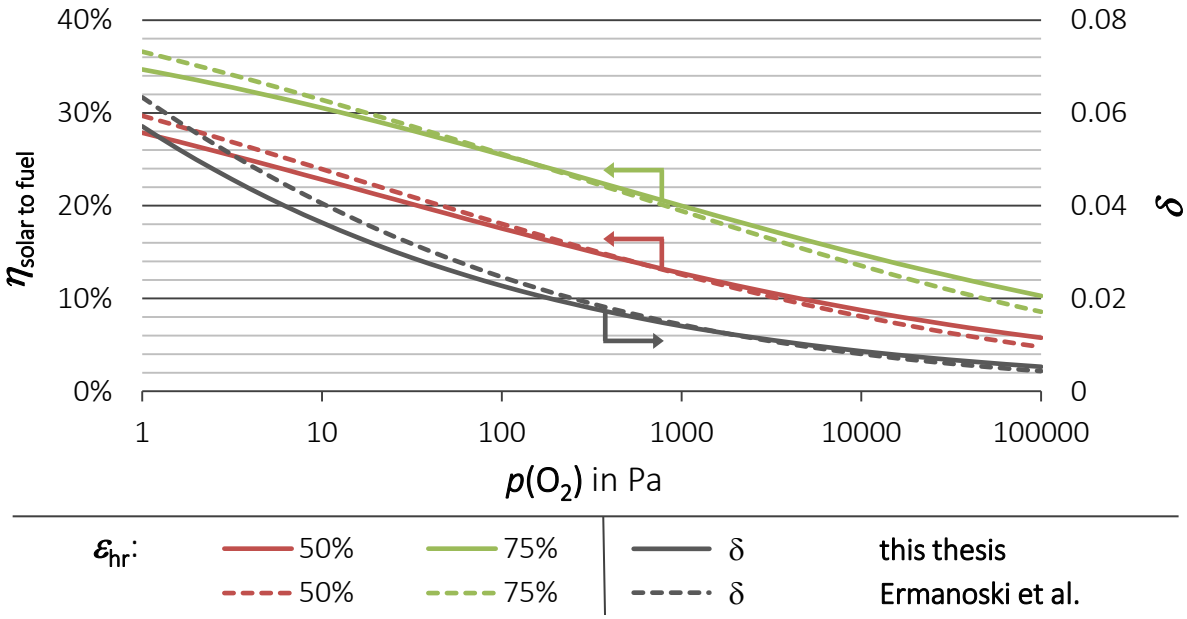

Figure 7.1: Results for pure ceria based on the reactor model described in the text. Solid lines display calculations employing the relations for δ and ΔH_{red} derived in chapter 6. Dashed lines are calculated with relations presented by Ermanoski et al. [Erma 13].

7.1.2 Expansion of the Model

7.1.2.1 Realistic Vacuum Pump Efficiency

As aforementioned, Ermanoski et al. suggest a constant electricity-to-pumping efficiency $\eta_{\text{elec to pump}}^{\text{Ermanoski}}$ independent on the pressure reached within the reduction chamber. In the model, the reached pressure corresponds to the partial pressure of oxygen $p(\text{O}_2)$. This approach seems incorrect, since it neglects the impact of random leakage on a pumping

system, which increases inevitably, when the vacuum pressure decreases. Recently, Bulfin et al. reported a relation that accounts for this effect [Bulf 15]. They studied the efficiency characteristics of various commercially available vacuum pumps and derived

$$\eta^{\text{Felinks}}_{\text{elec to pump}} = 0.0104 \cdot p(O_2)^{0.3848} \tag{7.12}$$

Note that the $\eta^{\text{Felinks}}_{\text{elec to pump}}$ is limited to a maximum value of 80%. Figure 7.2 presents $\eta_{\text{solar to fuel}}$ for pure ceria employing the electricity-to-pumping efficiency $\eta^{\text{Felinks}}_{\text{elec to pump}}$ compared to results employing the constant efficiency of 40%. $\eta^{\text{Felinks}}_{\text{elec to pump}}$ displays a double logarithmical shape and increases with increasing $p(O_2)$. For high $p(O_2)$, this dependency on $p(O_2)$ leads to $\eta_{\text{solar to fuel}}$ for the various ε_{hr} that are similar to the ones calculated by Ermanoski et al. At a certain partial pressure, however, the declining pump efficiency begins to dominate the process efficiency $\eta_{\text{solar to fuel}}$ and the shape changes. This partial pressure corresponds to the maximum efficiency $\eta^{\text{max}}_{\text{solar to fuel}}$ of the studied parametric set. Analogously, an optimal partial pressure of oxygen $p^{\text{opt}}(O_2)$ is defined that correlates with $\eta^{\text{max}}_{\text{solar to fuel}}$. $p^{\text{opt}}(O_2)$ decreases with decreasing ε_{hr}. Both, the maximum efficiency $\eta^{\text{max}}_{\text{solar to fuel}}$ and the optimal partial pressure of oxygen $p^{\text{opt}}(O_2)$ serve as characteristic numbers to compare variations of the model input parameters ε_{hr} and T_{red}.

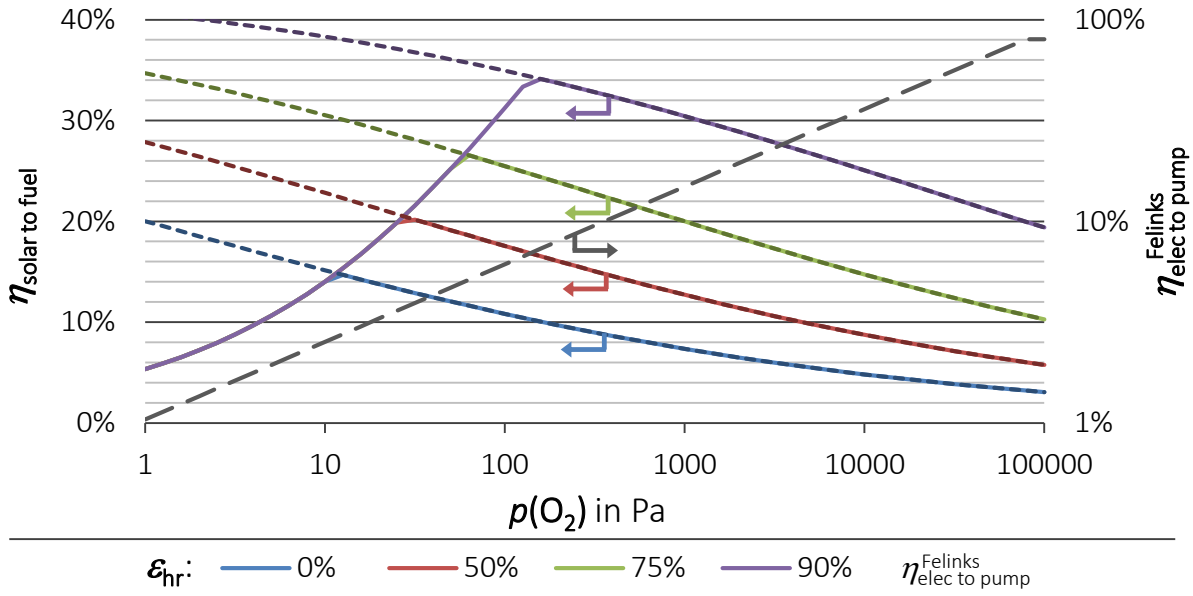

Figure 7.2: Solar-to-fuel efficiency $\eta_{\text{solar to fuel}}$ based on Ermanoski pump efficiency (dashed colored lines) and $\eta_{\text{solar to fuel}}$ based on Felinks pump efficiency (solid colored lines) of CeO_2 versus the partial pressure of oxygen $p(O_2)$ at a reduction temperature T_{red}= 1500°C and varying heat recuperator effectiveness ε_{hr}. Electricity to pumping work efficiency $\eta^{\text{Felinks}}_{\text{elec to pump}}$ (gray dashed line).

7.1.2.2 Solar Tower System

Concerning the technical realization, it seems more than challenging to implement a reactor containing as many various parts into a solar dish as the reactor that was suggested by Ermanoski et al. Dish concepts limit the space as well as the weight of the reactors. Furthermore, the reactors need to accommodate variable orientations relative to gravity. Taking these limitations into account as well as the importance of a potential scalability of the process, central receiver systems are the alternative to be considered [Kolb 08]. They offer much lower limitations of space compared to dishes and do not change the orientation of the receiver during operation. In addition, they allow for potential scalability. Basically, such systems, in the following referred to as tower, consist of a field of two-axis tracking heliostats that focus the sunlight onto a receiver mounted on the top of a tower [Rome 07]. Compared to the dish, the tower exhibits lower concentration ratios C as well as, in general, lower optical efficiencies η_{opt} [Kolb 08]. Nevertheless, since the technical advantages are as convincing, the tower system might be considered as the more realistic approach to implement TCCs. Therefore, the expanded process model considers both, the dish and the tower system. Typically, the concentration ratios of a solar tower range from 200 to 1000, which can be further enhanced by the incorporation of non-imaging secondary concentrators [Rome 12]. For the following calculations, an annual optical efficiency $\eta_{\text{opt}}^{\text{tower}} = 60\%$ and a solar concentration ratio $C^{\text{tower}} = 2000$ are supposed for the tower.

Figure 7.3 illustrates the impact of the two systems on $\eta_{\text{solar to fuel}}$ for pure ceria at a reduction temperature of $T_{\text{red}} = 1500°\text{C}$. At this temperature, the tower system features efficiencies that are approximately only half as high due to the lower $\eta_{\text{opt}} = 60\%$ and lower C^{tower}. The relative impact of ε_{hr} on $\eta_{\text{solar to fuel}}$ is similar. For each ε_{hr}, the optimal partial pressure of oxygen $p(O_2)$ is independent of the two systems, because the changes in η_{opt} and C do not effect the reactor efficiency $\eta_{\text{thermal to fuel}}$. Also, the reduction extent δ is the same for both systems, since it only depends on T_{red} and $p(O_2)$.

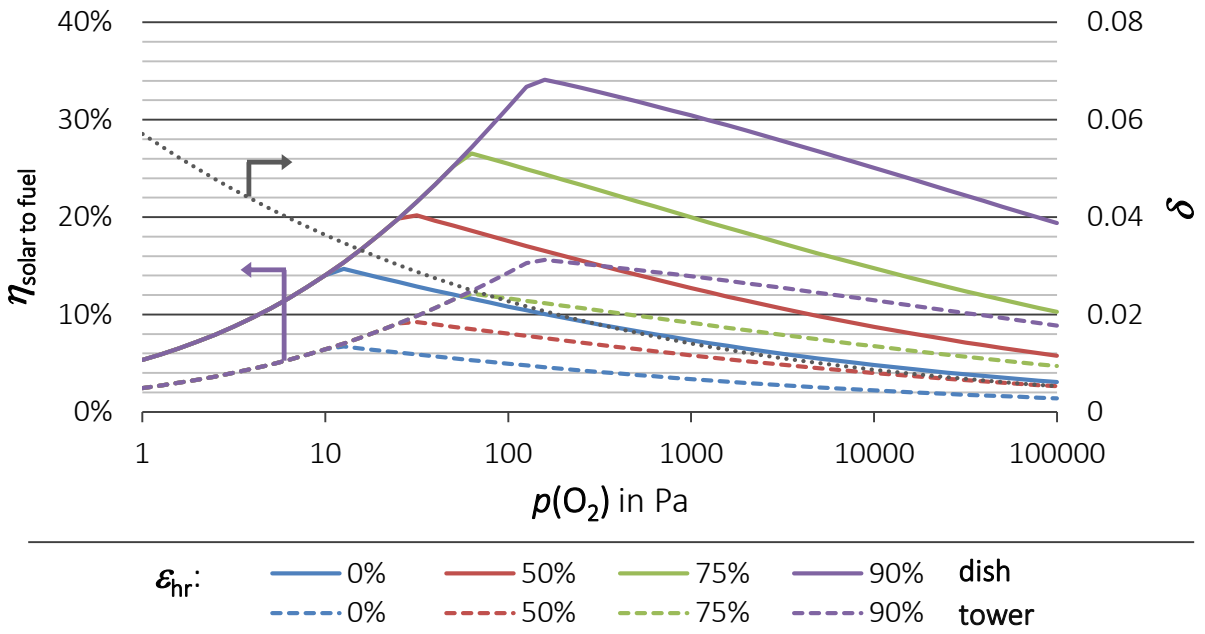

Figure 7.3: Solar-to-fuel efficiency $\eta_{solar\ to\ fuel}$ (colored lines) and reduction extent δ (gray dotted line) of CeO_2 at T_{red}= 1500°C and varying ε_{hr} versus the partial pressure of oxygen $p(O_2)$. Solid lines represent the dis, dashed lines the tower system.

7.2 Influence of Doping on the Efficiency

7.2.1 Results

The following section aims to evaluate the solar-to-fuel efficiencies $\eta_{solar\ to\ fuel}$ of the two systems, dish and tower, to produce hydrogen ($E_{fuel} = E_{H_2}$) with respect to

- the input parameters: the reduction temperature T_{red}, heat recuperator efficiency ε_{hr} and the partial pressure of oxygen $p(O_2)$. T_{red} is varied between 1200°C and 1500°C, since this range is covered from experimental data obtained in chapter 6. ε_{hr} is studied in the range of 0% to 90% and $p(O_2)$ between 1 and 100.000 Pa which is equivalent to 10^{-5} and 1 bar.
- the various compositions investigated: CeO_2, $Ce_{0.85}Zr_{0.15}O_2$, $Ce_{0.825}Zr_{0.15}Sm_{0.025}O_{1.99}$ and $Ce_{0.825}Zr_{0.15}La_{0.025}O_{1.99}$.

Exemplarily, in figures 7.4 and 7.5, the results of the parametric study for $Ce_{0.85}Zr_{0.15}O_2$ applying a dish are depicted. Figure 7.4 shows the efficiencies $\eta_{solar\ to\ fuel}$ of $Ce_{0.85}Zr_{0.15}O_2$ for varying ε_{hr} at T_{red} = 1500°C. For ε_{hr} = 90% in the dish, $\eta^{max}_{solar\ to\ fuel}$ = 46 % is reached, which corresponds to an increase of 12 percentage points, compared to pure ceria. This maximum efficiency is achieved at an even higher $p^{opt}(O_2)$ = 500 Pa instead of $p^{opt}(O_2)$ = 160 Pa observed for pure ceria.

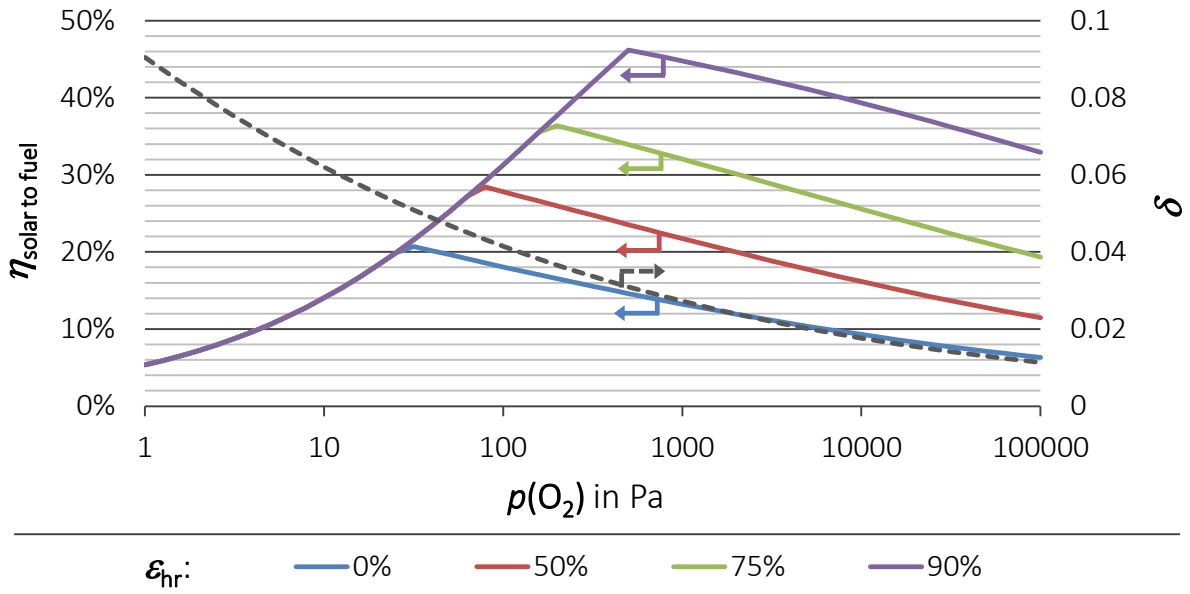

Figure 7.4: Solar-to-fuel efficiency $\eta_{solar\ to\ fuel}$ (solid lines) and reduction extent δ (dashed lines) of $Ce_{0.85}Zr_{0.15}O_2$. Derived from the expanded reactor model for the dish concept at T_{red}= 1500°C and varying ε_{hr}.

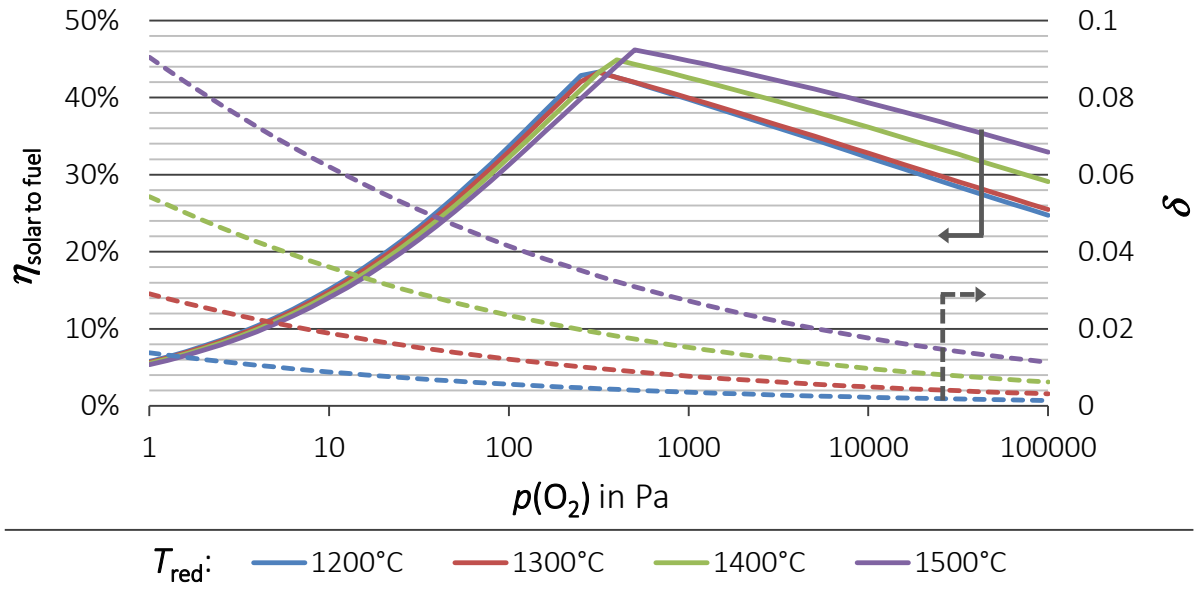

Figure 7.5: Solar-to-fuel efficiency $\eta_{solar\ to\ fuel}$ (solid lines) and reduction extent δ (dashed lines) of $Ce_{0.85}Zr_{0.15}O_2$. Derived from the expanded reactor model applying a dish at ε_{hr} = 90% and varying T_{red}.

Figure 7.5 indicates the dependency of $\eta_{solar\ to\ fuel}$ and δ on the reduction temperature T_{red}. Varying T_{red} leads to a deviation of $\eta_{solar\ to\ fuel}$ not only for $p(O_2) > p^{opt}(O_2)$, as it is observed for variation in ε_{hr}, but also for smaller $p(O_2)$. The maximum efficiency $\eta^{max}_{solar\ to\ fuel}$, however, only slightly varies as well as $p^{opt}(O_2)$. The positive finding that the efficiency $\eta^{max}_{solar\ to\ fuel}$ is somehow independent of the reduction temperature T_{red} is further discussed in the following.

7.2.2 Discussion

Figure 7.6 illustrates the impact of doping, the reduction temperature T_{red} and the heat recuperator effectiveness ε_{hr} on $\eta^{max}_{solar\ to\ fuel}$ in both systems, dish and tower. Concerning the impact of doping, the enhancement of the efficiency is significant. As expected from

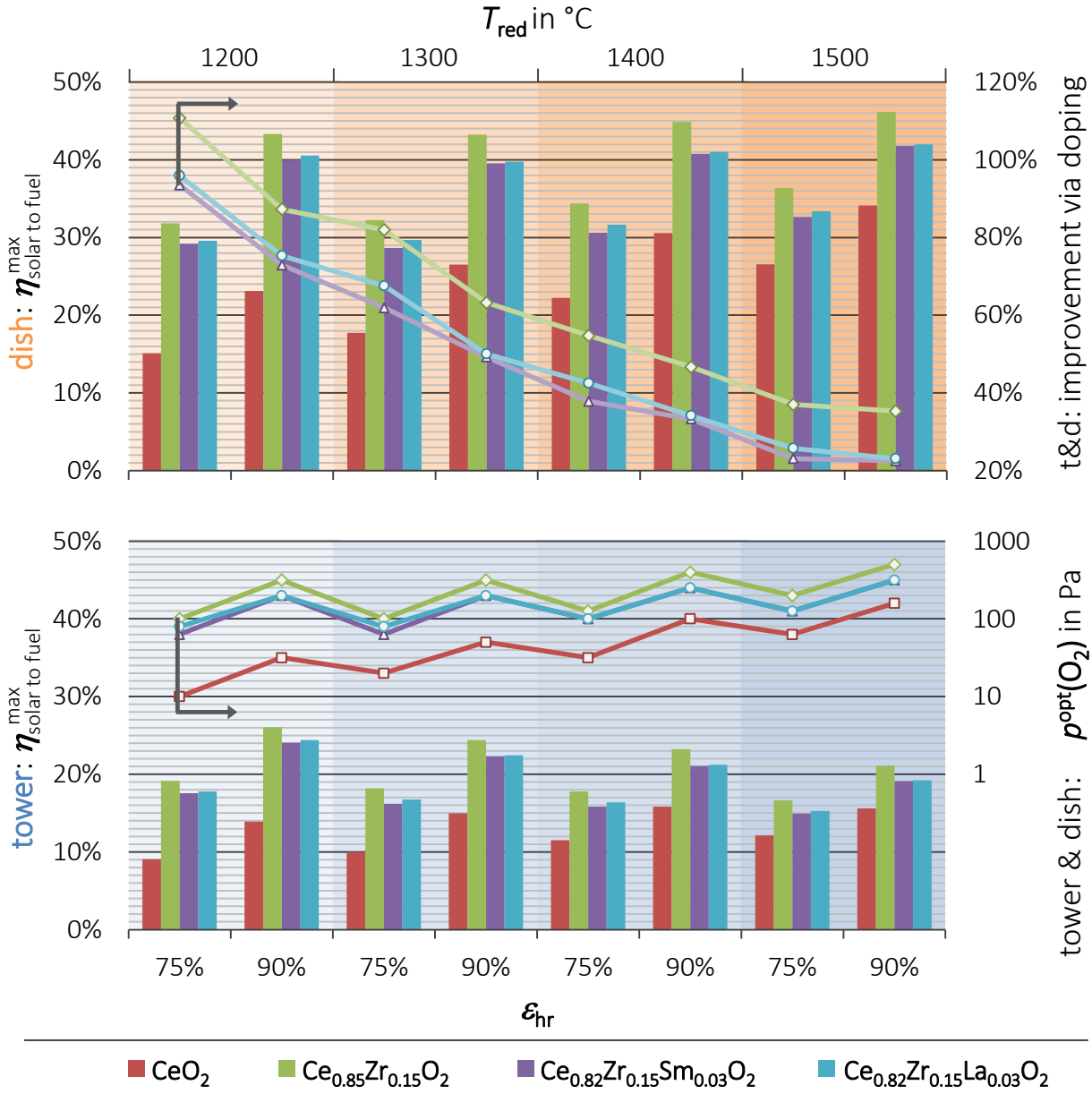

Figure 7.6: Maximum solar-to-fuel efficiency $\eta^{max}_{solar\ to\ fuel}$ (bars, left axis) of the materials (color code) investigated in chapter 6 at heat recuperator effectiveness ε_{hr} of 75% and 90% (bottom axis) and reduction temperatures T_{red} between 1200°C and 1500°C (top axis) applying a dish (top diagram, orange background) and a tower (bottom diagram, blue background). The lines (right axis) only depend on T_{red} and ε_{hr}, being independent of the two concepts. Considering the color code of the materials, they represent the relative enhanced efficiency of the doped materials with respect to pure ceria (top) and the optimal partial pressure $p^{opt}(O_2)$ for all four materials (bottom).

the experimental results, this improvement is found in particular for low temperatures. At a reduction temperature T_{red} as low as 1200°C and a heat recuperator effectiveness ε_{hr} of 75%, Zr-doping roughly doubles the maximum solar-to-fuel efficiency $\eta^{max}_{solar\ to\ fuel}$. On a tower, this corresponds to an increase of approximately ten percentage points. Furthermore, the optimal partial pressure of oxygen $p^{opt}(O_2)$ for this parameter set is one order of magnitude higher with respect to ceria. The higher $p^{opt}(O_2)$ might facilitate the technical realization of the process considerably. The increase in $p^{opt}(O_2)$ due to doping declines with increasing T_{red}.

For the following discussion, it is convenient to introduce a quantity $f_\eta^{i_p}$ that accounts for the relative improvement in $\eta^{max}_{solar\ to\ fuel}$ due to the change of one input parameter i_p. The influences on $\eta^{max}_{solar\ to\ fuel}$ for each material are summarized in table 7.2 .

Table 7.2: Relative change $\boldsymbol{f_\eta^{i_p}}$ in $\boldsymbol{\eta^{max}_{solar\ to\ fuel}}$ due to the variation of one input parameter $\boldsymbol{i_p}$. C: CeO_2, CZ: $Ce_{0.85}Zr_{0.15}O_2$, CZS: $Ce_{0.82}Zr_{0.15}Sm_{0.03}O_{1.99}$ and CZL: $Ce_{0.82}Zr_{0.15}La_{0.03}O_{1.99}$

	change in	T_{red} in °C				ε_{hr}			
	from	1200	1400	1200	1400	50%	75%	50%	75%
	to	1300	1500	1300	1500	75%	90%	75%	90%
	at	ε_{hr} = 75%		ε_{hr} = 90%		T_{red} = 1200°C		T_{red} = 1400°C	
dish	C	17%	19%	15%	12%	45%	53%	37%	38%
	CZ	1%	6%	0%	3%	36%	36%	32%	31%
	CZS	-2%	7%	-1%	3%	37%	37%	33%	33%
	CZL	0%	5%	-2%	2%	36%	37%	32%	30%
tower	C	10%	6%	7%	-1%	similar to dish, since ε_{hr} only effects the $\eta_{thermal\ to\ fuel}$			
	CZ	-5%	-6%	-6%	-9%				
	CZS	-8%	-6%	-7%	-9%				
	CZL	-6%	-7%	-8%	-9%				

The largest impact on $\eta^{max}_{solar\ to\ fuel}$ is found for ε_{hr}. At a certain T_{red}, increasing from ε_{hr} = 75% to ε_{hr} = 90% leads to a relative improvement in $\eta^{max}_{solar\ to\ fuel}$ in the range of $f_\eta^{\varepsilon_{hr}}$ = 35% to $f_\eta^{\varepsilon_{hr}}$ = 55% for pure ceria and between $f_\eta^{\varepsilon_{hr}}$ = 30% and $f_\eta^{\varepsilon_{hr}}$ = 40% in the case of the doped materials. The higher influence of ε_{hr} on pure ceria is ascribed to the lower reduction extent δ, leading to smaller ratios of active to passive material. Accordingly, more heat can be recuperated. The importance of this ratio was already discussed in section 2.1. The $f_\eta^{\varepsilon_{hr}}$ found here emphasize the need for an effective heat recuperation even for the improved materials. Increasing ε_{hr} from 50% to 75% (not shown in figure 7.6) results in similar $f_\eta^{\varepsilon_{hr}}$.

The enhancement due to increasing T_{red} is not as distinct. For the dish systesm, increasing the temperature by 100 K yields $f_\eta^{T_{red}}$ of 10 to 25% for pure ceria, whereas the doped materials exhibit $f_\eta^{T_{red}}$ only in the range of 2 to 7%. For both, pure and doped ceria, the highest $f_\eta^{T_{red}}$ is found for an increase of 1300°C to 1400°C. For lower and higher

temperatures, $f_{\eta}^{T_{red}}$ decreases. Regarding the tower system, for both, pure and doped ceria, the relative radiation losses increase more significant with temperature, due to the lower concentration ratio. In the case of pure ceria, this effect is dominated by the enhanced reducibility when increasing the temperature, yielding $f_{\eta}^{T_{red}}$ in the range of 0 to 10%. In contrast, for doped materials, the enhancement of the reduction extent δ with temperature is not as high. Therefore, raising T_{red} by 100 K, the surplus in δ does not compensate for the higher radiation losses resulting in $f_{\eta}^{T_{red}} -5$ to -10%. In other words, $\eta_{\text{solar to fuel}}^{\max}$ increases with decreasing temperature.

At this point, the question might arise, as to why no further parametric study was carried at even lower reduction temperatures, although the $\eta_{\text{solar to fuel}}^{\max}$ increases with decreasing temperatures, concerning the solar tower system. This is mainly due to the δ of less than 0.01 obtained already at $T_{red} = 1200°C$ for the doped material, even at low $p(O_2)$ (see figure 7.5). The smaller the fraction of reduced cerium, the less oxygen is released specifically. In order to meet the high efficiency and therewith, the high oxygen release rates, the mass flow $\dot{m}_{mat}$ of the redox material needs to increase. This might lead to mass flows $\dot{m}_{mat}$ through the reduction chamber that are not feasible. Note that this mass flow required to reach a certain efficiency might be adapted to other reactor designs such as monolithic structures. It just needs to be assured that the same amount of material reacts per second.

Exemplarily, figure 7.7 presents $\eta_{\text{solar to fuel}}^{\max}$ and corresponding mass flows $\dot{m}_{mat}$ of the redox material $Ce_{0.85}Zr_{0.15}O_2$ assuming a solar power incident on the first concentrator of $P_{sol} = 1$ MW. P_{sol} corresponds to a thermal power P_{th} within the reactor of 300 to 400 kW for the tower and 600 to 700 kW for the dish depending on the receiver temperature. Note that $\dot{m}_{mat} \propto P_{sol}$, enabling the simple assessment of $\dot{m}_{mat}$ for only one dish.

As observed in the top diagram of figure 7.7 , the required mass flow $\dot{m}_{mat}$ increases with decreasing T_{red} and increasing $p(O_2)$. Starting from low partial pressures of oxygen, the mass flow $\dot{m}_{mat}$ features a behavior similar to the one of the efficiency $\eta_{\text{solar to fuel}}$. At the maximum efficiency $\eta_{\text{solar to fuel}}^{\max}$, the behavior changes to a logarithmical slope inverse to the efficiency $\eta_{\text{solar to fuel}}$. The bottom diagram reveals that $\dot{m}_{mat}$ increases with increasing ε_{hr}. At high temperatures and high ε_{hr}, $\dot{m}_{mat} < 5$ kg·s^{-1} for the tower and $\dot{m}_{mat} < 10$ kg·s^{-1} for the dish, whereas at low temperatures, $\dot{m}_{mat}$ drastically raises. At a temperature of 1200°C, $\dot{m}_{mat} = 35$ kg·s^{-1} for the tower and $\dot{m}_{mat} = 55$ kg·s^{-1} for the dish. To compare such numbers, imagine a full-scale cement plant. This plant produces 2900 tons clinker per day corresponding to a mass flow of approximately 33.5 kg·s^{-1} [Kaan 04]. The production is carried out in a 60 meter long rotary kiln furnace at a temperature of about 1450°C with an energy input of roughly 100 MW. There is no doubt that there are major differences in the two processes. Nevertheless, the dimensions of an cement plant shall give an idea, that it is more than challenging to handle the required mass flow within a receiver with a thermal power of 300 to 700 kW.

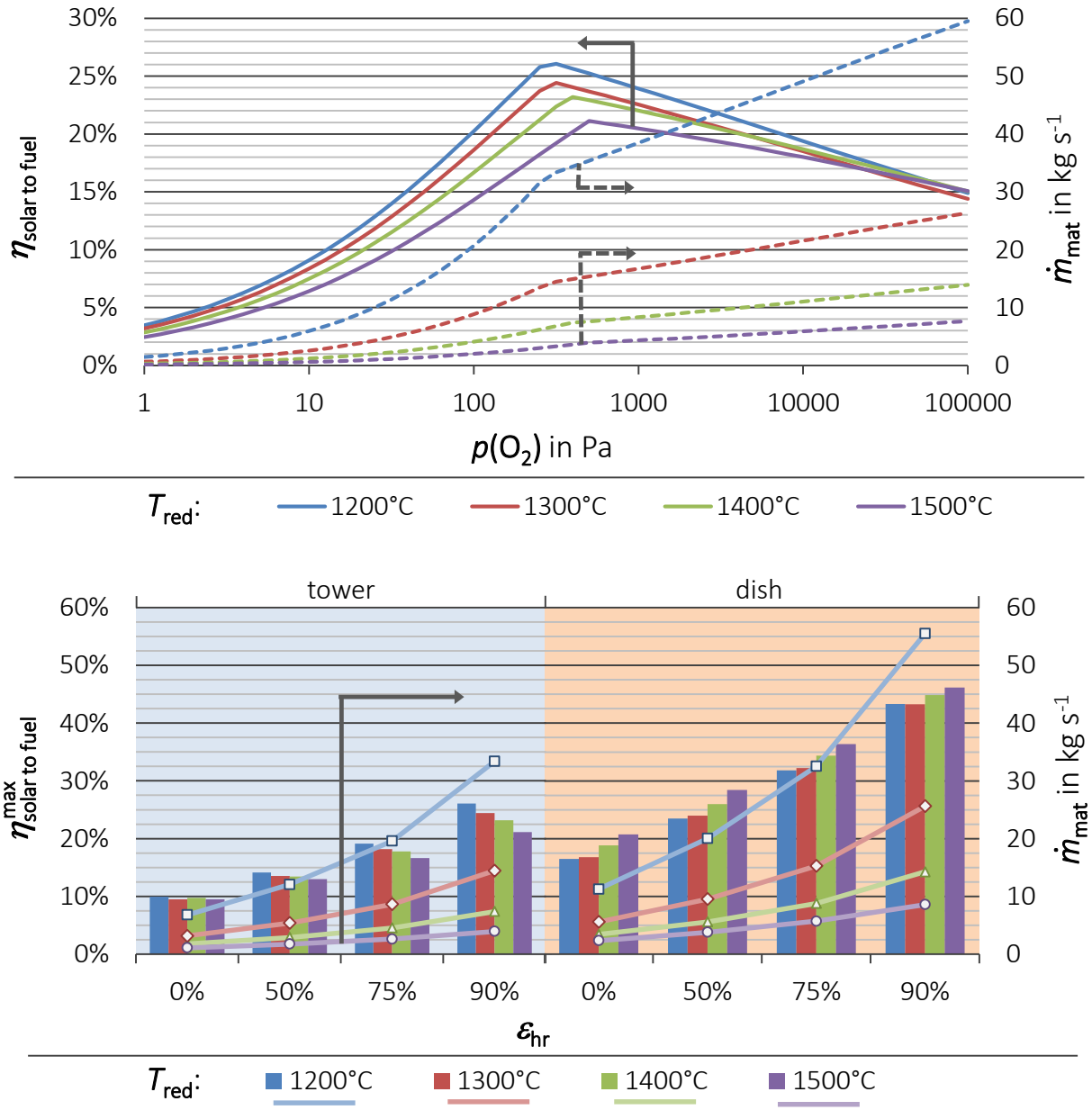

Figure 7.7: Efficiencies and corresponding mass flows for $Ce_{0.85}Zr_{0.15}O_2$ assuming a solar power input of P_{sol} = 1 MW. Top: $\eta_{solar\ to\ fuel}$ (left axis) and $\dot{m}_{mat}$ (right axis) at ε_{hr} = 90% and varying T_{red} on a tower . Bottom: Maximum solar-to-fuel efficiencies $\eta^{max}_{solar\ to\ fuel}$ (bars, left axis) $Ce_{0.85}Zr_{0.15}O_2$ at varying ε_{hr} and T_{red} for both, tower (left) and dish (right). The lines (right axis) correspond to the mass flow $\dot{m}_{mat}$.

Concerning the energetics, the impact of $\dot{m}_{mat}$ on $\eta_{solar\ to\ fuel}$ via the heat equivalent Q_{mech} to move the particles was neglected for the calculations agreeing to assumptions of Ermanoski et al.. This was done, because Q_{mech} was presumed to be a rather small contribution considering high temperatures. Now looking at lower temperatures and significant higher $\dot{m}_{mat}$, this assumptions might need to be reconsidered. However, without knowledge of the receiver/reactor design, the evaluation of reliable values for Q_{mech} depending

on $\dot{m}_{mat}$ is hardly possible.

High mass flows $\dot{m}_{mat}$ lead to implications regarding the feasibility of the process that are even more crucial. The higher $\dot{m}_{mat}$, the smaller is the potential residence time in the reduction chamber, leading to requirements on the reduction kinetics as well as on the duration to incorporate the required heat into the material. These requirements, in turn, depend on the reactor geometry via the volume of the reaction chamber as well as the concentration factor. An in-depth analysis of these relations cannot be carried out within the scope of this thesis and is left to subsequent research. Further considerations concerning the impact of the mass flow on reactor design, heat incorporation and reduction kinetics are provided in the conclusions of this chapter.

Apart from that, potential uncertainties of the model can be ascribed to the assumption of a constant heat capacity c_{mat} for all materials. Deviations concerning c_{mat} effect the $\eta^{max}_{solar\ to\ fuel}$, in particular, for low reduction extents corresponding to low ratios of active to passive material and assuming low heat recuperator effectiveness. Both conditions lead to a higher input heat P_{th} required for the process. c_{mat} of the doped materials needs to be evaluated experimentally for future studies.

7.3 Conclusions

In this chapter, the potential of ceria-based materials towards their application in TCCs was evaluated. The solar-to-fuel efficiencies of ceria-based materials were analyzed on the basis of the thermodynamical data derived in chapter 6 within a process model adapted from literature [Erma 13]. Expansion of the model considered the auxiliary process needs more realistically and included the solar tower system.

A parametric study concerning reduction temperature, partial pressure of oxygen and heat recuperation effectiveness was conducted regarding the application in a dish and a tower system. Especially, at low temperatures, doping significantly enhances the efficiency by more than 100% with respect to pure ceria. The results stress the significance of an efficient heat recuperation system to reach high solar-to-fuel efficiencies. Between the two systems, the dish features much higher efficiencies, due to the higher concentration ratios as well as better optical properties. Nevertheless, solar towers are more likely to be applied for the commercialization of the process, since they offer much less technical limitations.

Concerning the temperature dependency of the solar-to-fuel efficiency, on the one hand, high temperatures are not essentially needed to reach high efficiencies, in particular applying a solar tower. On the other hand, at temperatures of $<$1300°C, high mass flows $\dot{m}_{mat}$ of the redox material are required, since only small redox extents δ are achieved. These high mass flows lead to various implications for a future reactor design. The following discussion identifies the major challenges according to these findings that subsequent research needs to address to assess ceria-based material considering potential technical limitations. Therewith, solar-to-fuel efficiencies can be evaluated beyond sole energetics of the process.

Exemplarily, this discussion is carried out within a simplified reactor concept inspired by the particle reactor introduced by Ermanoski et al. [Erma 13]. In particular, the following relations might be adapted to the part, where the particles are irradiated and simultaneously reduced. Figure 7.8 presents such a simplified design. The irradiation enters the reactor from the top and is distributed onto the surface of the material. From the left, the material enters in its oxidized form and at a cold temperature level. The volume within the reactor dedicated to the material is calculated via the surface of the material times the height (gray area). The height corresponds to the thickness that needs to be permeated by heat. Exemplarily, this volume is divided into two tiers of particles. While passing the chamber, the top tier of the material is heated and simultaneously reduced to release oxygen. The heat is transferred into the volume of the material mainly via heat conduction assuming the operation under vacuum. Hence, the reduction of the second tier of the material is delayed. The material that leaves the reactor on the right features both, a temperature gradient and a reduction gradient within the material.

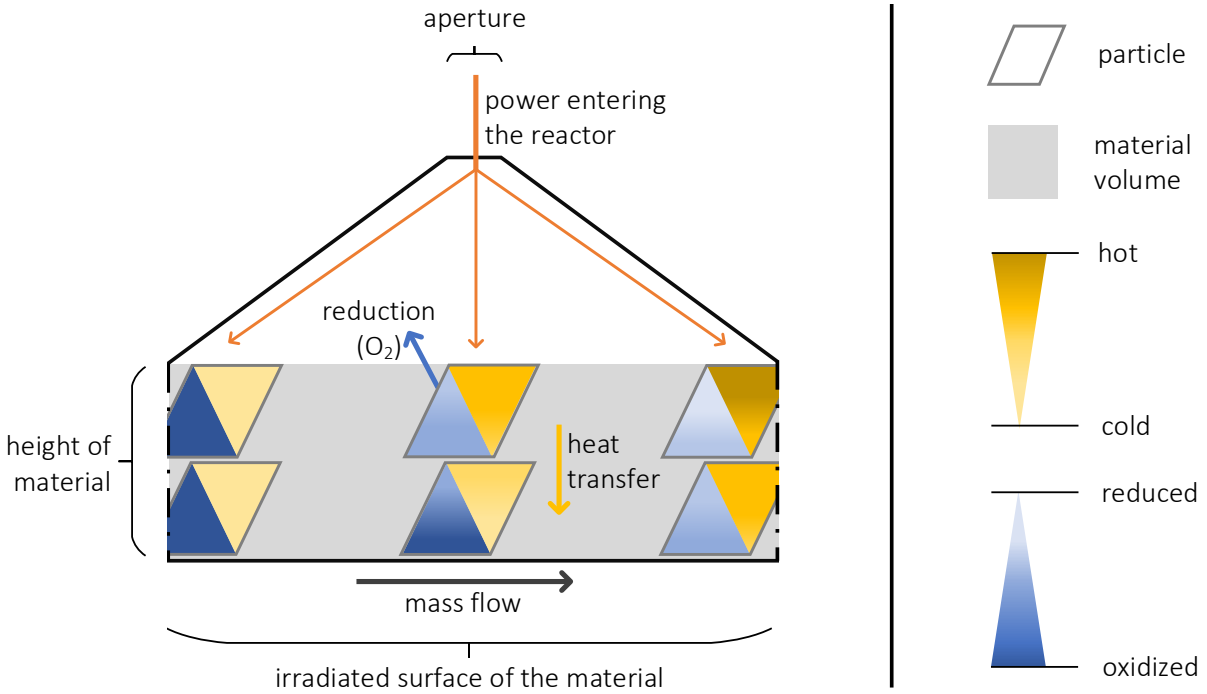

Figure 7.8: Schematic of a particle reactor.

According to the mass flow necessary to reach a certain efficiency, the required volume flow is derived via the density of the material. The ratio of this required volume flow to the volume dedicated to the material, yields the residence time of the material in the reactor. On the one hand, the size of the dedicated volume (gray area) should result in a residence time that corresponds to the reduction kinetics of the material. Hence, the volume should be rather big. On the other hand, height and surface of the volume have to be chosen, considering the heat incorporation into the material. The height of the material is limited due to the heat transfer into the bulk; the irradiated surface area is limited, because a certain heat flux is required. The reduction rate, in turn, depends on the actual temperature of the material and hence, is correlated with the heat incorporation and transfer that further complicates the analysis. In this regard, the structure of the material will play an important role. Porous materials feature much faster reduction rates than dense materials, but concerning the heat transfer, porous structures are disadvantageous, in particular, when operated under vacuum, where convection might be neglected. Furthermore, a porous material yields higher volume flows required within the reactor compared to dense materials.

All of the discussed relations come down to the correlation between reduction rate and heat incorporation and transfer. Knowledge of this correlation is essential for reactor design and technical realization of the process.

In short, the quintessence of this chapter is as follows:

Suitable doping roughly doubles the solar-to-fuel efficiency at reduction temperatures of 1200°C with regard to the adapted process model. At temperatures of 1500°C, doping relatively increases the solar-to-fuel efficiency by 20 to 40%.

Sufficient heat recuperation of the redox material is pivotal to assure efficient solar fuel production.

Taking realistic pumping efficiencies into account and assuming heat recuperation of 75%, the adapted model evaluates solar-to-fuel efficiencies with doped material in the range of 30 to 35% on a dish and 15 to 20% on a tower.

The high mass flows of the redox material required for such high efficiencies especially at low temperatures (< 1300°C) result in major challenges regarding the reactor design.

Knowledge of the correlation of reduction rate and heat incorporation is pivotal for the assessment of ceria-based materials applied in TCCs beyond sole energetic considerations.

8 Overall Conclusions

The overarching goal of this thesis was to pave the way towards the commercialization of thermochemical cycles harnessing the redox reaction of ceria with water/CO_2 to produce solar fuels. Because process analysis identified ceria as the major bottleneck, this thesis focused on the improvement and evaluation of ceria. Doping with zirconia and rare-earth metals served as the approach to improve its properties, thermogravimetry analysis as the method to evaluate its performance. Screening campaigns of various powder compositions identified the most promising doped compositions. The beneficial effect of doping was ascribed to modifications of the crystal structure that, in the case of zirconia, facilitate the reduction and, in the case of rare-earth metals, enhance the bulk diffusion. For following experimental campaigns, porous and dense pellets made of pure ceria and the most promising doped materials were manufactured. Investigations on the reaction kinetics of these pellets carried out in the thermobalance qualitatively assessed the impact of doping and microstructure. Since a quantitative interpretation of the experimental data seemed unreasonable, the determination of reliable reaction rates was left to subsequent research. The reduction extent δ in equilibrium-state at varying conditions was studied in a second campaign using pellets. Within a physical reaction model, the dependency of δ on temperature and partial pressure of oxygen was described. Based on the derived relations, Ellingham diagrams were established that convey the reduction enthalpy and entropy as a function of δ. Employing both, the δ-relation and the function of the reduction enthalpy in a process model estimated the maximum solar-to-fuel efficiencies of pure ceria as well as of the doped materials. A parametric study, including partial pressure of oxygen, temperature, heat recuperation and concentrating system, revealed efficiencies of the doped materials to be twice as high compared to pure ceria. Suitable doping improves the efficiency, in particular, at a temperature as low as 1200°C, which should facilitate the technical realization of the process considerably. However, because such low temperatures correspond to low specific yields, the mass flow of the material through the receiver drastically increases. The implications of high mass flows on the feasibility of the process are manifold and initiate various objectives of future research.

The first of the following sections summarizes the most important findings obtained in this thesis. Note that the conclusions sections of each chapter might provide further information. The objectives to be addressed in future research, according to these findings, are described in the second section.

8.1 Quintessence of this Thesis

On the level of thermodynamics, essential requirements on the redox materials were determined [Mere 09]. To establish a fuel production cycle that is thermodynamically favored, the enthalpy and entropy differences between the reduced and the oxidized phase of the material must feature certain values. Regarding conditions that are presumably technically feasible (partial pressure of oxygen $> 10^{-4}$ bar and reduction temperature $\leq$ 1500°C), the material has to feature reduction enthalpy changes of $\approx$ 350 kJ and entropy changes of > 0 J·K^{-1} per 0.5 mol of O_2. Large positive reduction entropies are especially featured by ceria due to the nonstoichiometric reaction, making ceria a promising candidate. To screen materials thermodynamically, the Ellingham diagram is the tool of choice [Jeff 08]. At a glance, such diagrams rank metal oxide systems concerning their CO_2- and H_2O-splitting abilities and state, whether the materials are thermally reducible. Beyond that, they identify the partial pressure of oxygen required for a certain temperature to reach the thermodynamical equilibrium of a redox reaction.

To evaluate promising dopants such as zirconium and rare-earth ions and estimate their optimal content in ceria, screening experiments were carried out employing powder samples in the thermobalance. Concerning the Zr content in $Ce_{1-x}Zr_xO_2$, the range $0.15 \leq x \leq 0.225$ was found to significantly enhance the fuel productivity. $Ce_{0.85}Zr_{0.15}O_2$ was identified as the optimal composition, displaying an increase of up to 50% with respect to pure ceria at the applied conditions. The beneficial effect of Zr-doping was attributed to lattice modification due to the incorporation of Zr^{4+}, which features smaller dimensions than Ce^{4+}. Zr^{4+} ions compensate for the expansion introduced by the transition from Ce^{4+} to Ce^{3+} that would suppress further reduction. Rare-earth metal doping in CeO_2-ZrO_2 solid solutions provided no improvements in terms of a higher fuel productivity. Possibly, the bigger trivalent ions compared to the tetravalent Ce^{4+} cause additional strain within the crystal structure. This strain adds to the strain introduced by oxygen vacancies created during reduction. Since Zr^{4+} cannot completely compensate for this cumulative strain, less vacancies are created and thus, less oxygen is released. Nevertheless, concerning long-term cycling, rare-earth metal doping was found to improve the oxidation kinetics. Constant fuel production for at least 80 cycles was achieved for $Ce_{0.82}Zr_{0.15}Sm_{0.03}O_{1.99}$, whereas the $Ce_{0.85}Zr_{0.15}O_2$ exhibited declining kinetics, although both materials suffered from decreasing specific surface. The increased kinetics of Sm-doping were ascribed to the structural vacancies present in the crystal structure due to the trivalent dopant. To further describe this mechanism, a reaction path was introduced.

Based on the findings of the powder test series, pellets were manufactured made of the three doped compositions ($Ce_{0.85}Zr_{0.15}O_2$, $Ce_{0.82}Zr_{0.15}Sm_{0.03}O_{1.99}$ and $Ce_{0.82}Zr_{0.15}La_{0.03}O_{1.99}$) and pure ceria. Two types of microstructures were applied: Dense and porous. The porous pellets exhibited pore channels, beneficial for the gas exchange during oxidation, whereas

the dense pellets presumably featured no pore channels, but more or less single, closed pores.

Qualitative analyses of the experiments carried out in the thermobalance confirmed the enhancement of Sm-doping for the oxidation at temperatures $< 900°C$ with respect to $Ce_{0.85}Zr_{0.15}O_2$. This result was in agreement with the results from long-term cycling. For the reduction, both doped materials showed improved reduction kinetics compared to pure ceria. In particular, the $Ce_{0.85}Zr_{0.15}O_2$ pellets featured higher reduction extents at much lower temperatures. A shift from a solely diffusion-controlled regime to an either surface-reaction or mass-transport controlled regime was identified at a temperature of 1100°C for $Ce_{0.85}Zr_{0.15}O_2$. Furthermore, the Sm-doping enhances the oxygen diffusion within the bulk material. Concerning the microstructure, porous structures drastically increased the oxidation rate due to higher gas exchange rates provided by open porosity. Also, porous materials reduced faster especially at lower temperatures, which was ascribed to faster diffusivity due to smaller characteristic diffusion lengths. Therefore, the porous materials are the first choice in real application to assure sufficient kinetics. In combination with slightly trivalent doped materials, the kinetics are considerably enhanced.

The equilibrium reducibility was analyzed on the basis of an experimental campaign subjecting dense pellets to thermogravimetric experiments at varying reduction temperatures from 1100°C to 1450°C and partial pressure of oxygen from 27 Pa to 1270 Pa. The experimental results indicated a higher impact of the reduction temperature on the reduction extent of pure ceria with respect to the doped-materials. On changes in partial pressure of oxygen, the reduction extents of both, pure ceria and the doped materials were found to respond similarly. An Arrhenius-based model was adapted that sufficiently fitted the experimental data [Bulf 13]. Therewith, the dependency of reduction extent δ on the reduction temperature and the partial pressure of oxygen was described with three parameters per material. With this δ—function, Ellingham diagrams of the investigated materials were constructed, illustrating fundamental relations of the reducibility and splitting ability of the materials. From Ellingham diagrams, reduction enthalpy and entropy were derived and fitted with respect to the reduction extend. The underlying mechanisms that led to the dependency of the reduction enthalpy on δ remain to be elucidated, whereas the reduction entropy dependency on δ could be ascribed to the change in configuration entropy due to the creation of vacancies. Deviation between the theoretically calculated configuration entropy and experimentally derived reduction entropy were attributed to solute vacancy pairs occurring due to doping. Taking the entire campaign into account, starting from experiments in the thermobalance under varying reduction conditions, the fundamental thermodynamics of the materials were obtained. This "tool" is of major interest for the evaluation of redox materials for the thermochemical fuel production.

On the basis of the derived δ— and enthalpy functions, the solar-to-fuel efficiencies of the investigated materials were analyzed within a process model adapted from litera-

ture [Erma 13]. The fundamental relations of this model are applicable to evaluate other continuously operating process designs, featuring separate chambers for reduction and oxidation, with a heat recuperation in between, and vacuum pumping during reduction. To consider the auxiliary needs of the process more realistically, the model was expanded by a function describing the dependency of the pump efficiency on the obtained vacuum [Bulf 15]. Besides a plant setup employing a dish, also a solar-tower setup was included. A parametric study was carried out to determine the solar-to-fuel efficiencies at varying partial pressures of oxygen, reduction temperatures and heat recuperator effectiveness. Concerning the impact of doping, the results indicated that doping significantly enhanced the efficiency, especially at low temperatures. For instance at 1200°C, doping more than doubles the solar-to-fuel efficiency. Comparing the dependencies of the solar-to-fuel efficiency on the temperature of the various materials, pure ceria displayed the most distinct dependency. The results of the parametric study also stressed the significance of an efficient heat recuperation system to reach high solar-to-fuel efficiency. Assuming heat recuperation of 75%, doped materials may reach solar-to-fuel efficiencies in the range of 30 to 35% on a dish and 15 to 20% on a tower. Although the tower concept yielded lower efficiencies, this concept is more likely to be applied for the commercialization of the process, since it offers much less technical limitations and better scalability. Employing the doped materials on a tower, on the one hand, led to solar-to-fuel efficiencies that decreased with increasing temperature for temperatures > 1200°C. This correlation was attributed to high radiation losses of the tower concept at these temperatures. On the other hand, since at such low temperature only small redox extents δ were reached, high mass flows of the redox material of up to 35 $\mathrm{kg \cdot s^{-1}}$ were required at 1200°C, assuming a solar power input of 1 MW of a tower. Such high mass flows might result in significant problems regarding the feasibility of the process. In particular, the correlation between reduction rate and heat incorporation was identified as the major bottle neck.

8.2 Recommendation for Subsequent Research

Within the frame of the objectives tackled in this thesis – identification of optimal doping of ceria, determination of its kinetics, evaluation of its reducibility and assessment of its potential – the following introduces my suggestions for subsequent research.

Identification of Optimal Doping

Paths to significantly improve the performance of ceria-based materials regarding their reducibility are rare. The most obvious doping paths, doping with zirconia and rare-earth elements (RE), have been pursued within this thesis. Nevertheless, numerous composition variations still require examination. For instance, Zr-contents in $Ce_{0.85-y-x}Zr_xRE_yO_{2-0.5y}$ that are higher than 15% with varying rare-earth metal contents and elements. There are more rare-earth dopants to be studied that were precluded in this thesis, such as praseodymium, neodymium and erbium. Other rare-earth metals might be too cost-intensive. However, improvements of fuel productivity in the range of orders or even of one order of magnitude are not expected, according to the extensive research of these materials carried out within the solid oxide fuel cell community [Trov 13].

Apart from these obvious doping paths, there are various other dopants that recent literature discusses. For instance, alkaline earth metals Mg, Ca, Sr, and Ba [Lee 13]. Since the solubility of these dopants is very limited, as discussed in section 2.3.1, the long-term stability of such compositions might be doubted due to segregation during cycling.

Determination of the Kinetics

Knowledge of reliable reaction rates are ineluctable to design reactors as well as the entire process. To determine the kinetics and identify rate limitations, a parametric study should be carried out in a testing facility that meets certain requirements. As observed in this thesis, the gas exchange is crucial for the oxidation. For the material design, this suggests the employment of porous structures. Further investigations concern the manufacturing of pellets or particles in a reproducible way and the identification of the optimal specific surface/porosity. The term "optimal" implies that, on the one hand, good reactivity is reached, but on the other hand, the stability of the structures is assured, in particular, concerning the long-term operation in a solar reactor. Here, sintering is not the major challenge, but rather the abrasion of the porous structures. To determine the oxidation rate of such porous materials, the testing facility needs to assure that the gas stream passes through the sample. Concerning the reduction, the facility should comprise a heating source that is able to provide heating rates as high as necessary to obtain high process efficiencies in on-sun operation. Among others, an infrared furnace as well as a

focused xenon lamp can provide such heating rates. In addition, operation under vacuum should be considered for this testing facility.

In combination to this parametric study, experimental techniques should be employed that directly measure the material-specific limitations of the kinetics, such as oxygen diffusivity and surface reaction. Among others, these techniques include secondary ion mass spectrometry and electrochemical impedance spectroscopy. The results of these techniques aid the clarification of kinetical limitations potentially observed in the parametric study.

Evaluation of the Reducibility

The methodology developed in this thesis to derive the essential thermodynamical data of a redox material, from experiments carried out in the thermobalance is proven to be sound. For future synthesized materials, this tool can be applied to evaluate their reduction-extent dependency on temperature and partial pressure of oxygen as well as their reduction entropy and enthalpy. These quantities are pivotal to the energetic assessment. Concerning the deviation found between the experimentally obtained and the theoretically calculated configuration entropies, a test series should confirm the assumption to attribute the deviation to solute vacancy pairs. If the assumption is correct, ceria based materials with lower dopant contents should feature smaller deviations and vice versa.

Assessment of the Potential

The process model adapted and expanded within this thesis serves as a suitable tool to assess the potential of ceria-based materials considering the major energetics involved in the process. However, the revealed high mass flows led to various implications, which could only be touched on a basic level within this thesis.

There is no doubt that the realization of such mass flows will be challenging. For the identification of the upper limits of the mass flow in a solar reactor, the correlation between reduction rate and heat incorporation and transfer was identified to be essential. From my point of view, the determination of this correlation needs to be in the major focus of future research, because it is the key to assess ceria-based materials beyond sole energetic considerations, yielding the realistic potential of these promising materials.

A Appendix

Contents

A.1 Ellingham diagrams

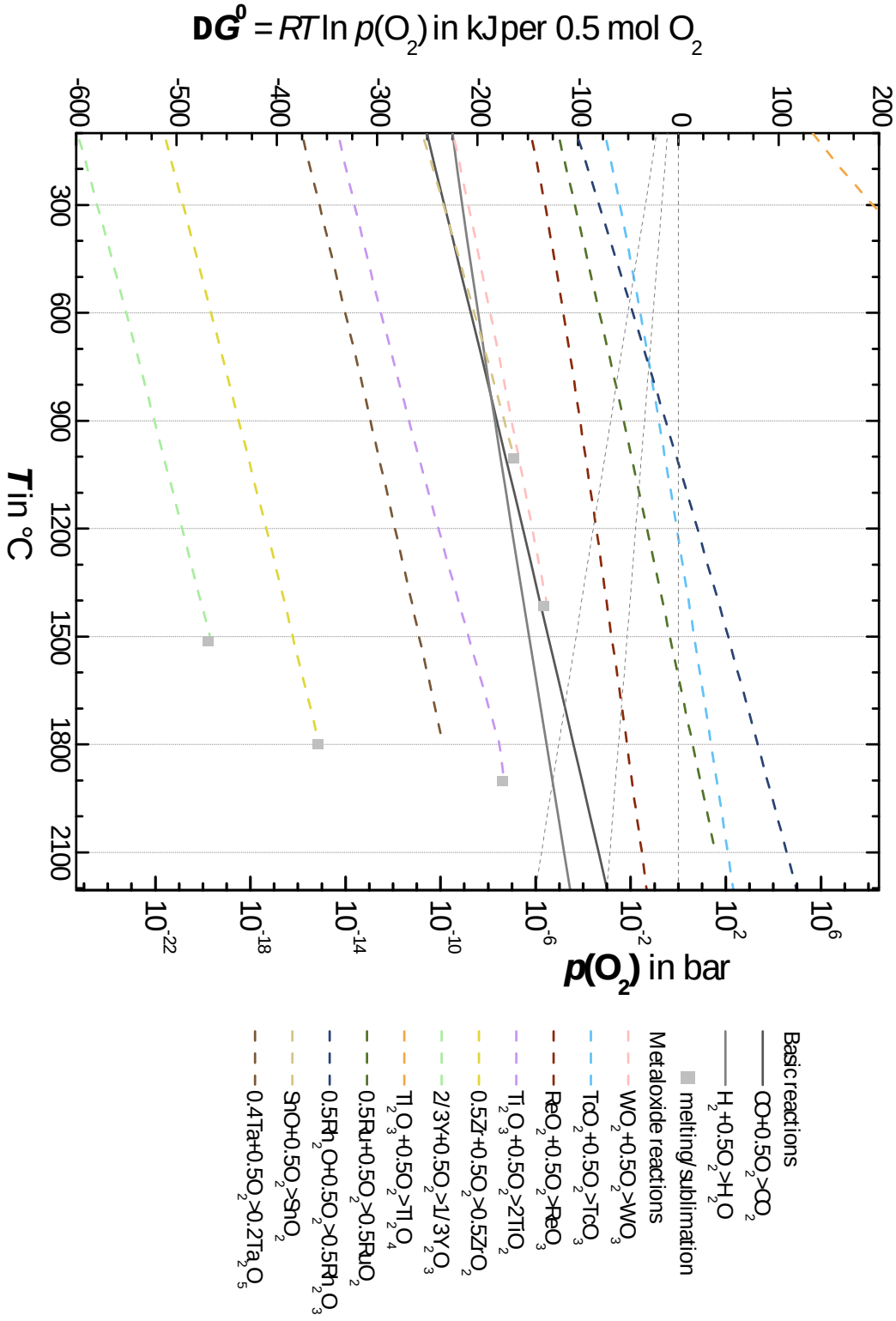

Figure A.1: Ellingham diagrams of transition metal I derived from FactSage calculations (databases Fact53 and SGPSBase).

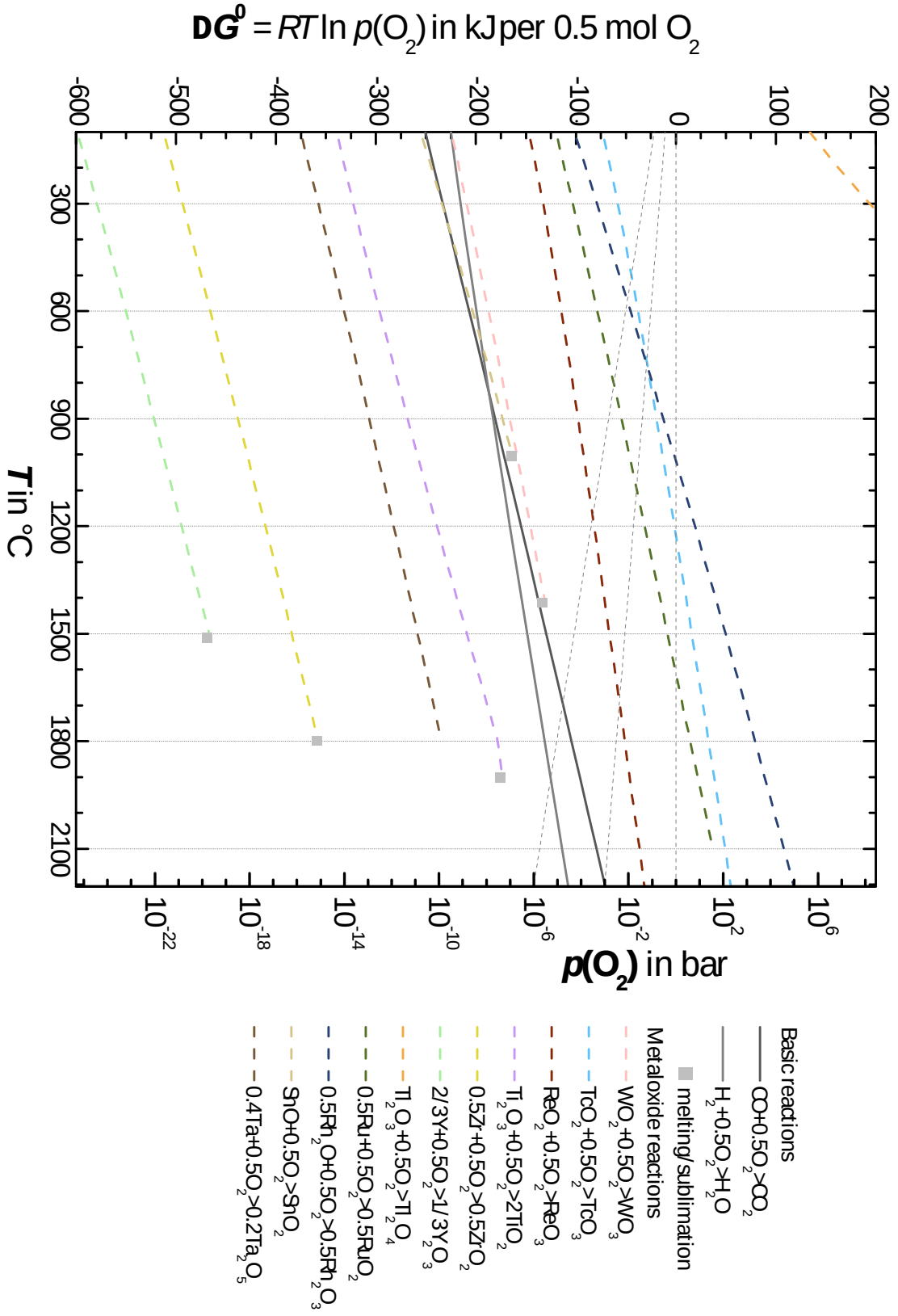

Figure A.2: Ellingham diagrams of transition metal II derived from FactSage calculations (databases Fact53 and SGPSBase).

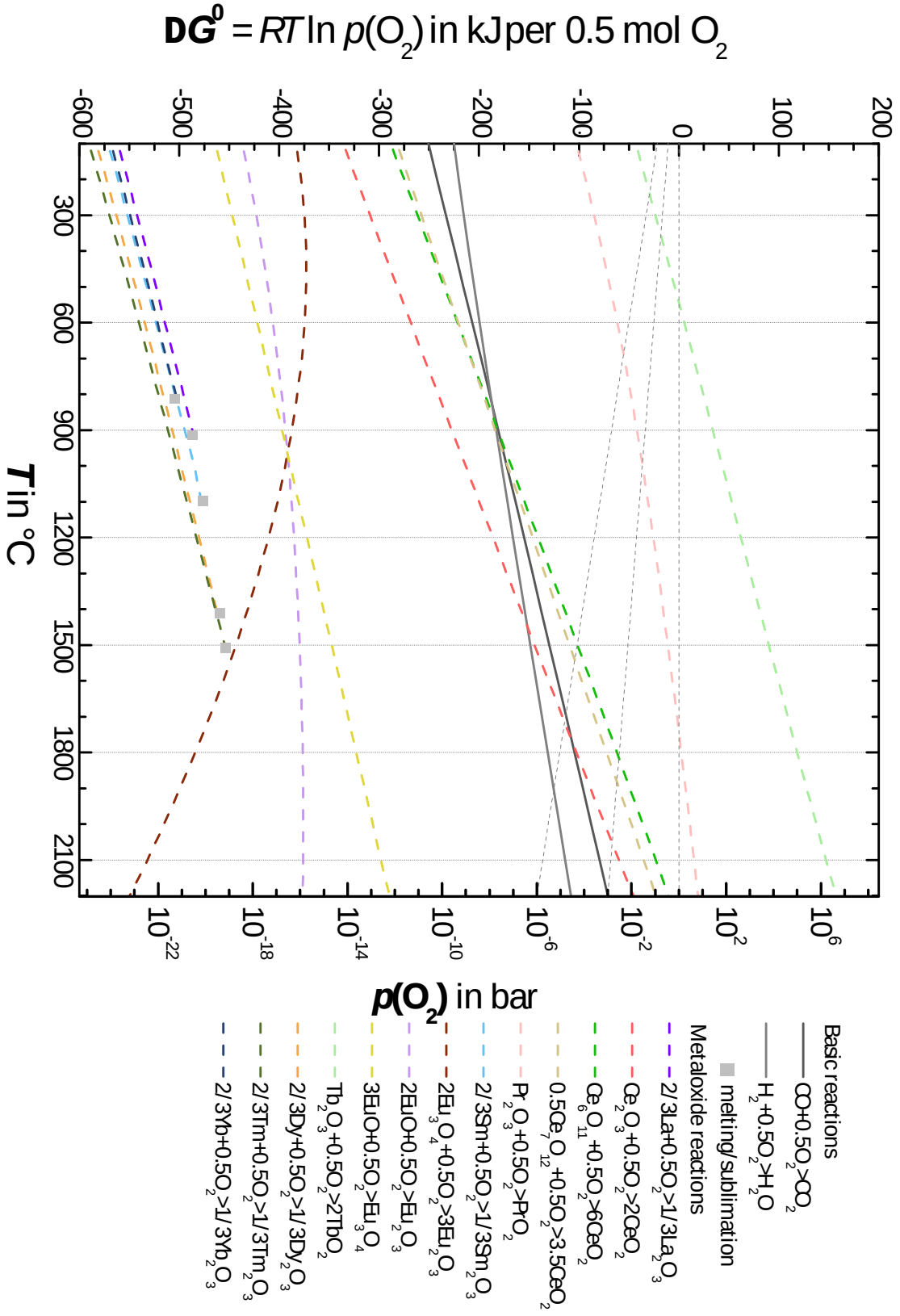

Figure A.3: Ellingham diagrams of lanthanides derived from FactSage calculations (databases Fact53 and SGPSBase).

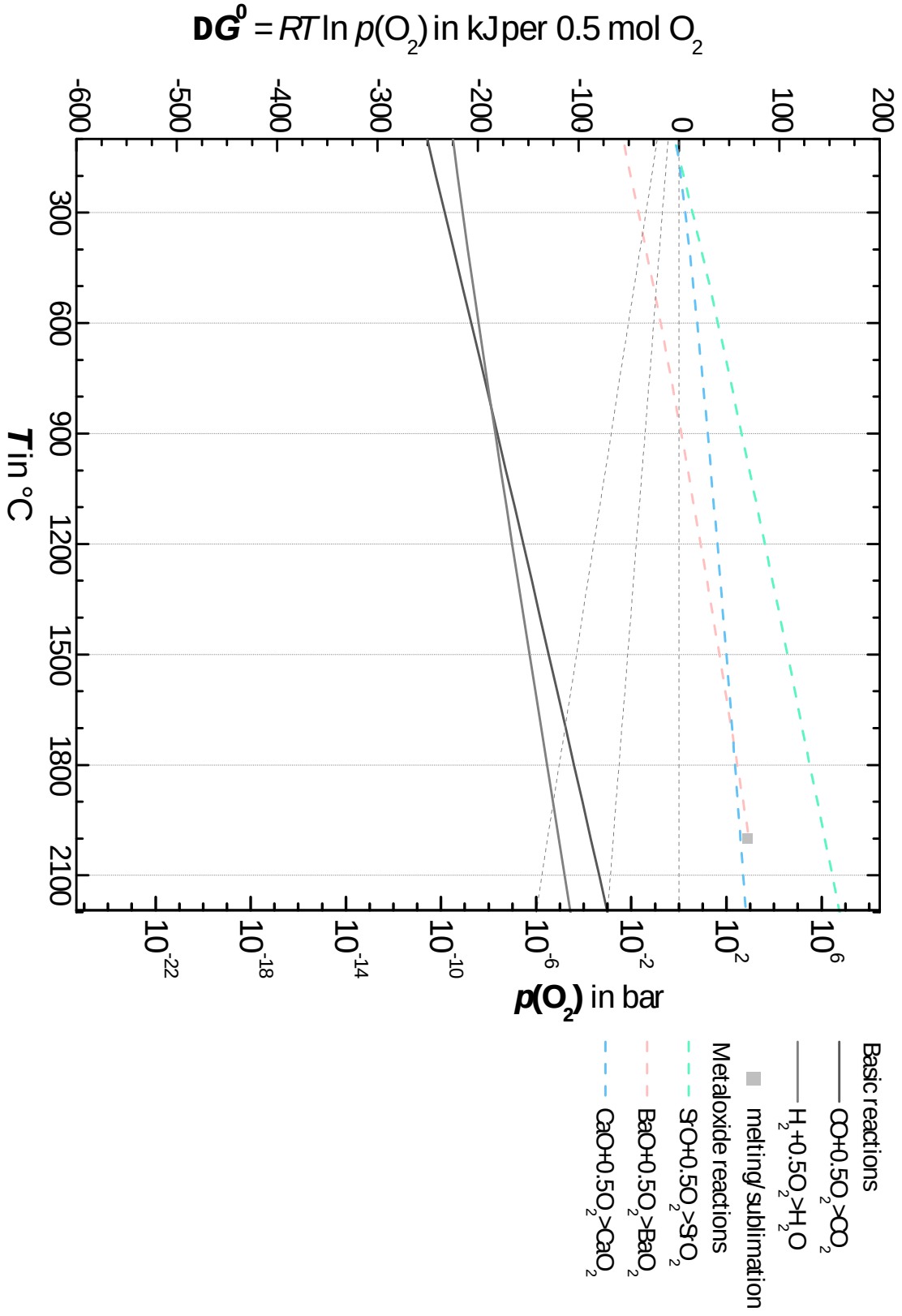

Figure A.4: Ellingham diagrams of alkalines derived from FactSage calculations (databases Fact53 and SGPSBase).

A.2 XRD patterns

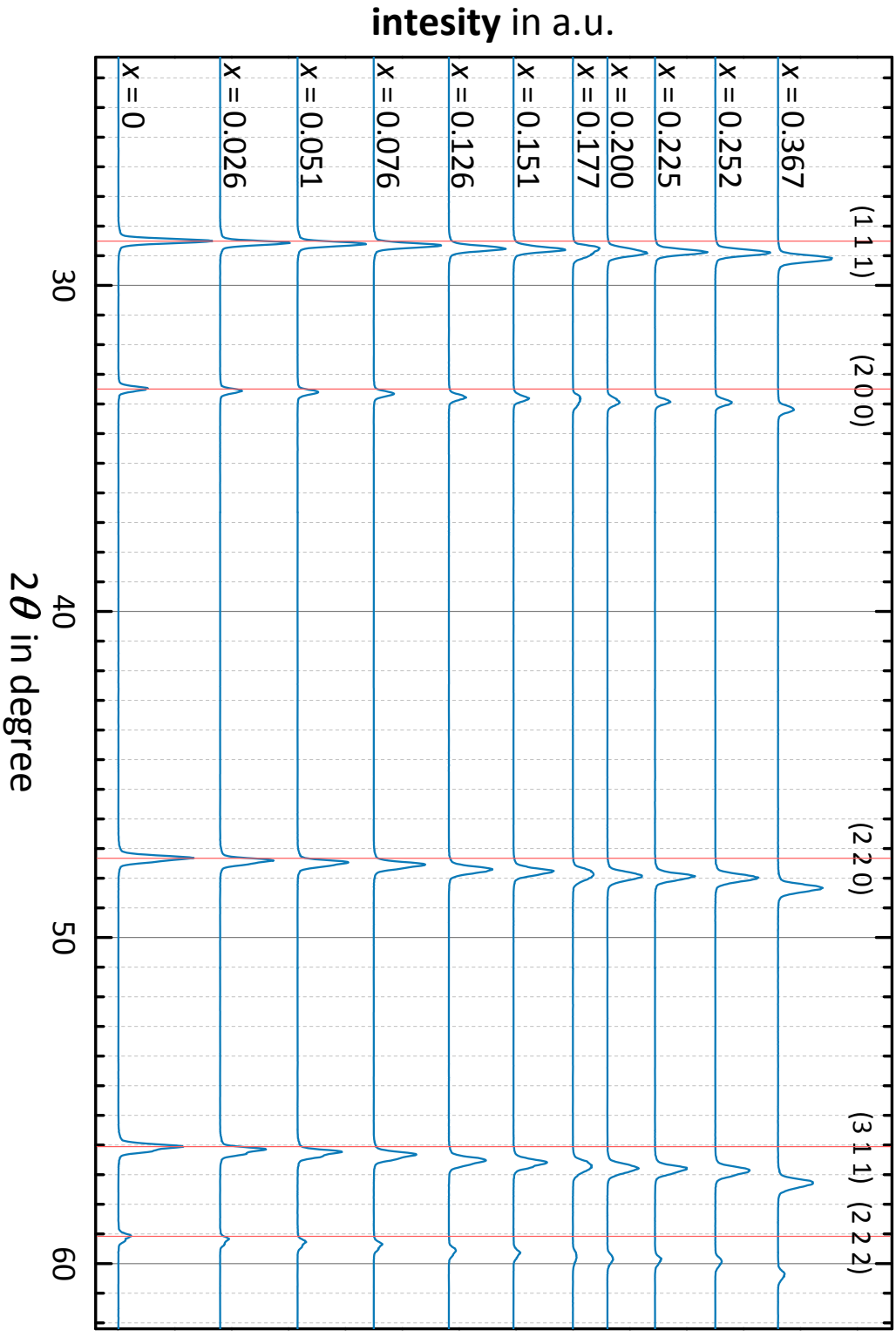

Figure A.5: XRD pattern of Zr-doped ceria powder materials: $Ce_{1-x}Zr_xO_2$.

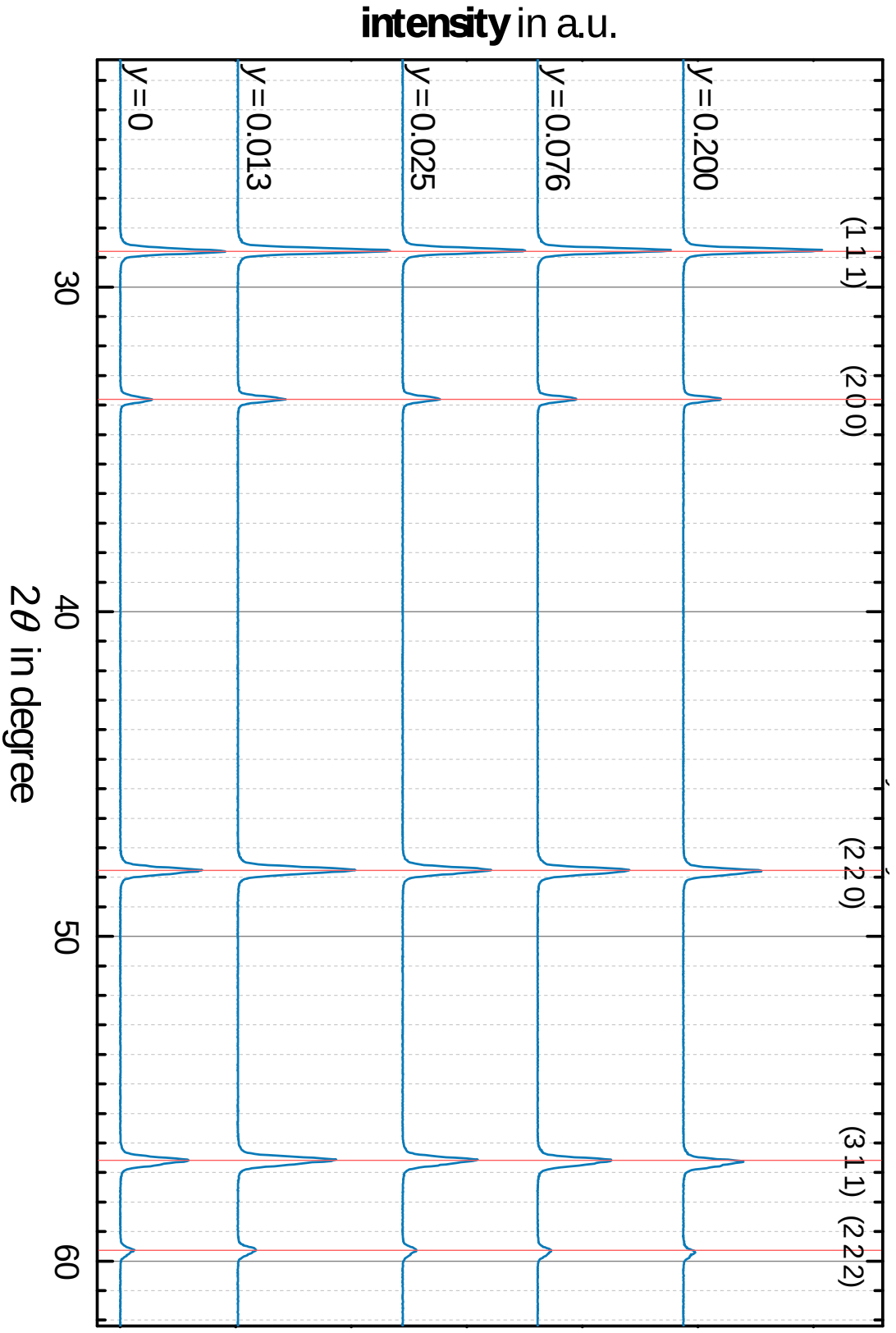

Figure A.6: XRD pattern of Y-doped Ce-Zr powder materials: $Ce_{0.85-x}Zr_{0.15}Y_yO_{2-0.5y}$.

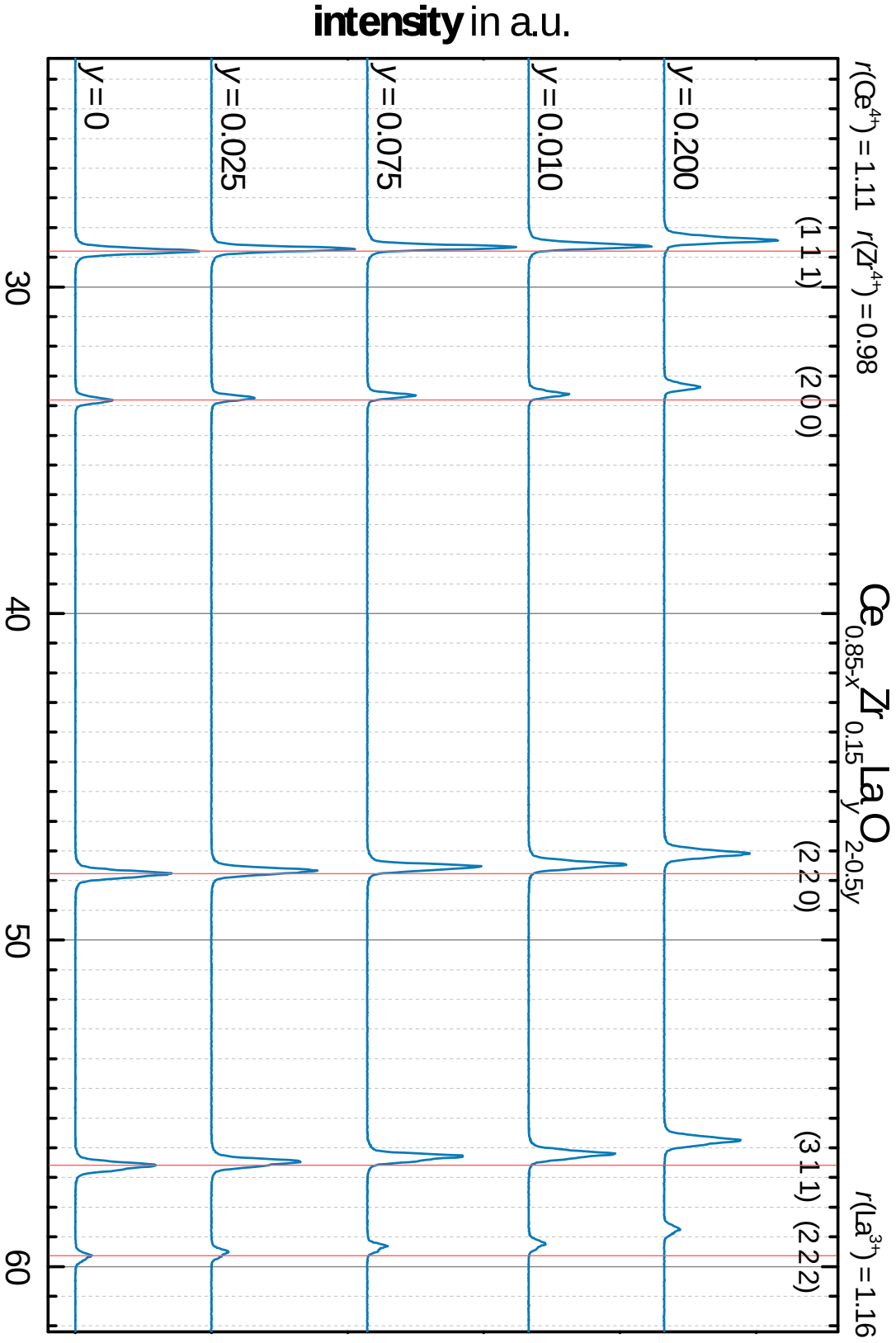

Figure A.7: XRD pattern of La-doped Ce-Zr powder materials: $Ce_{0.85-x}Zr_{0.15}La_yO_{2-0.5y}$.

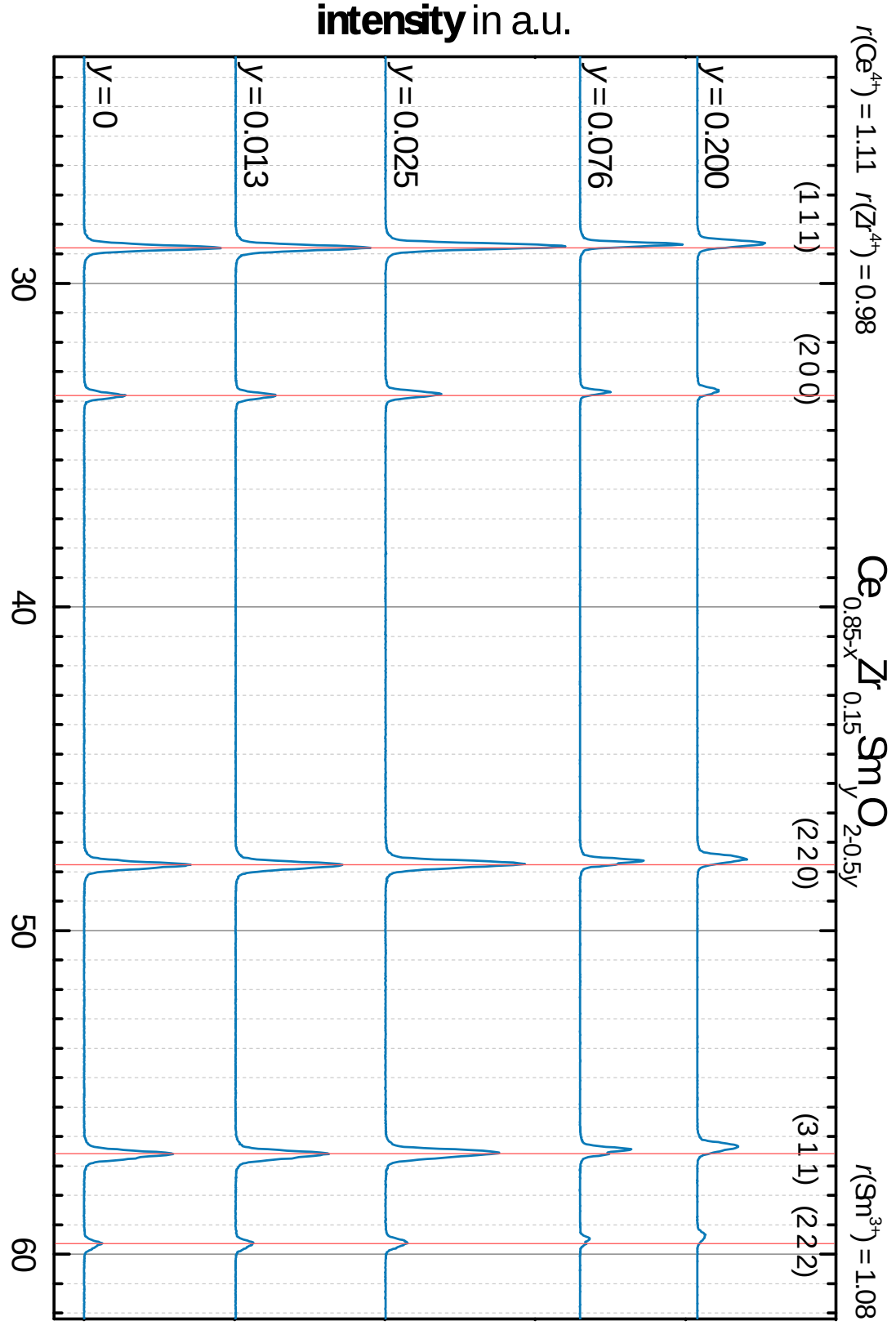

Figure A.8: XRD pattern of Sm-doped Ce-Zr powder materials: $Ce_{0.85-x}Zr_{0.15}Sm_yO_{2-0.5y}$.

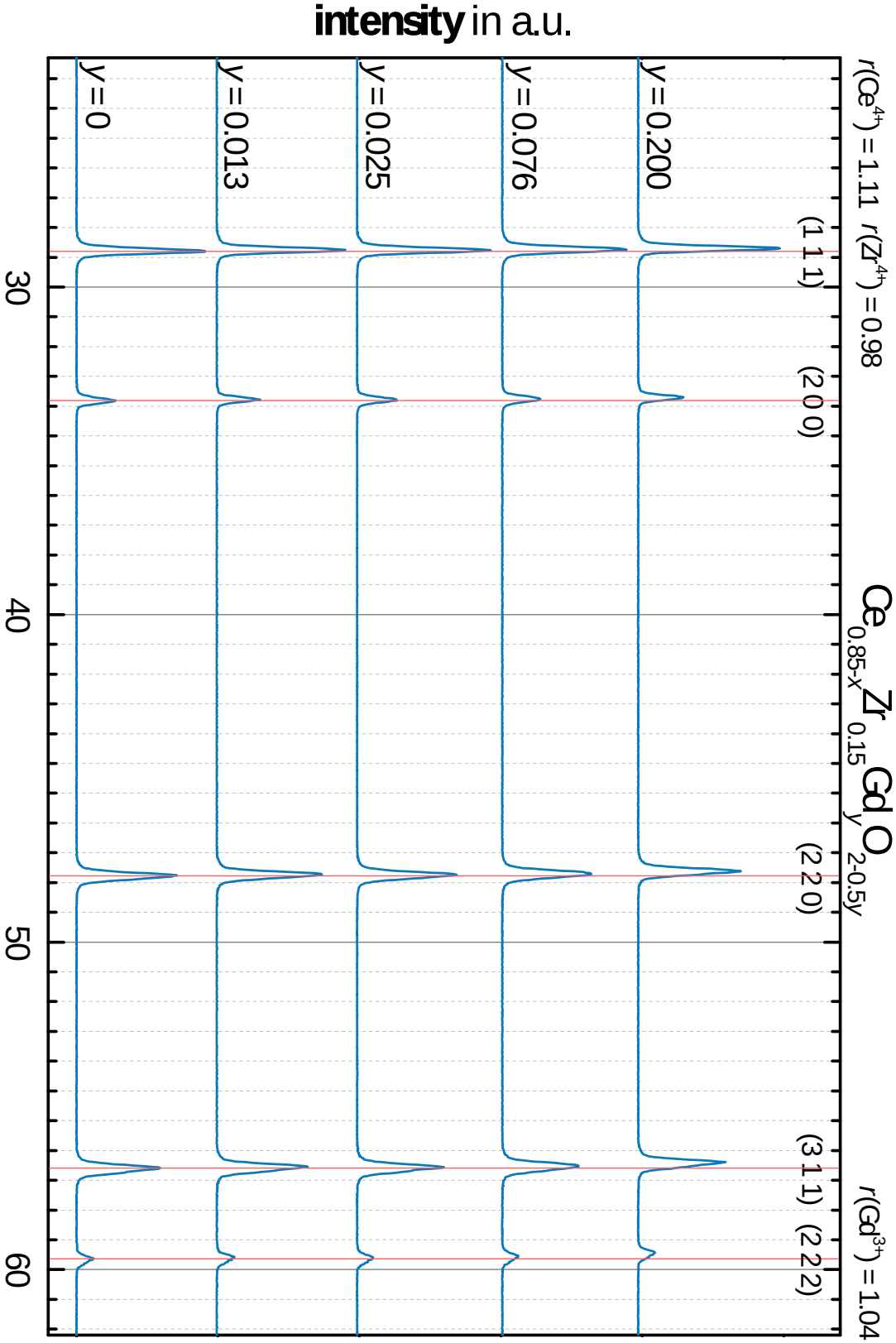

Figure A.9: XRD pattern of Gd-doped Ce-Zr powder materials: $Ce_{0.85-x}Zr_{0.15}Gd_yO_{2-0.5y}$.

A.3 Uncertainty in Pellet Cycling

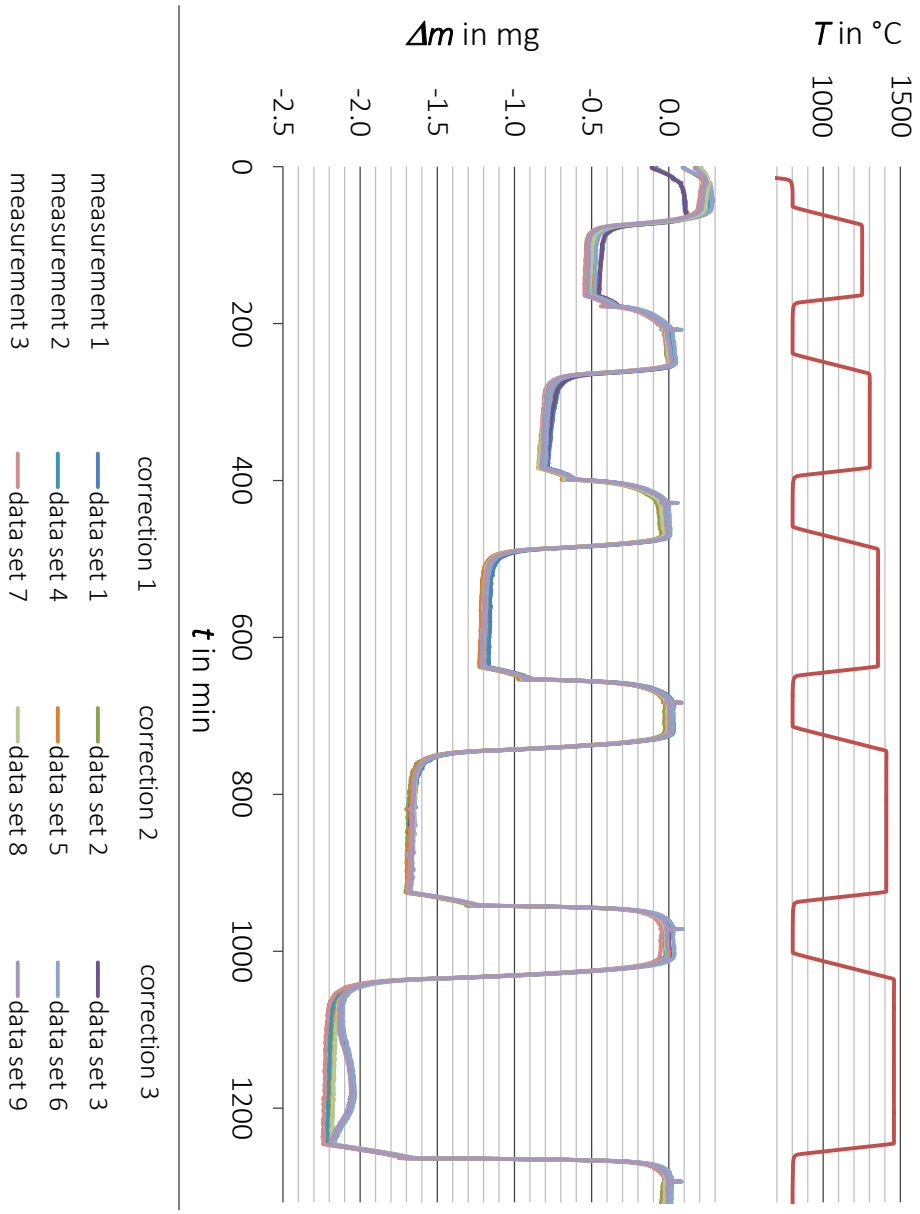

Figure A.10: Evaluation of the uncertainty of the equilibrium experiments carried out in chapter 6. Three experiments with the CZ:d600 pellet ($Ce_{0.85}Zr_{0.15}O_2$) corrected with three independent blank runs yielded nine data sets. Mass change between oxidized state ($\Delta m = 0$ mg) and equilibrium state reached in the isothermal step correspond to the reduction extent δ. Mean deviation of the resulting nine reduction extents δ per temperature was assumed to be the uncertainty for the other experiments carried out in chapter 6. The first cycle of these experiments was not considered for evaluation of $\delta\,(T_{red},\, p(O_2))$.

A.4 Validity of Ellingham Diagrams

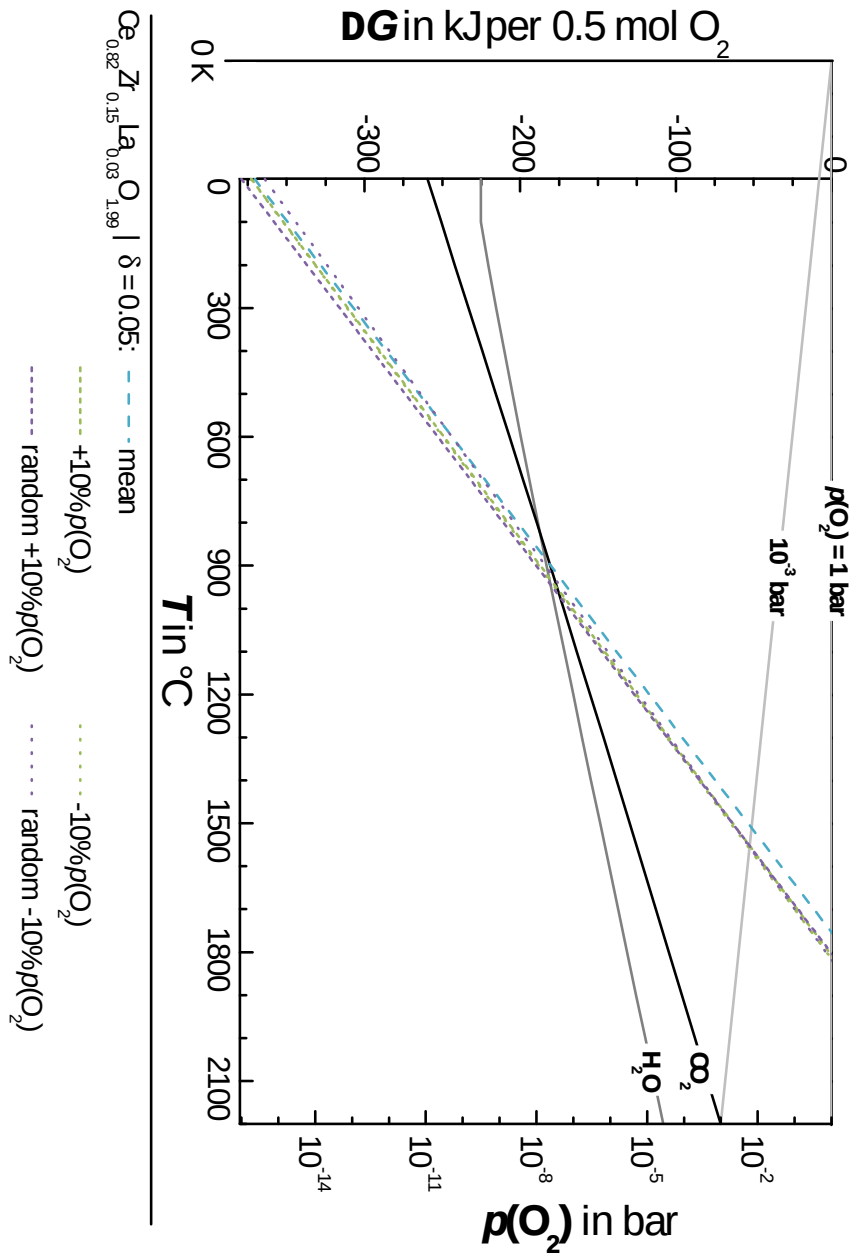

Figure A.11: This graph attempts to assess the validity of the Ellingham diagram derived in section 6.2. Uncertainties of the Ellingham lines directly effect the uncertainty of the entropy and enthalpy relations obtained. The Ellingham diagrams are evaluated using the $\delta\,(T_{\mathrm{red}},\ p(\mathrm{O_2}))$ function derived from fitting experimental data. The major uncertainties of the experimental data is found in the measurand partial pressure of oxygen $p(\mathrm{O_2})$ with is 10% of the measurand value. Changing this partial pressure by +10%, -10% (green lines) and random changes in between (purple lines) and employ this modified data set to derive the $\delta\,(T_{\mathrm{red}},\ p(\mathrm{O_2}))$, which in turn is used to derive Ellingham lines, yields no significant differences compared to the original evaluated line (petrol line). Therefore, the uncertainty of the relations of enthalpy (axis intercept of the Ellingham lines) and entropy (slope of the Ellingham lines) is assumed to be as small as 5%.

Bibliography

[Aban 06a] S. Abanades, P. Charvin, G. Flamant, and P. Neveu. "Screening of water-splitting thermochemical cycles potentially attractive for hydrogen production by concentrated solar energy". *Energy*, Vol. 31, No. 14, pp. 2805–2822, Nov. 2006.

[Aban 06b] S. Abanades and G. Flamant. "Thermochemical hydrogen production from a two-step solar-driven water-splitting cycle based on cerium oxides". *Solar Energy*, Vol. 80, No. 12, pp. 1611–1623, 2006.

[Aban 10] S. Abanades, A. Legal, A. Cordier, G. Peraudeau, G. Flamant, and A. Julbe. "Investigation of reactive cerium-based oxides for H_2 production by thermochemical two-step water-splitting". *Journal of Materials Science*, Vol. 45, No. 15, pp. 4163–4173, 2010.

[Adac 02] G. Adachi and T. Masui. "Synthesis and Modification of Ceria-Based Materials". In: A. Trovarelli, Ed., *Catalysis by Ceria and Related Materials*, Imperial College Press, 2002.

[Adac 04] G. Adachi, N. Imanaka, and Z. C. Kang. *Binary rare earth oxides*. Vol. 4, Springer, 2004.

[Adle 93] S. B. Adler and J. W. Smith. "Effects of long-range forces on oxygen transport in yttria-doped ceria: simulation and theory". *J. Chem. Soc., Faraday Trans.*, Vol. 89, No. 16, pp. 3123–3128, 1993.

[Agra 12] C. Agrafiotis, A. Zygogianni, C. Pagkoura, M. Kostoglou, and A. G. Konstandopoulos. "Hydrogen production via solar-aided water splitting thermochemical cycles with nickel ferrite: Experiments and modeling". *AIChE Journal*, Vol. 59, pp. 1213–1225, 2012.

[Ahre 95] T. J. Ahrens. *Global Earth Physics : A Handbook of Physical Constants*. American Geophysical Union: Washington, D.C., 1995.

[Alif 03] M. Alifanti, B. Baps, N. Blangenois, J. Naud, P. Grange, and B. Delmon. "Characterization of CeO_2-ZrO_2 mixed oxides. Comparison of the citrate and sol-gel preparation methods". *Chemistry of materials*, Vol. 15, No. 2, pp. 395–403, 2003.

[Anan 12] M. Anan'ev, E. K. Kurumchin, G. Vdovin, and N. Bershitskaya. "Kinetics of in-

teraction of gas phase oxygen with cerium-gadolinium oxide". *Russian Journal of Electrochemistry*, Vol. 48, No. 9, pp. 871–878, 2012.

[Aneg 06] E. Aneggi, M. Boaro, C. d. Leitenburg, G. Dolcetti, and A. Trovarelli. "Insights into the redox properties of ceria-based oxides and their implications in catalysis". *Journal of Alloys and Compounds*, Vol. 408, pp. 1096–1102, 2006.

[Aneg 13] E. Aneggi, C. de Leitenburg, and A. Trovarelli. "Ceria-Based Fomulations for Catalysts for Diesel Soot Combustion". In: A. Trovarelli and P. Fornasiero, Eds., *Catalysis by Ceria & Related Materials (Catalytic Science Series, vol. 2)*, Imperial College Press, London, 2013.

[Atki 06] P. Atkins and J. de Paula. *Physical Chemistry, Volume 1: Thermodynamics and Kinetics*. WH Freeman and Company: New York, 2006.

[Bade 13] R. Bader, L. J. Venstrom, J. H. Davidson, and W. Lipiński. "Thermodynamic analysis of isothermal redox cycling of ceria for solar fuel production". *Energy & Fuels*, Vol. 27, pp. 5533–5544, 2013.

[Bald 97] G. Balducci, J. Kašpar, P. Fornasiero, M. Graziani, M. S. Islam, and J. D. Gale. "Computer simulation studies of bulk reduction and oxygen migration in CeO_2-ZrO_2 solid solutions". *The Journal of Physical Chemistry B*, Vol. 101, No. 10, pp. 1750–1753, 1997.

[Bale 02] C. W. Bale, P. Chartrand, S. A. Degterov, G. Eriksson, K. Hack, R. B. Mahfoud, J. Melancon, A. D. Pelton, and S. Petersen. "FactSage thermochemical software and databases". *Calphad*, Vol. 26, No. 2, pp. 189–228, 2002.

[Bale 09] C. Bale, E. Bélisle, P. Chartrand, S. Decterov, G. Eriksson, K. Hack, I.-H. Jung, Y.-B. Kang, J. Melançon, A. Pelton, *et al.* "FactSage thermochemical software and databases – recent developments". *Calphad*, Vol. 33, No. 2, pp. 295–311, 2009.

[Boar 11] M. Boaro, S. Desinan, C. Abate, M. Ferluga, C. de Leitenburg, and A. Trovarelli. "Study on Redox, Structural and Electrical Properties of $Ce_xZr_{1-x}O_2$ for Applications in SOFC Anodes". *Journal of The Electrochemical Society*, Vol. 158, No. 2, pp. P22–P29, 2011.

[Bren 14] S. Brendelberger, J. Felinks, M. Roeb, and C. Sattler. "Solid Phase Heat Recovery and Multi Chamber Reduction for Redox Cycles". In: *ASME 2014 8th International Conference on Energy Sustainability collocated with the ASME 2014 12th International Conference on Fuel Cell Science, Engineering and Technology*, pp. V001T02A016–V001T02A016, American Society of Mechanical Engineers, 2014.

[Bulf 13] B. Bulfin, A. J. Lowe, K. A. Keogh, B. E. Murphy, O. Lübben, S. A. Krasnikov, and

I. V. Shvets. "Analytical Model of CeO_2 Oxidation and Reduction". *The Journal of Physical Chemistry C*, Vol. 117, No. 46, pp. 24129–24137, 2013.

[Bulf 15] B. Bulfin, F. Call, M. Lange, O. Lübben, C. Sattler, R. Pitz-Paal, and I. V. Shvets. "Thermodynamics of CeO 2 thermochemical fuel production". *Energy & Fuels*, Vol. 29, pp. 1001–1009, 2015.

[Butl 83] V. Butler, C. Catlow, B. Fender, and J. Harding. "Dopant ion radius and ionic conductivity in cerium dioxide". *Solid State Ionics*, Vol. 8, No. 2, pp. 109–113, 1983.

[Call 13] F. Call, M. Roeb, M. Schmücker, H. Bru, D. Curulla-Ferre, C. Sattler, and R. Pitz-Paal. "Thermogravimetric Analysis of Zirconia-Doped Ceria for Thermochemical Production of Solar Fuel". *American Journal of Analytical Chemistry*, Vol. 4, p. 37, 2013.

[Catl 83] C. Catlow. "Static lattice simulation of structure and transport in superionic conductors". *Solid State Ionics*, Vol. 8, No. 2, pp. 89–107, 1983.

[Chat 13] C. Chatzichristodoulou, P. T. Blennow, M. Sogaard, P. V. Hendriksen, and M. B. Mogensen. "Ceria and its Use in Solid Oxide Cells and Oxygen Membranes". In: A. Trovarelli and P. Fornasiero, Eds., *Catalysis by Ceria & Related Materials (Catalytic Science Series, vol. 2)*, Imperial College Press, London, 2013.

[Chen 10] H.-T. Chen and J.-G. Chang. "Oxygen vacancy formation and migration in $Ce_xZr_{1-x}O_2$ catalyst: A DFT+ U calculation". *The Journal of chemical physics*, Vol. 132, p. 214702, 2010.

[Chio 96] G. Chiodelli, G. Flor, and M. Scagliotti. "Electrical properties of the ZrO_2–CeO_2 system". *Solid State Ionics*, Vol. 91, No. 1, pp. 109–121, 1996.

[Chue 10a] W. C. Chueh, C. Falter, M. Abbott, D. Scipio, P. Furler, S. M. Haile, and A. Steinfeld. "High-Flux Solar-Driven Thermochemical Dissociation of CO_2 and H_2O Using Nonstoichiometric Ceria". *Science*, Vol. 330, pp. 1797–1801, 2010.

[Chue 10b] W. C. Chueh and S. M. Haile. "A thermochemical study of ceria: exploiting an old material for new modes of energy conversion and CO_2 mitigation". *Philosophical Transactions of the Royal Society A: Mathematical, Physical and Engineering Sciences*, Vol. 368, No. 1923, pp. 3269–3294, 2010.

[Coat 63] A. Coats and J. Redfern. "Thermogravimetric analysis. A review". *Analyst*, Vol. 88, pp. 906–924, 1963.

[Dawi 86] J. W. Dawicke and R. N. Blumenthal. "Oxygen association pressure measurements on nonstoichiometric cerium dioxide". *Journal of The Electrochemical Society*, Vol. 133, No. 5, pp. 904–909, 1986.

[Dega 09] F. Deganello, G. Marcì, and G. Deganello. "Citrate–nitrate auto-combustion

synthesis of perovskite-type nanopowders: A systematic approach". *Journal of the European Ceramic Society*, Vol. 29, No. 3, pp. 439–450, 2009.

[Delg 13] J. J. Delgado, E. del Rio, X. Chen, G. Blanco, J. M. Pintado, S. Bernal, and J. J. Calvino. "Understanding ceria-based catalytic materials: An overview of recent progress". In: A. Trovarelli and P. Fornasiero, Eds., *Catalysis by Ceria & Related Materials (Catalytic Science Series, vol. 2)*, Imperial College Press, London, 2013.

[Di M 04] R. Di Monte and J. Kašpar. "On the role of oxygen storage in three-way catalysis". *Topics in catalysis*, Vol. 28, No. 1-4, pp. 47–57, 2004.

[Di M 05a] R. Di Monte and J. Kašpar. "Heterogeneous environmental catalysis – a gentle art: CeO_2-ZrO_2 mixed oxides as a case history". *Catalysis today*, Vol. 100, No. 1, pp. 27–35, 2005.

[Di M 05b] R. Di Monte and J. Kašpar. "Nanostructured CeO2–ZrO2 mixed oxides". *Journal of Materials Chemistry*, Vol. 15, No. 6, pp. 633–648, 2005.

[Erma 13] I. Ermanoski, N. P. Siegel, and E. B. Stechel. "A New Reactor Concept for Efficient Solar-Thermochemical Fuel Production". *Journal of Solar Energy Engineering*, Vol. 135, p. 031002, 2013.

[Feli 14] J. Felinks, S. Brendelberger, M. Roeb, C. Sattler, and R. Pitz-Paal. "Heat recovery concept for thermochemical processes using a solid heat transfer medium". *Applied Thermal Engineering*, Vol. 73, No. 1, pp. 1006–1013, 2014.

[Fu 10] Y.-P. Fu, S.-H. Chen, and J.-J. Huang. "Preparation and characterization of $Ce_{0.8}M_{0.2}O_{2-\delta}$ (M= Y, Gd, Sm, Nd, La) solid electrolyte materials for solid oxide fuel cells". *International journal of hydrogen energy*, Vol. 35, No. 2, pp. 745–752, 2010.

[Furl 12a] P. Furler, J. Scheffe, M. Gorbar, L. Moes, U. Vogt, and A. Steinfeld. "Solar Thermochemical CO_2 Splitting Utilizing a Reticulated Porous Ceria Redox System". *Energy & Fuels*, Vol. 26, No. 11, pp. 7051–7059, 2012.

[Furl 12b] P. Furler, J. Scheffe, and A. Steinfeld. "Syngas production by simultaneous splitting of H_2O and CO_2 via ceria redox reactions in a high-temperature solar reactor". *Energy & Environmental Science*, Vol. 5, No. 3, pp. 6098–6103, 2012.

[Gard 09] D. Gardner. "Hydrogen production from renewables". *Renewable Energy Focus*, Vol. 9, No. 7, pp. 34–37, 2009.

[Gask 08] D. Gaskell. "Metal Production: Ellingham Diagrams". In: K. Buschow, Ed., *Encyclopedia of Materials: Science and Technology*, Elsevier: Oxford, 2008.

[Gior 01] F. Giordano, A. Trovarelli, C. de Leitenburg, G. Dolcetti, and M. Giona. "Some

insight into the effects of oxygen diffusion in the reduction kinetics of ceria". *Industrial & engineering chemistry research*, Vol. 40, No. 22, pp. 4828–4835, 2001.

[Goko 11] N. Gokon, T. Kodama, N. Imaizumi, J. Umeda, and T. Seo. "Ferrite/zirconia-coated foam device prepared by spin coating for solar demonstration of thermochemical water-splitting". *International Journal of Hydrogen Energy*, Vol. 36, No. 3, pp. 2014–2028, 2011.

[Goko 13] N. Gokon, S. Sagawa, and T. Kodama. "Comparative study of activity of cerium oxide at thermal reduction temperatures of 1300-1550° C for solar thermochemical two-step water-splitting cycle". *International Journal of Hydrogen Energy*, Vol. 38, No. 34, pp. 14402–14414, 2013.

[Gopa 12] C. Gopal and A. van de Walle. "Ab initio thermodynamics of intrinsic oxygen vacancies in ceria". *Physical Review B*, Vol. 86, pp. 134117–134125, 2012.

[Gopa 14] C. B. Gopal and S. M. Haile. "An electrical conductivity relaxation study of oxygen transport in samarium doped ceria". *Journal of Materials Chemistry A*, 2014.

[Gott 98] G. Gottstein. *Physikalische grundlagen der materialkunde*. Springer, 1998.

[GUM] *GUM: Evaluation of measurment data – Guide to the expression of uncertainty in measurement (JCGM Guide 100:2008)*. Geneva, International Organization for Standardization.

[Henc 90] L. L. Hench and J. K. West. "The sol-gel process". *Chemical Reviews*, Vol. 90, No. 1, pp. 33–72, 1990.

[Hern 10] W. Y. Hernandez, F. Romero-Sarria, M. A. Centeno, and J. A. Odriozola. "In Situ Characterization of the Dynamic Gold- Support Interaction over Ceria Modified Eu_{3+}. Influence of the Oxygen Vacancies on the CO Oxidation Reaction". *The Journal of Physical Chemistry C*, Vol. 114, No. 24, pp. 10857–10865, 2010.

[Hern 11] W. Hernandez, O. Laguna, M. Centeno, and J. Odriozola. "Structural and catalytic properties of lanthanide (La, Eu, Gd) doped ceria". *Journal of Solid State Chemistry*, Vol. 184, No. 11, pp. 3014–3020, 2011.

[Hook 13] M. Höök and X. Tang. "Depletion of fossil fuels and anthropogenic climate change – A review". *Energy Policy*, Vol. 52, pp. 797–809, 2013.

[Hoss 07] S. Hosseini Vajargah, H. Madaah Hosseini, and Z. Nemati. "Preparation and characterization of yttrium iron garnet (YIG) nanocrystalline powders by autocombustion of nitrate-citrate gel". *Journal of alloys and compounds*, Vol. 430, No. 1, pp. 339–343, 2007.

[Hwan 06] C.-C. Hwang, T.-H. Huang, J.-S. Tsai, C.-S. Lin, and C.-H. Peng. "Combustion

synthesis of nanocrystalline ceria (CeO_2) powders by a dry route". *Materials Science and Engineering: B*, Vol. 132, No. 3, pp. 229–238, 2006.

[IEA 12] IEA. "Energy Technology Perspectives 2012 - Pathway to a Clean Energy System". Tech. Rep., OECD/IEA, 2012.

[IFA 14] IFA. "GESTIS-Stoffdatenbank". January 2014.

[Janv 98] C. Janvier, M. Pijolat, F. Valdivieso, M. Soustelle, and C. Zing. "Thermal stability of $Ce_{1-x}Zr_xO_2$ solid solution powders". *Journal of the European Ceramic Society*, Vol. 18, No. 9, pp. 1331–1337, 1998.

[Jeff 08] J. Jeffes. "Ellingham Diagrams". In: K. Buschow, Ed., *Encyclopedia of Materials: Science and Technology*, Elsevier: Oxford, 2008.

[Kaan 04] U. Kääntee, R. Zevenhoven, R. Backman, and M. Hupa. "Cement manufacturing using alternative fuels and the advantages of process modelling". *Fuel Processing Technology*, Vol. 85, No. 4, pp. 293–301, 2004.

[Kane 07] H. Kaneko, T. Miura, H. Ishihara, S. Taku, T. Yokoyama, H. Nakajima, and Y. Tamaura. "Reactive ceramics of CeO_2-MO_x (M=Mn, Fe, Ni, Cu) for H_2 generation by two-step water splitting using concentrated solar thermal energy". *Energy*, Vol. 32, No. 5, pp. 656–663, 2007.

[Kane 08] H. Kaneko, H. Ishihara, S. Taku, Y. Naganuma, N. Hasegawa, and Y. Tamaura. "Cerium ion redox system in $CeO_{2-x}Fe_2O_3$ solid solution at high temperatures (1,273 - 1,673 K) in the two-step water-splitting reaction for solar H_2 generation". *Journal of Materials Science*, Vol. 43, No. 9, pp. 3153–3161, Feb. 2008.

[Kane 09] H. Kaneko and Y. Tamaura. "Reactivity and XAFS study on $(1-x)CeO_{1-x}NiO$ (x=0.025 - 0.3) system in the two-step water-splitting reaction for solar H_2 production". *Journal of Physics and Chemistry of Solids*, Vol. 70, No. 6, pp. 1008–1014, June 2009.

[Kane 11] H. Kaneko, S. Taku, and Y. Tamaura. "Reduction reactivity of CeO_2-ZrO_2 oxide under high O_2 partial pressure in two-step water splitting process". *Solar Energy*, Vol. 85, No. 9, pp. 2321–2330, 2011.

[Kane 12] H. Kaneko, Y. Naganuma, and Y. Tamaura. "Intermediate formation in the reduction of Ni-ferrite with irradiation of high-flux infrared beam up to 1823 K". *Journal of Physics and Chemistry of Solids*, Vol. 73, pp. 63–72, 2012.

[Kang 07] K.-S. Kang, C.-H. Kim, C.-S. Park, and J.-W. Kim. "Hydrogen Reduction and Subsequent Water Splitting of Zr-Added CeO_2". *J. Ind. Eng. Chem.*, Vol. 13, pp. 657–663, 2007.

[Kasp 00] J. Kašpar, M. Graziani, and P. Fornasiero. "Chapter 184: Ceria-containing

three-way catalysts". In: L. E. Karl A. Gschneidner, jr., Ed., *The Role of Rare Earths in Catalysis*, pp. 159 – 267, Elsevier, 2000.

[Kasp 99] J. Kašpar, P. Fornasiero, and M. Graziani. "Use of CeO_2-based oxides in the three-way catalysis". *Catalysis Today*, Vol. 50, No. 2, pp. 285–298, 1999.

[Kim 89] D.-J. Kim. "Lattice Parameters, Ionic Conductivities, and Solubility Limits in Fluorite-Structure MO_2 Oxide [M= Hf^{4+}, Zr^{4+}, Ce^{4+}, Th^{4+}, U^{4+}] Solid Solutions". *Journal of the American Ceramic Society*, Vol. 72, No. 8, pp. 1415–1421, 1989.

[Koda 09] T. Kodama, T. Hasegawa, A. Nagasaki, and N. Gokon. "A Reactive Fe-YSZ Coated Foam Device for Solar Two-Step Water Splitting". *Journal of Solar Energy Engineering*, Vol. 131, No. 2, pp. 021008–7, May 2009.

[Kolb 08] G. J. Kolb and R. B. Diver. "Screening Analysis of Solar Thermochemical Hydrogen Concepts". Tech. Rep. SAND2008-1900, Sandia National Laboratories, 2008.

[Kroe 56] F. Kroeger and H. Vink. *Solid state physics*. Vol. 3, New York: Academic Press, 1956.

[Kuhn 13] M. Kuhn, S. Bishop, J. Rupp, and H. Tuller. "Structural characterization and oxygen nonstoichiometry of ceria-zirconia ($Ce_{1-x}Zr_xO_{2-\delta}$) solid solutions". *Acta Materialia*, Vol. 61, pp. 4277–4288, 2013.

[Lai 05] W. Lai and S. M. Haile. "Impedance spectroscopy as a tool for chemical and electrochemical analysis of mixed conductors: a case study of ceria". *Journal of the American Ceramic Society*, Vol. 88, No. 11, pp. 2979–2997, 2005.

[Lane 00] J. Lane and J. Kilner. "Oxygen surface exchange on gadolinia doped ceria". *Solid State Ionics*, Vol. 136, pp. 927–932, 2000.

[Lang 14] M. Lange. *Efficiency Analysis of Solar-Driven Two-Step Thermochemical Water-Splitting Processes Based on Metal Oxide Redox Pairs*. PhD thesis, RWTH Aachen, 2014.

[Lapp 13] J. Lapp, J. Davidson, and W. Lipinski. "Heat transfer analysis of a solid-solid heat recuperation system for solar-driven nonstoichiometric redox cycles". *Journal of Solar Energy Engineering, Transactions of the ASME*, Vol. 135, No. 3, p. 031004, 2013. cited By (since 1996)0.

[Le G 11a] A. Le Gal and S. Abanades. "Catalytic investigation of ceria-zirconia solid solutions for solar hydrogen production". *International Journal of Hydrogen Energy*, Vol. 36, No. 8, pp. 4739–4748, 2011.

[Le G 11b] A. Le Gal, S. Abanades, and G. Flamant. "CO_2 and H_2O splitting for thermochemical production of solar fuels using nonstoichiometric ceria and ce-

ria/zirconia solid solutions". *Energy & Fuels*, Vol. 25, No. 10, pp. 4836–4845, 2011.

[Le G 12] A. Le Gal and S. Abanades. "Dopant Incorporation in Ceria for Enhanced Water-Splitting Activity during Solar Thermochemical Hydrogen Generation". *The Journal of Physical Chemistry C*, Vol. 116, No. 25, pp. 13516–13523, 2012.

[Le G 13] A. Le Gal, S. Abanades, N. Bion, T. Le Mercier, and V. Harlé. "Reactivity of doped ceria-based mixed oxides for solar thermochemical hydrogen generation via two-step water-splitting cycles". *Energy & Fuels*, 2013.

[Lee 13] C.-i. Lee, Q.-l. Meng, H. Kaneko, and Y. Tamaura. "Dopant effect on hydrogen generation in two-step water splitting with CeO_2–ZrO_2–MO_x reactive ceramics". *International Journal of Hydrogen Energy*, Vol. 38, No. 36, pp. 15934–15939, 2013.

[Lema 01] S. Lemaux, A. Bensaddik, A. Van der Eerden, J. Bitter, and D. Koningsberger. "Understanding of Enhanced Oxygen Storage Capacity in $Ce_{0.5}Zr_{0.5}O_2$: The Presence of an Anharmonic Pair Distribution Function in the Zr-O_2 Subshell as Analyzed by XAFS Spectroscopy". *The Journal of Physical Chemistry B*, Vol. 105, No. 21, pp. 4810–4815, 2001.

[Liu 12] G. Liu, J. Li, and K. Chen. "Combustion synthesis of refractory and hard materials: A review". *International Journal of Refractory Metals and Hard Materials*, Vol. 39, pp. 90–102, 2012.

[Llus 10] M. Llusar, L. Vitásková, P. Šulcová, M. Tena, J. Badenes, and G. Monrós. "Red ceramic pigments of terbium-doped ceria prepared through classical and non-conventional coprecipitation routes". *Journal of the European Ceramic Society*, Vol. 30, No. 1, pp. 37–52, 2010.

[Lore 08] S. Lorentzou, C. Agrafiotis, and A. Konstandopoulos. "Aerosol spray pyrolysis synthesis of water-splitting ferrites for solar hydrogen production". *Granular Matter*, Vol. 10, No. 2, pp. 113–122, 2008.

[Lout 10] P. G. Loutzenhiser, A. Meier, and A. Steinfeld. "Review of the Two-Step H_2O/CO_2-Splitting Solar Thermochemical Cycle Based on Zn/ZnO Redox Reactions". *Materials*, Vol. 3, No. 11, pp. 4922–4938, 2010.

[Maes 00] P. Maestro. "Foreword". In: L. E. Karl A. Gschneidner, jr., Ed., *The Role of Rare Earths in Catalysis*, pp. 159 – 267, Elsevier, 2000.

[Maha 05] T. Mahata, G. Das, R. Mishra, and B. Sharma. "Combustion synthesis of gadolinia doped ceria powder". *Journal of alloys and compounds*, Vol. 391, No. 1, pp. 129–135, 2005.

[Maha 11] N. Mahato, A. Gupta, and K. Balani. "Doped zirconia and ceria-based elec-

trolytes for solid oxide fuel cells: a review". *Nanomaterials and Energy*, Vol. 1, No. 1, pp. 27–45, 2011.

[Mere 09] B. Meredig and C. Wolverton. "First-principles thermodynamic framework for the evaluation of thermochemical H_2O - or CO_2 -splitting materials". *Physical Review B*, Vol. 80, No. 24, p. 245119, Dec. 2009.

[Mill 07] J. E. Miller. "Sandia Report: Initial Case for Splitting Carbon Dioxide to Carbon Monoxide and Oxygen". Tech. Rep. December, Sandia National Laboratories, 2007.

[Mill 08] J. E. Miller, M. D. Allendorf, R. B. Diver, L. R. Evans, N. P. Siegel, and J. N. Stuecker. "Metal oxide composites and structures for ultra-high temperature solar thermochemical cycles". *Journal of Materials Science*, Vol. 43, No. 14, pp. 4714–4728, Apr. 2008.

[Mill 09] J. E. Miller, L. R. Evans, N. P. Siegel, R. B. Diver, F. Gelbard, A. Ambrosini, and M. D. Allendorf. "Summary Report: Direct Approaches for Recycling Carbon Dioxide into Synthetic Fuel". Tech. Rep., Sandia National Laboratories, 2009.

[Moge 00] M. Mogensen, N. M. Sammes, and G. A. Tompsett. "Physical, chemical and electrochemical properties of pure and doped ceria". *Solid State Ionics*, Vol. 129, No. 1-4, pp. 63–94, Apr. 2000.

[Monk 44] R. G. Monk and H. J. T. Ellingham. "Transactions and Communications". *Journal of the Society of Chemical Industry*, Vol. 63, No. 5, pp. 125–160, 1944.

[Murr 12] J. Murray and D. King. "Climate policy: Oil's tipping point has passed". *Nature*, Vol. 481, No. 7382, pp. 433–435, 2012.

[Naka 10] A. Nakamura. "New defect-crystal-chemical approach to non-Vegardianity and complex defect structure of fluorite-based MO_2–$LnO_{1.5}$ solid solutions (M^{4+} = Ce, Th; Ln^{3+} = lanthanide): Part II: Model description and lattice-parameter data analysis". *Solid state ionics*, Vol. 181, No. 37, pp. 1543–1564, 2010.

[Naka 77] T. Nakamura. "Hydrogen production from water utilizing solar heat at high temperatures". *Solar Energy*, Vol. 19, No. 5, pp. 467–475, 1977.

[Newm 12] J. Newman, P. G. Hoertz, C. A. Bonino, and J. A. Trainham. "Review: an economic perspective on liquid solar fuels". *Journal of The Electrochemical Society*, Vol. 159, No. 10, pp. A1722–A1729, 2012.

[Ni 08] M. Ni, M. K. Leung, and D. Y. Leung. "Technological development of hydrogen production by solid oxide electrolyzer cell (SOEC)". *International Journal of Hydrogen Energy*, Vol. 33, No. 9, pp. 2337–2354, 2008.

[Niel 10] R. Nielsen and G. Wilfing. "Zirconium and zirconium compounds". *Ullmann's Encyclopedia of Industrial Chemistry*, 2010.

[Nowi 12] A. S. Nowick. *Diffusion in solids: recent developments*. Elsevier, 2012.

[Otsu 85] K. Otsuka, M. Hatano, and A. Morikawa. "Decomposition of water by cerium oxide of δ-phase". *Inorganica chimica acta*, Vol. 109, No. 3, pp. 193–197, 1985.

[Panl 75] R. Panlener, R. Blumenthal, and J. Garnier. "A thermodynamic study of non-stoichiometric Cerium dioxide". *Journal of Physics and Chemistry of Solids*, Vol. 36, No. 11, pp. 1213–1222, 1975.

[Para 13] T. Paraknewitz. *Herstellung von dichten und porösen $CeZrO_2$-Pellets zur thermochemischen Brennstoffherstellung*. Master's thesis, Fachhoschule Koblenz - WesterWaldCampus, 2013.

[Peng 02] C. Peng, Y. Zhang, Z. Cheng, X. Cheng, and J. Meng. "Nitrate–citrate combustion synthesis and properties of $Ce_{1-x}Sm_xO_{2-x/2}$ solid solutions". *Journal of Materials Science: Materials in Electronics*, Vol. 13, No. 12, pp. 757–762, 2002.

[Perk 04] C. Perkins and A. W. Weimer. "Likely near-term solar-thermal water splitting technologies". *International Journal of Hydrogen Energy*, Vol. 29, No. 15, pp. 1587–1599, 2004.

[Pijo 95] M. Pijolat, M. Prin, M. Soustelle, O. Touret, and P. Nortier. "Thermal stability of doped ceria: experiment and modelling". *Journal of the Chemical Society, Faraday Transactions*, Vol. 91, No. 21, pp. 3941–3948, 1995.

[Pric 04] R. J. Price, D. A. Morse, S. L. Hardy, T. H. Fletcher, S. C. Hill, and R. J. Jensen. "Modeling the Direct Solar Conversion of CO2 to CO and O2". *Industrial & engineering chemistry research*, Vol. 43, No. 10, pp. 2446–2453, 2004.

[Roeb 11] M. Roeb, J.-P. Säck, P. Rietbrock, C. Prahl, H. Schreiber, M. Neises, L. De Oliveira, D. Graf, M. Ebert, W. Reinalter, *et al.* "Test operation of a 100kW pilot plant for solar hydrogen production from water on a solar tower". *Solar Energy*, Vol. 85, No. 4, pp. 634–644, 2011.

[Roeb 12] M. Roeb, M. Neises, N. Monnerie, F. Call, H. Simon, C. Sattler, M. Schmücker, and R. Pitz-Paal. "Materials-Related Aspects of Thermochemical Water and Carbon Dioxide Splitting: A Review". *Materials*, Vol. 5, No. 11, pp. 2015–2054, 2012.

[Rome 07] M. Romero-Alvarez and E. Zarza. "Concentrating solar thermal power". *Handbook of energy efficiency and renewable energy*, 2007.

[Rome 12] M. Romero and A. Steinfeld. "Concentrating Solar Thermal Power and Thermochemical Fuels". *Energy & Environmental Science*, Vol. 5, pp. 9234–9245, 2012.

[Sche 02] K. Schermanz. "Mining, production, application and safety issues of cerium-based materials". In: A. Trovarelli, Ed., *Catalysis by Ceria and Related Mate-*

rials, Imperial College Press, 2002.

[Sche 10] J. R. Scheffe, J. Li, and A. W. Weimer. "A spinel ferrite/hercynite water-splitting redox cycle". *International Journal of Hydrogen Energy*, Vol. 35, No. 8, pp. 3333–3340, Apr. 2010.

[Sche 13a] J. R. Scheffe, A. H. McDaniel, M. D. Allendorf, and A. W. Weimer. "Kinetics and mechanism of solar-thermochemical H2 production by oxidation of a cobalt ferrite–zirconia composite". *Energy & Environmental Science*, Vol. 6, pp. 963–973, 2013.

[Sche 13b] J. R. Scheffe, R. Jacot, G. R. Patzke, and A. Steinfeld. "Synthesis, characterization and thermochemical redox performance of Hf, Zr and Sc doped ceria for splitting CO_2". *The Journal of Physical Chemistry C*, Vol. 117, pp. 24104–24114, 2013.

[Sck 12] J. Säck, M. Roeb, C. Sattler, R. Pitz-Paal, and A. Heinzel. "Development of a system model for a hydrogen production process on a solar tower". *Solar Energy*, Vol. 86, pp. 99–111, 2012.

[Shan 69] R. D. Shannon and C. T. Prewitt. "Effective ionic radii in oxides and fluorides". *Acta Crystallographica Section B Structural Crystallography and Crystal Chemistry*, Vol. 25, No. 5, pp. 925–946, 1969.

[Shan 76] R. D. Shannon. "Revised effective ionic radii and systematic studies of interatomic distances in halides and chalcogenides". *Acta Crystallographica Section A*, Vol. 32, No. 5, pp. 751–767, 1976.

[Sieg 13] N. P. Siegel, J. E. Miller, I. Ermanoski, R. B. Diver, and E. B. Stechel. "Factors Affecting the Efficiency of Solar Driven Metal Oxide Thermochemical Cycles". *Industrial & Engineering Chemistry Research*, Vol. 52, No. 9, pp. 3276–3286, 2013.

[Stam 12] A. Stamatiou, P. Loutzenhiser, and A. Steinfeld. "Syngas production from H2O and CO2 over Zn particles in a packed-bed reactor". *AIChE Journal*, Vol. 58, No. 2, pp. 625–631, 2012.

[Stap 99] G. Stapper, M. Bernasconi, N. Nicoloso, and M. Parrinello. "Ab initio study of structural and electronic properties of yttria-stabilized cubic zirconia". *Physical Review B*, Vol. 59, No. 2, p. 797, 1999.

[Stei 02] A. Steinfeld. "Solar hydrogen production via a two-step water-splitting thermochemical cycle based on Zn/ZnO redox reactions". *International Journal of Hydrogen Energy*, Vol. 27, No. 6, pp. 611–619, June 2002.

[Tama 12] Y. Tamaura. "Conversion of Concentrated Solar Thermal Energy into Chemical Energy". *AMBIO: A Journal of the Human Environment*, Vol. 41, pp. 108–111,

2012.

[Tesc 13] S. Tescari, C. Agrafiotis, S. Breuer, L. de Oliveira, M. Neises-von Puttkamer, M. Roeb, and C. Sattler. "Thermochemical solar energy storage via redox oxides: materials and reactor/heat exchanger concepts". In: *SolarPACES*, September 2013.

[Trai 12] J. Trainham, J. Newman, C. Bonino, P. Hoertz, and N. Akunuri. "Whither solar fuels?". *Current Opinion in Chemical Engineering*, Vol. 1, pp. 204–210, 2012.

[Trov 02] A. Trovarelli, Ed. *Catalysis by Ceria and Related Materials*. Imperial College Press, 2002.

[Trov 13] A. Trovarelli and P. Fornasiero. *Catalysis by Ceria & Related Materials (Catalytic Science Series, vol. 2)*. Imperial College Press, London, 2013.

[Trov 96] A. Trovarelli. "Catalytic properties of ceria and CeO_2-containing materials". *Catalysis Reviews*, Vol. 38, No. 4, pp. 439–520, 1996.

[Trov 97] A. Trovarelli, F. Zamar, J. Llorca, C. de Leitenburg, G. Dolcetti, and J. T. Kiss. "Nanophase Fluorite-Structured CeO_2-ZrO_2 Catalysts Prepared by High-Energy Mechanical Milling". *Journal of Catalysis*, Vol. 169, pp. 490–502, 1997.

[Vanp 14] D. E. P. Vanpoucke, S. Cottenier, V. Van Speybroeck, I. Van Driessche, and P. Bultinck. "Tetravalent Doping of CeO_2: The Impact of Valence Electron Character on Group IV Dopant Influence". *Journal of the American Ceramic Society*, Vol. 97, pp. 258–566, 2014.

[Vega 21] L. Vegard. "Die Konstitution der Mischkristalle und die Raumfüllung der Atome". *Zeitschrift für Physik*, Vol. 5, pp. 17–26, 1921.

[Vida 01] H. Vidal, J. Kašpar, M. Pijolat, G. Colon, S. Bernal, A. Cordón, V. Perrichon, and F. Fally. "Redox behavior of CeO_2–ZrO_2 mixed oxides: II. Influence of redox treatments on low surface area catalysts". *Applied Catalysis B: Environmental*, Vol. 30, No. 1, pp. 75–85, 2001.

[Vish 11] I. Vishnevetsky, A. Berman, and M. Epstein. "Features of solar thermochemical redox cycles for hydrogen production from water as a function of reactants main characteristics". *International Journal of Hydrogen Energy*, Vol. 36, No. 4, pp. 2817–2830, 2011.

[Wu 13] W. Wu, L. Amsbeck, R. Buck, R. Uhlig, and R. P-Paal. "Proof of concept test of a Centrifugal Particle Receiver". In: *SolarPACES - Energy Procedia*, 2013.

[Xin 10] Y. Xin, Y. Qi, X. Ma, Z. Wang, Z. Zhang, and S. Zhang. "Rare-earth (Nd, Sm, Eu, Gd and Y) enhanced CeO_2 solid solution nanorods prepared by co-precipitation without surfactants". *Materials Letters*, Vol. 64, No. 23, pp. 2659–2662, 2010.

[Yang 06] Z. Yang, T. K. Woo, and K. Hermansson. "Effects of Zr doping on stoichiometric and reduced ceria: A first-principles study". *The Journal of chemical physics*, Vol. 124, p. 224704, 2006.

[Yash 13] M. Yashima. "Crystal and Electronic Structures, Structural Disorder, Phase Transformation and Phase Diagram of Ceria-Based Materials". In: A. Trovarelli and P. Fornasiero, Eds., *Catalysis by Ceria & Related Materials (Catalytic Science Series, vol. 2)*, Imperial College Press, London, 2013.

[Yoko 04] H. Yokokawa, T. Horita, N. Sakai, K. Yamaji, M. Brito, Y.-P. Xiong, and H. Kishimoto. "Protons in ceria and their roles in SOFC electrode reactions from thermodynamic and SIMS analyses". *Solid State Ionics*, Vol. 174, No. 1, pp. 205–221, 2004.

[Zeli 66] A. N. Zelikman, O. E. Krein, and G. V. Samsonov. *Metallurgy of rare metals*. Jerusalem-Izrael Prog. F. Sci. Transl., 1966.

[Zhou 07] G. Zhou, P. R. Shah, T. Kim, P. Fornasiero, and R. J. Gorte. "Oxidation entropies and enthalpies of ceria–zirconia solid solutions". *Catalysis today*, Vol. 123, No. 1, pp. 86–93, 2007.

[Zhu 03] W. Zhu and S. Deevi. "A review on the status of anode materials for solid oxide fuel cells". *Materials Science and Engineering: A*, Vol. 362, No. 1, pp. 228–239, 2003.